Understanding Clay-Oil-Brine Interactions at the Nano-scale: Implications for Low-Salinity Enhanced Oil Recovery

Nipada Santha

A Thesis presented for the degree of Doctor of Philosophy

Department of Earth Sciences
University of Durham
England

July 2019

Understanding Clay-Oil-Brine Interactions at the Nano-scale: Implications for Low-Salinity Enhanced Oil Recovery

Nipada Santha

Submitted for the degree of Doctor of Philosophy

Abstract

The global crude oil consumption has sharply increased for half century; consequently, there has been a depletion of reserves and currently producing oil fields. Increasing the oil supply for the world markets can be achievable by either developing new oil reservoirs or by improving the recovery of current fields by means of enhanced oil recovery (EOR) technologies. The former choice requires new installations and infrastructure; resulting in high capital costs, environmental impact and the achievement of a productivity of only 30 to 50% of the original oil in place (OOIP). EOR techniques on the contrary do not require large capital costs and can greatly enhance the amount of recoverable oil, therefore extending the life of mature oil reservoirs. Low-salinity enhanced oil recovery (LSEOR) is one of the most interesting EOR methods because it is environmentally friendly, low cost, and has been proven to be able to achieve great effectiveness. It is a well-known fact that low salinity enhanced oil recovery (LSEOR) results from altering the wettability of the oil reservoir towards a more water-wet state. However, many theories exist regarding the determining fundamental mechanism controlling its effectiveness, with up to 17 having been invoked in the literature. Nevertheless, gaining this fundamental knowledge is crucial to increase the application of LSEOR in real-world conditions. In this work, we aim to understand how different chemical parameters (pH, concentration, cation type, ionic strength, Na^{+}:Ca^{2+} ratio) of bine, clay, and model oil affect the wettability of kaolinite (and pyrophyllite) at the nano and microscopic scale. Kaolinite having been selected because of it is ubiquitous presence in the pore space within sandstones reservoirs, and because clay minerals have been singled out as crucial to LSEOR due to their well-known chemical reactivity. To this end, various techniques were utilized to study wettability and proxy of wettability of clay surfaces, including chemical force microscopy, thermogravimetric

analysis and mass spectrometry, contact angle measurement, and, to a lesser extent, environmental scanning electron microscopy and Fourier-transform infrared spectrometry. The main parameters that influence wettability are: a) surface charge of kaolinite and pyrophyllite, b) cation type, significantly Ca^{2+} which plays a crucial role in increasing oil adhesion through cation bridging, rather than monovalent cation (Na^{+}), c) concentration, increases of Ca^{2+} concentration directly relates to more oil adsorption, whereas changes of Na^{+} concentration presents only a small effect on the amount oil adsorption, d) pH which controls the protonation state of the polar molecules (decanoic acid) as well as the charge of clay surface and can lead to increases (or decreases) in the amount of oil sorbed, e) type of functional group in oil components. The main conclusion of the theses is that surface complexation and cation bridging are the most important mechanisms in controlling oil sorption (adhesion) but at some conditions the electrical double layer effect can also play a crucial role.

Acknowledgements

First of all, I would like to gratefully thank to the Development and Promotion of Science and Technology Talents Project (DPST), the Royal Government of Thailand scholarship, for providing me with the opportunity to participate in education at a high level for almost 15 years by supporting me with full funding, and for fanning the flame of learning in sciences.

I would like to sincerely thank to my supervisor, Dr. Pablo Cubillas, who spends all of his hours continuously teaching, giving me honest comments, and greatly contributing to this research to bring it towards a successful completion. More than that, I would like to express my gratitude for his hospitality and friendship. My sincere thanks also go to my second supervisor, Prof. Chris Greenwell who openly accepted me to work in the Layered Mineral Group in Durham University. Thank you to him for his thoughtful discussions and collaborations at all stages of my research in Durham. I also extend my appreciation to The British Petroleum Company plc (BP) for partial funding and useful discussion and comments from their research team, and in particular comments from Dr. Ian Collins and Dr. Peter Salino. Special thanks to Prof. Cedric Carteret, Professor of Physical Chemistry at the University of Lorraine (France), who provided me with the precious opportunity to carry out experiments in his laboratory, and giving me useful discussions about my results. Working with all of these people as a supervisory team brings me much inspiration and provided me with a good experience which helped me to mature both academically and personally; it was a great opportunity to learn that enthusiasm and devotion are keys to success.

During my working time in Durham University, I am grateful to the laboratory staff, Mr. Douglas Carswell and Dr. Li Li, for their timely assistance during my analytical work. I cannot forget Dr. James Buckman from Heriot Watt University who immensely assisted me to conduct ESEM. Also, many thanks to all members of the Layered Mineral Group, Catriona, Nikos, Christos, Rikan, Valentina, Tom, Shansi, Zarina, Araceli and Tegan for their support, discussions, and friendship.

In a small county, Durham, I would like to thank all my friends, Ting, Pla, Milk, Themis, James, Job, Chen, Ethan, and Rob who made my life here easier and brighter. Thank you for listening my scientific and non-scientific rambles, for providing me enjoyable atmosphere during weekends, and giving me their friendship.

I heartily send my thanks and appreciation to my entire family: my beloved father and mother, my aunts and uncles for their true love and encouragement through all the

years of my education. I would also like to send my gratitude to my parents-in-law for their warm welcome and care in South Korea. Last, but not least I wish to express my sincere appreciation to my lovely husband, Jungwoo Choi, for his love and immense support. They are my strength that makes me never give up on this way. I appreciate all they have done for me and I love them with all my heart.

Declaration

The work in this thesis is based on research carried out in the Layered Mineral Group, the Department of Earth Sciences, Durham University, England. This work is my own. No part of this thesis has been submitted previously for any other degree or qualification, or any other university.

Dedicated to

My family and friends

List of Contents

List of Figures

List of Tables

1
Introduction

1.1 A global challenge

Global crude oil consumption has doubled in the last fifty years, from 45 million barrels of oil equivalent per day (mboe/d) in 1970 to 90 mboe/d in 2020, and it is projected to grow over 100 mboe/d by 2040 [1], as shown in Figure 1.1. Consequently, the oil industry is increasing production in order to meet the demands of world energy markets. This situation has accelerated the depletion of current producing fields (Figure 1.2) and has led to the paradoxical situation of higher demand and lower supply of oil, leading to a global energy challenge. To address this challenge, the oil and gas industry has looked into: 1) development of new fields, 2) production of non-conventional oil sources and 3) use of enhanced oil recovery techniques on currently-producing fields (Figure 1.2), in addition to the introduction of renewable energy technologies, as evidenced in Figure 1.1.

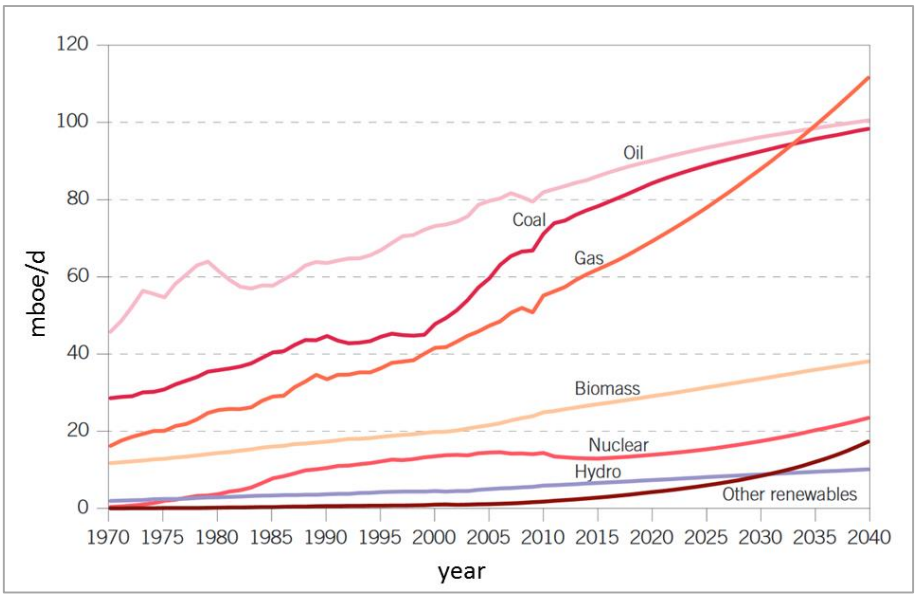

Figure 1.1 The projection of the global energy consumption by source from 1970 to 2040 (modified from World oil outlook 2015 [1]).

Development of new oil fields is expected to produce approximately 25 mboe/d in 2020, with 20% to come from yet to be found and not yet to be developed fields (Figure 1.2) [2]. However, even with these new resources the industry will struggle to increase global production or even maintain current production levels. Moreover, the exploration and development of the new oil production sites requires new infrastructure, resulting in high initial cost, intensive energy use, and a potentially large environmental impact [3, 4]. These high set-up costs, in addition to the need to increase overall oil production, have led to the development of enhanced oil recovery techniques on existing assets as being of key importance.

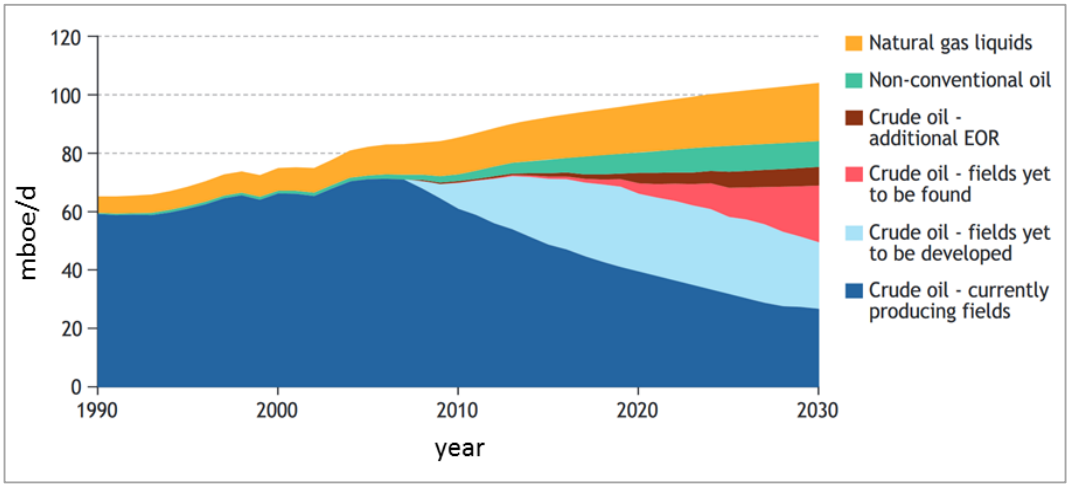

Figure 1.2 The projection of World oil production by source from 2006 to 2030 (modified from World Energy Outlook 2008 [5]).

During initial oil production, oil is produced by primary oil recovery, which is driven by the natural over pressure within the system owing to various natural physical mechanisms such as lithostatic overburden load. This recovery phase can extract between 5-10% of the OOIP (original oil in place) before the reservoir pressure equilibrates with the surface [6].

Beyond this, secondary recovery techniques are applied to maintain the pressure in the reservoir and increase the oil extraction through injection of either gas or water into an injection well. This process can produce a further 20-25% of the OOIP [7]. This means that the primary and secondary recovery methods can achieve a productivity of only 30 to 50% of the OOIP [8-10] (Figure 1.3). Therefore, the development of technologies for tertiary or enhanced oil recovery is of crucial importance to be able to meet the oil demand of the future, whereby the remaining circa 50% of the OOIP is targeted.

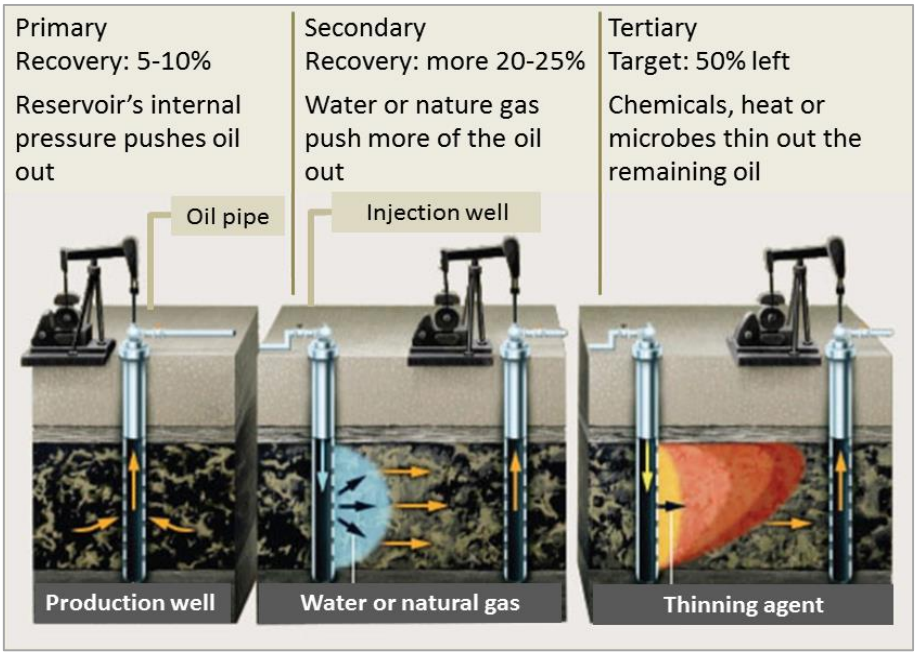

Figure 1.3 Primary, secondary, and tertiary oil production and their factors (modified from https://petgeo.weebly.com [11] accessed on 9 June 2019).

1.2 Enhanced oil recovery (EOR)

Enhanced oil recovery is defined as the set of advanced techniques for reducing oil saturation in the reservoir (and therefore, increasing oil production) that can be applied during the secondary or tertiary oil recovery phase [12-14]. These techniques mainly focus on the immobile oil which interfaces with pore-lining minerals or is trapped within the pore space of the reservoir. Enhanced oil recovery techniques include physical, chemical and biological processes [7]. One of the most widely used set of physical processes are the thermal methods which work by supplying heat to the reservoir in order to reduce oil viscosity, induce vaporization of the light hydrocarbons, and cracking of condensed hydrocarbons. Chemical processes utilize compounds such as polymers, surfactants, alkaline salt, or a mixture of them, in order to modify the interfacial tension of the aqueous and oil phases. Miscible processes normally use N_2 or CO_2 injection to displace and dissolve some of the remaining oil [15]. These methods have proven to increase final oil productivity and accelerate the rate of oil recovery from reservoirs [16]. Although enhanced oil recovery could result in optimal recovery, there are budgetary and environmental issues that should also be considered prior to their application.

1.3 Low salinity enhanced oil recovery (LSEOR)

LSEOR was documented for the first time in 1959, but its effectiveness was doubted due to variable results. For example, some coreflood experiments using diluted seawater resulted

in incremental oil recovery [17-19], however some reservoir-scale pilots showed increased oil recovery with both fresh water and diluted seawater injection [20, 21]. For this reason, LSEOR did not receive attention from the oil industry for several decades. In the last twenty years, however, low salinity water flooding EOR has gained increased interest after it was found to increase the amount of recoverable OOIP (both in secondary and tertiary recovery phases) in core-flood and sandstone oilfield tests [19, 22-25]. In fact, it has been proven that the oil recovery can be increased by up to 30 % through the use of this technique, leading up to a 70 % of total OOIP recovery [26]. Besides these proven results, LSEOR offers additional advantages over other enhanced oil recovery techniques, as injection water can be produced *in situ* from dilution or modification of seawater leading to relatively low operating costs and is also more environment-friendly and sustainable [27, 28].

1.4 Low salinity enhanced oil recovery applied to sandstone reservoirs

From the UK's perspective, for over 20 years LSEOR processes have been studied for application to the sandstone reservoirs of the North Sea, which are the UK's dominant petroleum reserves. Most of the experimental work led by BP has been performed through core flooding tests and have shown increased oil recovery during low salinity water floods [19, 29, 30]. Moreover, single-well tracer tests and log-inject-log measurements have illustrated that LSEOR indeed improves the oil recovery of reservoirs [31, 32]. This led BP to register the LoSal™ trademark in 2005, and to the decision to deploy a LSEOR operation at the Clair field, North Seas in November 2018, targeting 640 million barrels of recovery [33]. In addition, LSEOR has also shown to have the potential to be applied in other lithologies [34].

Authors have identified a series of key criteria required for the LSEOR effect to be effective These are: a) aluminosilicate clay minerals must be present within the reservoir rock [22, 29, 35]; b) polar functional groups must be contained by the oil [29, 35]; c) formation water (FW) must be present and contain divalent cations, i.e. Ca^{2+}, Mg^{2+} [22, 35, 36]; d) the salinity of the injected water must be significantly lower than that of the formation water [37-40]. Based on these key parameters, it is generally accepted that wettability alteration is the principal process responsible for LSEOR. However, many geochemical mechanisms could be responsible for this change in wettability. Sheng (2014) identified up to seventeen proposed mechanisms [28], of which the most important are thought to be: 1) multicomponent ion exchange (MIE) [22], 2) electric double layer (EDL) expansion effects [41], and 3) oil desorption by acid/base reactions [35]. These mechanisms are addressed in detail in Chapter 2. Despite the increased interest in understanding LSEOR during the last decade and the large number of studies that have

been published, many questions still remain on the identity of the most critical geochemical mechanism driving the enhanced release of oil and also about the role of clay-oil-brine interactions in this process.

1.5 Objectives

The main objective of this thesis is to understand the role of kaolinite-oil-brine interactions on the phenomena of low-salinity enhanced oil recovery. To this end, a series of fundamental experimental studies (at both nano- and micro-scale) were conducted using as-received kaolinite, model oil compounds (with polar and non-polar molecules) and brines of different compositions and pH. Kaolinite was selected for the study as it is the most commonly encountered clay mineral in most sandstone reservoirs. The studies presented in this thesis mainly focussed on understanding the dominant factors controlling the wettability alteration of the clay's surface, using various analytical techniques including: atomic force microscopy (AFM), thermal gravimetric analysis-mass spectrometry (TGA-MS) and contact angle measurements. The principal objectives of the thesis are:

To study the adhesion of several functional groups present in crude oil (-COOH and $-NH_2$) to kaolinite crystals under different brine conditions (cation identity, concentration and pH) at the atomic scale using chemical force microscopy (CFM).

To understand the role of the two types of kaolinite faces (silica tetrahedral vs. aluminol octahedral) in determining the adhesion of functional groups (-COOH and $-NH_2$) under different brine conditions (varying the brine cation identity, concentration and pH) at the atomic scale using chemical force microscopy (CFM).

To understand how the chemical properties of brine (salinity, cation type, pH, ionic strength and Na^+:Ca^{2+} ratio) determine the adhesion of model oil compounds (both polar and non-polar) to kaolinite surfaces at the microscopic scale, using contact angle measurements.

To determine how the chemical properties of brine (salinity, cation identity, pH), as connate water, determine the sorption of model oil (both polar and non-polar) to kaolinite and pyrophyllite samples, by means of TGA-MS.

1.6 Thesis outline

The thesis is divided in eight chapters.

Chapter 2. Literature review: this chapter presents a review of the current state of knowledge on low salinity enhanced oil recovery and the mechanisms behind it.

Chapter 3. Theoretical background: this chapter is divided into two sections: The first section describes clay minerals (including their physical and chemical properties), with a

focus on the two types of clay minerals used in this thesis, which are kaolinite and pyrophyllite. The second section describes the basic concept of wettability across multiple scales ranging from oil field, to microscopic and on to the molecular level.

Chapter 4. Experimental techniques: this chapter provides a description of the principles behind the different techniques utilized in the thesis.

Chapter 5. Adhesion studies at the nanoscale using chemical force microscopy. The main objective of this chapter is to understand at a fundamental (atomic) level the role of brine composition, cation type, pH and crystallographic orientation on the adhesion of three different functional groups (-COOH and NH_3^+) on kaolinite crystals This chapter has been published as a scientific paper in the journal Minerals:

Santha, N.; Cubillas, P.; Saw, A.; Brooksbank, H.; Greenwell, H.C. "Chemical Force Microscopy Study on the Interactions of COOH Functional Groups with Kaolinite Surfaces: Implications for Enhanced Oil Recovery". *Minerals* 2017, *7*, 250.

Chapter 6. The effect of salinity and pH on wettability alteration of kaolinite films studied by contact angle measurement: the main objective of this chapter was to study: 1) the effect of brine aging (representing connate or formation water) on determining the adhesion of model oil compounds (both polar and non-polar) to the siloxane (tetrahedral) kaolinite surface, and 2) the effect of brine washing (representing injection water) on altering the wettability of the kaolinite siloxane face (after aging in both connate water and model oil compounds). The effects of pH, concentration and cation type (Ca^{2+} and Na^+) were studied using microscopic contact angle measurements on oriented kaolinite films.

A significant portion of this chapter has been published on the proceedings of the 20th European Symposium on Improved Oil Recovery (IOR 2019) which was held in Pau, France from 8 - 11 April 2019 and it was available at http://earthdoc.eage.org/.

N. Santha, P. Cubillas and C. Greenwell. "*The effect of salinity and pH on wettability alteration of kaolinite films studied by contact angle measurement*". IOR 2019 – 20th European Symposium on Improved Oil Recovery, 2019. DOI: 10.3997/2214-4609.201900172.

Chapter 7. Adsorption of oil compounds on kaolinite and pyrophyllite as studied by TGA-MS: in this chapter TGA has been used to study the adsorption of non-polar/polar model oil compounds (dodecane/decanoic acid), on kaolinite and pyrophyllite after the clays have been subjected to different pre-treatments. Pre-treatments include using wet or dry clays as well as clays "aged" in solutions of NaCl and $CaCl_2$. By reproducing the sequence of events that occur on reservoir, were clay minerals are in contact with a concentrated brine solution (formation water) prior to the arrival of the oil phase, we aim to understand the factors that determine the adhesion of oil components to clay mineral phases. Kaolinite is

used due to its ubiquity in sandstone reservoirs; whereas pyrophyllite is used to discern the effect of the absence of an aluminol face on a low charge clay mineral (kaolinite has a low charge both possess two types of surfaces). This chapter is in submission to Journal of Colloid and Interface Science.

Chapter 8. Conclusions and future possibilities: this chapter summarizes the main conclusions of the theses and provides recommendations on future work on the topic of low salinity enhanced oil recovery.

1.7 References

[1] OPEC, 2015 World Oil Outlook, 2015. https://www.opec.org/opec_web/static_files_project/media/downloads/publications/WOO%202015.pdf. (Accessed 3 Jan 2019 2019).

[2] K. Aleklett, M. Höök, K. Jakobsson, M. Lardelli, S. Snowden, B. Söderbergh, The peak of the oil age–analyzing the world oil production reference scenario in world energy outlook 2008, Energy Policy 38(3) (2010) 1398-1414.

[3] J.E. Johnston, E. Lim, H. Roh, Impact of upstream oil extraction and environmental public health: A review of the evidence, Sci. Total Environ. (2018).

[4] F. Olsgard, J.S. Gray, A comprehensive analysis of the effects of offshore oil and gas exploration and production on the benthic communities of the Norwegian continental shelf, Marine Ecology Progress Series 122 (1995) 277-306.

[5] I.E. Agency, World energy outlook 2008, (2008) 501.

[6] T. Ahmed, P. McKinney, Advanced reservoir engineering, Elsevier2011.

[7] A. Muggeridge, A. Cockin, K. Webb, H. Frampton, I. Collins, T. Moulds, P. Salino, Recovery rates, enhanced oil recovery and technological limits, Philosophical Transactions of the Royal Society A: Mathematical, Physical and Engineering Sciences 372(2006) (2014) 20120320.

[8] S. Kokal, A. Al-Kaabi, Enhanced oil recovery: challenges & opportunities, World Petroleum Council: Official Publication 64 (2010).

[9] T. Castor, W. Somerton, J. Kelly, Recovery mechanisms of alkaline flooding, Surface phenomena in enhanced oil recovery, Springer1981, pp. 249-291.

[10] S. Farouq-Ali, C. Stahl, Increased oil recovery by improved waterflooding, Earth Miner. Sci.;(United States) 39(4) (1970).

[11] B. R., Recovery Techniques (Extraction of petroleum), 2019. https://petgeo.weebly.com/thereservoir.html. (Accessed 9 June 2019 2019).

[12] A.O. Gbadamosi, J. Kiwalabye, R. Junin, A. Augustine, A review of gas enhanced oil recovery schemes used in the North Sea, Journal of Petroleum Exploration and Production Technology 8(4) (2018) 1373-1387.

[13] A. Agi, R. Junin, R. Shirazi, G. Afeez, N. Yekeen, Comparative study of ultrasound assisted water and surfactant flooding, Journal of King Saud University-Engineering Sciences (2018).

[14] A.H. Abbas, W.R.W. Sulaiman, M.Z. Jaafar, A.A. Aja, Micelle formation of aerosol-OT surfactants in sea water salinity, Arabian Journal for Science and Engineering 43(5) (2018) 2515-2519.

[15] M. Blunt, F.J. Fayers, F.M. Orr Jr, Carbon dioxide in enhanced oil recovery, Energy Conversion and Management 34(9-11) (1993) 1197-1204.

[16] A. Abidin, T. Puspasari, W. Nugroho, Polymers for enhanced oil recovery technology, Procedia Chemistry 4 (2012) 11-16.

[17] J.C. Martin, The effects of clay on the displacement of heavy oil by water, Venezuelan annual meeting, Society of Petroleum Engineers, 1959.

[18] E.H. Mayer, R.L. Berg, J.D. Carmichael, R.M. Weinbrandt, Alkaline Injection for Enhanced Oil Recovery - A Status Report, J Petrol Technol 35(01) (1983) 209-221.

[19] G. Tang, N.R. Morrow, Salinity, temperature, oil composition, and oil recovery by waterflooding, SPE Reservoir Engineering 12(04) (1997) 269-276.

[20] J.C. Trantham, H.L. Patterson, Jr., D.F. Boneau, The North Burbank Unit, Tract 97 Surfactant/Polymer Pilot Operation and Control, J Petrol Technol 30(07) (1978) 1068-1074.

[21] S.A. Pursley, R.N. Healy, E.I. Sandvik, A Field Test of Surfactant Flooding, Loudon, Illinois, J Petrol Technol 25(07) (1973) 793-802.

[22] A. Lager, K.J. Webb, C. Black, M. Singleton, K.S. Sorbie, Low salinity oil recovery-an experimental investigation1, Petrophysics 49(01) (2008).

[23] H. Yildiz, N. Morrow, Effect of Brine Composition on Recovery of Moutray Crude Oil by Waterflooding,|| Petroleum Science & Engineering, (1996).

[24] A. Al-adasani, B. Bai, Y.-S. Wu, Investigating low-salinity waterflooding recovery mechanisms in sandstone reservoirs, SPE Improved Oil Recovery Symposium, Society of Petroleum Engineers, 2012.

[25] B. Suijkerbuijk, J. Hofman, D.J. Ligthelm, J. Romanuka, N. Brussee, H. van der Linde, F. Marcelis, Fundamental investigations into wettability and low salinity flooding by parameter isolation, SPE Improved Oil Recovery Symposium, Society of Petroleum Engineers, 2012.

[26] T. Austad, A. RezaeiDoust, T. Puntervold, Chemical mechanism of low salinity water flooding in sandstone reservoirs, SPE improved oil recovery symposium, Society of Petroleum Engineers, 2010.

[27] M. Jackson, J. Vinogradov, G. Hamon, M. Chamerois, Evidence, mechanisms and improved understanding of controlled salinity waterflooding part 1: Sandstones, Fuel 185 (2016) 772-793.

[28] J. Sheng, Critical review of low-salinity waterflooding, Journal of Petroleum Science and Engineering 120 (2014) 216-224.

[29] G.-Q. Tang, N.R. Morrow, Influence of brine composition and fines migration on crude oil/brine/rock interactions and oil recovery, Journal of Petroleum Science and Engineering 24(2-4) (1999) 99-111.

[30] N.R. Morrow, G.-q. Tang, M. Valat, X. Xie, Prospects of improved oil recovery related to wettability and brine composition, Journal of Petroleum science and Engineering 20(3-4) (1998) 267-276.

[31] P. McGuire, J. Chatham, F. Paskvan, D. Sommer, F. Carini, Low salinity oil recovery: An exciting new EOR opportunity for Alaska's North Slope, SPE western regional meeting, Society of Petroleum Engineers, 2005.

[32] K. Webb, C. Black, H. Al-Ajeel, Low salinity oil recovery-log-inject-log, Middle East Oil Show, Society of Petroleum Engineers, 2003.

[33] B. p.l.c., Clair Ridge, 2019. https://www.bp.com/en_gb/united-kingdom/home/where-we-operate/north-sea/north-sea-major-projects/clair-ridge.html. (Accessed 25 May 2019 2019).

[34] V. Alvarado, E. Manrique, Enhanced oil recovery: an update review, Energies 3(9) (2010) 1529-1575.

[35] T. Austad, A. Rezaeidoust, T. Puntervold, Chemical Mechanism of Low Salinity Water Flooding in Sandstone Reservoirs, SPE Improved Oil Recovery Symposium, Society of Petroleum Engineers, Tulsa, Oklahoma, USA, 2010, p. 17.

[36] A. Lager, K. Webb, C. Black, Impact of brine chemistry on oil recovery, IOR 2007-14th European Symposium on Improved Oil Recovery, 2007.

[37] M. Sharma, P. Filoco, Effect of brine salinity and crude-oil properties on oil recovery and residual saturations, SPE Journal 5(03) (2000) 293-300.

[38] Y. Zhang, N.R. Morrow, Comparison of secondary and tertiary recovery with change in injection brine composition for crude-oil/sandstone combinations, SPE/DOE symposium on improved oil recovery, Society of Petroleum Engineers, 2006.

[39] Y. Zhang, X. Xie, N.R. Morrow, Waterflood performance by injection of brine with different salinity for reservoir cores, SPE annual technical conference and exhibition, Society of Petroleum Engineers, 2007.

[40] G.R. Jerauld, K.J. Webb, C.-Y. Lin, J.C. Seccombe, Modeling Low-Salinity Waterflooding, SPE Reservoir Eval. Eng. 11(06) (2008) 1000-1012.

[41] D.J. Ligthelm, J. Gronsveld, J. Hofman, N. Brussee, F. Marcelis, H. van der Linde, Novel Waterflooding Strategy By Manipulation Of Injection Brine Composition, EUROPEC/EAGE conference and exhibition, Society of Petroleum Engineers, 2009.

2
Literature Review

As detailed in Chapter 1, global crude oil consumption has increased sharply in the previous decades and it is projected to grow even more in the near future [1]. At the same time, primary and secondary recovery methods at oil reservoirs only achieve a productivity of approximately 30% to 50% of the original oil in place (OOIP). This means that over 50% of the OOIP is not currently utilised to supply the world energy markets. To improve this situation, operators are increasingly employing so-called enhanced oil recovery (EOR) methods, and amongst these, low salinity water-flooding EOR (LSEOR) is one of the most promising. Nevertheless, LSEOR has been proven in numerous experimental and field tests, the underpinning geochemical processes that control it are still not fully understood. Many authors, however, have concluded that in order for LSEOR to work, certain conditions have to be met by the reservoir, and these are: the presence of polar crude oil components; the presence of a connate, high salinity, brine (formation water – FW); the presence of clay minerals within the reservoir rock and the so-called "salinity shock" where the injected brine water contains a significantly reduced salinity, compared to the connate water [2-6]. Sheng summarized up to seventeen possible mechanisms controlling LSEOR [6], including many geochemical mechanisms that could, in principle, be responsible for the change in wettability associated with the increase in oil production. The most important nanogeochemical mechanisms are: multicomponent ion exchange (MIE), electric double layer (EDL) effects, and desorption by acid/base reactions. These mechanisms are explained at length in this chapter.

2.1 Low salinity enhanced oil recovery (LSEOR)

LSEOR was documented for the first time by Martin who observed increased oil recovery after he used fresh water injection to displace viscous oil in highly permeable sandstone reservoir cores [7]. Martin proposed that fresh water affected the clay minerals in the rock and therefore its permeability, causing an increase in the efficiency of oil extraction [7]. Later, Reiter performed core flooding experiments using four times diluted flooding water which had chloride concentration approximately 3,100 ppm, when the connate water was 12,100 ppm of chloride ions [8]. They observed a 12.6% increase of oil recovery when using low salinity injection, compared with one at high salinity [8]. Later on, Bernard carried on further sandstone core-flooding experiments using fresh water and brines with various concentrations of NaCl [9]. He found an increase in the oil recovery when reducing the NaCl solution composition from 1 to 0.1%, so this work preliminarily established that the low salinity effect only occurs in a specific salinity range (0–1000 ppm). At that time, however, the promising results were considered somewhat ambiguous as authors reported different values of increased oil recovery under similar experimental conditions. For these reasons the technique did not receive attention from the oil industry.

In the past twenty years, however, low salinity water flooding EOR has gained increased interest after the technique has been verified to increase the amount of recoverable OOIP through both secondary and tertiary recovery tests in core floods [3, 10-12], near wellbore [13-16], inter-well [17, 18] and field scale experiments [15, 19]. The higher oil recovery obtained from low salinity injection has been called a 'low salinity effect or low salinity benefit'. The oil recovery of a reservoir after using low salinity injection (in the tertiary phase) can reach up to 70% of OOIP in high permeability and high porosity reservoirs [20], whereas for heterogeneous sandstone reservoirs, where there is a large permeability contrast between lithologies, LSEOR can push the recovery factor up to 30% OOIP [21, 22]. Beyond its effectiveness in improving oil release, low salinity enhanced oil recovery (LSEOR) is beneficial over other EOR technologies because of other factors, such as operational cost reduction and environmental considerations [23, 24]. This is because the injection water can be produced *in situ* from dilution or modification of seawater which is freely available for offshore platforms, environment-friendly and sustainable [23, 25].

2.2 Low salinity enhanced oil recovery applied to reservoirs

In general, sandstone rocks provide an ideal environment for the storage and extraction of hydrocarbons, due to its high porosity and permeability properties, compared to those of carbonate reservoirs where oil extraction occurs through natural fractures which create complex flow networks in the reservoir. Consequently, the movement of hydrocarbons in

sandstone reservoirs is better established and can be reasonably predicted, whereas in carbonate reservoirs it is often not as expected [26]. Derkani et al. review the studies of low salinity water injection in carbonate reservoirs and state that sandstone reservoirs gave more consistent oil production responses than carbonate reservoirs [27]. For these reasons, sandstone reservoirs show a high potential to implement LSEOR successfully relative to other lithology types (e.g. carbonates and turbidites) [28].

Low salinity enhanced oil recovery has been studied extensively not just through laboratory experiments but also on field tests in both carbonate [29, 30] and sandstone reservoirs [31, 32]. Yousef and colleagues [30] studied smart water injection (tertiary phase) into two well sites in Saudi Arabian carbonate reservoirs where they observed an oil recovery increase up to 11% when utilizing 100-times diluted sea water and an oil recovery increase of 5 % when using 10-times diluted seawater.

In the case of sandstone reservoirs a greater number of field studies have been performed than for carbonates. Robertson looked at the performance of low salinity injection in three different wells in Wyoming and the results confirmed the experimental results on the low salinity effect, with enhanced oil recovery been almost linearly correlated with a decrease in the injection water salinity [33]. Seccombe et al. also reported the successful application of low salinity flooding at inter-well distances of 1040 ft at BP's Endicott field, Alaska [18]. The results of core floods and single-well tracer tests identified that low salinity injection in a clayey-sandstone reservoir gave significant incremental oil recovery [18]. Vledder et al. also observed an incremental recovery of 10-15% of the original oil in place (OOIP) in sandstone reservoirs in the Omar Field, Syria [19].

2.3 Factors that control low salinity enhanced oil recovery

Most of the research on LSEOR has shown that the phenomenon depends on the complex interactions between rock, crude oil, and injected/connate brine [34-36]. Although the true nature and role of some of these interactions still needs to be fully understood and established, a series of "pre-requisite" conditions have been identified as necessary for LSEOR to occur [24]. These are listed below:

- Clay minerals must be present in the reservoir rock [2, 32, 37].
- Polar functional groups must be contained by the oil phase [2, 32].
- Initial formation water (FW) must contain divalent cations, i.e. Ca^{2+}, Mg^{2+} and high salinity [32, 38].
- Injection water must have a much lower salinity ("salinity shock") than previous injected or connate water [2, 13, 24, 39].

2.3.1 Clay minerals

Clay minerals are a frequently encountered constituent of sandstone rocks and they commonly present as a coating of detrital fine grains (known collectively as fines) on pore surfaces, or filling pore spaces. Therefore, clay minerals are generally in contact with the brine and oil phases in the reservoir. It has been suggested that clay minerals are involved with oil migration because they interact heavily with the crude oil [40-43]. Martin, who first established the fundaments of LSEOR, wrote that clay migration could influence the relative permeability and oil migration [7]. Bernard suggested that the improved recovery could be affected by either fines migration or clay swelling, through a reduction of pore volume [9]. Tang and Morrow noticed that clay mineral-containing sandstones produced more oil recovery than clean sandstone, concluding that clay minerals present in the core in order for LSEOR to be successful [2], relating the increase in oil recovery to the mobilization of mixed-wet fines, as the oil would be bound to these. At the same time, a reduction in the permeability of the rock was observed, although it never reached the catastrophic levels sometimes observed on pure-water core-flooding tests [2]. Furthermore, Lager et al. and Seccombe et al. performed experiments in the presence of clay minerals, in particular kaolinite [18, 32]. They concluded that the amount of kaolinite positively related to low salinity enhanced oil recovery. However, the well observations of Lager et al. and Zhang et al. did not show permeability reduction after low-salinity water injection [3, 39]. Cissokho et al. and Boussour et al. reported that although their experiments detected higher pressure in core samples, the results did not show an increase on the oil recovery effectiveness [44, 45].

Due to these early studies and the well-known reactivity of clay minerals many investigations on LSEOR in the last decade have been devoted to studying the role of clay type, (kaolinite, illite, montmorillonite, and chlorite), surface charge, and cation exchange capacity [46-48] on determining oil adhesion and the extent of low-salinity effect. Clementz found that highly charged montmorillonite can rapidly adsorb organic compounds [49], and Ballah reported that highly charged clay minerals were likely to respond more positively to low salinity brines [50]. However, kaolinite, which has a low charge and low cation exchange capacity (CEC), has been reported as an essential clay mineral in controlling oil sorption and LSEOR [4, 51]. Bantignies et al. reported that the interaction of kaolinite minerals with crude oil could generate an oil-wet to mixed-wet reservoir system due to asphaltene adsorption by hydroxyl groups present at the aluminol face [52]. The adsorption between kaolinite and crude oil components generates an oil wet to mixed wet reservoir system[2, 53-55]. Puntervold et al. also studied the adsorption of oil components

to kaolinite, and found that the adsorption organic bases on was strongly dependent on pH [51].

The kaolinite-oil interaction has also been studied within the context of low salinity enhanced oil recovery as well. Tang and Morrow[2] performed low salinity injection in sandstone cores containing kaolinite, as well as on the acidified version (with kaolinite removed). They observed the incremental oil recovery only on the kaolinite-containing sandstone and which indicates a key role of the presence of kaolinite on the low salinity effect. Lager et al. and Seccombe et al. carried out water injection in various clay mineral content (especially kaolinite) sandstones and they concluded that oil recovery related to amount of kaolinite [14, 56]. Shan et al. confirmed an incremental oil recovery 1.9% in the injection into kaolinite-contained core [57]. Fogden performed experiments on kaolinite films that had been in contact with crude oil, i.e. where initially oil wet [58]. They injected different low salinity brines at three different pH values and measured the changes in the deposits left on the kaolinite substrates. They reported a decrease in the amount of oil-residue left as the brines departed from neutral pH, this was explained by an increase in interfacial repulsion mechanism that resulted in an enhanced oil separation from the surfaces.

2.3.2 Polar crude oil fraction

Crude oil components can be separated into two fractions based on their polarity: non polar (saturates and aromatics), and polar (resins and asphaltenes) [59]. The majority of molecules belonging to the polar fraction contain oxygen, in the form of carboxylic acids (-COOH) or hydroxyl (-OH) groups [60-62]. A minor polar fraction contains sulphur (namely sulphides, triophenes, and mercaptans) and nitrogen compounds (including carbazoles, amides, porphyrins, and quinolines) [60]. Tang and Morrow argued that the presence of oil polar components were essential to observe LSEOR, as their experiments showed no EOR effect when refined oil was used [2]. Many subsequent studies have shown that the polar components have the highest affinity to the negatively-charged surfaces of clay minerals in the pore space [63]. Kumar et al. and Abdallah also supported the idea that the polar fraction of the crude oil was involved in the enhanced oil recovery mechanism since it induced wettability alteration [61, 64]. Zhang et al. investigated LSEOR with crude oil and refined oil; and found that the refined oil, which did not contain the polar fraction, did not give incremental recovery oil [39].

2.3.3 Connate water and Injection water salinity

Connate water or formation brine occurs naturally within the pores of reservoir. Depending on the geological evolution of the reservoir this water is normally denser and with an

increased salinity compared to seawater, with values ranging from 7000 to 270000 ppm of total dissolved solids (TDS). In addition the pH of connate waters tends to be slightly acidic (pH 5.5- 6.8) [65-67]. The dominant ions are Na^+ (6000-33000 ppm), Cl^- (10000-87000 ppm), Ca^{2+} (150-11000 ppm) and Mg^{2+} (20-1500 ppm). The pioneering studies on the role formation water has in affecting the size of the LSEOR effect were undertaken by Sharma and Filoco who observed an increase in oil recovery during core-flood experiments carried out with different concentrations of formation water containing 0.3%, 3% and 20% NaCl, and an injection brine of 3% NaCl [68]. They reported a larger increase in oil recovery when the salinity of the connate water was the lowest, and attributed this to changes in wettability towards mixed wet conditions. These results were supported by experiments performed by McGuire et al. and Zhang and Morrow who also observed improved oil recovery with lower salinity of the initial connate water [31, 69]. Shehata and Nasr-El-Din looked into the effect of cationic composition (Na^+, Ca^{2+} and Mg^{2+}) of the connate water on oil recovery [70]. They performed imbibition and core-flooding experiments and observed that higher recovery rates were obtained when the connate water had divalent cations (Ca^{2+} and Mg^{2+}) in comparison with the recovery on samples with Na^+ containing connate waters. Suijkerbuijk also observed a positive correlation between the amount of divalent cations in the formation water and the oil-wetness of sandstone cores [12]. Similar effects have been observed in carbonate rocks, where the cation identity can also play a role in determining the reactivity of mineral surfaces [71]. In this study, experiments showed additional oil recovery with increasing calcium ion concentration of the formation water.

The role of the injection brine has been the most studied factor, for obvious reasons, with studies focusing on the effect of total ion concentration or the role of different cations. Tang and Morrow were only interested in the effect of salinity and performed tests in sandstone cores using various dilution factors of the initial reservoir's brines [72]. Their investigation reported higher oil recovery with decreasing concentration of the invading brine, up to 0.01 dilution factors (1 ml brine + 99 ml water). Yildiz and Morrow studied the effect of both salinity and cations, and performed their investigations using two types of crude oil and two different brine compositions, one containing only $CaCl_2$ (2%) the other a combination of NaCl and $CaCl_2$ [10]. Depending on the type of crude oil and the sequence of connate water and water injection they observed conflicting results (for one type of oil, flooding with the higher concentration brine led to a higher oil recovery compared to the NaCl mixed with $CaCl_2$ brine, despite its lower salinity). Nevertheless, the results highlighted the role of cation identity (mono vs. divalent) on the enhanced oil recovery effect. Subsequently, Yildiz and Morrow repeated the waterflooding experiments with Prudhoe Bay crude oil and a brine containing 4% NaCl + 0.5% $CaCl_2$, this yielded a 16%

greater oil recovery than the brine containing 2% $CaCl_2$ [73]. On a separate study using the single-well chemical tracer test (SWCTT) method in an Alaskan reservoir, McGuire et al. reported that a necessary point is not only the relative percentage of cations but also their concentration, because they observed no effective oil recovery when the injected brine concentration was higher than 7000 ppm [31]. In the same way, Webb et al. tested with diluted brine at 5% (for a total concentration of 1000–4000 ppm) [74]; while Zhang et al. diluted connate water to 5% for a concentration of 1500 ppm [29]. In the latter case, they found a higher oil recovery at 1500 ppm, but no increase after a dilution of 8000 ppm, even after removing the divalent cations [29]. Jerauld et al. suggested that the proper concentration to generate the low salinity effect should be 10–25% of formation water (or 1000-2000 ppm) [75]. Rezaeidoust et al. performed tertiary oil recovery tests on outcrop sandstone and observed that low salinity water injection (around 1000 ppm) gave incremental oil recovery independ of the ion composition [76]. However, Reinholdtsen et al. and Skrettingland et al. found no low salinity EOR effects after successively flooding a reservoir core with formation water (35000 ppm), sea water and low salinity water (500 ppm NaCl) [77, 78].

From the somewhat conflicting results of these laboratory and field studies, it became clear that understanding the underlying mechanisms for low salinity EOR directly from the effects of the chemical properties (salinity, cation identity, concentration) of the connate water and injection brine on increasing oil production was not possible. Therefore, this situation has led to a large number of more fundamental studies that have attempted to shed light into these underpinning mechanisms.

2.4 LSEOR proposed mechanisms

Recently, Sheng published a review on fundamental LSEOR studies and summarized up to seventeen possible mechanisms controlling EOR [24]. Among the seventeen mechanisms, five have been deemed as the most important. These, in turn, can be divided into 2 classes: fine migration and wettability alteration following Table 2.1.

Table 2.1 Summary of the main mechanisms behind LSEOR.

Mechanism	Class	Source
Fines migration	Fines Mobilization	Tang and Morrow [2]
Salinity induced pH change	Wettability alteration	McGuire et al. [31]
Multicomponent ionic exchange	Wettability alteration	Lager et al. [56]
Electric double layer expansion	Wettability alteration	Ligthelm et al. [79]
Desorption by acid/base reaction	Wettability alteration	Austad et al. [37]

As mentioned above, some core-flooding studies have shown an increase in the oil release accompanied by the release of clay minerals [2, 7, 9]. During low salinity water floods, the switch from high salinity (connate water) to low salinity can induce clays to be less stable and mobilize (due to an increase on the zeta potential, or net surface charge, produced by the lower concentration of charge-balancing cations, which, in turn, increases the repulsion forces among particles), carrying any oil particles attached to them or increasing sweep efficiency by decreasing the flow rate of high permeability channels and forcing water through additional paths. This, however can lead to such a large permeability reduction that oil recovery is increased [3, 39]. Nevertheless, other studies have shown no reduction in permeability or evidenced fines migration, and at the same time observed an increase in oil recovery with low-salinity water injection [4, 56]. Therefore, it can be concluded that this physical effect is not the underlying mechanism behind LSEOR [3].

Wettability alteration, conversely, can be described as an umbrella term covering the result of the interplay between the chemical properties of connate and injection brine, the chemical composition of oil, and the clay mineral surfaces, and therefore, it can explain the low-salinity effect. Many authors have indeed invoked wettability alteration as the principal mechanism responsible for LSEOR [24, 80-83].

However, many nanogeochemical mechanisms could, in turn, be responsible for this alteration in wettability. These nanogeochemical scale mechanisms could be summarized as: 1) multicomponent ion exchange (MIE) [56], 2) electric double layer (EDL) effects [79] and 3) desorption by acid/base reactions [37].

2.4.1 Multicomponent ion exchange (MIE)

Lager et al. introduced the concept of the MIE mechanism for LSEOR. This concept had already been applied to the study of fresh waters into saline aquifers [56] where it was observed that different cations types (monovalent *vs.* divalent) will "compete" differently for sorption into mineral surfaces [84]. Based on this, Lager et al. hypothesized that cations present in the formation water would be adsorbed to the clay mineral surface, which is negatively charged [56]. These authors pointed out that MIE will have an effect in disturbing 4 of the 8 possible organo-mineral binding mechanisms defined by Sposito [85]. These include: cation exchange, cation bridging, ligand exchange and water bridging (Figure 2.1). Cation exchange is the mechanism where positively charged organics ions (amine/ammonium groups or nitrogen-containing heterocyclic compounds) replace the inorganics cations that are normally screening the charge of clay surface. Cation bridging occurs when divalent cations (Ca^{2+} or Mg^{2+}), act as an electrostatic bridge or an ionic bond between the negatively-charged clay surface and the negatively-charged polar oil molecule,

leading to an ionic binding phenomenon. Ligand bridging involves the formation of a covalent bond between the oxygen atom of an organic group and a divalent cation, which is also bonded to an oxygen atom on the mineral surface. Water bridging occurs when the water molecules of a partially hydrated, multivalent cation (balancing the negatively charge of the clay surface), binds to a polar, functional group in the organic molecules through a dipole–dipole interaction.

Based on these mechanisms, it is easy to see how the presence of cations in the reservoir (from the connate or formation water) will lead to the formation of metal-organic bonding complexes at clay surfaces after oil migration, altering the mineral surfaces to become oil-wet. Then, during the low salinity brine injection phase, the divalent cations bridging the oil molecules would be substituted by monovalent cations at the negatively charged clay surface leading to the release of the oil molecules. Lager et al. supported these assumptions through their investigations of North Slope cores using low salinity waterflooding, when they observed a considerable decline of Mg^{2+} and Ca^{2+} concentration in the effluent [56]. This meant that Ca^{2+} and Mg^{2+} cations were strongly adsorbed on the rock matrix. To further test the MIE hypothesis, they devised an experiment whereby a core was saturated with a brine containing only Na^{+} and was then aged in oil. In this way no cation bridging would occur (no divalent cations). This was followed with a high salinity flood that lead to high oil recovery (48%) and no-further oil recovery was observed with a subsequent low salinity injection. Therefore, it was proven that the presence of divalent cations in the connate water would lead to the binding of oil-molecules through cation bridging. However, the MIE mechanism cannot explain the experiments of Sharma and Filoco who observed that oil recovery increased in the initial and tertiary injection, even though the injected water had the same composition. This means that Na^{+} might not substitute Ca^{2+}, at least in certain conditions [68]. Ligthelm et al. pointed that oil desorption was controlled mainly by ionic strength, not ion exchange of oil-cation-clay bridges [79]. They performed three brine injections with the same ionic strength: monovalent-only brine and mixed monovalent divalent solution; and observed increasing oil recovery in all cases.

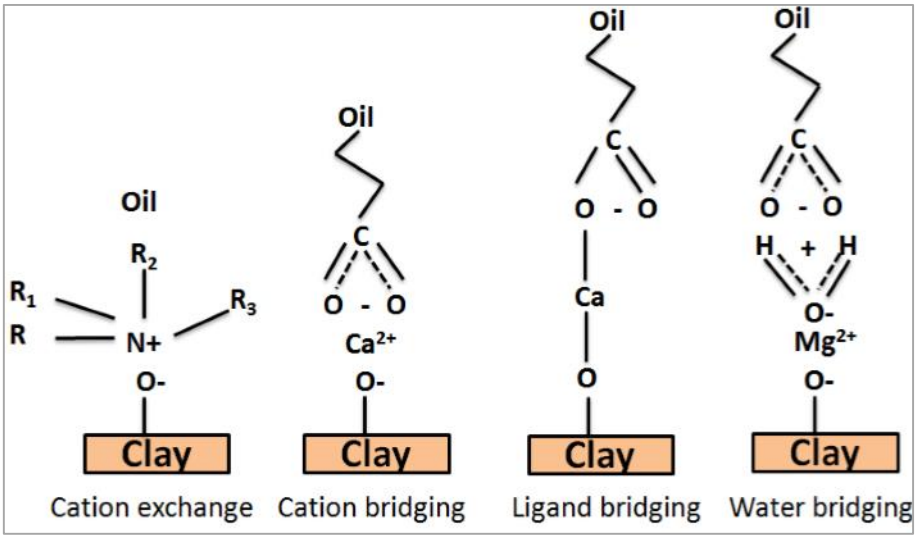

Figure 2.1 Schematic of the MIE mechanisms occurring between clay mineral surfaces and crude oil during low salinity water injection (taken from Lager et al. [56]).

2.4.2 Electric double layer (EDL) effect

One of the well-known aspects of the brine, clay mineral, and oil interaction is the electrical double layer, a concept which was first introduced by Helmholtz [86]. He suggested that a mineral's surface charge can be neutralized by an excess of opposite-charge ions from the solution as they are attracted to it [86]. Then, Gouy and Chapman further developed the Helmholtz's model, considering the ionic concentration and the charge distribution as a function of the distance from the surface [87, 88]. Afterwards, the model was extended by Stern to include the Stern layer [89]. This model is illustrated in Figure 2.2 and it can be divided in two layers: an inner layer (Stern layer) and a diffuse layer or outer section. At the inner area the counter ions (de-solvated) adhere on the surface and are therefore motionless. This is followed by the shear plane, where the ions can drift away into the diffuse layer. At the outer layer, the ions are mobile with dispersion from the surface until the electrical potential becomes zero; in other words, the density of adsorbed ions decreases away from the interface until it reaches that of the bulk solution. Ligthelm et al. suggested EDL expansion as the dominant mechanisms of oil desorption. In their paper they argued that although the multivalent cations, namely Mg^{2+} and Ca^{2+}, from the brine bonded to the negatively charged oil and clay surfaces, the removal of the organic polar compounds was caused by the reduction of the solution's ionic strength not by an ion exchange reaction [79]. They reached this conclusion after a tertiary injection of low salinity brine composed of only Na^{+} (which followed a secondary flushing with a much higher NaCl concentration) still yielded an increase in oil recovery. Since the secondary flooding had already removed all divalent cations (via MIE) only the expansion of the EDL

could have led to the oil release [79]. This situation is described schematically in Figures 2.3a and 2.3b. At high salinity the repulsive electrostatic forces decrease in extent allowing oil molecules to approach and bind to the clay's surface, but when the concentration decreases, the EDL expands and oil molecules are "expelled" away from the surface. The end result of this effect would be a change in the wettability state of the clay. Similarly, Nasralla and Naser-El-Din tested the EDL effect by controlling the low salinity concentration and changing pH which also resulted in the modification of electrical surface charge [90]. They revealed that when the pH increased in the low salinity brine, there were protons to screen off the negative charge. As a consequence, there was a weaker negatively charge at the brine-mineral and oil-brine interfaces which produced enough repulsion forces to push each other or to modify the wettability state to water-wet [90]. Lee et al. conducted measurements of the diffuse layer around silica particles dispersed in brine and oil, with the electrochemical properties of the surface of the particles adjusted to be clay-like. They found that high salinity (high ionic strength) reduced the size of the diffuse layer, which provided greater adsorption, and also that divalent cations shad a larger effect in reducing the width of the layer, compared to monovalent cations [91]. This suggested that the electrical double layer is related to the expansion of the diffuse layer, and that the type of ion in solution is a significant key into the adsorption/desorption mechanism. More recently, a study of the adhesion between organic functional groups and different reservoir rocks (chalk and sandstones) was undertaken using atomic force/chemical force microscopy where mineral surfaces were directly exposed to the brine [92]. This has allowed them to directly measure the adhesion between functionalised probes and mineral surfaces at the nanoscale in order to study the mechanisms leading to EOR. Hassenkam et al. measured adhesion between a $COOH/COO^-$ functionalised AFM tip, which represents oil, and the surfaces of sandstone samples (outcrop and reservoir core) in the presence of several brines. The authors found that at high brine concentration (sea water) adhesion was observed between the mineral surface (i.e chalk, quartz, calcite) and the –COOH tip [92]. The authors suggested that high concentration produced a narrow electrical double layer, while salinity decreases extends the length of the electrical double layer. Hilner et al. used chemical force microscopy (CFM) to measure the adhesion between quartz grains and $-CH_3$ functionalized tips and they found a significant decrease in adhesion between nonpolar oil molecules and natural quartz surfaces at a similar threshold salinity to that at which the low salinity effects is typically observed [93]. Their results show a release of the organic molecules at low salinity conditions, which is consistent with the EDL mechanism [92, 93]. However, their study focused only on non-polar oil ($-CH_3$ terminated tip), which

may not offer a full picture of the mechanism as many authors have stated that the presence of a polar fraction is a necessary condition for LSEOR to occur [2, 35].

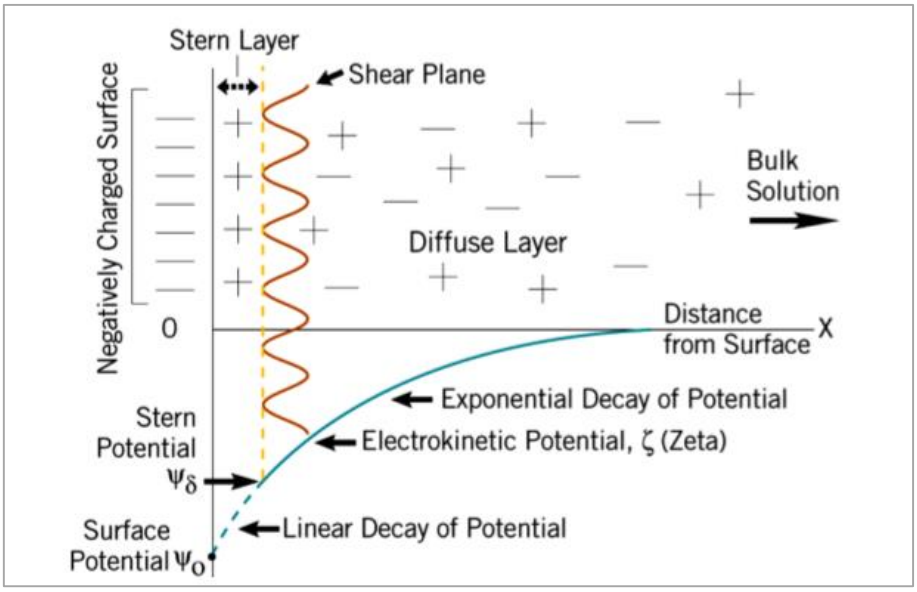

Figure 2.2 Model of the Electrical Double Layer at a charged interface in aqueous solution (taken from Fairhurst [94]).

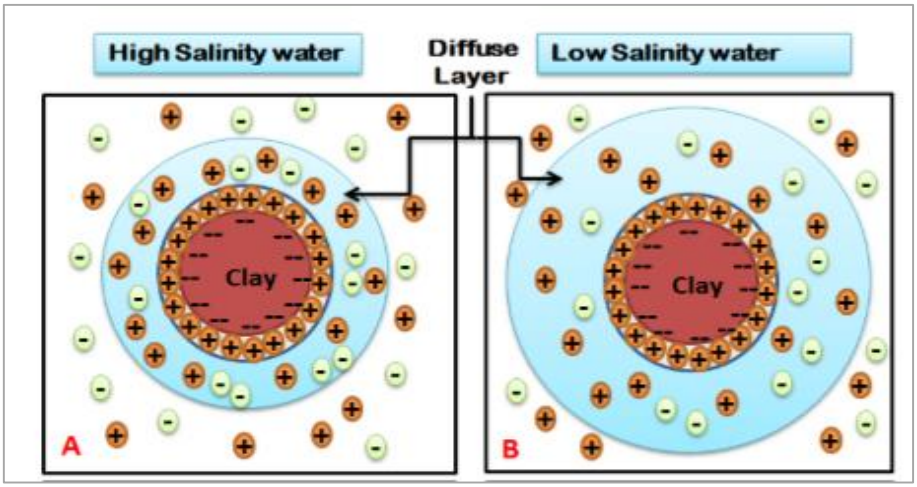

Figure 2.3 Schematic diagram showing the variation in thickness of the electrical double layer with salinity. In the case of high salinity water (high ionic strength), the double layer is more compact (left); under low salinity conditions, the double layer expands (right).

2.4.3 Desorption by acid/base reaction

Austad et al. proposed that pH could alter the wettability state and cause oil desorption, after brine injection they noticed an increase in the effluent pH [37]. This was explained as

an initially local pH increase close to the clay's surfaces due to ion exchange reactions. The authors' explanation for the mechanisms is summarized in Figure 2.4. As the clays possess a negative charge at their surface, cations in the connate water will adsorb to it. In addition positively-charged oil molecules (basic) could directly attach to a clay surface, whereas other acidic polar molecules (such as those containing –COOH groups) could adsorb through hydrogen bonding on protons already adsorbed to the clay mineral's surface (especially at low pH values) [95]. During the low salinity injection, after the amount of Ca^{2+} in the bulk has been reduced, the clay surface will exchange its charge balancing Ca^{2+} with protons following Equation 2.1 [37].

$$\text{Clay-}Ca^{2+} + H_2O \leftrightharpoons \text{Clay-}H^{+} + Ca^{2+} + OH^{-} \qquad \text{(Equation 2.1)}$$

As a result of the reaction described in Equation 1, hydroxyl ions (OH^-) will be released, resulting in a local increase of pH near the clay mineral surface [37]. Under these basic conditions, the crude oil functional groups can deprotonate to combine with OH^- via simple acid-base reactions, forming H_2O (Equations 2.2 and 2.3). The deprotonated functional group will interact more weakly with the clay mineral and therefore will be released into the solution.

$$\text{Clay-}RNH_3^{+} + OH^{-} \leftrightharpoons \text{Clay} + RNH_2 + H_2O \qquad \text{(Equation 2.2)}$$

$$\text{Clay-}RCOOH + OH^{-} \leftrightharpoons \text{Clay} + RCOO^{-} + H_2O \qquad \text{(Equation 2.3)}$$

These reactions lead to the release of oil and therefore will alter the mineral surface to a more water-wet state. Austad et al. found experimental proof of this mechanism by observing an increase in pH on the effluent solutions of core-flooding test with low salinity brines [37]. However, they also pointed out that the total pH change would be controlled by the release, or presence in the injection water, of divalent cations, which will tend to bind with the released OH^- groups. In addition they pointed out that the effectiveness of the described mechanism will depend on the type of clay present in the reservoir as their relative affinity for protons or other cations will be different [96].

Further evidence for and against the mechanism of oil desorption by acid/base reaction can be found in the literature. One of the studies that supported it is that by Rezaeidoust et al. who injected high salinity NaCl brine into a set of cores aged in crude oil and $CaCl_2$, and the results showed that a low concentration of NaCl in the injected brine produced the largest pH increase of the effluent, from, approximately 6 to 8 [76]. They

explained this by indicating that Ca^{2+} ions are initially sorbed to the clay surface, and then they are replaced by a proton from a molecule of water, releasing a hydroxyl group and the Ca^{2+} as indicated in the following equation 2.4.

$$[Clay^{-}...Ca^{2+}] + H_2O \leftrightharpoons [Clay^{-}....H^{+}] + OH^{-} + Ca^{2+} \qquad \text{(Equation 2.4)}$$

Several other studies, however, present evidence against the local pH effects. For example, Cissokho et al. and Hege et al. performed core-flooding experiments and reported that the pH increase they observed in produced water was not related to and improved oil recovery [44, 97]. Similar results were reported by Kia et al. who carried out on core-injection experiments using fresh water and brines at pH 6.5 [98]. They observed an increase of produced water pH to 8.3, but could not relate it to an increase in oil release.

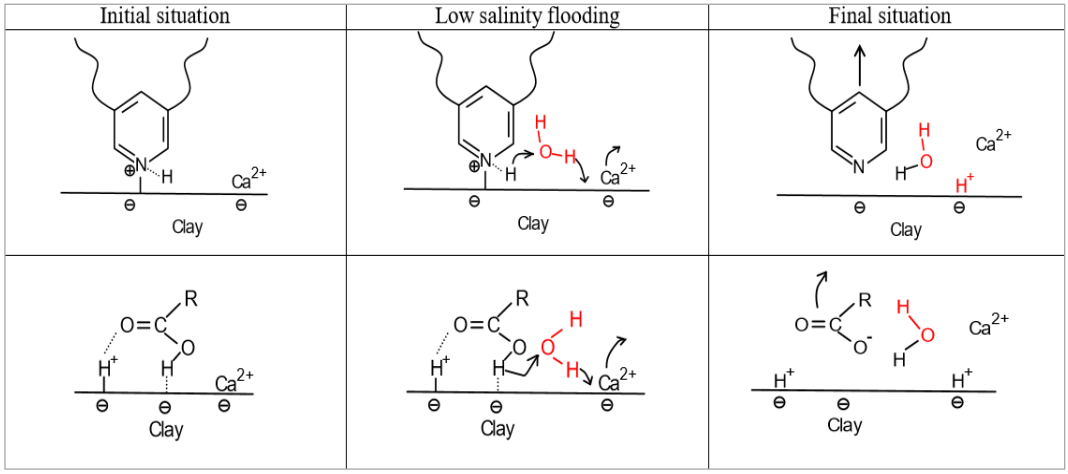

Figure 2.4 Diagram of the proposed mechanisms of the desorption of basic (upper) and acidic (lower) materials in low salinity enhanced oil recovery at pH 5 (taken from Austad et al. [37]).

2.5 Summary

As has been established through this review chapter, to date, the main requirements accepted for the occurrence of the low salinity effect on a reservoir are: the presence of clay minerals, polar oil, formation water and a low salinity brine "shock", however, no consensus exists on how these factors are related through the nanogeochemical mechanisms that drive LSEOR nor on which of the nanogeochemical mechanism is the most crucial. The main reason behind the lack of agreement in the literature results from the inherent large scale and heterogeneity of the sandstone reservoir system. Published studies tend to focus on either coreflooding experiment or limited pilots at reservoirs, both of which cannot

completely encompass the inherent heterogeneity. At the same time, and even though, some authors have performed studies at the nanoscale, a significant amount of them have focused on either proxy surfaces or actual rock fragments (both sandstone and carbonate), and only a reduced number have focused on clay minerals/surfaces which are the most reactive to both brine and oil in the reservoir. For these reasons, this work aims to study the interactions of kaolinite (and in some cases pyrophyllite as comparison) with model oil (in some cases to specific functional groups (-COOH and -NH_2,) and brines with fixed chemical properties (concentration, cations types, pH, ionic strength, and ratio of Na^+:Ca^{2+}. To gain a relative broad understanding on these interactions at both the micro and nanoscale, experiments encompass the use of chemical force microscopy, contact angle measurements on clay films and TGA-MS to quantify the model oil adsorption/desorption (a proxy of wettability) on kaolinite and pyrophyllite.

2.6 References

[1] OPEC, 2015 World Oil Outlook, 2015. https://www.opec.org/opec_web/static_files_project/media/downloads/publications/WOO%202015.pdf. (Accessed 3 Jan 2019 2019).

[2] G.-Q. Tang, N.R. Morrow, Influence of brine composition and fines migration on crude oil/brine/rock interactions and oil recovery, Journal of Petroleum Science and Engineering 24(2-4) (1999) 99-111.

[3] A. Lager, K.J. Webb, C. Black, M. Singleton, K.S. Sorbie, Low salinity oil recovery-an experimental investigation1, Petrophysics 49(01) (2008).

[4] A. Lager, K. Webb, C. Black, Impact of brine chemistry on oil recovery, IOR 2007-14th European Symposium on Improved Oil Recovery, 2007.

[5] D.J. Ligthelm, J. Gronsveld, J. Hofman, N. Brussee, F. Marcelis, H. van der Linde, Novel Waterflooding Strategy By Manipulation Of Injection Brine Composition, EUROPEC/EAGE conference and exhibition, Society of Petroleum Engineers, 2009.

[6] J. Sheng, Critical review of low-salinity waterflooding, Journal of Petroleum Science and Engineering 120 (2014) 216-224.

[7] J.C. Martin, The effects of clay on the displacement of heavy oil by water, Venezuelan annual meeting, Society of Petroleum Engineers, 1959.

[8] P.K. Reiter, A water-sensitive sandstone flood using low salinity water, University of Oklahoma, 1961.

[9] G.G. Bernard, Effect of floodwater salinity on recovery of oil from cores containing clays, SPE California Regional Meeting, Society of Petroleum Engineers, 1967.

[10] H.O. Yildiz, N.R. Morrow, Effect of brine composition on recovery of Moutray crude oil by waterflooding, Journal of Petroleum science and Engineering 14(3-4) (1996) 159-168.

[11] A. Al-adasani, B. Bai, Y.-S. Wu, Investigating low-salinity waterflooding recovery mechanisms in sandstone reservoirs, SPE Improved Oil Recovery Symposium, Society of Petroleum Engineers, 2012.

[12] B. Suijkerbuijk, J. Hofman, D.J. Ligthelm, J. Romanuka, N. Brussee, H. van der Linde, F. Marcelis, Fundamental investigations into wettability and low salinity flooding by parameter isolation, SPE Improved Oil Recovery Symposium, Society of Petroleum Engineers, 2012.

[13] K. Webb, C. Black, H. Al-Ajeel, Low salinity oil recovery-log-inject-log, Middle East Oil Show, Society of Petroleum Engineers, 2003.

[14] J.C. Seccombe, A. Lager, K.J. Webb, G. Jerauld, E. Fueg, Improving Wateflood Recovery: LoSalTM EOR Field Evaluation, SPE Symposium on Improved Oil Recovery, Society of Petroleum Engineers, Tulsa, Oklahoma, USA, 2008, p. 19.

[15] P. McGuire, J. Chatham, F. Paskvan, D. Sommer, F. Carini, Low salinity oil recovery: An exciting new EOR opportunity for Alaska's North Slope, SPE western regional meeting, Society of Petroleum Engineers, 2005.

[16] F. Abdulla, H.S. Hashem, B. Abdulraheem, M. Al-Nnaqi, A. Al-Qattan, H. John, P. Cunningham, P. Briggs, R. Thawer, First EOR trial using low salinity water injection in the greater burgan field, Kuwait, SPE Middle East Oil and Gas Show and Conference, Society of Petroleum Engineers, 2013.

[17] A. Lager, K.J. Webb, I.R. Collins, D.M. Richmond, LoSal Enhanced Oil Recovery: Evidence of Enhanced Oil Recovery at the Reservoir Scale, SPE Symposium on Improved Oil Recovery, Society of Petroleum Engineers, Tulsa, Oklahoma, USA, 2008, p. 12.

[18] J. Seccombe, A. Lager, G. Jerauld, B. Jhaveri, T. Buikema, S. Bassler, J. Denis, K. Webb, A. Cockin, E. Fueg, Demonstration of low-salinity EOR at interwell scale, Endicott field, Alaska, SPE improved oil recovery symposium, Society of Petroleum Engineers, 2010.

[19] P. Vledder, I.E. Gonzalez, J.C. Carrera Fonseca, T. Wells, D.J. Ligthelm, Low salinity water flooding: proof of wettability alteration on a field wide scale, SPE Improved Oil Recovery Symposium, Society of Petroleum Engineers, 2010.

[20] T. Austad, A. Rezaeidoust, T. Puntervold, Chemical Mechanism of Low Salinity Water Flooding in Sandstone Reservoirs, SPE Improved Oil Recovery Symposium, Society of Petroleum Engineers, Tulsa, Oklahoma, USA, 2010, p. 17.

[21] M. Baviere, Basic Concepts in Enhanced Oil Recovery Processes, (1991) 432.

[22] T. Castor, W. Somerton, J. Kelly, Recovery mechanisms of alkaline flooding, Surface phenomena in enhanced oil recovery, Springer1981, pp. 249-291.

[23] M.D. Jackson, J. Vinogradov, G. Hamon, M. Chamerois, Evidence, mechanisms and improved understanding of controlled salinity waterflooding part 1: Sandstones, Fuel 185 (2016) 772-793.

[24] J.J. Sheng, Critical review of low-salinity waterflooding, Journal of Petroleum Science and Engineering 120(0) (2014) 216-224.

[25] B.G. Thomas, A. Iliyas, T.E. Johansen, K. Hawboldt, F. Khan, Towards sustainable and environmentally friendly enhanced oil recovery in offshore Newfoundland, Canada, Offshore Technology Conference, Offshore Technology Conference, 2010.

[26] S. Ehrenberg, P. Nadeau, Sandstone vs. carbonate petroleum reservoirs: A global perspective on porosity-depth and porosity-permeability relationships, AAPG bulletin 89(4) (2005) 435-445.

[27] M. Derkani, A. Fletcher, W. Abdallah, B. Sauerer, J. Anderson, Z. Zhang, Low salinity waterflooding in carbonate reservoirs: review of interfacial mechanisms, Colloids and Interfaces 2(2) (2018) 20.

[28] V. Alvarado, E. Manrique, Enhanced oil recovery: an update review, Energies 3(9) (2010) 1529-1575.

[29] Y. Zhang, X. Xie, N.R. Morrow, Waterflood Performance By Injection Of Brine With Different Salinity For Reservoir Cores, SPE Annual Technical Conference and Exhibition, Society of Petroleum Engineers, Anaheim, California, U.S.A., 2007, p. 12.

[30] A.A. Yousef, S.H. Al-Saleh, A. Al-Kaabi, M.S. Al-Jawfi, Laboratory investigation of the impact of injection-water salinity and ionic content on oil recovery from carbonate reservoirs, SPE Reservoir Eval. Eng. 14(05) (2011) 578-593.

[31] P.L. McGuire, J.R. Chatham, F.K. Paskvan, D.M. Sommer, F.H. Carini, Low Salinity Oil Recovery: An Exciting New EOR Opportunity for Alaska's North Slope, Society of Petroleum Engineers, 2005.

[32] A. Lager, K.J. Webb, I.R. Collins, D.M. Richmond, LoSal Enhanced Oil Recovery: Evidence of Enhanced Oil Recovery at the Reservoir Scale, Society of Petroleum Engineers, 2008.

[33] E.P. Robertson, Low-salinity waterflooding to improve oil recovery-historical field evidence, Idaho National Laboratory (INL), 2007.

[34] W.G. Anderson, Wettability Literature Survey-Part 3: The Effects of Wettability on the Electrical Properties of Porous Media, J Petrol Technol 38(12) (1986) 1371-1378.

[35] J. Buckley, Y. Liu, S. Monsterleet, Mechanisms of wetting alteration by crude oils, Spe J 3(01) (1998) 54-61.

[36] A. Bera, K. S, K. Ojha, T. Kumar, A. Mandal, Mechanistic Study of Wettability Alteration of Quartz Surface Induced by Nonionic Surfactants and Interaction between Crude Oil and Quartz in the Presence of Sodium Chloride Salt, Energy Fuels 26(6) (2012) 3634-3643.

[37] T. Austad, A. RezaeiDoust, T. Puntervold, Chemical mechanism of low salinity water flooding in sandstone reservoirs, SPE improved oil recovery symposium, Society of Petroleum Engineers, 2010.

[38] A.M. Shehata, H.A. Nasr-El-Din, Reservoir Connate Water Chemical Composition Variations Effect on Low-Salinity Waterflooding, Abu Dhabi International Petroleum Exhibition and Conference, Society of Petroleum Engineers, 2014.

[39] Y. Zhang, X. Xie, N.R. Morrow, Waterflood performance by injection of brine with different salinity for reservoir cores, SPE annual technical conference and exhibition, Society of Petroleum Engineers, 2007.

[40] N. Hancock, A. Taylor, Clay mineral diagenesis and oil migration in the Middle Jurassic Brent Sand Formation, Journal of the Geological Society 135(1) (1978) 69-72.

[41] K. Bjørlykke, Lithological control on fluid flow in sedimentary basins, Fluid flow and transport in rocks, Springer1997, pp. 15-34.

[42] Ø. Marcussen, T.E. Maast, N.H. Mondol, J. Jahren, K. Bjørlykke, Changes in physical properties of a reservoir sandstone as a function of burial depth–The Etive Formation, northern North Sea, Marine and Petroleum Geology 27(8) (2010) 1725-1735.

[43] K. Bjørlykke, J. Jahren, Open or closed geochemical systems during diagenesis in sedimentary basins: Constraints on mass transfer during diagenesis and the prediction of porosity in sandstone and carbonate reservoirs, AAPG bulletin 96(12) (2012) 2193-2214.

[44] M. Cissokho, H. Bertin, S. Boussour, P. Cordier, G. Hamon, Low salinity oil recovery on clayey sandstone: Experimental study, Petrophysics 51(05) (2010).

[45] B. Soraya, C. Malick, C. Philippe, H.J. Bertin, G. Hamon, Oil recovery by low-salinity brine injection: Laboratory results on outcrop and reservoir cores, SPE Annual Technical Conference and Exhibition, Society of Petroleum Engineers, 2009.

[46] S. Wu, A. Firoozabadi, Effect of salinity on wettability alteration to intermediate gas-wetting, SPE Reservoir Eval. Eng. 13(02) (2010) 228-245.

[47] A. Borysenko, B. Clennell, R. Sedev, I. Burgar, J. Ralston, M. Raven, D. Dewhurst, K. Liu, Experimental investigations of the wettability of clays and shales, Journal of Geophysical Research: Solid Earth 114(B7) (2009).

[48] S. Yariv, The effect of tetrahedral substitution of Si by Al on the surface acidity of the oxygen plane of clay minerals, Int. Rev. Phys. Chem. 11(2) (1992) 345-375.

[49] D.M. Clementz, Clay stabilization in sandstones through adsorption of petroleum heavy ends, J Petrol Technol 29(09) (1977) 1,061-1,066.

[50] J. Ballah, Oil recovery by low salinity waterflooding, Université Pierre et Marie Curie-Paris VI, 2017.

[51] T. Puntervold, A. Mamonov, Z. Aghaeifar, G.O. Frafjord, G.M. Moldestad, S. Strand, T. Austad, Role of Kaolinite Clay Minerals in Enhanced Oil Recovery by Low Salinity Water Injection, Energy Fuels 32(7) (2018) 7374-7382.

[52] J.-L. Bantignies, C.C. dit Moulin, H. Dexpert, Wettability contrasts in kaolinite and illite clays: characterization by infrared and X-ray absorption spectroscopies, Clays Clay Miner. 45(2) (1997) 184-193.

[53] J. Yang, Z. Dong, M. Dong, Z. Yang, M. Lin, J. Zhang, C. Chen, Wettability alteration during low-salinity waterflooding and the relevance of divalent ions in this process, Energy & Fuels 30(1) (2015) 72-79.

[54] E.V. Lebedeva, A. Fogden, T.J. Senden, M.A. Knackstedt, Kaolinite Wettability—The Effect of Salinity, pH and Calcium, Society of Core Analysts (2010).

[55] E.V. Lebedeva, A. Fogden, Adhesion of oil to kaolinite in water, Environ. Sci. Technol. 44(24) (2010) 9470-9475.

[56] A. Lager, K.J. Webb, C.J.J. Black, M. Singleton, K.S. Sorbie, Low Salinity Oil Recovery - An Experimental Investigation1, Petrophysics 49(01) (2008) 8.

[57] S. Jiang, P. Liang, Y. Han, Effect of Clay Mineral Composition on Low-Salinity Water Flooding, Energies 11(12) (2018) 3317.

[58] A. Fogden, Removal of crude oil from kaolinite by water flushing at varying salinity and pH, Colloids Surf. Physicochem. Eng. Aspects 402 (2012) 13-23.

[59] T. Fan, J. Wang, J.S. Buckley, Evaluating crude oils by SARA analysis, SPE/DOE improved oil recovery symposium, Society of Petroleum Engineers, 2002.

[60] W.G. Anderson, Wettability Literature Survey- Part 1: Rock/Oil/Brine Interactions and the Effects of Core Handling on Wettability, J Petrol Technol 38(10) (1986) 1125-1144.

[61] K. Kumar, E. Dao, K.K. Mohanty, AFM study of mineral wettability with reservoir oils, Journal of Colloid and Interface Science 289(1) (2005) 206-217.

[62] E. Haugvaldstad, Clay minerals in sandstone reservoirs: implications for" smart water" injection, University of Stavanger, Norway, 2014.

[63] S. Strand, T. Puntervold, T. Austad, Water based EOR from clastic oil reservoirs by wettability alteration: A review of chemical aspects, Journal of Petroleum Science and Engineering 146 (2016) 1079-1091.

[64] W. Abdallah, J.S. Buckley, A. Carnegie, J. Edwards, B. Herold, E. Fordham, A. Graue, T. Habashy, N. Seleznev, C. Signer, Fundamentals of wettability, Technology 38(1125-1144) (1986) 268.

[65] R.H. Worden, Dawsonite cement in the Triassic Lam Formation, Shabwa Basin, Yemen: a natural analogue for a potential mineral product of subsurface CO2 storage for greenhouse gas reduction, Mar. Pet. Geol. 23(1) (2006) 61-77.

[66] P.K. Egeberg, P. Aagaard, Origin and evolution of formation waters from oil fields on the Norwegian shelf, Appl. Geochem. 4(2) (1989) 131-142.

[67] K. Bjørlykke, R. Aagaard, P.K. Egeberg, S.P. Simmons, Geochemical constraints from formation water analyses from the North Sea and the Gulf Coast Basins on quartz, feldspar and illite precipitation in reservoir rocks, The geochemistry of reservoirs, Geological Society Special Publication 80 (1995) 17.

[68] P.R. Filoco, M.M. Sharma, Effect of brine salinity and crude oil properties on relative permeabilities and residual saturations, SPE Annual Technical Conference and Exhibition, Society of Petroleum Engineers, 1998.

[69] Y. Zhang, N.R. Morrow, Comparison of secondary and tertiary recovery with change in injection brine composition for crude-oil/sandstone combinations, SPE/DOE symposium on improved oil recovery, Society of Petroleum Engineers, 2006.

[70] A.M. Shehata, H.A. Nasr-El-Din, Laboratory investigations to determine the effect of connate-water composition on low-salinity waterflooding in sandstone reservoirs, SPE Reservoir Eval. Eng. 20(01) (2017) 59-76.

[71] P. Zhang, M.T. Tweheyo, T. Austad, Wettability alteration and improved oil recovery by spontaneous imbibition of seawater into chalk: Impact of the potential determining ions Ca2+, Mg2+, and SO42−, Colloids Surf. Physicochem. Eng. Aspects 301(1-3) (2007) 199-208.

[72] G. Tang, N.R. Morrow, Salinity, temperature, oil composition, and oil recovery by waterflooding, SPE Reservoir Engineering 12(04) (1997) 269-276.

[73] H.O. Yildiz, M. Valat, N.R. Morrow, Effect of Brine Composition On Wettability And Oil Recovery of a Prudhoe Bay Crude Oil, J. Can. Pet. Technol. 38(01) (1999) 6.

[74] K. Webb, C. Black, I. Edmonds, Low salinity oil recovery–The role of reservoir condition corefloods, IOR 2005-13th European Symposium on Improved Oil Recovery, 2005.

[75] G.R. Jerauld, K.J. Webb, C.-Y. Lin, J.C. Seccombe, Modeling Low-Salinity Waterflooding, SPE Reservoir Eval. Eng. 11(06) (2008) 1000-1012.

[76] A. Rezaeidoust, T. Puntervold, T. Austad, A Discussion of the Low-Salinity EOR Potential for a North Sea Sandstone Field, SPE Annual Technical Conference and Exhibition, Society of Petroleum Engineers, Florence, Italy, 2010, p. 12.

[77] A.J. Reinholdtsen, A. RezaeiDoust, S. Strand, T. Austad, Why Such a Small Low Salinity EOR–Potential from the Snorre Formation?, IOR 2011-16th European Symposium on Improved Oil Recovery, 2011.

[78] K. Skrettingland, T. Holt, M.T. Tweheyo, I. Skjevrak, Snorre Low-Salinity-Water Injection--Coreflooding Experiments and Single-Well Field Pilot, SPE Reservoir Eval. Eng. 14(02) (2011) 182-192.

[79] D.J. Ligthelm, J. Gronsveld, J. Hofman, N. Brussee, F. Marcelis, H. van der Linde, Novel Waterflooding Strategy By Manipulation Of Injection Brine Composition, EUROPEC/EAGE Conference and Exhibition, Society of Petroleum Engineers, Amsterdam, The Netherlands, 2009.

[80] N.R. Morrow, Wettability and its effect on oil recovery, J Petrol Technol 42(12) (1990) 1,476-1,484.

[81] N.R. Morrow, G.-q. Tang, M. Valat, X. Xie, Prospects of improved oil recovery related to wettability and brine composition, Journal of Petroleum science and Engineering 20(3-4) (1998) 267-276.

[82] S. Berg, A.W. Cense, E. Jansen, K. Bakker, Direct Experimental Evidence of Wettability Modification By Low Salinity, Petrophysics 51(05) (2010) 9.

[83] R.A. Nasralla, H.A. Nasr-El-Din, Impact of Electrical Surface Charges and Cation Exchange on Oil Recovery by Low Salinity Water, SPE Asia Pacific Oil and Gas Conference and Exhibition, Society of Petroleum Engineers, Jakarta, Indonesia, 2011, p. 18.

[84] A.J. Valocchi, R.L. Street, P.V. Roberts, Transport of ion-exchanging solutes in groundwater: Chromatographic theory and field simulation, Water Resour. Res. 17(5) (1981) 1517-1527.

[85] G. Sposito, Geochemistry in soil science, Encyclopedia of Soil Science (2008) 283-289.

[86] H.V. Helmholtz, Studien über electrische Grenzschichten, Annalen der Physik 243(7) (1879) 337-382.

[87] M. Gouy, Sur la constitution de la charge électrique à la surface d'un électrolyte, J. Phys. Theor. Appl. 9(1) (1910) 457-468.

[88] D.L. Chapman, LI. A contribution to the theory of electrocapillarity, The London, Edinburgh, and Dublin philosophical magazine and journal of science 25(148) (1913) 475-481.

[89] A. Stern, On the counter-transference in psychoanalysis, Psychoanal. Rev. 11(2) (1924) 166-174.

[90] R.A. Nasralla, H.A. Nasr-El-Din, Double-Layer Expansion: Is It a Primary Mechanism of Improved Oil Recovery by Low-Salinity Waterflooding?, (2014).

[91] S.Y. Lee, K.J. Webb, I. Collins, A. Lager, S. Clarke, M. O'Sullivan, A. Routh, X. Wang, Low salinity oil recovery: increasing understanding of the underlying mechanisms, SPE improved oil recovery symposium, Society of Petroleum Engineers, 2010.

[92] T. Hassenkam, L.L. Skovbjerg, S.L.S. Stipp, Probing the intrinsically oil-wet surfaces of pores in North Sea chalk at subpore resolution, Proceedings of the National Academy of Sciences of the United States of America 106(15) (2009) 6071-6076.

[93] E. Hilner, M.P. Andersson, T. Hassenkam, J. Matthiesen, P.A. Salino, S.L.S. Stipp, The effect of ionic strength on oil adhesion in sandstone – the search for the low salinity mechanism, Scientific Reports 5 (2015) 9933.

[94] D. Fairhurst, An Overview of the Zeta Potential - Part 1: The Concept, 2013. https://www.americanpharmaceuticalreview.com/Featured-Articles/133232-An-Overview-of-the-Zeta-Potential-Part-1-The-Concept/. (Accessed 2 Fabuary 2018).

[95] A. Meunier, Clays, Springer Science & Business Media2005.

[96] R. Kleven, J. Alstad, Interaction of alkali, alkaline-earth and sulphate ions with clay minerals and sedimentary rocks, Journal of petroleum Science and Engineering 15(2-4) (1996) 181-200.

[97] H.C. Wideroee, H. Rueslaatten, T. Boassen, C.M. Crescente, M. Raphaug, G.H. Soerland, H. Urkedal, Investigation of low salinity water flooding by NMR and CryoESEM, Proceedings

of the 2010 International Symposium of the Society of Core Analysts, Halifax, Nova Scotia, 2010, pp. 4-7.

[98] S. Kia, H.S. Fogler, M. Reed, Effect of salt composition on clay release in Berea sandstones, SPE International Symposium on Oilfield Chemistry, Society of Petroleum Engineers, 1987.

3
Theoretical background

This chapter is divided into two sections. In the first section, an overview on the chemical and physical properties of clay minerals, including a discussion on their surface interactions (as described by DLVO theory) is given. Special attention is given to kaolinite and pyrophyllite, the two clay mineral types selected for study in this thesis. In the case of kaolinite, which is important as major constituent of reservoir sandstones, it has very specific properties owing to its 1:1 clay structure, with siloxane-terminated and aluminol-terminated faces. Pyrophyllite, although not commonly present in sandstones, was selected for being a low-charge 2:1 clay (i.e. displaying only siloxane-terminated faces), making it ideal to act as a control to discern the role of the aluminol phase by comparison to kaolinite. The second part of the chapter devoted to the concept of wettability. Wettability is defined as a predilection for a solid surface to form a contact with one type of fluid rather than another. In view of this, and within the context of oil recovery, a mineral can be designated following the wetting phase preference such as water-wetting, oil-wetting and mixed-wetting. The concept of wettability is normally utilized to explain rock, oil, and brine interaction in oil reservoirs. Studies have shown that altering the wettability of a reservoir toward more water-wet increases enhanced oil recovery. Understanding how wettability changes on the fundamental minerals in the reservoir (clay minerals) as a function of salinity and polar fraction of the crude oil is therefore crucial to gain an understanding of the nanogeochemical mechanism involved in LSEOR.

3.1 Clay minerals

Clay minerals are the most important class of accessory minerals in sandstone rocks. From a LSEOR perspective, they are one of the most important minerals as they are heavily exposed on the pore space, and therefore in contact with both formation water and oil. Clay content in sandstone reservoirs has been used to predict the quality of the source rock, to determine its diagenetic history and reservoir quality, since clay minerals control crucial parameters such as permeability and porosity preservation in reservoirs [1-6]. Clay minerals have also been found to chemically interact with the crude oil phase, and therefore to play a role in controlling oil migration [7-10]. Clay minerals can also affect the physical mechanisms and chemical reactions involved in EOR processes [11-14].

3.1.1 Mineralogy

From a strictly geological point of view, the term clay strictly refers to mineral grains with a size of less than 2 μm, without consideration of their chemical composition, while clay minerals naturally can have a maximum particle diameter of 3.9 μm with specific and different chemical properties [15]. From a mineralogical point of view, a clay mineral is a phyllosilicate (with an alumino silicate composition), which has a distinctly layered structure. Within each layer there is repetition of two different types of sheets, one tetrahedral and the other octahedral.

The tetrahedral sheet is formed by SiO_4 tetrahedra where a Si^{4+} (sometimes substituted by Al^{3+} and Fe^{3+}) central cation is coordinated to four oxygen anions (O^{2-}) (located at the vertices of each tetrahedral) (Figure 3.1a). Tetrahedra are interconnected by sharing three oxygens (called basal) out of four across a common plane, with the remaining, or apical, oxygen "pointing" in a perpendicular direction to the plane and binding to the octahedral sheet. This arrangement leads to a hexagonal network of tetrahedra across the layers, as shown in Figure 3.1b.

The octahedral sheet consists of either divalent cations (i.e. Mg^{2+}, Fe^{2+}) or trivalent cations (i.e. Al^{3+}), bonded to six oxygens or hydroxyl groups, in an octahedral coordination as shown in Figure 3.1c. Each unit cell of the layer is composed of three octahedral positions. When the central cation is trivalent, only two positions need to fill in order to have a charge-balanced structure, and in this case, the layer is referred as being dioctahedral (Figure 3.1d). On the other hand when is composed of divalent cations, all three octahedral are occupied by the metal, resulting in a trioctahedral or brucite-like layer.

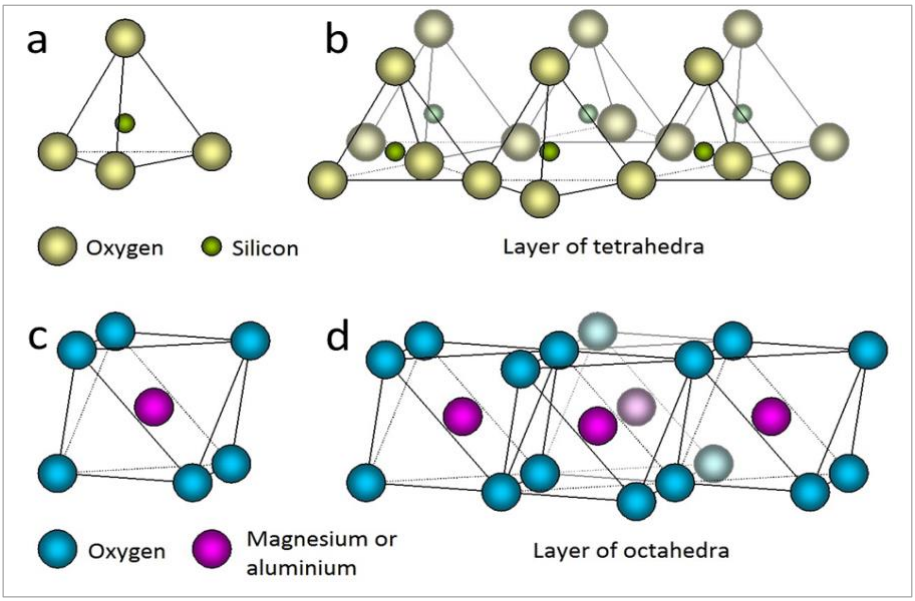

Figure 3.1 a) Single tetrahedral. b) Tetrahedral layer. c) Single octahedral. d) Octahedral layer (taken from Jordan [16]).

3.1.2 Classification of clay minerals

Clay minerals are classified into two main types following the ratio of combination between tetrahedral and octahedral layers. Bilayer phyllosilicates are composed of one tetrahedral (T) and one octahedral (O) layer and therefore, are referred as 1:1, or OT clay minerals. Each bilayer is formed from the bonding of the apices of a tetrahedral sheet to some of the hydroxyl groups of an octahedral sheet. This arrangement results in some unbound hydroxyl groups to be located on the apical oxygen plane and will be oriented differently depending on the type of octahedral layer. Each bilayer has two faces, one composed of the unshared plane of the octahedral sheet (terminated in -OH groups), and the other, composed of distorted basal oxygen atoms of the tetrahedral sheet as shown in Figure 3.2. The bilayer units are then bonded to each other via Van der Waal forces and hydrogen bonds (between octahedral sheet hydroxyl groups and the oxygen atoms of the adjacent silica sheet. An example of a 1:1 clay mineral is kaolinite, the main clay mineral used in this study, which will be further discussed in Section 3.3.1.

Trilayer phyllosilicates are composed of a single octahedral sheet "sandwiched" by two tetrahedral layers, and is therefore normally referred as 2:1 type, or TOT clay minerals. In this case, hydroxyl groups of both sides of the octahedral sheet condense with apical oxygens of two tetrahedral sheets (Figure 3.2b). This arrangement means that both "external" faces of each trilayer sheets are terminated by basal oxygen atoms of the tetrahedral sheets. Bonding between trilayer units occur mainly though van der Waals interactions [15].

In its purest form, the tetrahedral sheet would be composed of Si^{4+}; however, isomorphic substitutions are common whereby Al^{3+} enters the structure, which leads to a negatively charged surface. For the octahedral sheet, it is also very common to observe substitutions of either Al^{3+} (on dioctahedral layers) or Mg^{2+} (on trioctahedral layers). These substitutions can be homovalent (for example Al^{3+} being substituted by Fe^{3+}, or Mg^{2+} replaced by Fe^{2+}), or heterovalent (for example Fe^{3+} for Fe^{2+}). For the latter case, a negative charge is produced by the substitution. The unbalanced charge of the bilayer or trilayer clay is the by the intercalation of individual cations and/or hydrated cations within the interlayer space.

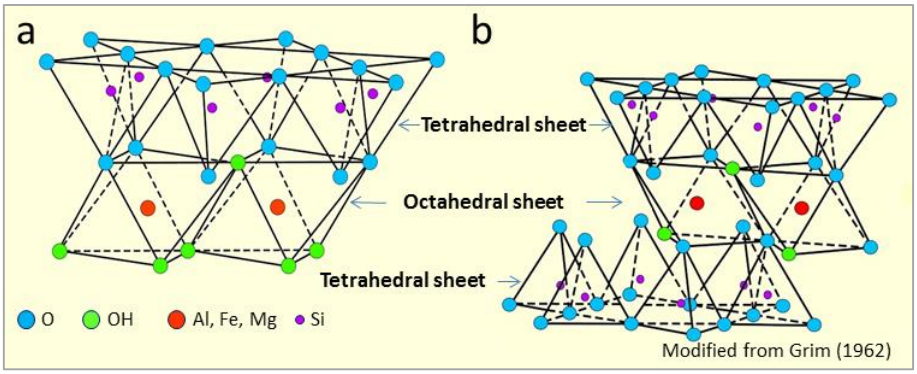

Figure 3.2 Bilayer and trilayer clay minerals (taken from USGS [17]).

At the edge of the clay, the tetrahedral silica sheets and octahedral alumina sheets are "broken", resulting in cleaved Si-O-Si or Al-O-Al bonds. This gives rise to the formation of silanol (Si-OH) and aluminol (Al–OH) groups. The protonation state (and therefore charge) of both Si-OH and Al-OH sites are pH-dependent [18]. For the Si-O sites, the high valency of the Si^{4+} sites means that the hydroxyl groups are strongly bonded and therefore less affected by pH variations (at low pH no protonation occurs), whereas deprotonation to $Si-O^-$ only occurs above pH 8. In contrast, Al-OH will protonate below pH 2 (given rise to a positively charged edge) and deprotonate above pH 5 leading to a negatively charged edge. The importance of these sites can be relatively high in kaolinite crystals, due to their relatively small size (10 nm to 10 μm) [15].

The 1:1 and 2:1 mineral groups are subdivided into eight major sub-groups according type of octahedral sheet (dioctahedral or trioctahedral), its composition (and therefore charge imbalance) and type of interlayer. Each sub-group show different physical and chemical properties [15] presented in Table 3.1.

Table 3.1 Clay mineral types, Int. Sp is stranded for internal space (modified after Meunier [15], Gupta [19], Brindley and Brown [20]).

Type	Octahedral sheet	Crystalline feature	Group	Sub-group	Species
1:1	Dioctahedral	Electric charge of layer ~ 0 T+O+ Int. Sp =7Å	serpentine-kaolin	kaolins	kaolinite Dickite, Nacrite
	Trioctahedral	-		serpentines	Lizardite, Antigorite, Chrysotile
1:2	Dioctahedral	Electric charge of layer ~ 0 T+O+ Int. Sp = 9Å	talc-pyrophyllite	pyrophyllite	pyrophyllite
	Trioctahedral	-		talc	Talc, Willemseite
	Dioctahedral	Electric charge of layer = -0.2 to -0.6 T+O+T+Int. Sp = 10 -18Å Int. Sp: cations ± hydrated (Ca^{2+}, Na^{+})	smectite	montmoril-lonites	Montmoril-lonite, beidellite
	Trioctahedral			saponites	saponite, hectorite
	Dioctahedral	Electric charge of layer = -0.6 to -0.9 T+O+T+Int. Sp = 10 -15Å Int. Sp: cations ± hydrated (Ca^{2+}, Na^{+})	vermiculite	dioctahedral vermiculite	dioctahedral vermiculite
	Trioctahedral			trioctahedral vermiculite	trioctahedral vermiculite
	Dioctahedral	Electric charge of layer = -1 T+O+T+ Int.Sp =10Å Int. Sp : not hydrated cations (K^{+}, Na^{+})	mica	dioctahedral mica	muscovite
	Trioctahedral			trioctahedral mica	phlogopite, biotite, lepidolite
	Dioctahedral	Electric charge of layer = -2 T+O+T+ Int. Sp.=10 Å Int.Sp: not hydrated cations (Ca^{2+})	brittle mica	dioctahedral Brittle Mica	margarite
	Trioctahedral			trioctahedral brittle Mica	clintonite
	Dioctahedral	Variable LEC T+O+T+O (Int. Sp.) =14 Å octahedral layers	Chlorite	dioctahedral chlorite	donbassite
	Trioctahedral			trioctahedral chlorite	clinichlore
	Dioctahedral, Trioctahedral			trioctahedral dioctahedral chlorite	cookeite

3.2 Clay's properties

3.2.1 Cation exchange capacity (CEC)

As the discussion in Section 3.1.1 notes, cation substitution in both tetrahedral and octahedral layers produce charge imbalance on the clay mineral surface. This fact leads to

the description of clay minerals as cation exchange minerals. Cation exchange capacity is defined as the clay's capacity to retain the interlayer cations. It is measured as the quantity of interlayer cations trapped at a given pH (usually pH 7) and is expressed in milliequivalents (meq) per 100 g of clay [15]. Table 3.2 lists approximate CEC values for different types of clay minerals. The values are dependent on the type of clay (i.e. surface ions)[21, 22], as well as other factors such as crystal size (surface area) [23, 24]. In addition, the physical and chemical properties of surrounded solutions, including pH (which affects the net surface charge and that of edge sites) and the cation type play a role. The cation's affinity on the clay surface decreased in the order of $Cs^{+} < Rb^{+} < K^{+} < Na^{+} < Li^{+} < Ba^{2+} < Sr^{2+} < Ca^{2+} < Mg^{2+}$ [25, 26] and concentration (effect to the thickness of the electric double layer is reduced (as explained in Section 3.2.3.1)[27].

Table 3.2 CEC and other physical properties of the main types of clay minerals (modified from Meunier, [15]).

Property	Kaolinite	Pyrophyllite	Illite	Montmoril-lonite	Chlorite
Structure	1:1	2:1	2:1	2:1	2:1:1
Surface area (m^2/gm)	15-25	11-13	50-110	30-80	140
Surface charge	Low negative	Low negative	Negative	Negative	Positive
CEC (meq/100g)	3-15	1.3-1.6	10-40	80-150	10-40
Particle size (μm)	5-0.5	Large sheets to 0.17	Large sheets to 0.5	2-0.1	5-0.1

3.2.2 Inter-particle forces

Clay minerals are typically small-sized phyllosilicates of less than 2 μm, and therefore could show both the behaviour of a suspension (sizes larger than 1 μm) or colloid (sizes between 1nm to 1μm) [28]. However, inter-particle forces will also play a role on the type of behaviour displayed, as agglomeration of crystals (even if they are individually colloid-sized) could lead to variation of their rheological properties [29]. As natural colloids, clay minerals carry an electrical charge which can produce adsorptive or repulsive forces between crystals. In a stable state, repulsive forces prevail and the colloids remain in dispersion. On the contrary, if the colloids are stabilised electrostatically (i.e. adsorption and repulsion are equal), the colloidal substance aggregates and settles. Whether the inter-particle forces are attractive or repulsive depends on the net charge on the material surface. In general the colloid phenomenon is controlled by the inter-particle interactions, which are mainly of three types: hydrodynamics, Brownian forces, and colloid forces [29].

Hydrodynamic forces drive colloid motion depending on particle concentration, and size distribution. Brownian force arises from thermal dynamics and helps retain the equilibrium of a suspension, but motion decrease with the size of particles [29]. Colloidal forces are discussed in more detail bellow due to their relevance to the project.

3.2.2.1 Colloidal force

Colloidal forces or clay interaction's force consists of the sum of all attractive (e.g. van der Waals and bridging) and repulsive forces (electrical double layer and hydration) [30]. In the simplest case, a clay suspension without flocculants and surfactants can be described by the DLVO theory (Dejarguin and Landau, Verwey and Overbeek) [31, 32]. This theory combines the effects of the attractive van der Waals interactions with the repulsive forces arising from the overlap of the electrostatic double layers between particles (which shifts as a function of the distance between them) as can be explained by equation 3.1 [33].

$$V_T = V_A + V_R \qquad \text{(Equation 3.1)}$$

The total potential energy of the interaction between two similar particles is the summation of attractive interaction and repulsive as expressed in Equation 3.1. Where V_T is the total energy (J); V_A is the attractive energy (J); V_R is the repulsive energy (J) [29].

Van der Waals or attractive forces arise from either temporary or permanent induced dipoles in atoms, molecules, or colloid particles. These forces can be divided in three types: 1) interactions between two permanent dipoles (Keesom forces); 2) interactions between a permanent dipole and an induced dipole (Debye forces); and 3) interactions between two induced dipoles (London forces) [34, 35]. Van der Waals interaction potentials decrease inversely with the sixth power of the distance between particles, as expressed in Equation 3.2.

$$\omega_{(r)} = \frac{C_T}{r^6} = \frac{C_k + C_d + C_L}{r^6} \qquad \text{(Equation 3.2)}$$

Where $\omega_{(r)}$ is interaction potential (J); C_T is constant of interaction (Jm^6); r is the distant molecules centre to centre (m); C_k is the constant interaction of Keesom force(Jm^6); C_d is the constant interaction of Debye (Jm^6); C_k is the constant interaction of London (Jm^6) [34]. Van der Waals interactions are relatively weak at long ranges, with an effect up to 100 nm from a particle's surface [34, 36], and it has the markedly potential interaction when the distance between two particles is smaller than the radius of the particles [30].

At the microscopic scale, however, the summation of the interaction potentials, shows a much slower decay with distance than when considering the interaction of just two molecules. Hamaker studied these microscopic interactions theoretically and proposed an interaction coefficient, which subsequently has been referred as the Hamaker constant (A_H) [37]. The total potential energy between two spheres is presented in Equation 3.3.

$$F = \frac{-A_H}{6D^2}\frac{R_1 R_2}{R_1 + R_2} \qquad \text{(Equation 3.3)}$$

$$F = \frac{-A_H R}{6D^2} \qquad \text{(Equation 3.4)}$$

Where F is total force (N); A_H is Hamaker constant; D is distant between two particle's surface (m.); R_1 is radius of sphere 1 (m.); R_2 is radius of sphere 2 (m.), whereas that between a sphere and a flat surface is shown in Equation 3.4 (where F is total force; A_H is Hamaker constant; D is distant between two particle's surface; R is radius of sphere) [34]. It can be seen in both equations that the Van der Waals forces decrease hyperbolically with the distance. The electrical double layer theory explains the electrical repulsive force that develops between similarly charged particles in solution.

The electrical double layer concept was initially developed by Helmholtz in 1879 by means of a simple model which explained the neutralization of a negatively-charged surface using the adsorption and desorption of counter-ions. This model was later improved by Gouy (1910), Chapman (1913) and later by Stern (1924). The Stern model, which offers the most realistic explanation of the charge distribution away from a charged surface, consists of two layers: an inner region, or Stern layer, and diffuse layer (Figure 3.3). At the inner, or Stern layer, counter ions adhere on the surface and are therefore motionless; this is followed by a shear plane, where the ions can drift away from the particle. The electrical potential at the shear plane is the so-called zeta potential, which can be measured experimentally [38-40]. Beyond the shear plane resides the outer layer, where ions are mobile and where, in some occasions, a deficit of ions of the same charge as the surface may occur. As the distance away from the surface increases, the density of adsorbed ions decreases until reaching its bulk composition. As the bulk is charged balanced, the electrical potential away from the surface will become zero at this point (Figure 3.3).

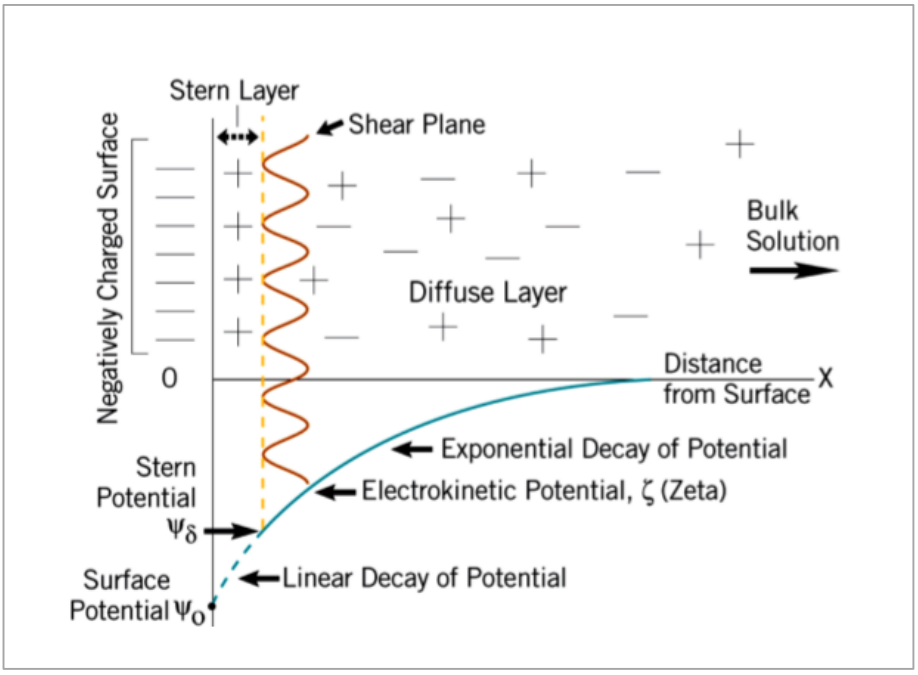

Figure 3.3 Model of an electrical double layer next to a charged interface in aqueous solution (taken from Fairhurst, [41]).

The thickness of the electrical double layer is referred as the Debye length (K^{-1}) and can be calculated from Equation 3.5.

$$K^{-1} = \left(\frac{\varepsilon_0 \varepsilon k_B T}{e^2 I}\right)^{0.5} \qquad \text{(Equation 3.5)}$$

Where ε_0 is the dielectric constant of the bulk vacuum ($CV^{-1}m^{-1}$); ε is dielectric constant of solution ($CV^{-1}m^{-1}$); k_B is Boltzmaan constant (JK^{-1}); e is charge of electron(C); T is temperature of charge of electron (K); I is ionic strength [42].

As can be seen from Equation 3.5, the thickness of the electrical field is dependent on the ionic strength (I) of the solution, which can be calculated using Equation 3.6,

$$I = 0.5 \sum(n_i z_i^2) \qquad \text{(Equation 3.6)}$$

Where n_i is concentration of ions (mol/L); z_i is charge of ions. According to Equation 3.5, therefore, the size of the electrical double layer is inversely related to the ionic strength of the solution. In low ionic strength solutions, a small amount of the counter-ions would partially screen the surface charge, resulting in a relatively expanded double layer (Figure 3.4). This would lead to relatively strong repulsive forces between the particles that would operate at relatively large distances. In a colloidal suspension, it is this type of force that

will keep the particles dispersed in solution. In contrast, in high ionic strength of solutions, a larger amount of counter ions will be attracted to the charged surface and, therefore, its charge will be more strongly screened, resulting in a narrower electrical double layer (Figure 3.4) and weaker repulsive forces. In a colloidal suspension this would allow particles to move closer together and "precipitate" or "flocculate" out of solution.

In conclusion, DLVO theory is a very useful tool to predict the behaviour of clay minerals in electrolyte solutions, and also to understand how their charged surfaces interact with other charged (or polar) molecules, including organic compounds. Therefore, it has been used successfully to try to understand low salinity EOR effects [43-46].

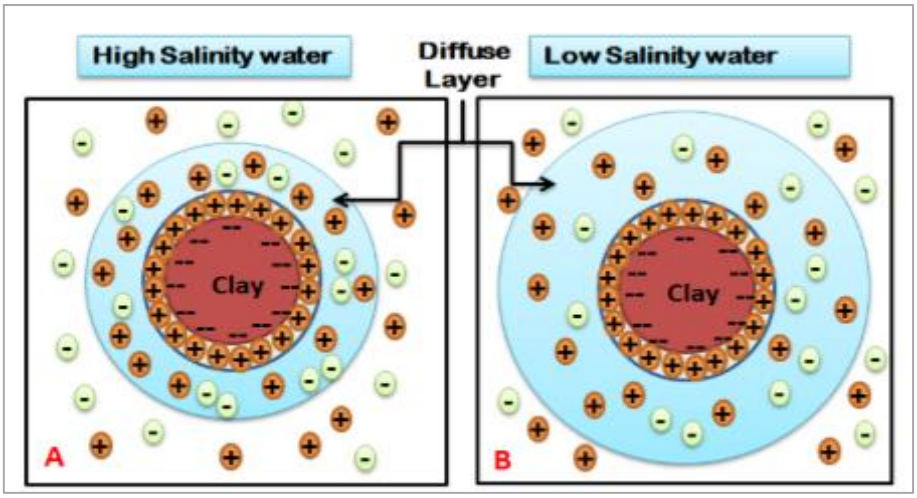

Figure 3.4 Schematic diagram showing how double layer width changes as function of the salinity of the bulk solution on which the charged particle is immersed. a) At high salinity conditions, the amount of adsorbed counter-ions is large and therefore the length of the double layer is small. b) At low salinity conditions, the size of the double layer increases (i.e. the repulsion force range of action increases).

3.3 Kaolinite and pyrophyllite

The two different layered minerals used for this study are described below.

3.3.1 Kaolinite

Kaolinite is one of the most abundant clay minerals in sandstones, and in particular in North Sea petroleum reservoirs [7, 9]. Most kaolinite is produced by chemical weathering or low-temperature hydrothermal alteration of other aluminum silicate minerals such as feldspar and mica [47]. It is normally present in sandstones as a matrix and/or coating within its pores and normally exhibits a pseudo hexagonal morphology. The platy crystals can then

be stacked in a booklet-type pattern or on a worm-like, vermiform pattern (forming a so-called kaolinite-verm) [48]. Those laminated stacks show a ratio of diameter to thickness that can vary from 2 up to 36 [49, 50].

Kaolinite, which has the chemical formula $Al_4Si_4O_{10}(OH)_8$ (SiO_2, 46.54%; Al_2O_3, 39.50%; and H_2O, 13.96%) [51] is a 1:1 dioctahedral clay, with each layer composed of a single silica tetrahedral sheet (siloxane face) and an aluminol hydroxide (or brucite-type) octahedral sheet (aluminol face). As described before, these two sheets bound together via sharing of the apical oxygen ion on the silica tetrahedral plane with some of the basal oxygen atoms (from an OH- group) of the octahedral sheet [15]. The binding between the layers occurs mainly through hydrogen bonds (hydroxyls and basal oxygen groups) with some contributions from Van der Waals and electrostatic forces.

Kaolinite's structure can have minor isomorphous substitutions of Al^{3+} for Si^{4+} in the tetrahedral face and of Mg^{2+} for Al^{3+} in the alumina octahedral layer, but in general these are considered almost negligible. Despite this, the basal plane of kaolinite has been found to carry a permanent negative charge, while the edges (formed by silanol and aluminol groups) could be positive or negative depending on pH [52, 53]. In recent years, the kaolinite surface has been studied at the nano-scale (mostly using atomic force microscopy). These studies have shown that the surface charge of kaolinite is, in fact, dependent on pH [54, 55] as shown in Figure 3.5, although it is always negative. The same study showed that the aluminol face charge was more heavily dependent on the pH, as expected due to the protonation and deprotonation of the aluminol groups, and "switched" from being positively-charged to negatively-charged within the pH range of 6-7 (Figure 3.5). More recently, Liu et al. calculated the effect of ionic strength on the surface potential of the kaolinite basal planes (Figure 3.6), with their results showing a decrease with increased ionic strength, corresponding to an increase in counter ions at the surface and compression of the electrical double layer [55]. All this information indicates that the kaolinite basal surface sites are also electrical active sites and, therefore, can adsorb and exchange ions and/or larger molecules depending on the pH and electrolyte concentration [15, 56]. Finally, AFM results have also shown that the siloxane face exhibit a low degree of hydrophobicity (similar to that of talc and pyrophyllite), whereas the aluminol phase is hydrophilic (due to the presence of hydrogen-bonding, hydroxyl groups) [57]. The adsorption of cations on kaolinite's surface was studied by Kopittke et al. [58]. They found that the cation's affinity for kaolinite follows the order of $Na^+ > Ca^{2+}$; however, the study of Kleven and Alstad showed that Ca^{2+} has higher affinity than Na^+. This contradiction probably indicates that the electrolyte concentration also controls the ion adsorption [59].

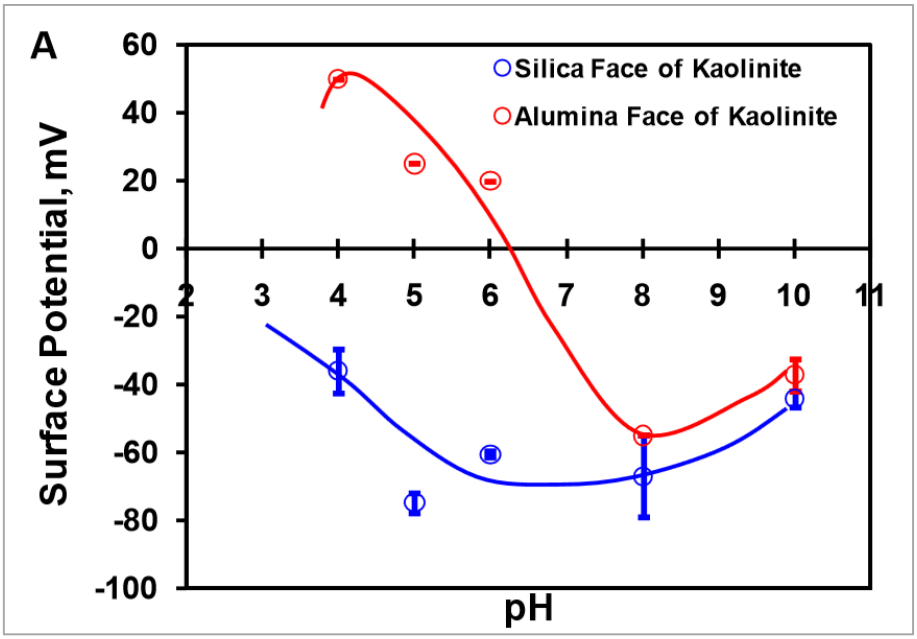

Figure 3.5 Surface charged of silica tetrahedral face and alluminol octahedral face of kaolinite as a function of pH (taken from Gupta, [19]).

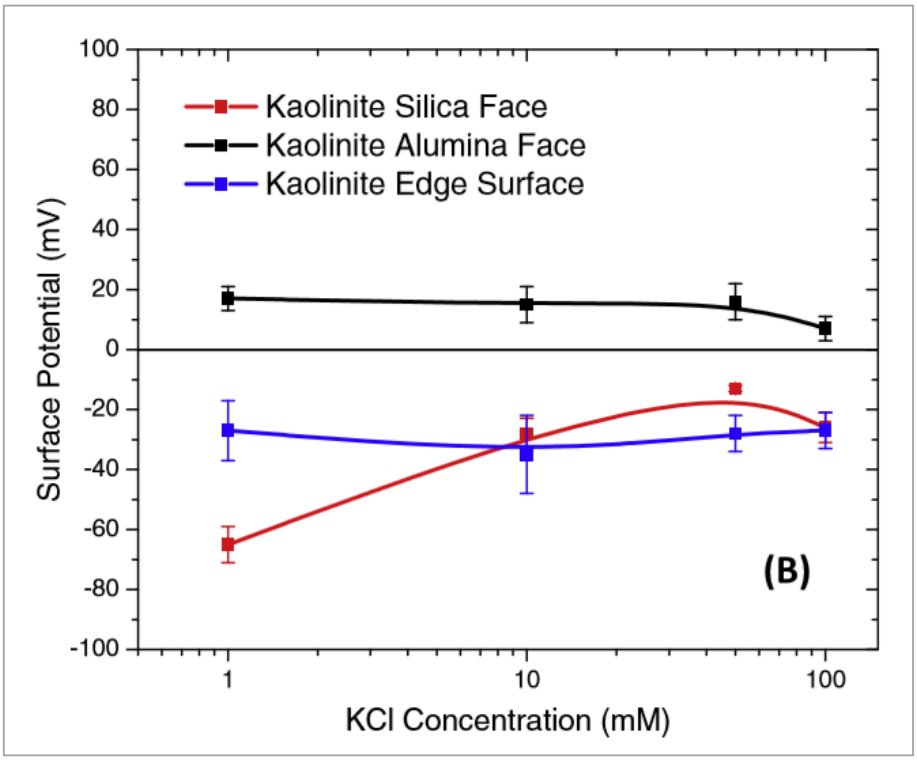

Figure 3.6 Surface charge of kaolinite surfaces as a function of ionic strength at pH 5.6 (from taken from Liu et al. [55]).

3.3.2 Pyrophyllite

Pyrophyllite, with the chemical formula:$Si_4Al_2O_{10}(OH)_2$ (67% SiO_2, 28% Al_2O_3 and 5% H_2O) [60], is a 2:1 clay mineral composed of a single aluminium hydroxide (or brucite-type) octahedral sheet sandwiched by to silica tetrahedral basal sheets. Both tetrahedral and octahedral layers of pyrophyllite have only minor isomorphous substitutions of Al^{3+} for Si^{4+} in the tetrahedral face and of Mg^{2+} for Al^{3+} in the octahedral sheet [33]. Due to this fact, the exposed silicate faces are generally not charge-balanced by counter ions and consequently contain no interlayer species. The interlayer bonding is dominated by weak electrostatic and Van der Waals bonding across the narrow interlayer space [61]. Being a 2:1 clay, the exterior surfaces, are entirely composed of "siloxane" units, which would contain a small negative charge, similarly to what occurs with the kaolinite tetrahedral basal plane. This fact, in addition to the low degree of isomorphic substitutions, results in the hydrophobic character of this mineral [62, 63].

The influences of pH and electrolyte on the pyrophyllite surface charge are similar to that on the siloxane face of kaolinite. Lui and Bai studied the surface potential and found that bulk pyrophyllite has a permanent always a negative charge within the pH range of 2-12, although this becomes more negative as the pH increases [64], as shown in Figure 3.7. Furthermore, Kopittke et al. found that Ca^{2+} has a higher affinity to pyrophyllite compared to Na^{+} [58].

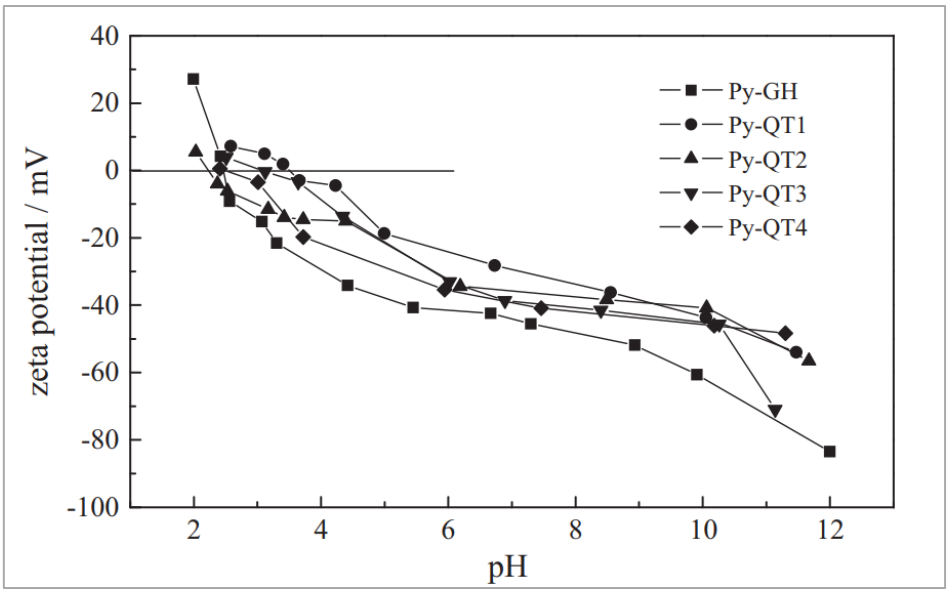

Figure 3.7 The measured zeta potentials (surface charge) of pyrophyllite samples from five sources as a function of pH (taken from Lui and Bai, [64]).

Pyrophyllite is not commonly found in sandstone reservoirs; its use in this study was for the purpose of comparison with the results obtained with kaolinite. As pyrophyllite exposes on siloxane faces with a similar charge to that of kaolinite. Comparing results will allow to discriminate between the roles of the siloxane and aluminol faces in their interaction with oil molecules (see Chapter 7).

3.4 Wettability

Wettability is defined as the predilection of a solid surface to contact with a fluid rather than another. In the case of two immiscible liquids interacting with a solid, one fluid will adhere to the surface more strongly than the other one, but any other favourable fluid may compete to replace it at the solid interface [65]. In terms of oil recovery, wettability can be defined across many scales, from a macroscopic, reservoir-wide, scale, down to the micro and nanoscale when dealing with single mineral phases.

3.5 Wettability at the reservoir scale

In general terms, and in spite of its inherent heterogeneity and complexity, the wettability of a reservoir is normally categorized following the three categories: water-wet, mixed-wet, and oil-wet. In the water-wetting reservoir, the rock has a higher affinity to the formation water (or brine) than oil. In this condition the brine will fully occupy small pores, whereas in larger pores, it will "coat" the rock surface as a brine film and the residual oil will be pushed to the centre of the cavity [65], as can be seen in Figure 3.8. If the reservoir is oil-wet, the situation will be reversed, with small pores filled with oil and oil films coating the pore-lining minerals in larger pores and formation water will be pushed to the centre of the pore (Figure 3.8). Finally, a reservoir is described as mixed-wet when some portion of the pore surfaces prefers to be water-wet and others are oil-wetting [65]. Defining the wetting state of the reservoir is crucial for EOR applications as this will influence the oil recovery process through its effect on the location, flow and distribution of brine and oil within the reservoir [66]. Despite this, it must be noted that the wettability definition in such a complex system if more of a conceptual definition of use in engineering applications, while, the actual wettability should be measured in individual minerals.

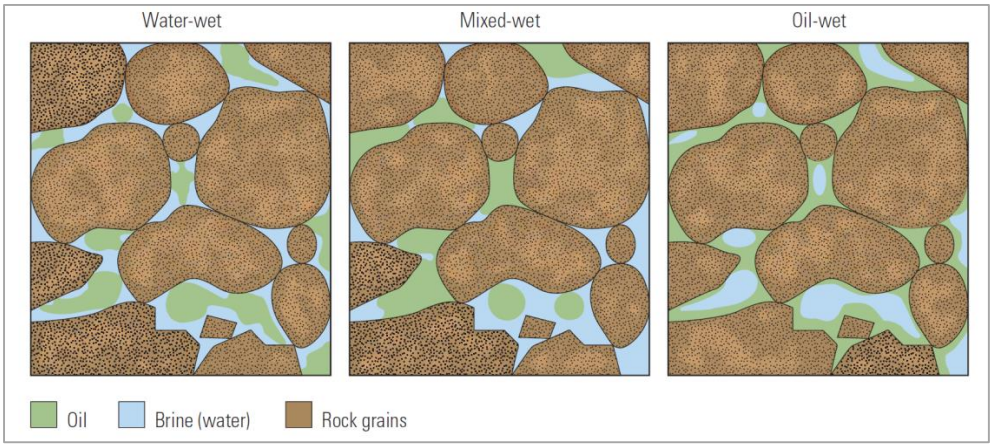

Figure 3.8 Schematic view describing the three main types of wettability states on a porous rock: water-wet shows oil remaining in the centre of pores, mixed-wet shows that oil has displaced water at some of the mineral grains' surfaces and oil-wet shows that oil is in contact with the mineral grains (taken from Abdallah et al. [65]).

3.6 Wettability at the microscopic scale

Wetting degree at the microscopic scale is normally established by measuring the shape of a drop of the fluid of interest on over the solid surface or through the measurement of contact angle at either a gas-liquid-solid, or a liquid-liquid-solid system (Figure 3.9). At the three phase junction, the liquid drop shape behaves as an elastic film whose shape is determined by the interplay between the so called *cohesive* and *adhesive* forces. The cohesive forces are the attractive forces (mostly van der Waals) that occur between like-molecules in the bulk, whereas the adhesive forces are the forces that occur between different molecules across an interface (Figure 3.10). In the bulk, the liquid ideally has uniform bonding across all directions, however, at the interface molecules do not have fully satisfied bonds, as they are only surrounded by half the number of neighbouring like-molecules (as in the bulk). The atoms at the interfaces can either be brought up closer to the bulk molecules or adhere to other phase, in order to re-balance the chemical bonds. The new equilibrium at the solid-liquid interface and the liquid-gas interface can therefore be determined by the relative strength of intermolecular interactions (cohesive *vs*. adhesive) from the three phases at the molecular scale [67]. Strong adhesion and weak cohesion produces low contact angles with nearly complete wetting; conversely, low adhesion in solid/liquid interactions leads to larger contact angles or a decrease in wetting (Figure 3.9). To reach the new equilibrium of bulk and surface energy, the intermolecular force that creates the new surface is called the surface tension for the interaction of gas and liquid,

whereas it is called the interface tension, when it involves two liquids. The units for surface and interfacial tension are force per length (N/m), or unit of work per unit area (J/m²).

$$\text{Surface tension} = \frac{\text{Force(N)}}{\text{Length (m)}} \qquad \text{(Equation 3.7)}$$

$$\text{Surface energy } \left(\frac{\text{N}}{\text{m}}\right) = \frac{\text{Energy(J)}}{\text{Area (m}^2\text{)}} = \frac{\text{Energy (Nm)}}{\text{Area (m}^2\text{)}} \qquad \text{(Equation 3.8)}$$

At the new equilibrium configuration of any three phases, the surface tension between each pair is responsible for the shape of the liquid droplet or contact angles, as expressed by the Young's equation.

$$\sigma_{ws} = \sigma_{os} + \sigma_{ow}\cos\theta \qquad \text{(Equation 3.9)}$$

Where σ_{os} is the interfacial energy between oil and solid (J/m²); σ_{ws} is the interfacial energy between brine and solid (J/m²); σ_{ow} is the interfacial energy between oil and brine (J/m²); θ is contact angle at the oil, brine, and solid boundary (°) [68].

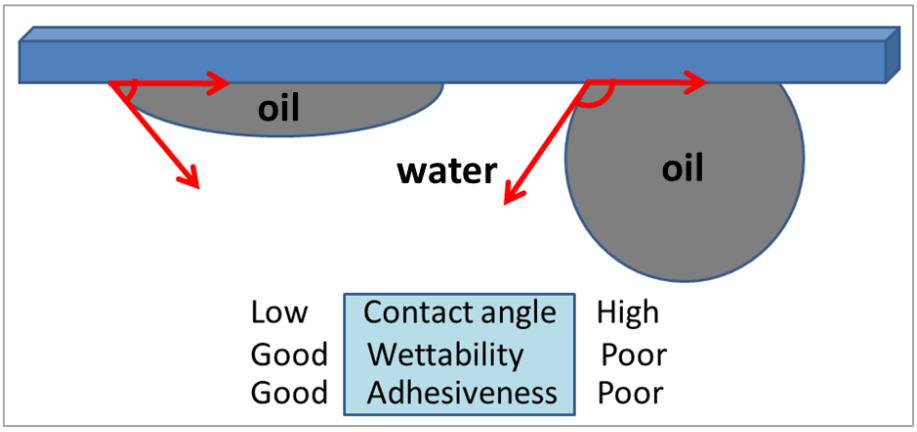

Figure 3.9 The contact angle is linked to wettability and adhesiveness.

Although wettability is studied through measurements at various scales, including core test, contact angle and adhesion/adsorption measurements, the study at the core scale may not reflect the actual wetting because in porous media there are the additional complexities of geometry, composition and roughness. All these factors contribute to the complexity of the observed wetting phenomenon [69-71]. As a consequence, the measurement of contact angle on flat surfaces is only effectively an indicator of wettability [72]. Therefore, to study the mechanisms behind wettability alteration at a fundamental/microscopic level, it can be

noted that contact angle measurement and interaction force are considered to be a measurement of the degree of wetting [66, 73, 74].

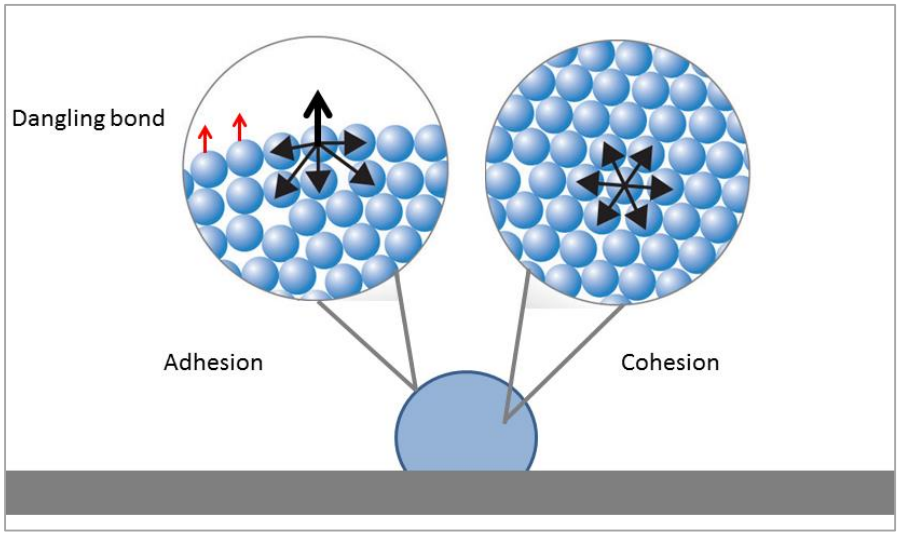

Figure 3.10 Schematic of cohesion, adhesion, and dangling bonding in water droplet.

3.7 Factors that control wettability

The wettability of reservoirs has long been studied. Authors generally accepted that the wetting condition results from the interaction of rock/brine/crude oil [69, 75-77]. Therefore, there are a multitude of factors inherent to the different phases involve, that can affect or control the wettability condition of an oil reservoir. These include: the type of mineral surfaces [11, 70, 78-80], brine composition [66, 81-84], the crude oil [75, 76]; water saturation [85-88], surface roughness [89] and reservoir temperature and pressure [90-92]. Among these parameters the most significant from a chemically fundamental level are those related to the type of mineral surface, crude oil and brine composition.

3.7.1 Mineral surface

As has been explained before, the low salinity effect results from the wettability alteration of the rock of the reservoir, from an oil-wet state to one of more mixed-wet or water-wet, i.e. it is controlled by the adsorption/desorption behaviour of crude oil components on the mineral surfaces exposed on the rock's pore space. The active surface chemistry of clay minerals makes them a more determining factor on controlling the oil wetness of the rock that more "inert" minerals, such as quartz [70, 80, 93-95]. Clementz found rapid adsorption of oil compounds on montmorillonite, and stated that the clay-organic compounds interactions induced a change in wettability from water-wet to oil-wet [96]. Somerton and Radke also observed that the type and amount of clay mineral play a role in core flooding, in which would make clay minerals can alter wettability [97]. Yang et al., Lebedeva et al.,

and Lebedeva and Fogden said that asserted that crude oil adsorbs to kaolinite in the pore space, therefore generating an oil wet to mixed-wet reservoir system reservoir [79, 98, 99].

3.7.2 Oil composition

The wettability state of a reservoir changes from water-wet to oil-wet when the oil migrate into it; as the rock's surface is directly contacted by the oil phase [66] which, as has been already stated, consist of a mixture of organic molecules with a wide range of complexity, molecular weight and functional groups. Denekas et al. found a relation between the molecular weight of the organic molecules in the oil and their influence on the wetting property of sandstone. The authors found that the crude oil fraction with the higher molecular weight was the more effective in modified the wettability state of sandstone to oil-wet [100]. Donaldson et al. and Cuiec reported that polar components present in the crude oil, especially in the heavy asphaltenes and the resin fraction, are those that exhibit a higher affinity for mineral surfaces and therefore influence the most the wetting conditions in reservoirs' rocks [75, 101]. Buckley et al. also showed that polar components are the most significant factor in determining the rock's wettability state. Specifically, they looked at the sorption of basic and acidic oil components into mineral surfaces and concluded that this takes place by electrical interaction. The polar functional groups which either behaves as acids (giving up a proton and becoming negatively charged) or bases (gaining a proton and thus getting a positive charge) adsorb on the counter charged mineral surfaces [102].

3.7.3 Brine composition

The pore spaces in a reservoir are always completely saturated with brine (formation water) before oil migration. It is a fact well known that the chemical properties of this brine (composition, salinity, and pH) have an influence on the surface chemistry of the mineral phases exposed in the pore space and, by extension, in the wetting state they will adopt after oil migration. Several researchers have studied the effects of salinity and pH of formation brine in pre-determining the oil wetness of rocks and individual mineral phases. Burg et al. and Mahani et al. performed oil absorption experiments on kaolinite films pretreated with high concentration brine and observed that this high concentration is a good condition for oil adsorption [103, 104]. Moreover, it has also been observed that pH can have a profound effect on determining the wettability of all types of rocks [14, 81, 105, 106]. For example, authors have shown that high ionic strength and high pH (>7) induced the mineral surface to be oil-wet by changing the surface charge of the rock reservoir and attracting crude oil to the surface [81, 106]. This mechanism was studied by applying DLVO theory [12](detailed in Section 3.2.2). Ligthelm et al. explained the wettability alteration through DLVO theory, indicating that cations significantly screens off the negatively

charged mineral surface [12]. An increase in the salinity of the brine or valence of cations present in the brine therefore causes a decreased of the electrical diffuse double layer. This allows the oil molecules close and adsorb to mineral surface. In contrast, when a lower salinity of brine is present in the reservoir less counter ions would screen the surface charge. Consequently, the electrical double layer would expand and the oil molecules are repelled from the mineral surface. This leads to oil desorption or a more water-wet surface. Other studies have looked at the effect of specific cation types [40]. Shehata and Nars-El-Din observed a positive correlation between the amount of divalent cations in the formation water and the oil-wetness of sandstone cores [40]. As a result, Lager et al., and others proposed the mechanism of multivalent cation-bridging, whereby divalent cations, such as $Ca^{2+,}$ act as bridges in the brine phase between a negatively charged polar end, such as the deprotonated carboxylate group in crude oil, and negatively charged sites on the mineral surfaces exposed in the pore space [13].

3.8 Measurement of wettability

Wettability analysis techniques play a vital role in the oil industry, therefore a variety of methods have been developed for the accurate quantification of wettability [66, 69, 107-110]. Salathiel gives a comprehensive description of reservoir wettability measurement methods. Most of the techniques were laboratory measurements assessing reservoir core samples [110]. Examples of techniques include spontaneous imbibition tests [69], the US Bureau of Mines (USBM) test [69, 101], nuclear magnetic resonance [111-113], and resistivity measurements (logs) [114, 115].

- Spontaneous imbibition methods (such as the Amott and Amott-Harvey), are those where different quantities of brine and oil are imbibed by a core sample by force or spontaneously [69, 116]. This method is based on the principle that the wetting phase will displace (and therefore imbibe the sample) a non-wetting phase (until its residual saturation is achieved). Although spontaneous imbibition test directly represents reservoir conditions, the wettability can measure the amount of oil that is displaced by water imbibition into a core, but this method took too over 100 days [117].
- The U.S. Bureau of Mines (USBM) method was developed by accelerating a fluid displacement in a centrifuge [69, 101]. This method is similar to imbibition tests, but in this case, centrifugation force is used to accelerate the fluid displacement into the solid core sample [69]. A disadvantage of the

USBM test is the plug-size core because the studied core must be able to be installed into a centrifuge.

- Nuclear magnetic resonance (NMR) uses magnetic fields spin flip atomic nuclei [118], especially hydrogen protons in pore fluid molecules. NMR is directly sensitive to the nature of the fluid either oil or water on in the porous media. Therefore, NMR can measure wettability in the reservoir's core [119].
- Resistivity measurements (logs) can measure the wettability by interpretation from resistivity logs [114, 115].
- Relative permeability can be used to evaluate wettability from the shape and magnitudes of relative-permeability, as introduced by Craig [120] and Jennings [121]. However, this method has the limit of the measurement of intermediate wetting property which is the case in many reservoir,; because it is not possible to assess from the shape of relative permeability curves under these conditions [122, 123].

Although these above methods can reflect the quality of the reservoir and provide an approximation on the quantity of wettability and the potential of a reservoir, it is still essential to noted that, conceptually, it is individual minerals that significantly explain nanogeochemical wettability alteration and the potential of low-salinity EOR. To achieve an accurate conceptual model of the nano-geochemical mechanisms, it is necessary to determine the wettability of individual mineral phases within the reservoir, and this can only be achieved through the use of microscopic techniques. The most commonly used of these techniques is the contact angle measurement (more details in Chapter 4). Also, wettability can be calculated from adhesion/adsorption measurements such as those derived from including thermal gravimetric analysis coupled mass spectrometry (TGA-MS), chemical force microscopy (CFM) and chemical bonding analysis by Fourier transform infrared spectroscopy (FTIR). Details of these methods are provided in Chapter 4.

3.9 References

[1] A. Thomson, Preservation of porosity in the deep Woodbine/Tuscaloosa trend, Louisiana, (1979).

[2] S. Ehrenberg, Relationship between diagenesis and reservoir quality in sandstones of the Garn formation, Haltenbanken, mid-Norwegian Continental shelf (1), AAPG bulletin 74(10) (1990) 1538-1558.

[3] V. Billault, D. Beaufort, A. Baronnet, J.C. Lacharpagne, A nanopetrographic and textural study of grain-coating chlorites in sandstone reservoirs, Clay Miner. 38(3) (2018) 315-328.

[4] A. Berger, S. Gier, P. Krois, Porosity-preserving chlorite cements in shallow-marine volcaniclastic sandstones: Evidence from Cretaceous sandstones of the Sawan gas field, Pakistan, AAPG bulletin 93(5) (2009) 595-615.

[5] J.M. Ajdukiewicz, R.H. Lander, Sandstone reservoir quality prediction: The state of the art, AAPG bulletin 94(8) (2010) 1083-1091.

[6] R. Worden, S. Morad, Quartz cementation in oil field sandstones: a review of the key controversies, Quartz cementation in sandstones (2000) 1-20.

[7] N. Hancock, A. Taylor, Clay mineral diagenesis and oil migration in the Middle Jurassic Brent Sand Formation, Journal of the Geological Society 135(1) (1978) 69-72.

[8] K. Bjørlykke, K. Høeg, Effects of burial diagenesis on stresses, compaction and fluid flow in sedimentary basins, Mar. Pet. Geol. 14(3) (1997) 267-276.

[9] Ø. Marcussen, T.E. Maast, N.H. Mondol, J. Jahren, K. Bjørlykke, Changes in physical properties of a reservoir sandstone as a function of burial depth–The Etive Formation, northern North Sea, Marine and Petroleum Geology 27(8) (2010) 1725-1735.

[10] K. Bjørlykke, J. Jahren, Open or closed geochemical systems during diagenesis in sedimentary basins: Constraints on mass transfer during diagenesis and the prediction of porosity in sandstone and carbonate reservoirs, AAPG bulletin 96(12) (2012) 2193-2214.

[11] G.-Q. Tang, N.R. Morrow, Influence of brine composition and fines migration on crude oil/brine/rock interactions and oil recovery, Journal of Petroleum Science and Engineering 24(2-4) (1999) 99-111.

[12] D.J. Ligthelm, J. Gronsveld, J. Hofman, N. Brussee, F. Marcelis, H. van der Linde, Novel Waterflooding Strategy By Manipulation Of Injection Brine Composition, EUROPEC/EAGE Conference and Exhibition, Society of Petroleum Engineers, Amsterdam, The Netherlands, 2009.

[13] A. Lager, K.J. Webb, C.J.J. Black, M. Singleton, K.S. Sorbie, Low Salinity Oil Recovery - An Experimental Investigation1, Petrophysics 49(01) (2008) 8.

[14] T. Austad, A. RezaeiDoust, T. Puntervold, Chemical mechanism of low salinity water flooding in sandstone reservoirs, SPE improved oil recovery symposium, Society of Petroleum Engineers, 2010.

[15] A. Meunier, Clays, Springer Science & Business Media2005.

[16] A. Jordan, Lightening the clay (II), 2014.

https://blogs.egu.eu/divisions/sss/2014/09/page/3/. (Accessed 3 May 2018.

[17] U.S.G. Survey, A Laboratory Manual for X-Ray Powder Diffraction, 2001. https://pubs.usgs.gov/of/2001/of01-041/htmldocs/clays/illite.htm. (Accessed 27 May 2017.

[18] G. Lagaly, M. Ogawa, I. Dékány, .3 Clay mineral organic interactions, Developments in Clay Science 1 (2006) 309-377.

[19] V. Gupta, Surface charge features of kaolinite particles and their interations, Metallurgical Engineering, The University of Utah, ProQuest Dissertations Publishing, ProQuest Dissertations Publishing, 2011, p. 210.

[20] G.W. Brindley, G. Brown, Crystal Structures of Clay Minerals and their X-Ray Identification, Mineralogical Society of Great Britain and Ireland1980, pp. 411-438.

[21] B. Jańczuk, E. Chibowski, M. Hajnos, T. Białopiotrowicz, J. Stawiński, Influence of exchangeable cations on the surface free energy of kaolinite as determined from contact angles, Clays Clay Miner. 37(3) (1989) 269-272.

[22] J. Shang, M. Flury, J.B. Harsh, R.L. Zollars, Contact angles of aluminosilicate clays as affected by relative humidity and exchangeable cations, Colloids Surf. Physicochem. Eng. Aspects 353(1) (2010) 1-9.

[23] A. Synytska, L. Ionov, S. Minko, M. Motornov, K. Elchorn, M. Stamm, K. Grundke, Tuning wettability by controlled roughness and surface modification using core-shell particles, Polym. Mater. Sci. Eng. 90 (2004) 624-625.

[24] B. Yang, S. Song, A. Lopez-Valdivieso, Effect of particle size on the contact angle of molybdenite powders, Miner. Process. Extr. Metall. Rev. 35(3) (2014) 208-215.

[25] J. Cases, I. Berend, M. Francois, J. Uriot, L. Michot, F. Thomas, Mechanism of adsorption and desorption of water vapor by homoionic montmorillonite: 3. The Mg super (2+), Ca super (2+), Sr super (2+) and Ba super (2+) exchanged forms, Clays Clay Miner. 45(1) (1997) 8-22.

[26] L.J. Michot, C. Baravian, I. Bihannic, S. Maddi, C. Moyne, J.F. Duval, P. Levitz, P. Davidson, Sol– gel and isotropic/nematic transitions in aqueous suspensions of natural nontronite clay. Influence of particle anisotropy. 2. Gel structure and mechanical properties, Langmuir 25(1) (2008) 127-139.

[27] H.v. Olphen, An introduction to clay colliod chemistry, Intersciences Publisher, New York, 1964.

[28] N.M. DeNovio, J.E. Saiers, J.N. Ryan, Colloid movement in unsaturated porous media, Vadose Zone J 3(2) (2004) 338-351.

[29] R.J. Hunter, Introduction to Modern Colloid Science, Oxford University Press 1994.

[30] S.B. Johnson, G.V. Franks, P.J. Scales, D.V. Boger, T.W. Healy, Surface chemistry–rheology relationships in concentrated mineral suspensions, Int. J. Miner. Process. 58(1-4) (2000) 267-304.

[31] D.G. Grier, Optical tweezers in colloid and interface science, Curr. Opin. Colloid Interface Sci. 2(3) (1997) 264-270.

[32] S. Das, P. Sreeram, A. Raychaudhuri, A method to quantitatively evaluate the Hamaker constant using the jump-into-contact effect in atomic force microscopy, Nanotechnology 18(3) (2007) 035501.

[33] H.v. Olphen, An introduction to clay colloid chemistry, for clay technologists, geologists, and soil scientists, 1977.

[34] W.R. Bowen, N. Hilal, Atomic force microscopy in process engineering: an introduction to AFM for improved processes and products, Butterworth-Heinemann2009.

[35] P.C. Hiemenz, R. Rajagopalan, Principles of Colloid and Surface Chemistry, revised and expanded, CRC press1997.

[36] J. Israelachvili, Intermolecular and Surface Forces 3rd Edition, Academic Press Academic Press 2011, p. 704.

[37] H.C. Hamaker, The London—van der Waals attraction between spherical particles, Physica 4(10) (1937) 1058-1072.

[38] R.A. Nasralla, H.A. Nasr-El-Din, Double-Layer Expansion: Is It a Primary Mechanism of Improved Oil Recovery by Low-Salinity Waterflooding?, (2014).

[39] S.A. Hussain, Ş. Demirci, G. Özbayoğlu, Zeta potential measurements on three clays from Turkey and effects of clays on coal flotation, J. Colloid Interface Sci. 184(2) (1996) 535-541.

[40] A.M. Shehata, H.A. Nasr-El-Din, Reservoir Connate Water Chemical Composition Variations Effect on Low-Salinity Waterflooding, Abu Dhabi International Petroleum Exhibition and Conference, Society of Petroleum Engineers, 2014.

[41] D. Fairhurst, An Overview of the Zeta Potential - Part 1: The Concept, 2013. https://www.americanpharmaceuticalreview.com/Featured-Articles/133232-An-Overview-of-the-Zeta-Potential-Part-1-The-Concept/. (Accessed 2 Fabuary 2018).

[42] P. Debye, E. Hückel, De la theorie des electrolytes. I. abaissement du point de congelation et phenomenes associes, Physikalische Zeitschrift 24(9) (1923) 185-206.

[43] T. Hassenkam, C.S. Pedersen, K. Dalby, T. Austad, S.L.S. Stipp, Pore scale observation of low salinity effects on outcrop and oil reservoir sandstone, Colloids and Surfaces A: Physicochemical and Engineering Aspects 390(103) (2011) 179-188.

[44] T. Hassenkam, A.C. Mitchell, C.S. Pedersen, L.L. Skovbjerg, N. Bovet, S.L.S. Stipp, The low salinity effect observed on sandstone model surfaces, Colloids and Surfaces A: Physicochemical and Engineering Aspects 403(0) (2012) 79-86.

[45] L.L. Skovbjerg, T. Hassenkam, E. Makovicky, C.P. Hem, M. Yang, N. Bovet, S.L.S. Stipp, Nano sized clay detected on chalk particle surfaces, Geochimica et Cosmochimica Acta 99(0) (2012) 57-70.

[46] E. Hilner, M.P. Andersson, T. Hassenkam, J. Matthiesen, P.A. Salino, S.L.S. Stipp, The effect of ionic strength on oil adhesion in sandstone – the search for the low salinity mechanism, Scientific Reports 5 (2015) 9933.

[47] C.E. Weaver, L.D. Pollard, The Chemistry of Clay Minerals. Developments in Sedimentology, Geological Magazine 111(2) (2009) 185-185.

[48] M. Osborne, R. Haszeldine, A. Fallick, Variation in kaolinite morphology with growth temperature in isotopically mixed pore-fluids, Brent Group, UK North Sea, Clay Miner. 29(4) (1994) 591-608.

[49] M. Zbik, R.S.C. Smart, H. Kodama, A. Mermut, J. Torrance, Atomic force microscopy in the estimation of aspect ratio of colloidal kaolinite, (1999).

[50] M.S. Żbik, N.A. Raftery, R.S.C. Smart, R.L. Frost, Kaolinite platelet orientation for XRD and AFM applications, Appl. Clay Sci. 50(3) (2010) 299-304.

[51] H. Murray, Developments in Clay Science, Applied Clay Mineralogy, Occurrences, Processing and Application of Kaolins, Bentonites, Palygorskite-Sepiolite, and Common Clays: Structure and Composition of the Clay Minerals and their Physical and Chemical Properties, from Elsevier Science, (2006).

[52] B. Rand, I.E. Melton, Particle interactions in aqueous kaolinite suspensions: I. Effect of pH and electrolyte upon the mode of particle interaction in homoionic sodium kaolinite suspensions, J. Colloid Interface Sci. 60(2) (1977) 308-320.

[53] S.B. Johnson, A.S. Russell, P.J. Scales, Volume fraction effects in shear rheology and electroacoustic studies of concentrated alumina and kaolin suspensions, Colloids Surf. Physicochem. Eng. Aspects 141(1) (1998) 119-130.

[54] V. Gupta, A.H. Marc, A.V. Nguyen, J.D. Miller, Crystal lattice imaging of the silica and alumina faces of kaolinite using atomic force microscopy, Journal of Colloid and Interface Science 352(1) (2010) 75-80.

[55] J. Liu, L. Sandaklie-Nikolova, X. Wang, J.D. Miller, Surface force measurements at kaolinite edge surfaces using atomic force microscopy, J. Colloid Interface Sci. 420 (2014) 35-40.

[56] V. Gupta, J.D. Miller, Surface force measurements at the basal planes of ordered kaolinite particles, Journal of Colloid and Interface Science 344(2) (2010) 362-371.

[57] X. Yin, J. Miller, Wettability of kaolinite basal planes based on surface force measurements using atomic force microscopy, Mining, Metallurgy & Exploration 29(1) (2012) 13-19.

[58] P. Kopittke, H. So, N. Menzies, Effect of ionic strength and clay mineralogy on Na–Ca exchange and the SAR–ESP relationship, Eur. J. Soil Sci. 57(5) (2006) 626-633.

[59] R. Kleven, J. Alstad, Interaction of alkali, alkaline-earth and sulphate ions with clay minerals and sedimentary rocks, Journal of petroleum Science and Engineering 15(2-4) (1996) 181-200.

[60] T.K. Mukhopadhyay, S. Ghatak, H.S. Maiti, Pyrophyllite as raw material for ceramic applications in the perspective of its pyro-chemical properties, Ceram. Int. 36(3) (2010) 909-916.

[61] A. Essalhi, M. Essalhi, A. Toummite, A. El Mostadi, Y. Raddi, Mineralogical and textural arguments for a metasomatic origin of the Ougnat pyrophyllite, Eastern Anti-Atlas, Morocco.

[62] R. Giese, P. Costanzo, C. Van Oss, The surface free energies of talc and pyrophyllite, Phys. Chem. Miner. 17(7) (1991) 611-616.

[63] S. Kelebek, G. Smith, J. Finch, S. Yörük, Critical surface tension of wetting and flotation separation of hydrophobic solids, Sep. Sci. Technol. 22(6) (1987) 1527-1546.

[64] X. Liu, M. Bai, Effect of chemical composition on the surface charge property and flotation behavior of pyrophyllite particles, Adv. Powder Technol. 28(3) (2017) 836-841.

[65] W. Abdallah, J.S. Buckley, A. Carnegie, J. Edwards, B. Herold, E. Fordham, A. Graue, T. Habashy, N. Seleznev, C. Signer, Fundamentals of wettability, Technology 38(1125-1144) (1986) 268.

[66] W.G. Anderson, Wettability Literature Survey- Part 1: Rock/Oil/Brine Interactions and the Effects of Core Handling on Wettability, J Petrol Technol 38(10) (1986) 1125-1144.

[67] C.S. Vijapurapu, The effect of rock and fluids characteristics on reservoir wettability, Petroleum Engineering, Louisiana State University, 2002, p. 92.

[68] O. Vizika, J. Lombard, Wettability and spreading: two key parameters in oil recovery with three-phase gravity drainage, SPE Reservoir Engineering 11(01) (1996) 54-60.

[69] W. Anderson, Wettability Literature Survey- Part 2: Wettability Measurement, J Petrol Technol 38(11) (1986) 1246-1262.

[70] N.R. Morrow, Wettability and its effect on oil recovery, J Petrol Technol 42(12) (1990) 1,476-1,484.

[71] A.W. Adamson, A.P. Gast, Physical chemistry of surfaces.

[72] S. Alsayari, M. Dernaika, M.J. Blunt, The Influence of Wettability on Petrophysical Properties, SCA2009.

[73] A. Tartakovsky, P. Meakin, Modeling of surface tension and contact angles with smoothed particle hydrodynamics, Phys Rev E 72(2) (2005) 026301.

[74] J.W. Tyrrell, P. Attard, Images of nanobubbles on hydrophobic surfaces and their interactions, Phys. Rev. Lett. 87(17) (2001) 176104.

[75] L. Cuiec, Rock/crude-oil interactions and wettability: An attempt to understand their interrelation, SPE Annual Technical Conference and Exhibition, Society of Petroleum Engineers, 1984.

[76] J. Buckley, Y. Liu, S. Monsterleet, Mechanisms of wetting alteration by crude oils, Spe J 3(01) (1998) 54-61.

[77] A. Bera, K. S, K. Ojha, T. Kumar, A. Mandal, Mechanistic Study of Wettability Alteration of Quartz Surface Induced by Nonionic Surfactants and Interaction between Crude Oil and Quartz in the Presence of Sodium Chloride Salt, Energy Fuels 26(6) (2012) 3634-3643.

[78] Y. Zhang, X. Xie, N.R. Morrow, Waterflood performance by injection of brine with different salinity for reservoir cores, SPE annual technical conference and exhibition, Society of Petroleum Engineers, 2007.

[79] J. Yang, Z. Dong, M. Dong, Z. Yang, M. Lin, J. Zhang, C. Chen, Wettability alteration during low-salinity waterflooding and the relevance of divalent ions in this process, Energy & Fuels 30(1) (2015) 72-79.

[80] A. Borysenko, B. Clennell, R. Sedev, I. Burgar, J. Ralston, M. Raven, D. Dewhurst, K. Liu, Experimental investigations of the wettability of clays and shales, Journal of Geophysical Research: Solid Earth 114(B7) (2009).

[81] A. Fogden, Removal of crude oil from kaolinite by water flushing at varying salinity and pH, Colloids Surf. Physicochem. Eng. Aspects 402 (2012) 13-23.

[82] G. Q. Tang, N.R. Morrow, Influence of brine composition and fines migration on crude oil/brine/rock interactions and oil recovery, Journal of Petroleum Science and Engineering 24(204) (1999) 99-111.

[83] A. Lager, K. Webb, C. Black, Impact of brine chemistry on oil recovery, IOR 2007-14th European Symposium on Improved Oil Recovery, 2007.

[84] S.A. Farzaneh, M. Sohrabi, Experimental investigation of CO2-foam stability improvement by alkaline in the presence of crude oil, Chem. Eng. Res. Des. 94 (2015) 375-389.

[85] J. Buckley, Asphaltene precipitation and crude oil wetting, SPE Advanced Technology Series 3(01) (1995) 53-59.

[86] P. Jadhunandan, N.R. Morrow, Effect of wettability on waterflood recovery for crude-oil/brine/rock systems, SPE reservoir engineering 10(01) (1995) 40-46.

[87] G. Tang, N.R. Morrow, Salinity, temperature, oil composition, and oil recovery by waterflooding, SPE Reservoir Engineering 12(04) (1997) 269-276.

[88] X. Zhou, N.R. Morrow, S. Ma, Interrelationship of wettability, initial water saturation, aging time, and oil recovery by spontaneous imbibition and waterflooding, Spe J 5(02) (2000) 199-207.

[89] C. Della Volpe, D. Maniglio, M. Morra, S. Siboni, The determination of a 'stable-equilibrium'contact angle on heterogeneous and rough surfaces, Colloids Surf. Physicochem. Eng. Aspects 206(1-3) (2002) 47-67.

[90] O. Hjelmeland, L. Larrondo, Experimental investigation of the effects of temperature, pressure, and crude oil composition on interfacial properties, SPE Reservoir Engineering 1(04) (1986) 321-328.

[91] J. Schembre, G.-Q. Tang, A. Kovscek, Wettability alteration and oil recovery by water imbibition at elevated temperatures, Journal of Petroleum Science and Engineering 52(1-4) (2006) 131-148.

[92] F. Civan, Reservoir formation damage, Gulf Professional Publishing2015.

[93] O.C. Baptist, E.J. White, Clay content and capillary behavior of Wyoming reservoir sands, (1957).

[94] S. Yariv, The effect of tetrahedral substitution of Si by Al on the surface acidity of the oxygen plane of clay minerals, Int. Rev. Phys. Chem. 11(2) (1992) 345-375.

[95] S. Wu, A. Firoozabadi, Effect of salinity on wettability alteration to intermediate gas-wetting, SPE Reservoir Eval. Eng. 13(02) (2010) 228-245.

[96] D.M. Clementz, Clay stabilization in sandstones through adsorption of petroleum heavy ends, J Petrol Technol 29(09) (1977) 1,061-1,066.

[97] W.H. Somerton, C.J. Radke, Role of Clays in the Enhanced Recovery of Petroleum From Some California Sands Society of Petroleum Engineers 35(03) (1983) 11.

[98] E.V. Lebedeva, A. Fogden, Adhesion of oil to kaolinite in water, Environ. Sci. Technol. 44(24) (2010) 9470-9475.

[99] E.V. Lebedeva, A. Fogden, T.J. Senden, M.A. Knackstedt, Kaolinite Wettability—The Effect of Salinity, pH and Calcium, Society of Core Analysts (2010).

[100] M.O. Denekas, C.C. Mattax, G.T. Davis, Effects of Crude Oil Components on Rock Wettability, Society of Petroleum Engineers, 1959, p. 4.

[101] E.C. Donaldson, R.D. Thomas, P.B. Lorenz, Wettability Determination and Its Effect on Recovery Efficiency, SPE-2338-PA 9(01) (1969) 13-20.

[102] J.S. Buckley, Y. Liu, S. Monsterleet, Mechanisms of Wetting Alteration by Crude Oils, (1998).

[103] S. Berg, A.W. Cense, E. Jansen, K. Bakker, Direct Experimental Evidence of Wettability Modification By Low Salinity, Petrophysics 51(05) (2010) 9.

[104] H. Mahani, S. Berg, D. Ilic, W.-B. Bartels, V. Joekar-Niasar, Kinetics of low-salinity-flooding effect, SPE-169143-PA 20(01) (2015) 8-20.

[105] A. RezaeiDoust, T. Puntervold, S. Strand, T. Austad, Smart Water as Wettability Modifier in Carbonate and Sandstone: A Discussion of Similarities/Differences in the Chemical Mechanisms, Energy & Fuels 23 (2009) 4479-4485.

[106] Y. Liu, W. Yao, G. Wang, Y. Wang, A.S. Moita, Z. Han, L. Ren, Reversibly switchable wettability on aluminum alloy substrate corresponding to different pH droplet and its corrosion resistance, Chem. Eng. J. 303 (2016) 565-574.

[107] W.G. Anderson, Wettability literature survey-part 6: the effects of wettability on waterflooding, J Petrol Technol 39(12) (1987) 1,605-1,622.

[108] W.G. Anderson, Wettability literature survey-part 4: Effects of wettability on capillary pressure, J Petrol Technol 39(10) (1987) 1,283-1,300.

[109] W.G. Anderson, Wettability literature survey part 5: the effects of wettability on relative permeability, J Petrol Technol 39(11) (1987) 1,453-1,468.

[110] R.A. Salathiel, Oil Recovery by Surface Film Drainage In Mixed-Wettability Rocks, (1973).

[111] H. Guan, D. Brougham, K. Sorbie, K. Packer, Wettability effects in a sandstone reservoir and outcrop cores from NMR relaxation time distributions, Journal of Petroleum Science and Engineering 34(1-4) (2002) 35-54.

[112] J. Vevle, NMR measurements of wettability alternation in Berea Sandstone, The University of Bergen, 2011.

[113] C.A. Prather, J.M. Bray, J.D. Seymour, S.L. Codd, NMR study comparing capillary trapping in Berea sandstone of air, carbon dioxide, and supercritical carbon dioxide after imbibition of water, Water Resour. Res. 52(2) (2016) 713-724.

[114] E. Spinler, Determination of in-situ wettability from laboratory and well log measurements for a carbonate field, SPE Annual Technical Conference and Exhibition, Society of Petroleum Engineers, 1997.

[115] G. Hamon, Field-wide variations of wettability, SPE Annual Technical Conference and Exhibition, Society of Petroleum Engineers, 2000.

[116] E. Amott, Observations relating to the wettability of porous rock, (1959).

[117] D.C. Standnes, T. Austad, Wettability alteration in carbonates - Interaction between cationic surfactant and carboxylates as a key factor in wettability alteration from oil-wet to water-wet conditions, Colloids and Surfaces a-Physicochemical and Engineering Aspects 216(1-3) (2003) 243-259.

[118] G.R. Coates, L. Xiao, M.G. Prammer, NMR logging: principles and applications, Haliburton Energy Services Houston1999.

[119] F.R. Branco, N.A. Gil, NMR study of carbonates wettability, Journal of Petroleum Science and Engineering 157 (2017) 288-294.

[120] F.F. Craig, The reservoir engineering aspects of waterflooding, HL Doherty Memorial Fund of AIME New York1971.

[121] H. Jennings Jr, Effect of Laboratory Core Cleaning on Water-Oil Relative Permeability, Fall Meeting of the Society of Petroleum Engineers of AIME, Society of Petroleum Engineers, 1957.

[122] J. Heaviside, C. Black, Fundamentals of relative permeability: experimental and theoretical considerations, SPE Annual Technical Conference and Exhibition, Society of Petroleum Engineers, 1983.

[123] J. Heaviside, C. Brown, I. Gamble, Relative permeability for intermediate wettability reservoirs, SPE Annual Technical Conference and Exhibition, Society of Petroleum Engineers, 1987.

4

Experimental and analytical techniques

This thesis is focused on the study of the wettability alteration of two clay minerals (kaolinite and pyrophyllite) as a function of brine composition (cation identities, concentration, pH, ratio of Na^+:Ca^{2+} and ionic strength) and oil character (polar vs non-polar), with the goal of advancing our understanding on the nanogeochemical mechanisms behind low salinity enhanced oil recovery. A range of techniques were used to assess different aspects of the oil-brine-mineral interactions at both the nano and the microscale:

Part 1: Study at the nanoscale

- Measurement of "adhesion", as a proxy of wettability, using chemical force microscopy (CFM) on kaolinite tetrahedral (siloxane) and octahedral (aluminol) faces.
- Study of the chemical bonding between brine, model oil, and clays (kaolinite and pyrophyllite) using Fourier transform infrared (FTIR) spectroscopy.

Part 2: Study at the microscopic scale

- Measurement of the amount of "model oil" adsorption (and the influence of brine-pre-treatment) on kaolinite by thermal gravimetric analysis – mass spectrometry (TGA-MS) and nitrogen adsorption (BET).
- Measurement of "model oil" contact angles on kaolinite films in the presence of brine using a goniometer and environmental scanning electron microscopy (ESEM) with the roughness control, as observed using scanning electron microscopy (SEM) and measured using white light interferometry.

The brief description on the basics of operation of each of the used techniques is given in this chapter, whereas the details of the specific experiments and procedures are summarised in the individual chapters where the results from the different techniques are described.

4.1 Chemical force microscopy (CFM)

In order to study the adhesion interaction of specific functional groups with kaolinite surfaces under different solutions, CFM, which is a derivative technique of atomic force microscopy (AFM) was used. CFM has the same basic instrument principles as AFM, but it uses chemically functionalized tips/probes in the force spectroscopy mode of operation instead of standard silicon or silicon nitride probes.

4.1.1 Introduction to AFM

AFM was initially developed to study the topography and surface structure of materials at extremely high resolution in the vertical (sub-nanometre) and lateral directions (nanometre) and it has the advantage of being able to be used in the presence of gas, liquid or even vacuum. [1, 2]. The principle of operation of an AFM is similar to that of a profilometer, i.e. a very sharp tip is used to raster the surface of a material and an image reproducing its topography is produced. In the case of an AFM a very sharp tip or probe (a few nm in diameter) is attached to a cantilever which in turn is secured by a holder (Figure 4.1). This tip is rastered against the sample surface on the lateral X and Y directions (or, in some cases, the sample is rastered or scanned against an immobile probe) by means of piezoelectric tube. During scanning, the cantilever-probe assembly is deflected in the z direction (as well as experiencing a torsional movement due to friction) as it traverses over the topographic features of the sample. In order to detect this deflection a laser beam is focused on the deflected area of the cantilever near the tip. This laser then reflects back into a mirror, and from there into a quadruple photodiode detector. The horizontal and vertical movement of the laser spot over the detector helps discriminate between the torsional and vertical deflection movement of the cantilever-probe assembly. The signal from the photodiode is then fed into a proportional/integral/differential (PID) feedback controller, which compares the measured vertical deflection to a user-determined set point value (in contact mode operation). The resultant value (error signal) is then used to send a correcting signal to the piezoelectric tube to move the tip (or sample) up or down, in order to try to maintain a constant vertical deflection (defined by the user through the set-point value). This operation results in the reproduction of the surface topography by the piezoelectric tube vertical displacement (height image) [2, 3] as shown in Figure 4.1. The force applied by the cantilever during scanning can be calculated based on the linear extension (Δd) of a spring of elastic constant K according to Hooke's law as derived in Equation 4.1.

$$F = -K\,\Delta d \qquad \text{(Equation 4.1)}$$

Where F is force (N); -K is spring constant (N/m); and Δd is displacement of spring (m).

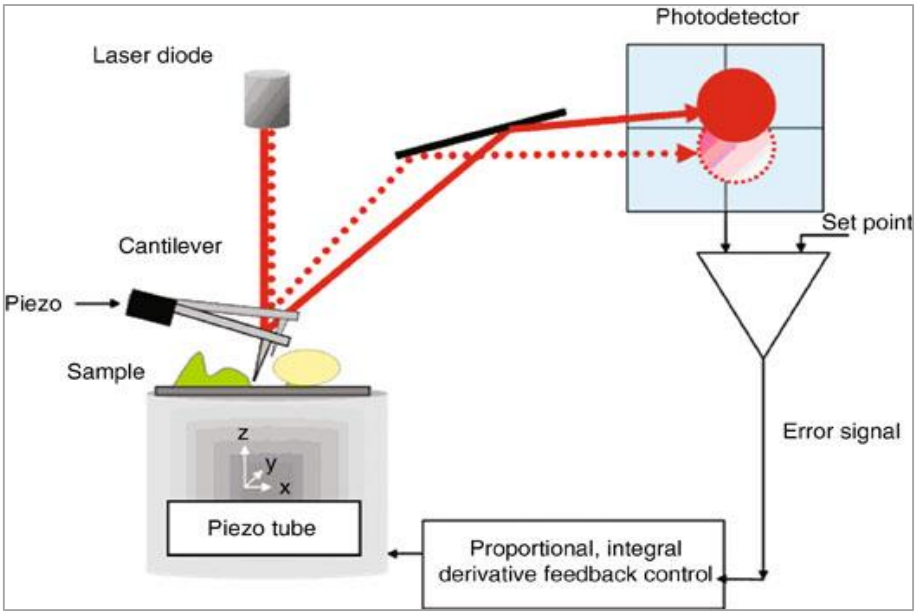

Figure 4.1 Diagram of AFM operation (modified after Cohen-Bouhacina and MaAli [4]).

The characteristic spring constant of a cantilever used for AFM can vary between from a few mN/m up to more than 200 N/m. For very low spring constants, the cantilever can be used as a force sensor to study the different interaction forces between tip and sample. In air, the most relevant forces are long-range van der Waals interactions, short-range repulsive forces, adhesion and capillary forces. When performing the experiment in solution, additional forces appear including: solvation and electrical double layer interactions. Interaction forces between the tip and samples are normally studied by performing so-called force-distance curves (Figure 4.2). This curve is constructed by bringing the tip/probe into contact with the sample up to a certain, user-defined, force value (trigger point) and then the tip/probe is retracted away from the surface until reaching its initial position. At a large separation distance from the surface, the tip is not subjected to any forces and therefore the cantilever is not deflected (position 1, Figure 4.2). As the tip is brought onto the surface, it will reach a distance where attraction forces may prevail and "snap" it against the surface (position 2, Figure 4.2). This will deflect the curve (and therefore the laser position against the photodiode detector will change, registering a change in force). As the tip continues to approach the surface, repulsive forces will increase and the cantilever will be deflected in the opposite direction, until reaching the trigger point of maximum force against the surface (position 3, Figure 4.2). During retraction, the bending of the cantilever will decrease in intensity, resulting in a decrease of the force on

the surface. In the presence of adhesion forces, the cantilever will continue to be in contact with the surface past the initial deflection value (horizontal line, Figure 4.2) until it "snaps off" the surface (position 4, Figure 4.2). The force measured at that point (against the initial deflection value) will represent the maximum adhesion force achieved.

4.1.2 Imaging AFM modes

Multiple imagining modes for AFM have been developed over the years. Some of these also include the detection of other physical properties of the sample, including magnetic (magnetic force microscopy) and electric forces (electric force microscopy), or measurement of mechanical properties (force modulation, friction force microscopy). Below, we cover the two more widely used pure topographical modes.

4.1.2.1 Contact mode

In this mode, the tip is always kept in contact with the sample during scanning, in other words, it operates within the repulsive regime (inclined part of the force-distance curve, Figure 4.2). Before scanning, the tip is brought into contact until a given deflection of the cantilever (or force) is achieved (as registered by a change in the output voltage of the photodiode detector). This value is defined as the set-point and can be changed by the user, in order to decrease, or increase, the pressure over the scanned surface. During scanning, the feedback mechanism will try to keep the set-point value constant during scanning by moving the tip or sample up or down using the Z-scanner, as explained above.

Although contact mode is simple to operate the continuous force applied by the tip and, more importantly, the drastic changes on force experienced during scanning can damage or modify the surface of soft samples and may also wear, or even break the tip. The appearance of lateral forces or friction forces appearing at the sample-tip contact only increases the chances of damaging soft samples. To address this problem, Binning et al. [1] proposed a new mode of operation where the cantilever-probe assembly would be oscillated at its resonance frequency whilst scanning.

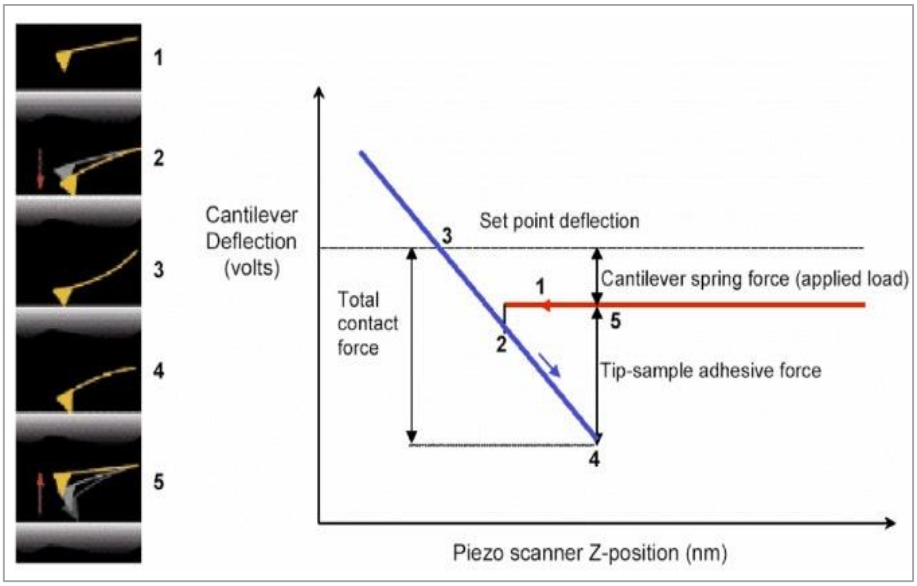

Figure 4.2 Force distance curve of contact mode (modified after Keammer [5]).

4.1.2.2 Intermittent contact mode (tapping mode)

Tapping mode microscopy is operated by oscillating the tip at its resonant frequency, normally by means of a small piezoelectric actuator located on the cantilever holder (Figure 4.3). In this mode, the amplitude of the vibration is defined by the user and is used as the set point for the purpose of engaging and tracking the surface during scanning (through the feedback control mechanism). In its most common application the oscillation occurs at values between 1-100 nm, i.e. within the repulsive and attractive regimes, as observed on a force-distance curve (Figure 4.4). The advantages of tapping mode are a significant reduction in lateral or friction forces whilst scanning and increased lateral resolution in certain situations. This prevents damage of the sample and also wearing on the probe, making it an ideal choice to scan biological or other soft materials, such as hydrated clay mineral films [2].

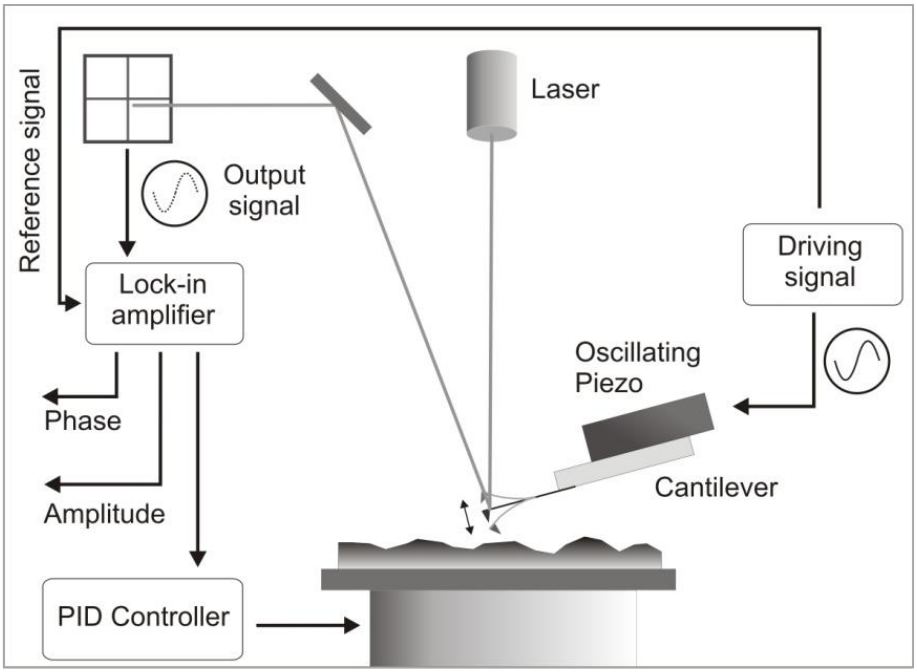

Figure 4.3 Schematic diagram showing the components utilized for intermittent contact mode operation (taken from Cubillas and Anderson [6]).

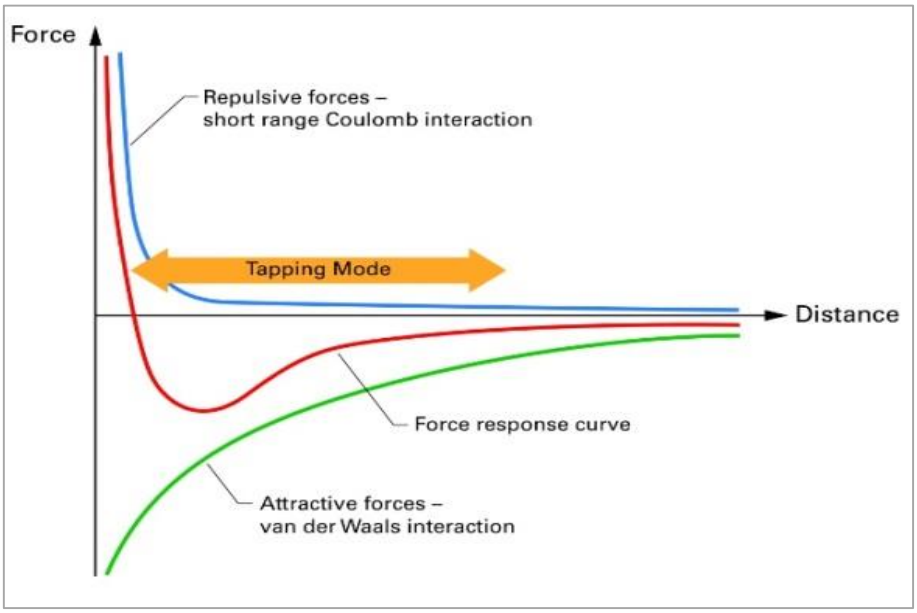

Figure 4.4 Force distance curve of tapping mode (modified after Keammer [5]).

4.1.3 Force spectroscopy

Besides the imaging modes, AFMs can also be utilized in the force spectroscopy mode. In this mode, the cantilever-probe assembly is brought repeatedly into and away from contact with the surface from a user-specified distance, i.e. performing force-distance curves in each instance. In most AFMs these curves can be performed over the same contact point or

over a surface, either at specific positions or over a "grid" pattern with dimensions and resolution (force-curves per distance) defined by the user. The latter mode is called "force-volume mode" and allows for the creation of height maps to which additional nanomechanical information (derived from the force curves) can be overlaid. Figure 4.5 shows an example of a real force curve and the different regions from which mechanical information can be derived, including plastic and elastic indentation as well as the adhesion force between probe and sample and the work of adhesion. In addition, to this, the portion of the curve where the tip is subjected to repulsive forces can also be fitted to a continuum mechanics model, such as Johnson–Kendall–Roberts (JKR) [7] or Derjaguin–Muller–Toporov (DMT)[8]) in order to calculate the elastic modulus of the sample [9]. Although a potentially very useful technique, for practical reasons force volume mode is a very slow mode of operation, which makes it a very hard technique to use on small samples (potential drift problems), in addition, the large data files had been a problem to handle until recent software advances. This situation has changed dramatically over the last decade with the development of the Peak-Force™ mode of operation by DI/Bruker and the Quantitative Imaging mode developed by JPK (now owned by Bruker)[5, 10]. Both techniques have reduced operation times by at least an order of magnitude over conventional force-volume mode in addition to offering inline data fitting to produce maps of different mechanical properties.

4.1.3.1 Chemical Force Spectroscopy (CFM)

CFM can be considered a derivative technique of the force-volume mode of operation. In this mode, however, the probe/tip is functionalized with organic functional groups (more below) so specific chemical interactions between tip and sample can be probed. The use of this technique on enhanced oil recovery research was pioneered by the group of Prof. Susan Stipp at Copenhagen, where they initially used CFM to measure the adhesion between a tip functionalized with $-CH_3$ groups (representing non-polar oil molecules) and chalk rock surfaces[11].

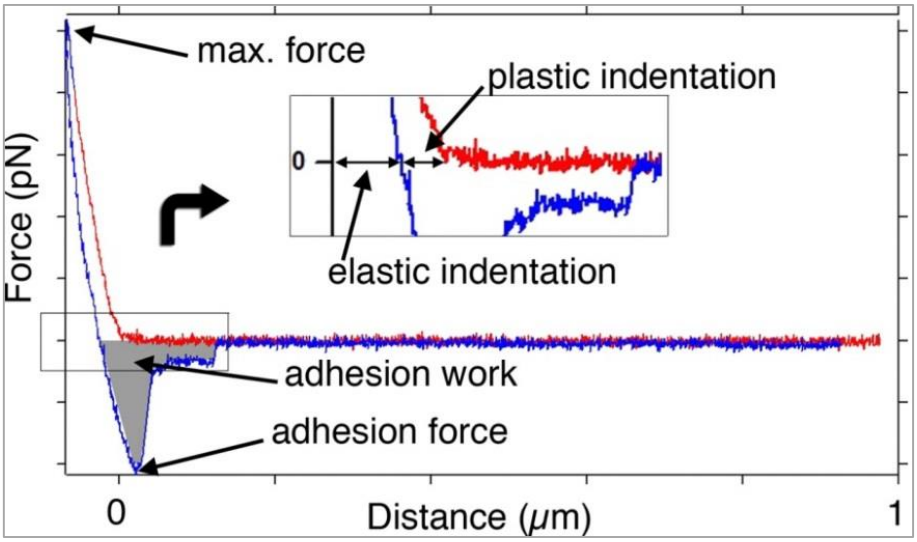

Figure 4.5 Example of a real force-distance curve indicating some of the regions from which the sample's mechanical information can be obtained (taken from Hassenkam et al. [11]).

4.1.4 Tip functionalisation

As can be readily understood, the most important part of the process when operating in chemical force microscopy mode is a correct and robust functionalisation of the tip/probe to be utilized. Most commercial AFM probes are made of Si_3N_4 or doped silicon, and both types can be functionalized, as explained below, using different techniques. In addition, the probes utilized in CFM have to be sufficiently soft (less than 1 N/m of spring constant) to be able to detect the small intermolecular forces responsible for adhesion (sometimes below the nN range) [12].

4.1.4.1 Tip functionalization strategies

The tip modification techniques rely on chemical strategies which can separated into two methods [12, 13]. Direct functionalization by silanization or esterification/amination via a thiol-based self-assembled monolayer (SAM) on a gold-coated tip. These approaches are depicted schematically in Figure 4.6 [14].

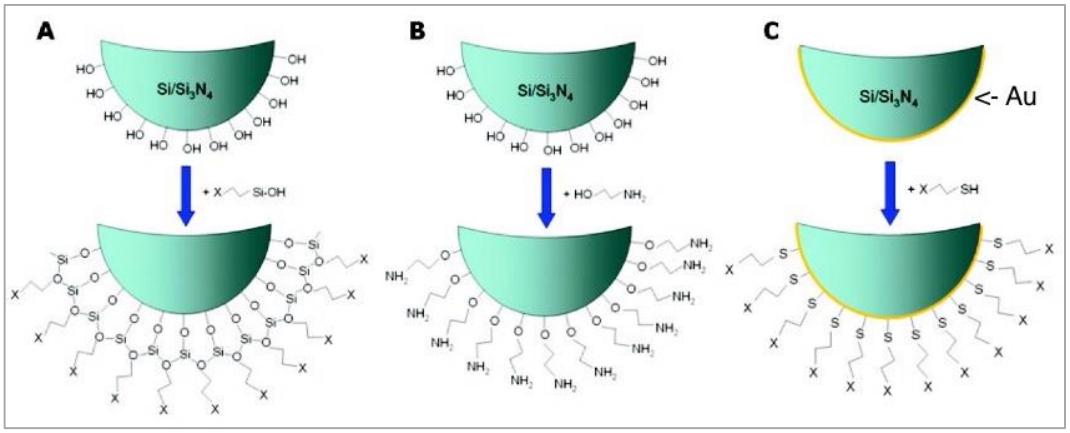

Figure 4.6 Tip functionalization by (a) Silanisation (b) Etherification (c) thiol-based self-assembled monolayer (SAM) on a gold-coated tip (modified after Berquand [14]).

4.1.4.2 Direct animation on tip: Silanisation and Etherification

In the silanisation process Si-containing organic molecules are directly bonded to the hydroxyl-terminated tip (or silanol layer (Si-OH)) by using a silanisation reagent of the form $RSi(OR')_3$ [12], where R is often an aminoalkyl chain and R' can be the desired functional group. In some cases, however, a new molecule maybe bound to the organosilane, in which case they act as a linker molecule. Binding to the AFM probe occurs due to the reaction between the organosilane and the silanol layer covering the tip, resulting in the formation of a covalent bonded (Si-O-Si) linkage. The most, commonly used organosilane reagent is 3-aminopropyltriethoxysilane (APTES) which directly leads to a $-NH_2$ functionalised probe. The $-C_2H_5$ in APTES can react with Si in the silanol layer and combine with it via a covalent bond [12], following Figure 4.7. APTES is commonly used in silanisation because it produces a short chain linkage, which results in a good arrangement of molecules in monolayers [15].

Different methods have been published to optimize the silanisation reaction. Luderer and Walschus [15] suggested liquid phase salinisation protocols. After the AFM tip is plasma-cleaned, it is dipped into a solution containing 1% v/v APTES and 99 % acetone with water for 15 minutes. Afterwards, the tip is washed with acetone for 5 cycles, each lasting 5 min. Finally, the tip is dried in an oven at 110 °C for 45 minutes.

Blanchette et al. [12] used a gas phase method of silanisation. In their method, the tip is initially cleaned with ethanol and dried with nitrogen gas. Afterwards, the tip is immersed in piranha solution, (a solution of H_2SO_4 and H_2O_2 70:30 v/v) [2, 15]. The tip is then rinsed with deionized water to remove the Piranha solution. Lastly, the tip is re-rinsed by ethanol, dried by nitrogen gas, and placed in an oven at 100-150 °C for one hour.

Subsequently, the cleaned tip is suspended over a sealed vial containing an organosilane solution. The evaporated silanes then accumulate over the tip to form a monolayer (Figure 4.8). Finally, the tip is placed in an oven at 100-150 °C for 15 minutes to remove any moisture and dried by nitrogen gas flow.

In a similar same way, amination by etherification can be achieved through the same salinization principle. Etherification occurs from the chemical reaction of surface silanol groups (which is approximately an alcohol); and ethanolamine ($HO\text{-}(CH_2)_2\text{-}NH_2$) which is alcohol (Figure 4.7). Etherification is recommended when the tip requires a slightly higher density of amino groups [14, 16].

4.1.4.3 Gold coating and Self-Assembled Monolayer (SAMs)

The most common method to functionalize AFM tips is by gold coating followed by the attachment of self-assembled monolayers (SAMs, containing the desired functional group) using thiol chemistry (Blanchette et al., 2010). Initially, the silicon or silicon nitride tips are coated by a thin (few nm) layer of a metal such as chromium or titanium. This is followed, by deposition of a thicker layer of gold (few tenths of nm) using either physical vapor deposition (PVD) or chemical vapor deposition (CVD) methods. Finally, the tip is exposed to a solution (normally using ethanol as solvent) containing an alkane molecule (of various carbon lengths) functionalized at one end with a thiol group (-SH) and the other with the desired functional group such as –COOH or $-CH_3$. The thiol groups have a great affinity for gold and therefore bind to the coated tip, leading to the development of a well ordered assembly of molecules [12] combining covalent binding or strong chemisorption (e.g. gold-thiol) [14]. Luderer and Walschus [15] highlighted that one sulfur in each thiol group strongly coordinates with three gold atoms with typical bond energy of 30 kcal/mol. The research by Blanchette et al. [12] also supported this finding, with a calculated bond strength between 20-35 kcal/mol. This point is important as it indicated a suitable durability of SAMs-functionalized tips to perform AFM experiments.

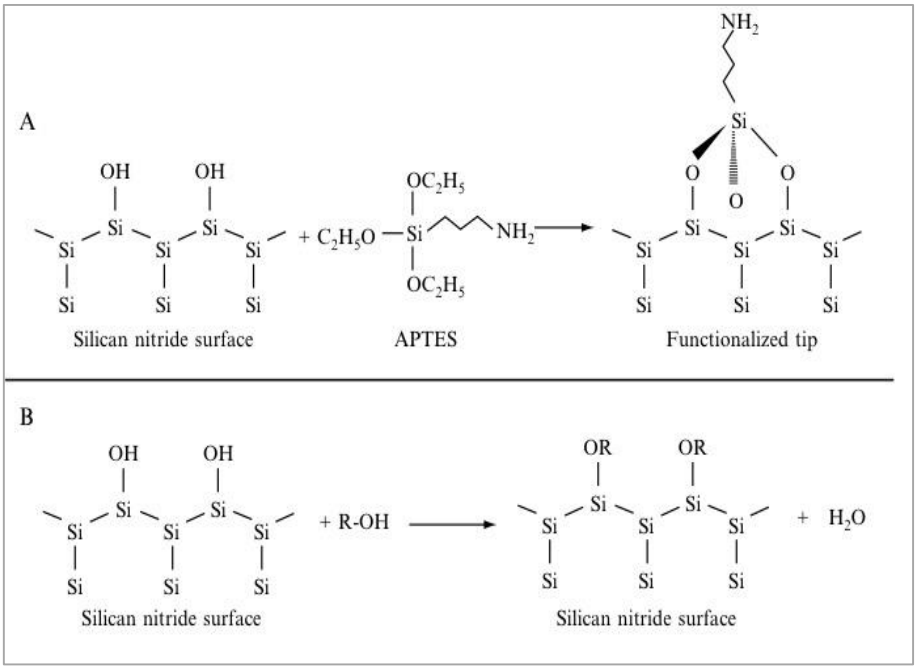
A
OH
OH
Si
Si
Si

The quality of functionalisation for a given method is prone to difficulties due to the small scales involved and other technical difficulties. Vezenov et al. [17] determined the quality of the functionalization by force titrations. These were achieved by performing force-curves of functionalized tips over substrates functionalized in the same manner in the presence of solutions of varying pH. Protonation and deprotonation reaction led to the development of repulsive or attractive forces which translated into decreases or increases in the measured adhesive forces (Figure 4.9).

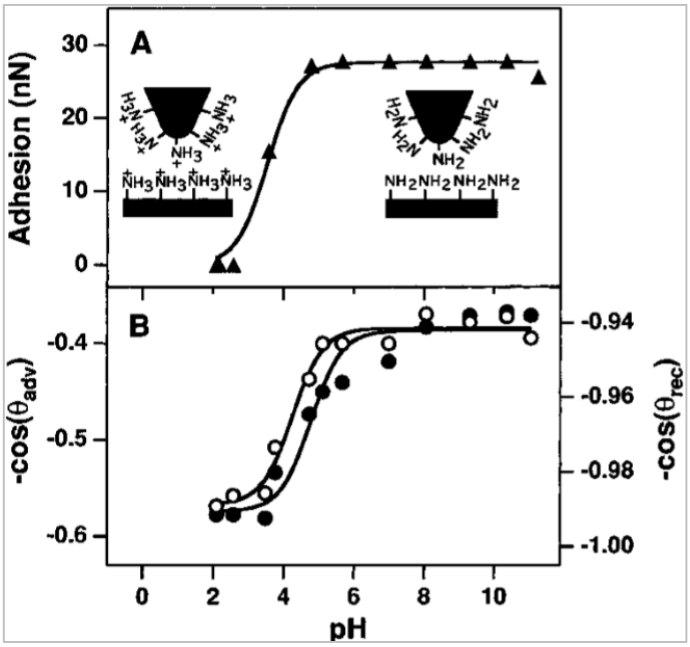

Figure 4.9 Adhesion vs. pH curve for experiments performed using a tip functionalized with $-NH_2$ groups over a likely-functionalized substrate. Low adhesion at low pH values corresponds with repulsive forces between protonated $-NH_3^+$ groups. Increased adhesion at large pHs is reflects the formation of hydrogen bonding between deprotonated $-NH_2$ groups (taken from Vezenov et al. [17]).

4.2 Thermal gravimetric analysis with mass spectroscopy (TGA-MS)

4.2.1 Principle

Thermogravimetric analysis-mass spectrometry (TGA-MS) combines both the function of TGA and MS. TGA is a technique that can measure the change in weight of a sample as a function of temperature increase under a controlled atmosphere (He, Ar, or N_2). TGA techniques are used to characterize the thermal stability and decomposition of organic and inorganic materials. TGA can also provide information on the kinetics of physicochemical

processes affecting the sample, such as desorption, absorption, reduction, oxidation, etc. [18, 19].

Mass spectroscopy, on the other hand, is a technique that allows the characterization of molecules according to their fragmentation behaviour after being bombarded by high-energy electrons. The charged particles are separated by electrical and magnetic means under vacuum conditions. Results are expressed in mass *vs.* charge (m/z) units. The technique is also used in trace element analysis.

The thermogravimetric data is compiled into a plot of mass (or percentage of initial mass) on the y-axis versus either temperature or time on the x-axis. The shape of the graph allows for the identification of the reaction occurring in the chamber. For example, a flat line on a TGA plot means no reaction has taken place (Figure 4.10a). A gradual slope can indicate physical transitions (i.e. vaporization, evaporation, desorption) (Figure 4.10b). An abrupt weight lost (Figure 4.10c) is typically caused by a chemical reaction (i.e. decomposition, combustion, dehydroxylation) [20]. TGA data can also be presented as the derivative of the TG plot (named derivative thermogravimetry-DTG) in order to determine inflection points useful for in-depth interpretations as well as differential thermal analysis. For TGA-MS coupled apparatus, the mass spectrometry (m/z) data is produced at the same time and shown as a plot of a specific m/z intensity as a function of time.

4.2.2 The TGA instrument

As can be seen in Figure 4.11, TGA consists of a sample pan, supported on a precision weight scale, and a furnace that can control the temperature (either increase or decrease). The temperature can be changed in steps of 1°C (of different duration) and can be increased up to a few thousand degrees Celsius. The mass of the sample is monitored throughout the duration of the experiment. The chamber is purged by flow of an inert gas (i.e. He, N_2), to avoid reaction with the sample. The vaporized gas expelled from the sample is transferred to a mass spectrometer by a helium gas carrier. In the mass spectrometer's chamber, the compounds are bombarded with a high-energy electron beam that ionises the molecules by knocking off one electron. The ions are then separated according to their mass to charge ratio (m/z) using a magnetic or electric field (with lighter mass being more deflected) until they reach a detector were only cations are detected.

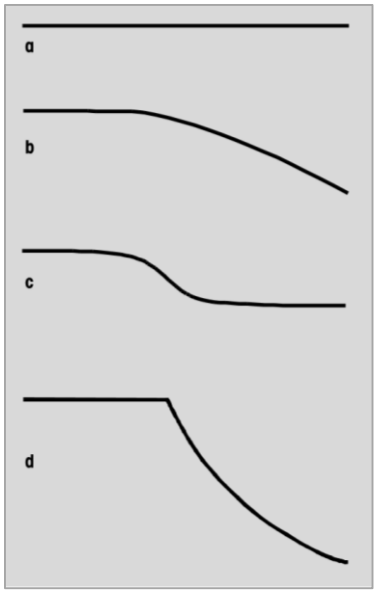

Figure 4.10 Representative example of TGA results identifying different possible reactions: a)no reaction (or physical change with no change in mass, such as melting or crystallization); b: volatile melt or evaporation; c: moisture loss; d: decomposition (taken from Widmann [20]).

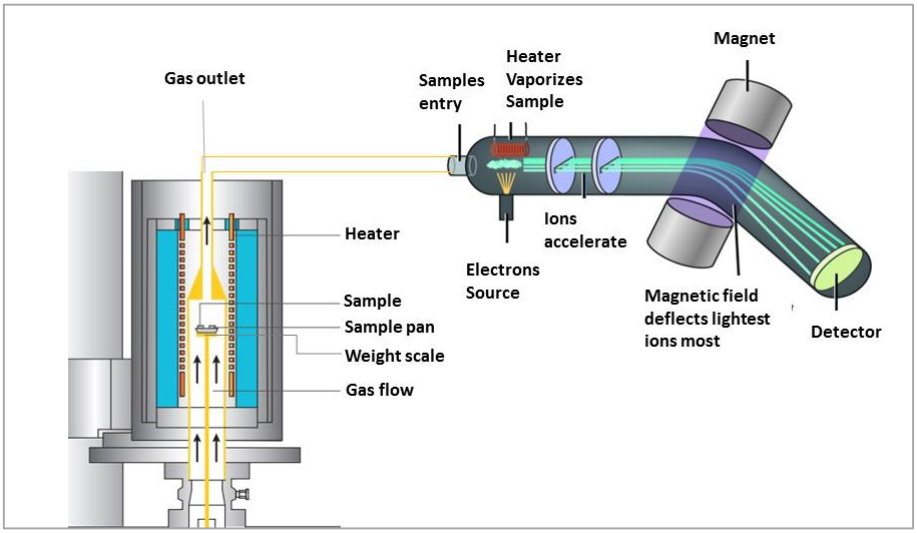

Figure 4.11 A diagram of a thermal gravimetric apparatus coupled to a mass spectrometer (modified after Linseis GmbH [21]and Openstax [22]).

4.2.3 TGA-MS application on adsorption of organic matter on clay minerals

TGA-MS has been used to qualitatively and quantitatively study different properties of clay minerals, including their thermal stability, chemical composition, oxidative stability, and kinetics of decomposition [18, 19]. For example, Thomas et al. [23] investigated the release of organic compounds from clay minerals, as indicated by a loss of weight in a TG plot. The

temperature of the weight loss indicated how strongly the adsorbate was bound to the surface. Low-temperature losses (below 250 °C) indicated volatilization (desorption) of the organic without the disruption of any chemical (intramolecular) bonds. High-temperature weight losses (> 250 °C) occurred when the organic molecule combusted or decomposed, before desorbed from the surface. Therefore, low temperature weight losses indicated a weak, physical adsorption, and high-temperature weight losses indicated a strong, chemical or ionic adsorption. From the magnitude of the weight losses, the authors managed to quantify the amount of organic material on the surface [23]. In a more recent study, Alipour-Tabrizy used TGA to measure the monolayer adsorption of various organic compounds on calcite, quartz and kaolinite and linked this to the wettability alteration of the mineral's surfaces which enhanced residual oil in reservoir rock pores [24].

4.3 Fourier transform infrared (FTIR) spectroscopy

4.3.1 Principle

IR spectroscopy deals with the interaction of electromagnetic radiation with matter within the infrared part of the spectrum (0.7 to 1000 μm). Figure 4.12 shows a Jablonski's diagram within the range of electromagnetic radiation from microwaves to ultraviolet (lower to higher energy). The interaction of radiation within this range leads to changes in the electronic structure of ions and molecules (ultraviolet), as well as changes in the vibrational (UV-IR) and rotational energies (IR-microwave) of molecules.

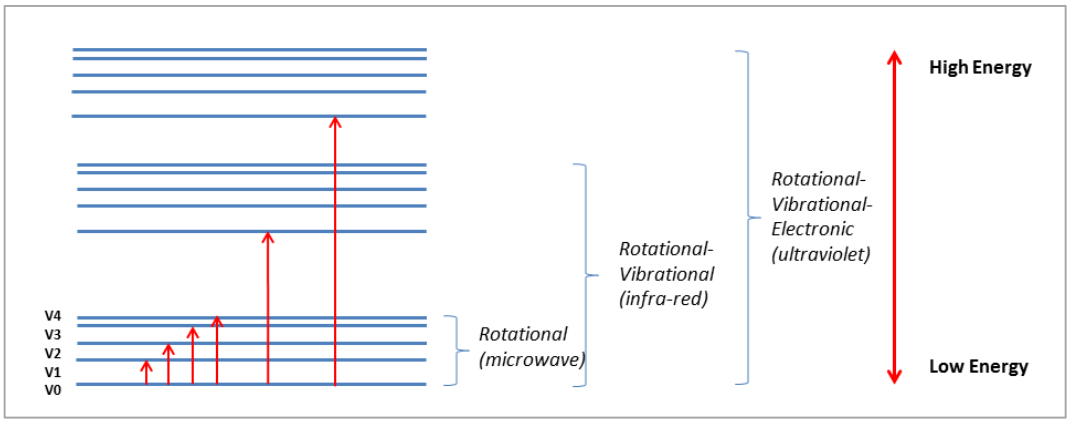

Figure 4.12 Jablohski's diagram for energy levels for molecule a) rotational transitions; b) rotational-vibrational transitions; c) rotational-vibrational-electronic transitions (modified from Osibanjo et al. [25]).

The IR region of the electromagnetic is subdivided into three regions: near IR, mid IR and far IR (Table 4.1). Near IR is normally associated to overtones or combinations of bands of

molecular vibrations, and in practice it requires intense radiation sources, resulting in disadvantages of low absorption and high noise to signal ratio, however it is able to penetrate deep into a material, which means that can be used in samples with little amount of pre-analysis preparation. Spectra obtained in this region consist mostly of broad peaks, which can be difficult to interpret, but recent advancements in data treatment has led to a wider utilization of NIR in many fields, from agriculture to astronomy [26-28]. NIR has also been used in agriculture, owing to the fact that all molecules containing hydrogen atoms have a measurable near-IR spectrum, resulting in a larger range of organic materials in plant samples being suitable for near-IR analysis in comparison to mid-IR [29]. Mid IR is the most commonly used IR range in chemistry. The energy of radiation at this range corresponds to the vibrational energy of molecules, in particular with the stretching and bending of covalent bonds between molecules. As bonds between different atoms have different vibration frequencies (or energies), IR spectroscopy allows the identification of the type of bonds within a molecule (C=O vs O-H, for example). Far IR deals with low-frequency molecular vibrations, as well as rotations in small molecules.

Table 4.1 IR spectral regions with wave length, wave number and frequencies (taken from Osibanjo et al. [25])

Region	**Wavelength**	**Wavenumbers (V), cm^{-1}**	**Frequencies (v), HZ**
Near	0.78 -2.5	12800 - 4000	3.8×10^{14} - 1.2×10^{14}
Middle	2.5 - 50	4000 - 200	3.8×10^{14} - 1.2×10^{14}
Far	50 -1000	200 -10	3.8×10^{14} - 1.2×10^{14}
Most Used	2.5 -15	4000 -670	3.8×10^{14} - 1.2×10^{14}

Due to its ability to differentiate between functional groups in the studied sample, IR spectroscopy is used to identify the fingerprint of chemicals, including type, structure, and bonding. It can be employed to study both inorganic and organic samples and for the analysis of solids, liquids and gases.

In an IR spectrophotometer, a polychromatic light is passed through the matter. The intensity of the transmitted light is then measured at each frequency. The absorbance and transmittance of the input electromagnetic radiation will correspond specifically to the bonds present in the molecule. The transmittance is defined as Equation 4.2.

$$T = \frac{I_r}{I_t} \times 100\% \qquad \text{(Equation 4.2)}$$

Where T is transmittance; I_r is the intensity of the initial electronmagnetic radiation; I_t is the intensive of the transmitted radiation after adsorption. Transmittance is related to absorbance according to Beer's law as derived in Equation 4.3.

$$A = -\log T \qquad \text{(Equation 4.3)}$$

Where A is absorbance and T is transmittance.

4.3.2 Basic instrument

FTIR is a development from dispersive infrared spectrometry which combines the use of the Fourier Transform mathematical tool (which allows for the inter-conversion of frequency andtime functions). This allows for the sample to be irradiated by a beam containing all the frequencies in the IR region, which is then transformed (mathematically, through a computer) into a "standard" IR spectrum. The most notable issues are that the application of FTIR is an increase inaccuracy, higher resolution and a decrease in noise. A simplified diagram of a "generic" FTIR interferometer is shown in Figure 4.13.

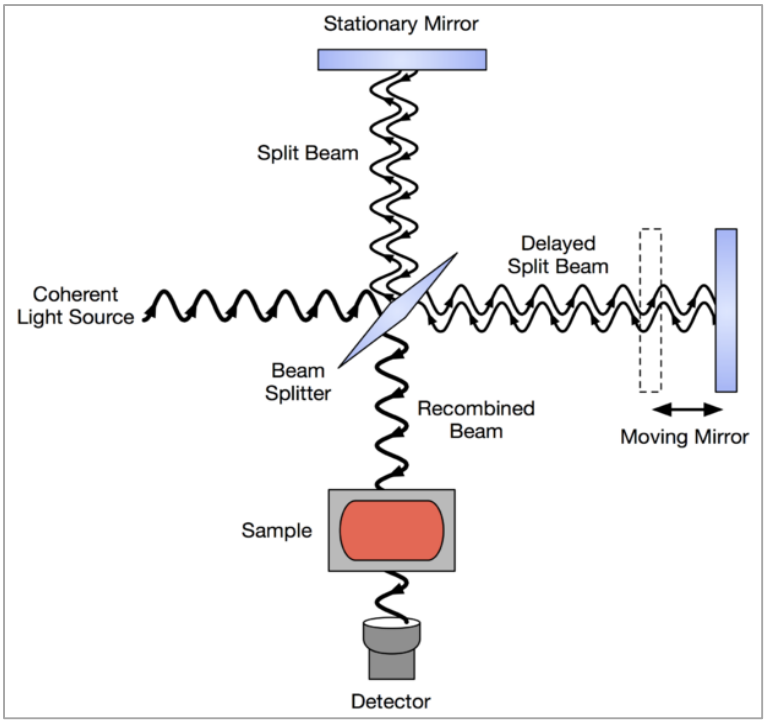

Figure 4.13 Typical schematic diagram of a generic FTIR (modified from Sanchonx, [30]).

The light source is passed through a beam splitter which divides into two beams. One beam is reflected into a mirror; and the other one is transmitted to a moving mirror which is sometimes blocked or transmitted. This produces a very precise laser wave-length in the

system. This interferogram goes back to the beam splitter and some fraction of the original light passes into the sample, where some energy is absorbed and some is transmitted. Eventually, the transmitted portion reaches the detector that reads the raw data (an interferogram) in every wavelength in the infrared range. The interferogram is then converted into an infrared spectrum using a Fourier transformation. In practice, a reference scan is taken first (in air or in the same solvent as the sample) and then is subtracted from the sample spectrum. Due to its fast scanning speeds, several scans can be taken in relatively small amounts of time and superimposed, increasing the signal to noise ratio of the final spectrum, and therefore facilitating the detection of small amounts of sample. The correlation chart of carboxylic acid and acid halide, which is similar to this study, was shown in Table 4.2. For example, chemical bonding can be identified from the adsorption at 1577 cm^{-1} for the antisymmetric stretching vibration of carboxylate group ($-COO^-$). This is important for understanding clay-oil-brine interactions [31], as can be seen from Figure 4.14.

Table 4.2 IR frequency classified by compound class (modified from Merck 2019® [32]).

Compound Class	Group	Absorption (cm^{-1})	Appearance
carboxylic acid	O-H stretching	3300-2500	strong, broad
	C=O stretching	1760	strong
	C=O stretching	1720-1706	strong
	O-H bending	1440-1395	medium
acid halide	C=O stretching	1815-1785	Strong
alkane	C-H stretching	3000-2840	medium
	C-H bending	1465	medium
	C-H bending	1450	medium
	C-H bending	1385-1380	medium

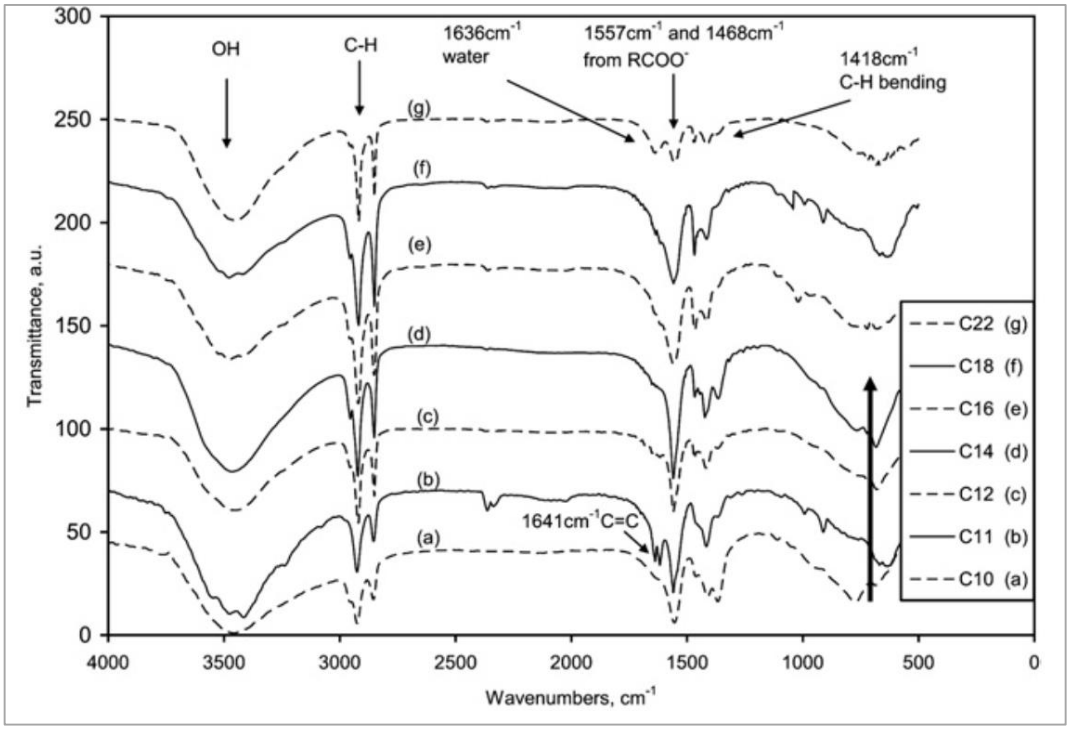

Figure 4.14 The example of FTIR's results showed the adsorption at various wavenumber to identified the chemical bonding between linear alkyl carboxylates ($CH_3(CH_2)nCOO^-$ (similar to decanoic acid) and MgAl–LDH (similar to cations screening on clay mineral) (taken from Nyambo et al. [33]).

4.4 Contact angle measurements

4.4.1 Principle

The contact angle method is the most-widely used technique to quantitatively, determine the wettability state of a sample. It is a direct measurement of the angle formed by the three phase boundary on a drop profile. At this point, equilibrium is achieved between adhesive and cohesive forces that exist between the molecules at the liquid-solid interface. Contact angle is related to the interfacial tension of the different contacts by Young's equation as derived in Section 3.6.

Contact angle measurements are direct and easy to perform; in addition they have the additional advantage that only small volumes of fluid are required, in addition to small substrate sizes. On the other hand, the small volumes may prove a disadvantage if care is not taken to remove or avoid impurities (on both the surface and the fluid face). In addition, care must be taken to determine the contact line between all phases in a consistent manner. Fortunately, the use of image processing software has recently much improved this procedure, which used to be performed by research "by eyes".

4.4.2 Parameters influencing contact angle measurement

Contact angle measurements can be affected by the heterogeneity and topography (roughness) of the surface [34, 35]. In fact, these two parameters can lead to contact angle hysteresis, where the contact angle from an advancing droplet over a surface is different than the one measured during the receding (or withdrawn) of the droplet.

Heterogeneity: in order to obtain the most representative contact angles, the studied solid surfaces must be uniform and homogenous in terms of both its chemical and atomic structure. In addition, the solid surface must not swell [36]. These parameters are difficult to control when studying clay minerals, but at the very minimum imply the use of samples of well-oriented crystals (with a small size variation) and chemical conditions that prevent swelling.

Surface roughness: This parameter can affect the achievement of a minimum energy position of the surface contact through the local variation of the slope of the sample surface, which has the effect of creating barriers that may pin the motion of the contact line [37]. As a result of this, the actual and apparent contact angle values can deviate substantially from each other. Wenzel [38] assumed that the droplet penetrates into the roughness grooves (as in Figure 4.15) and developed an equation to calculate the theoretical contact angle as derived in Equation 4.4.

$$\cos\theta_m = r\cos\theta_y \qquad \text{(Equation 4.4)}$$

Where θ_m is the measured contact angle, θ_y is contact angle from Young's equation, and r is the roughness ratio. The roughness ratio is defined as the ratio between the actual and projected solid surface area. If the ratio is equal to 1, it means a smooth surface; and if the ratio is more than 1, it indicates a rough surface. According to Equation 4.4, Wenzel stated that an increase in roughness enhanced the degree of wettability of a surface.

Later, Cassie and Baxter [39] stated that, for certain roughness values, the liquid cannot penetrate through the grooves due to the trapped air (Figure 4.15). This means that the liquid droplet will not cover all the actual surface area of the sample. These authors derived an equation to calculate theoretical contact angles on heterogeneous surfaces and porous materials, in the case of non-penetrating liquid (into surface grooves or pores) as shown in Equation 4.5.

$$\cos\theta_m = X_1(\cos\theta_y + 1) - 1 \qquad \text{(Equation 4.5)}$$

Where θ_m is the measured contact angle; θ_y is contact angle from Young's equation; X_1 is proportion of the actually wetted surface.

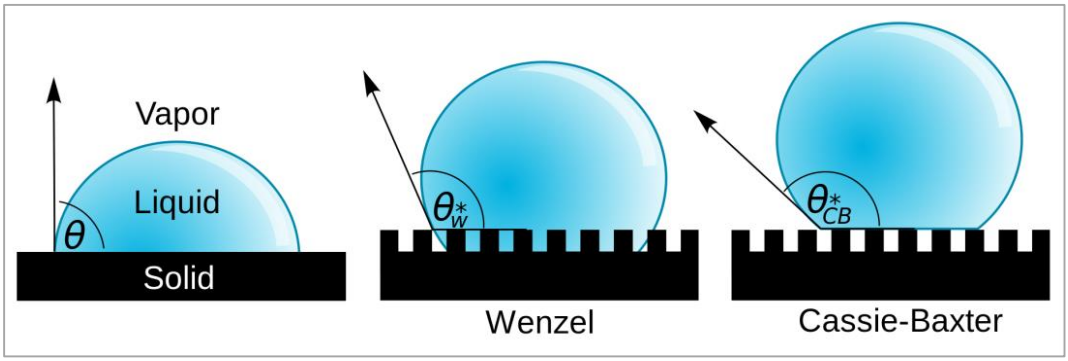

Figure 4.15 Basic states of surface wetting on a smooth surface (left) and on a grooved surface according to Wenzel (middle) and Cassie-Baxter (right) (taken from Vladsinger [40]).

4.4.3 Basic instrument

The most commonly utilized instrument to measure contact angles is the "telescope-goniometer" (or simply the goniometer). This instrument allows the visual inspection of the contact point between droplet and sample surface and the direct measurement of the contact angle at the three phase contact point. When the droplet drops on the surface, a light source shines on it and the image is magnified by a small telescope. Then, a high-resolution camera is used to capture an image of the liquid droplet that sits over the sample's surface (sessile drop), so it can be subsequently analyzed with software. In this study, the used software is DropImage Pro from Ramé-Hart Instrument Co [41]. An image of the droplet can be projected onto a screen and the outlines traced. The contact angle is then automatically measured 10 times every 5 seconds. The machine measures both sides (left and right) at the intersection line between the droplet and the surface. It calculates the average angle, standard deviation, height, width, and volume of droplet as shown in Figure 4.16.

4.4.4 Contact angle measurement techniques

4.4.4.1 Sessile Drop

The sessile drop technique is normally performed in the presence of air. In this technique, a controlled volume of liquid is dropped onto the sample's surface using a micro syringe. Important factors to control when using this technique in order to achieve consistent results are equilibration time and volume [42]. The three phase contact line of air-liquid-

solid can be measured in static position of advancing/receding mode (to determine contact angle hysteresis (Figure 4.17).

Date	:	7/24/2018	Remarks	:	Comments here
Experiment	:	clay film	Method	:	clay_film.met
Drop phase	:	Water	Density	:	0.7500
Extern. Phase	:	Water	Density	:	0.9987
Solid phase	:	clay film	Drop Type	:	Contact angle LR

No.	Time	Theta (L)	Theta(R)	Mean	Dev.	Height	Width	Area	Volume	Messages
1	0.0	143.20	145.07	144.13	0.94	1.902	1.580	14.13	5.94	
2	5.0	143.29	144.64	143.96	0.67	1.902	1.580	14.12	5.94	
3	10.0	143.33	144.63	143.98	0.65	1.900	1.581	14.11	5.93	
4	15.0	143.32	145.27	144.29	0.98	1.900	1.577	14.12	5.93	
5	20.0	143.40	144.65	144.02	0.63	1.901	1.579	14.11	5.93	
6	25.0	143.39	144.09	143.74	0.35	1.902	1.581	14.09	5.93	
7	30.0	143.49	144.35	143.92	0.43	1.902	1.579	14.11	5.93	
8	35.0	143.64	144.48	144.06	0.42	1.901	1.578	14.11	5.93	
9	40.0	143.73	144.45	144.09	0.36	1.902	1.578	14.11	5.94	
10	45.0	143.82	144.46	144.14	0.32	1.902	1.578	14.12	5.94	
Mean:		143.46	144.61	144.03	0.57	1.902	1.579	14.11	5.93	
Stand.dev.:		0.07	0.11	0.05	0.08	0.000	0.000	0.00	0.00	

Figure 4.16 Example of contact angle measurement's results from DropImage Pro.

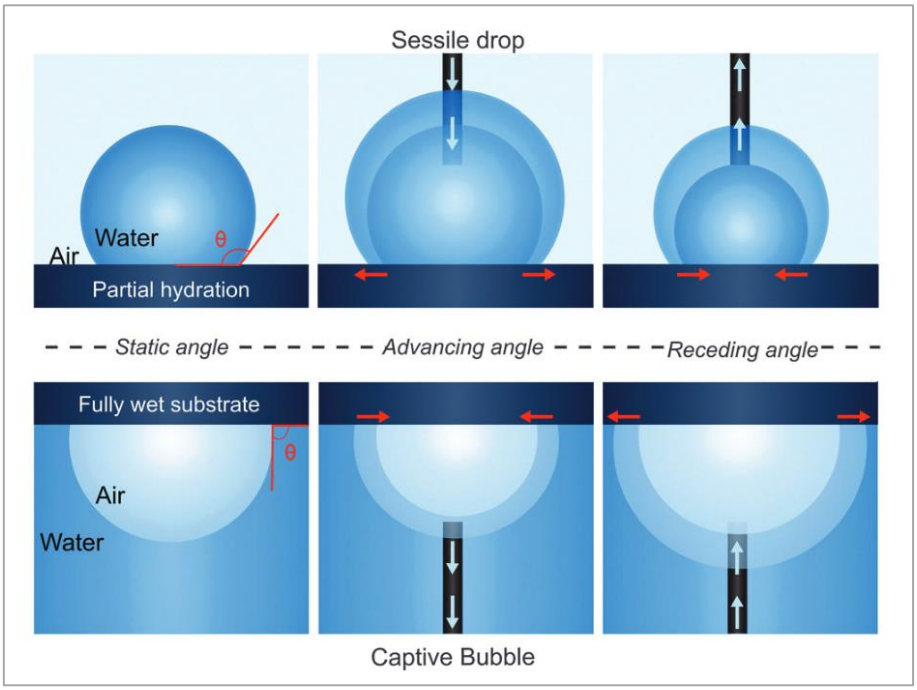

Figure 4.17 The two most utilized techniques of contact angle measurement employed to characterize wettability. The sessile drop technique (top) and the captive bubble technique (bottom) (taken from Due et al. [43]).

4.4.4.2 Captive Bubble

In the case of liquid-liquid (or air)-solid interfaces, the captive bubble/drop is the recommended method for contact angle measurement. Initially, a solid surface is placed inside a transparent glass tank on two stable supports with flat surfaces. The container is filled with a liquid, and then an air/fluid droplet is generated onto the surface using U-shaped needle attached to a micro syringe. The contact angle is a result of buoyancy and collision. An important point to consider is that the new liquid phase must be immiscible with water, not soluble in water, and possess a lower density than water. This is the method used for this thesis.

4.5 Scanning Electron Microscopy

4.5.1 Principle of operation

Scanning electron microscopy (SEM) is an essential imaging technique used to investigate the surface features of samples, with wide application in the natural and physical sciences. In addition, modern SEM can also perform detailed chemical analysis of the sample's surface using energy dispersive X-ray detectors. A typical SEM has a lateral resolution of better than 10 nm (typically 5 nm) which is more than 300 times the depth of field of a of a light microscopy. An SEM works by rastering an electron beam (with a spot size of about 5-10 nm), referred to as the primary electron beam (PE), over a surface, which is produced by creating a voltage difference between a cathode and anode. This electron beam interacts with the sample in different ways resulting in the release of different types of signals, including secondary electrons (SE), backscattered electrons (BSE), and X-rays, as shown in Figure 4.18.

Secondary electrons are produced from the interaction of the primary electrons with the most external electrons (and weakest in terms of bonding) in the sample. Some of the energy from the PE is transferred to these external electrons which allow them to "escape". Due to their low energy they are produced at the outermost part of the sample. Secondary electrons (SE) are then detected through the main detector in the instrument. The signal intensity produce from the secondary electron emission from the sample at each x and y data point during rastering of the electron beam across the surfaces is measured. The convex part of the sample is bright and the concave parts are dark on the image. This can produce very high-resolution images of the specimen's topography.

Back-scattered electrons (BSE) are produced by the elastic scattering of the primary electrons due to interactions with the positively charged nuclei of the sample's atoms. These electrons have a higher energy than SE and are produced deeper into the sample. In BSE images, contrast is dependent on average atomic number between areas in

the sample. More electrons are dispersed by the nuclei of heavier atoms; consequently, they are visualized as bright spots on the image. A BSE image, therefore, could reflect a compositional contrast, but it does not provide the identity of the elements present.

X-rays are created after the collision of primary electrons with internal electron layers. As the electrons from the inner layer are "expelled" from the atom, electrons from outer shells replace them, releasing energy in the form of X-rays in the process. These X-rays are characteristic of each element type; therefore, their detection can allow for the identification and measurement of the abundance of elements in the sample and to map their distribution. Two different methods, which are based on X-ray detection, can be used for microanalysis, Energy Dispersive Spectrometry (EDS) or Wave Dispersive Spectrometry (WDS).

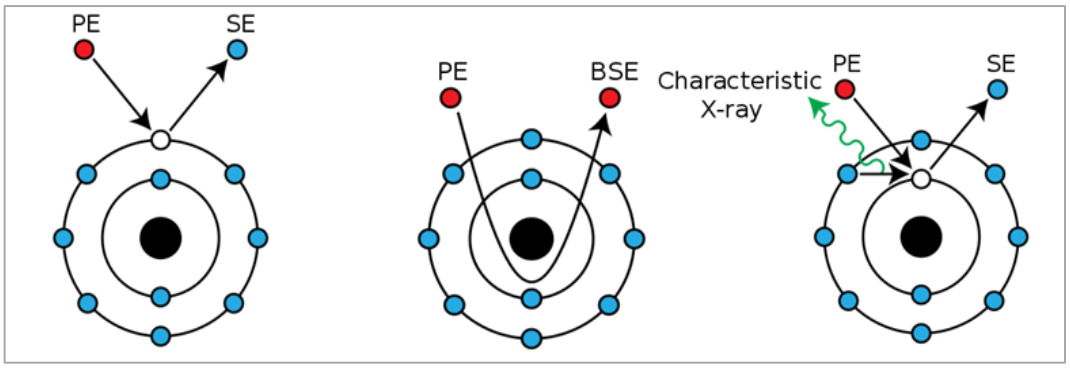

Figure 4.18 Schematic diagram of the interactions occurring at an atom bombarded by primary electrons, leading to the production of secondary electrons, backscattered electrons and X-rays (modified from Hurt [44]).

4.5.2 The basic instrument of SEM

The main SEM components are electron gun, condenser lenses, sample's stage, and detectors for all signals of interest, display/data output devices, and the vacuum system (Figure 4.19). The operation of the SEM requires high vacuum in the chamber in order to refine the electron beam. Initially, the electron gun generates the high energy primary electron beam. The spot size of this beam is too large (10-50 μm) and therefore it needs to be demagnified. This is achieved by one or two condenser lens and an objective lens that focus the beam on to the sample surface. The beam then is scanned from point-to-point (raster) across the specimen. The results of the interaction with the sample, including secondary electrons, backscattered electron and X-rays, are then recorded by various detectors located around the sample stage. The signals are then converted to photons via a

scintillator, amplified in a photomultiplier, and converted to electrical signals and used to modulate the intensity of the image.

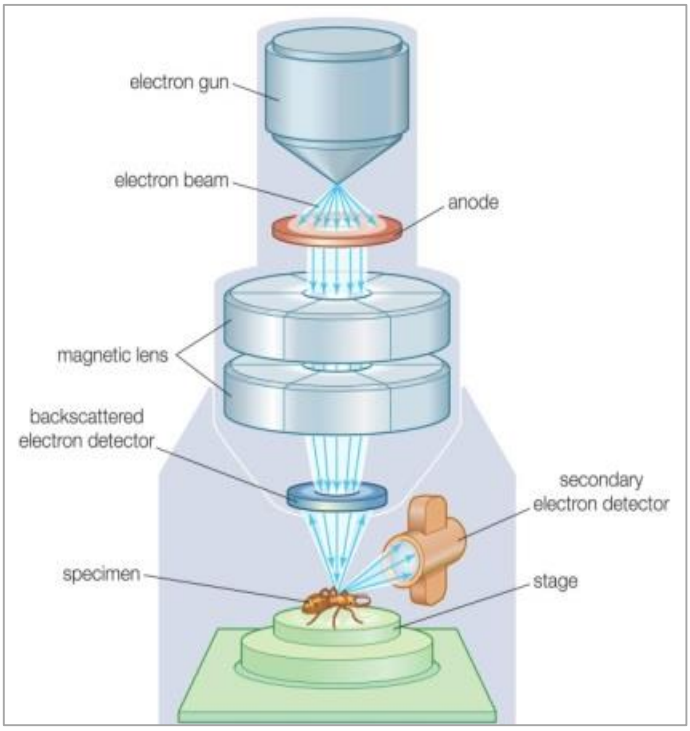

Figure 4.19 Schematic diagram of a generic SEM (Encycopedia Britanica, [45]).

4.5.3 Focused ion beam (FIB) SEM

FIB SEM is one type of SEM which is similar with the basic principle of SEM. This technology involves using an ion beam (typically gallium ions) directed onto a hard sample instead of electron beams. The ion beam can focused to an extremely fine probe size (<10 nm). Gallium (Ga^+) normally use for primary ion beam. It hits the sample surface and sputters a small amount of material, which leaves the surface as either secondary ions (either positive or negative charged) or neutral atoms. The primary beam also produces secondary electrons (e^-). As the primary beam raster's on the sample surface, the signal from the sputtered ions or secondary electrons is collected to form an image. According to the primary beam, FIB SEM outweighs than the typical SEM, because FIB SEM have higher resolution imaging capability. The current FIB SEM easily achieves 5 nm imaging. Therefore, a great deal of FIB SEM allows precision milling of the specimen down to micrometer and nanoscale.

Sample preparation for FIB SEM requires two main issues. Firstly, samples must to be dried because FIB SEM operated in high vacuum will pulled out the water out of sample and it cause the damages of microscope. Secondly, samples must be electrically conductive,

because non-conductive sample become negatively charged as the incident electrons reach it and the beam is then repelled by the sample. If the sample is inherently non-conductive need to conductive need to be coated a thin layer of gold and carbon. Surface coating, as would be required as in SEM.

4.5.4 Environmental Scanning Electron Microscopy (ESEM)

As was mentioned above, standard SEM requires a low vacuum and, thus, a low gaseous environment (a few Torr) for operation, resulting in the requirement for dried samples. The ESEM was developed from conventional SEM in order to apply it to wet (or nonconductive) samples. ESEM has a sophisticated differential pumping system. The electron gun and electron column are both kept at high vacuum with the standard vacuum pressures (10^{-7} – 10^{-6} Torr) for good focusing and low beam diffusion. However, the sample's stage maintains a low gas pressure (2-20 Torr), which can be water vapour, allowing for wet samples to remain stable during examination. In addition, primary electrons interacting with water vapour or gas molecules produce ions that revert back to the sample surface allowing for the reduction of charging.

For imaging, ESEM generate the electron beam in the same way as in an SEM (Figure 4.20). The primary electron beam, which is very energetic, penetrates through the gas or water vapors and impinges on the specimen. The distance between the sample stage and electron gun compartment is the need to reduce to a minimum. Afterwards, the secondary electrons are amplified with certain differences in the detector design due to its low energies and high collision rates with gas molecules. Lastly, the intensity of that signal is converted into a brighter or darker contrast.

The fact that wet or hydrated samples can be imaged by ESEM, in addition to the fact that dynamic experiments can be performed, makes it a potentially ideal technique to study wettability [46, 47]. Water condensation on the sample can be achieved by adjusting the chamber's pressure and temperature (therefore controlling the relative humidity), as can be seen in the diagram shown in Figure 4.21. For example, in Figure 421, when the temperature of the sample is maintained at 2 °C, the pressure in the sample chamber could be in the range from *f* to *a*. It can be gradually increased the pressure. At the point c, d, e is the equilibrium point (at about 5.0 Torr) and then as the relative humidity inside the chamber reaches 100%, water will condense as droplets onto the surface of the cooled sample, allowing observation of the contact angle between the sample and water droplets [47]. At the equilibrium point, the sample can be kept fully hydrated allowing for the examination of drop let formation (and dynamics), therefore allowing for the quantitative assessment of the wettability on the wet samples.

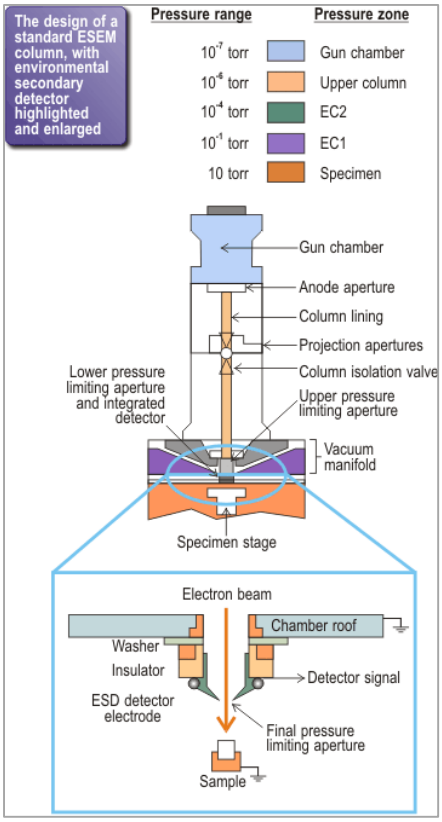

Figure 4.20 Schematic diagram of ESEM (taken from AZoM, [48]).

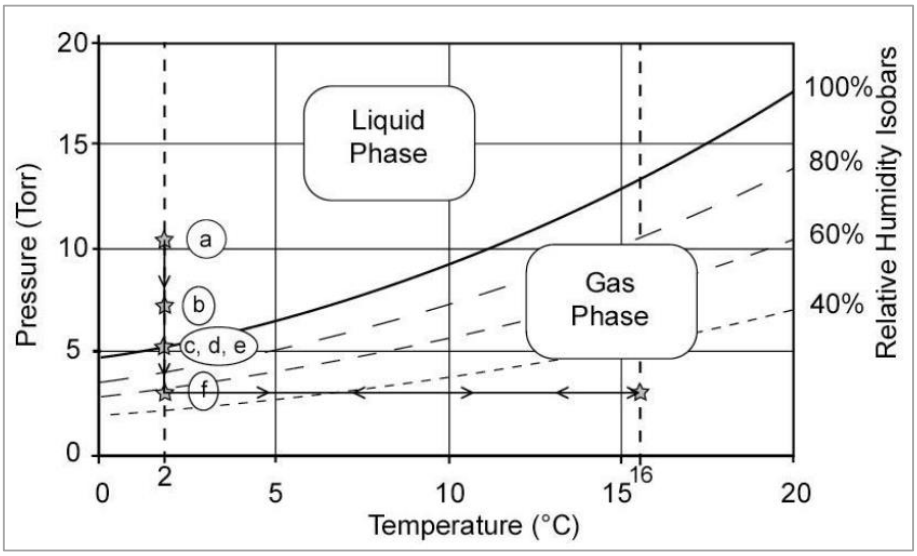

Figure 4.21 Graph shows the relative humidity with the relation of temperature and pressure inside the ESEM sample chamber (modified from Volland-Tuduri et al. [49]).

4.6 Brunauer, Emmett and Teller (BET) Surface Area Analysis

4.6.1 Principle

BET is one of most widely used techniques to measure the surface area and porosity of solid materials. To achieve this, the technique uses the physical sorption of a gas and the sorption theory developed by Brunauer, Emmett and Teller (hence the term BET) [50, 51]. BET theory assumes that gas can adsorb onto a solid surface in a multilayer arrangement and relates this to the relative pressure (P/P_0) of the gas phase above the sample's surface [52]. The amount of adsorbed gas, as determined by a measured gas isotherm (Figure 4.22), is correlated to the total surface area of the particles, including porosity, as derived in Equation 4.9. Two factors are needed for the calculation. The monolayer capacity of surface and the BET constant are calculated from the adsorption isotherm using Equations 4.10 and 4.11 respectively.

$$\frac{p}{n_a(p_0 - p)} S_{total} = \frac{1}{n_m C} + \frac{(C-1)}{n_m C} \times \frac{p}{p_0} \qquad \text{(Equation 4.9)}$$

$$n_m = \frac{1}{\text{gradient} - \text{intercept}} \qquad \text{(Equation 4.10)}$$

$$C = 1 + \frac{\text{gradient}}{\text{intercept}} \qquad \text{(Equation 4.11)}$$

Where P is the equilibrium pressure; P_0 is the saturation pressure of adsorbates at the temperature of adsorption; n_a is the adsorbed gas quantity; n_m is the monolayer capacity; C is BET constant.

Experimentally, samples must be "cleaned", in order to obtain an accurate measurement. This is achieved by degassing the samples in a vacuum at high temperatures. The highest temperature possible that will not damage the sample's structure is usually chosen in order to shorten the degassing time (which can be as long as 16 hrs). The samples are weighed before and after cleaning, and this value must be equal. Samples are placed inside a measuring cell (made of glass) and glass rods are added to minimize the dead volume. Before surface area analysis, the dead volume is calibrated by injecting helium gas, because helium does not adsorb onto the sample. When the cleaned sample is ready, the cells are placed into heating mantles and connected to the outgas port of the machine. The temperature is controlled around the boiling point of adsorbate (nitrogen -196 °C or 77 K), to increase adsorption. The gas slowly flows through the sample, and it's adsorbed to the

surface of the particles. The volume of gas adsorption is measured as a function of increasing values of P/P_0. When nitrogen is used as the adsorbate gas, P/P_o values of 0.10, 0.20, and 0.30 are often suitable.

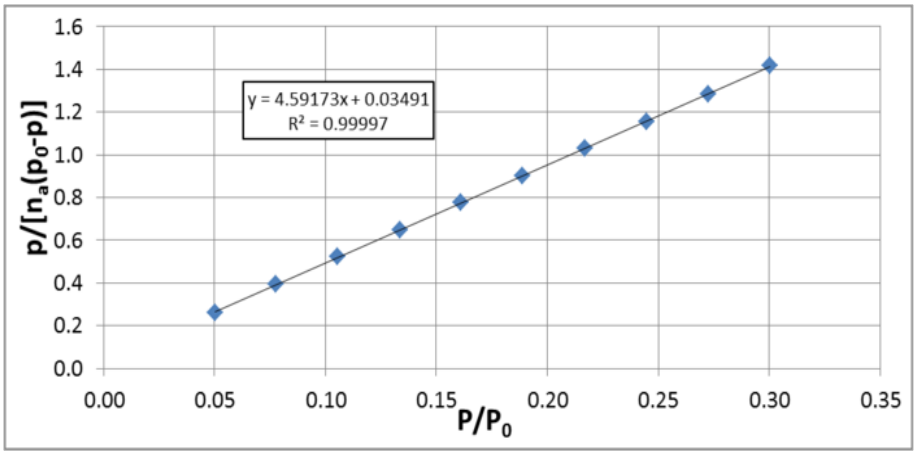

Figure 4.22 The example of a gas adsorption isotherm.

4.7 References

[1] G. Binnig, C.F. Quate, C. Gerber, Atomic Force Microscope, Physical Review Letters 56(9) (1986) 930-933.

[2] P. Cubillas, M.W. Anderson, Atomic force microscopy, Multi Length-Scale Characterisation (2014) 121-193.

[3] G. Haugstad, Atomic force microscopy: understanding basic modes and advanced applications, John Wiley & Sons2012.

[4] T. Cohen-Bouhacina, A. MaAli, Biomolecules to Living Cells in: R. Borsali, R. Pecora (Eds.), AFM Imaging in Physiological Environment, Springer, Netherlands, 2008, pp. 1379-1438.

[5] S.B. Kaemmer, Introduction to Bruker's ScanAsyst and PeakForce Tapping AFM Technology, (2011) 12.

[6] P. Cubillas, M.W. Anderson, Atomic Force Microscopy, in: D.W. Bruce, D. O'Hare, R.I. Walton (Eds.), Multi Length-Scale Characterisation: Inorganic Materials Series, John Wiley & Sons, Chichester, United Kingdom, 2014, pp. 121-195.

[7] K.L. Johnson, K. Kendall, A. Roberts, Surface energy and the contact of elastic solids, Proceedings of the royal society of London. A. mathematical and physical sciences 324(1558) (1971) 301-313.

[8] B.V. Derjaguin, V.M. Muller, Y.P. Toporov, Effect of contact deformations on the adhesion of particles, J. Colloid Interface Sci. 53(2) (1975) 314-326.

[9] H.J. Butt, B. Cappella, M. Kappl, Force measurements with the atomic force microscope: Technique, interpretation and applications, Surface science reports 59(1-6) (2005) 1-152.

[10] J.I. AG, NanoWizard® AFM User Manual Version 4.2 2012.

[11] T. Hassenkam, L.L. Skovbjerg, S.L.S. Stipp, Probing the intrinsically oil-wet surfaces of pores in North Sea chalk at subpore resolution, Proceedings of the National Academy of Sciences of the United States of America 106(15) (2009) 6071-6076.

[12] C.D. Blanchette, A. Loui, T.V. Ratto, Tip functionalization: Applications to chemical force spectroscopy, Handbook of Molecular Force Spectroscopy, Springer2008, pp. 185-203.

[13] D.V. Vezenov, A. Noy, P. Ashby, Chemical force microscopy: Probing chemical origin of interfacial forces and adhesion, Journal of Adhesion Science and Technology 19(3-5) (2005) 313-364.

[14] A. Berquand, Common Approaches to Tip Functionalization for AFM-Based Molecular Recognition Measurements, 2010, p. 6.

[15] F. Luderer, U. Walschus, Immobilization of Oligonucleotides for Biochemical Sensing by Self-Assembled Monolayers: Thiol-Organic Bonding on Gold and Silanization on Silica Surfaces, pringer-Verlag Berlin Heidelberg2005.

[16] A. Ebner, P. Hinterdorfer, H.J. Gruber, Comparison of different aminofunctionalization strategies for attachment of single antibodies to AFM cantilevers, Ultramicroscopy 107(10-11) (2007) 922-927.

[17] D.V. Vezenov, A. Noy, L.F. Rozsnyai, C.M. Lieber, Force Titrations and Ionization State Sensitive Imaging of Functional Groups in Aqueous Solutions by Chemical Force Microscopy, Journal of the American Chemical Society 119(8) (1997) 2006-2015.

[18] C. Baffi, M.T. Dell'Abate, A. Nassisi, S. Silva, A. Benedetti, P.L. Genevini, F. Adani, Determination of biological stability in compost: A comparison of methodologies, Soil Biol. Biochem. 39(6) (2007) 1284-1293.

[19] M.J. Fernández-Gómez, M. Díaz-Raviña, E. Romero, R. Nogales, Recycling of environmentally problematic plant wastes generated from greenhouse tomato crops through vermicomposting, International Journal of Environmental Science and Technology 10(4) (2013) 697-708.

[20] G. Widmann, Interpreting TGA curves, 2001, p. 20.

[21] L. GmbH, Instruments for Thermogravimetry. Thermogravimetric Analysis / Thermogravimetry / Thermobalance (TGA). https://www.linseis.com/en/products/thermogravimetry/.

[22] O. College. http://cnx.org/contents/havxkyvS@9.58:ZV-IsnqQ@8/Atomic-Structure-and-Symbolism. (Accessed 12 March 2019.

[23] M.M. Thomas, J.A. Clouse, J.M. Longo, Adsorption of organic compounds on carbonate minerals: 1. Model compounds and their influence on mineral wettability, Chemical geology 109(1-4) (1993) 201-213.

[24] V. Alipour Tabrizy, R. Denoyel, A.A. Hamouda, Characterization of wettability alteration of calcite, quartz and kaolinite: Surface energy analysis, Colloids and Surfaces A: Physicochemical and Engineering Aspects 384(1–3) (2011) 98-108.

[25] R. Osibanjo, R. Curtis, Z. Lai, Infrared: Theory, 2019. https://chem.libretexts.org/Bookshelves/Physical_and_Theoretical_Chemistry_Textbook_Maps/Supplemental_Modules_(Physical_and_Theoretical_Chemistry)/Spectroscopy/Vibrational_Spectroscopy/Infrared_Spectroscopy/Infrared%3A_Theory. (Accessed 2 Fabuary 2018).

[26] Q. Zhou, Y. Xi, H. He, R.L. Frost, Application of near infrared spectroscopy for the determination of adsorbed p-nitrophenol on HDTMA organoclay—implications for the removal of organic pollutants from water, Spectrochimica Acta Part A: Molecular and Biomolecular Spectroscopy 69(3) (2008) 835-841.

[27] R.L. Frost, J.T. Kloprogge, Z. Ding, Near-infrared spectroscopic study of nontronites and ferruginous smectite, Spectrochimica Acta Part A: Molecular and Biomolecular Spectroscopy 58(8) (2002) 1657-1668.

[28] H. Cheng, J. Yang, Q. Liu, J. Zhang, R.L. Frost, A spectroscopic comparison of selected Chinese kaolinite, coal bearing kaolinite and halloysite—A mid-infrared and near-infrared study, Spectrochimica Acta Part A: Molecular and Biomolecular Spectroscopy 77(4) (2010) 856-861.

[29] M. Manley, Near-infrared spectroscopy and hyperspectral imaging: non-destructive analysis of biological materials, Chem. Soc. Rev. 43(24) (2014) 8200-8214.

[30] Sanchonx, FTIR Interferometer.png, 2011. https://commons.wikimedia.org/wiki/File:FTIR_Interferometer.png. (Accessed 5 April 2019).

[31] J.-J. Max, C. Chapados, Infrared Spectroscopy of Aqueous Carboxylic Acids: Comparison between Different Acids and Their Salts, The Journal of Physical Chemistry A 108(16) (2004) 3324-3337.

[32] Merck, IR Spectrum Table & Chart, 2019. https://www.sigmaaldrich.com/technical-documents/articles/biology/ir-spectrum-table.html. (Accessed 6 June 2019).

[33] C. Nyambo, P. Songtipya, E. Manias, M.M. Jimenez-Gasco, C.A. Wilkie, Effect of MgAl-layered double hydroxide exchanged with linear alkyl carboxylates on fire-retardancy of PMMA and PS, J. Mater. Chem. 18(40) (2008) 4827-4838.

[34] A. Marmur, Thermodynamic aspects of contact angle hysteresis, Adv. Colloid Interface Sci. 50 (1994) 121-141.

[35] L. Gao, T.J. McCarthy, Contact angle hysteresis explained, Langmuir 22(14) (2006) 6234-6237.

[36] S.K. Wisniewska, Surface analysis of selected hydrophobic matrials, Department o f Metallurgical Engineering, University of Utah, 2005.

[37] C.D. Volpe, D. Maniglio, M. Morra, S. Siboni, The determination of a 'stable-equilibrium' contact angle on heterogeneous and rough surfaces, Colloids Surf. Physicochem. Eng. Aspects 206(1) (2002) 47-67.

[38] R.N. Wenzel, Resistance of solid surfaces to wetting by water, Industrial & Engineering Chemistry 28(8) (1936) 988-994.

[39] A. Cassie, S. Baxter, Wettability of porous surfaces, Transactions of the Faraday society 40 (1944) 546-551.

[40] Vladsinger, Contant angle measurement, 2014. (Accessed 31 August 2018).

[41] F.K. Hansen, A program system for interfacial tension and contact angle measurement by image analysis, USA, 1990.

[42] J. Shang, M. Flury, J.B. Harsh, R.L. Zollars, Comparison of different methods to measure contact angles of soil colloids, J. Colloid Interface Sci. 328(2) (2008) 299-307.
[43] C. Duc, A. Vlandas, G.G. Malliaras, V. Senez, Wettability of PEDOT:PSS films, Soft Matter 12(23) (2016) 5146-5153.
[44] R. Hurt, Electron emission mechanisms.svg, 2015. https://commons.wikimedia.org/w/index.php?curid=50931451. (Accessed 12 April 2019).
[45] E. Britannica, Encyclopædia Britannica, 2019.
[46] R. Kareem, Towards a Nanoscopic understanding of oil-sandstone wettability-implications for enhanced oil recovery, IOR 2015-18th European Symposium on Improved Oil Recovery, 2015.
[47] J. Buckman, A. Todd, P. Hill, Observations on Reservoir Rock Wettability Using an Environmental SEM, Microscopy and Analysis (2000) 35-38.
[48] AZoM, Environmental Scanning Electron Microscopy - ESEM, 2002. https://www.azom.com/article.aspx?ArticleID=1556. (Accessed 14 March 2019).
[49] N. Volland-Tuduri, M. Brossard, A. Bruand, H. Garreau, Direct analysis of microaggregates shrinkage for drying: Application to microaggregates from a Brasilian clayey Ferralsol, Comptes Rendus Geoscience 336(11) (2004) 1017-1024.
[50] S.S. International Organization for Standardization. Technical Committee ISO/TC 24. Particle characterization including sieving, Particle characterization, Determination of the Specific Surface Area of Solids by Gas Adsorption: BET Method, ISO2010.
[51] S. Brunauer, P.H. Emmett, E. Teller, Adsorption of gases in multimolecular layers, J. Am. Chem. Soc. 60(2) (1938) 309-319.
[52] M. Thommes, K. Kaneko, A.V. Neimark, J.P. Olivier, F. Rodriguez-Reinoso, J. Rouquerol, K.S. Sing, Physisorption of gases, with special reference to the evaluation of surface area and pore size distribution (IUPAC Technical Report), Pure Appl. Chem. 87(9-10) (2015) 1051-1069.

5

Chemical force microscopy study on the interactions of COOH and NH_2 functional groups with kaolinite surface: Implications for enhanced oil recovery

Clay-oil interactions play a critical role in determining the wettability of sandstone oil reservoirs, which in turn governs the effectiveness of enhanced oil recovery methods. In this study we have measured the adhesion between –COOH functional groups and the siloxane and aluminol faces of kaolinite clay minerals by means of chemical force microscopy as a function of pH, salinity (0.001 to 1 M) and cation identity (Na^+ *vs.* Ca^{2+}). Results from measurements on the siloxane face show that Ca^{2+} displays a reverse low-salinity effect (adhesion decreasing at higher concentrations) at pH 5.5, and a low salinity effect at pH 8. At a constant Ca^{2+} concentration of 0.001 M, however, an increase in pH leads to larger adhesion. In contrast, a variation in the Na^+ concentration showed less effect in varying the adhesion of –COOH groups to the siloxane face. Measurements on the aluminol face showed a reverse low-salinity effect at pH 5.5 in the presence of Ca^{2+}, whereas an increase in pH with constant ion concentration resulted in a decrease in adhesion for both Ca^{2+} and Na^+. Results are explained by looking at the kaolinite's surface complexation and the protonation state of the functional group and highlight a more important role of the multicomponent ion exchange mechanism in controlling adhesion than the double layer expansion mechanism. Moreover, -NH_2 and kaolinite surface interacts by surface complexation, electrostatic interaction, and hydrogen bond (or EDL).

5.1 Introduction

Global crude oil consumption has sharply increased in the last decades, however, primary and secondary recovery methods may still leave up to 65% of the original oil in place (OOIP) in the reservoir [1, 2]. In order to increase oil yield, the petroleum industry uses tertiary or enhanced oil recovery methods, as well as modified secondary recovery approaches. Enhanced oil recovery methods include steam and CO_2 injection, chemical flooding, pH alteration, *inter alia*. One method that is currently highlighted is low salinity enhanced oil recovery (LSEOR) owing its use of a low-cost, environment-friendly substance, its sustainability, and its effectiveness [3, 4]. For this reason, a multitude of studies have been conducted to understand the fundamental geochemical processes driving LSEOR; nevertheless, a debate still exists on the exact nature and importance of these processes and hence whether LSEOR can be applied to any given field [3, 4]. Most authors agree, however, on a series of factors or conditions that need to be met for low salinity EOR to be effective, these include: the presence of clay minerals, the presence of a saline connate water (containing multivalent ions), exposure of the rock to acidic and basic oil components, and a significant reduction of salinity in the flooding water [3].

LSEOR processes applied to sandstone reservoirs are believed to improve oil yields through the overall modification of wettability [5]. This change of wettability would drive the detachment of oil molecules from the mineral-lined pore surfaces of the sandstone. Lager et al. proposed that multicomponent ion exchange (MIE) of divalent cations (Mg^{2+} and Ca^{2+}) was the main mechanism responsible for increasing oil yields on their core brine injection experiments [6]. In their model the divalent cations preferentially acted as an electrostatic bridge between the negatively charged clay surfaces and the negatively charged polar oil molecules. During the low salinity brine injection phase, monovalent cations would substitute the divalent cations bridging the clay mineral surface and the oil molecules, resulting in the release of oil from the clay surface, which would induce the overall reservoir wettability state to more water-wetting. However, both Strand et al. and Austad et al. have pointed out that wettability is not controlled only by low cation concentration, but also through a pH effect [5, 7]. These authors proposed that carboxylate functional groups (-COOH), some of the most common found in crude oil, are more preferential adsorbed through hydrogen linkage than Ca^{2+} bridging on a negative clay surface. In other words, polar crude oil directly adsorbs on clay surfaces, as divalent cations screen its charge. A low salinity injection will then reduce the amount of Ca^{2+}, with water also dissociating into to H^+ and OH^-. H^+ will then replace the Ca^{2+}, whereas OH^- compete for the H from crude oil functional groups (–COOH) effectively breaking the hydrogen linkages that bound the oil to the clay. This means that if the brine contains a large number of OH^-,

or high pH, the polar crude oil components might release more easily from the clay surfaces. From looking at these two different mechanisms, two questions arise with regard to clay-oil interactions: 1) how does the polar crude oil adsorb onto a clay surface, is it cation bridging or direct bonding? 2) What is the main factor controlling the release of the polar oil, a decrease in brine concentration or increasing pH, or a combination of the two?

Sandstone mainly consists of quartz, feldspar, and clay minerals. The latter has been suggested to be fundamental to the low salinity effect [4] as they are overwhelmingly present on the sandstones pore surfaces, even coating optically clear quartz surfaces as nanoparticles [8, 9]. In addition, clay minerals display a permanent negative charge on their basal surfaces, which increases their reactivity and propensity to interact with oil molecules and ions in solution [5]. Kaolinite is one of the most important clay minerals present in sandstones, sometimes accounting for more than 50% of the clay minerals surface exposed at the pore surface [8]. Studies on the low salinity effect mechanisms generally assume clays present negatively charged surfaces [6, 7]; however kaolinite, is in fact a 1:1 clay mineral composed of two different faces (Figure 5.1), namely a silica tetrahedral basal plane (siloxane face) and an aluminum hydroxide (or brucite-type) octahedral sheet (aluminol face). Kaolinite has a theoretical chemical composition of $Al_2Si_2O_5(OH)_4$, however, it does have a small amount of isomorphous substitutions, mostly the substitution of Al^{3+} for Si^{4+} in the tetrahedral layer and of Mg^{2+} for Al^{3+} in the octahedral plane. Consequently, the siloxane face possesses a small, permanent negative charge [10-13], whereas the aluminol face has a pH-dependent surface charge [10, 11, 13]. For these reasons, a difference in the wetting behavior (and affinity to oil molecules) across the two different exposed surfaces is to be expected.

Atomic force microscopy is a widely-used technique in the study of mineral-solution interface phenomena [14]. For this reason, it has been increasingly used in the search of the main mechanism behind LSEOR, through the determination of surface charge [12, 13] or by measuring the adhesion of organic functional groups to mineral or model surfaces, in the so-called chemical force microscopy (CFM) mode. Surface area normalized adhesion force can be directly correlated to macroscopic contact angle measurements, therefore, in principle can be used to measure the wetting behavior of a mineral surface, as has been shown by Hassenkam et al. [15]. CFM studies on LSEOR have been varied and focused mostly on measurements on cored samples (both carbonate and sandstones) [15-23], but have also included studies on quartz [24], muscovite [24], feldspar [25] and model sapphire [26] surfaces. Although results of these studies vary, the general conclusion is that they point out to the prevalence of the double layer expansion mechanism as the most important driving LSEOR; and, most importantly, to the role of sorbed organic material into

controlling the adhesion of oil molecules in reservoir rocks. Nevertheless, no study solely using oriented clay minerals in CFM experiments has been reported.

In this study, CFM has been used to measure the adhesion between –COOH and –NH_2 functionalized AFM probes and the aluminol and siloxane surfaces of kaolinite. The effect of cation identity (Ca^{2+} vs Na^{+}), concentration (from 1 M to 0.001 M) as well as pH (5-9) on the measured adhesion was assessed. The main objective of the study is to understand the role, if any, of the chemistry of the two different exposed crystal basal surfaces in driving the LSEOR mechanism.

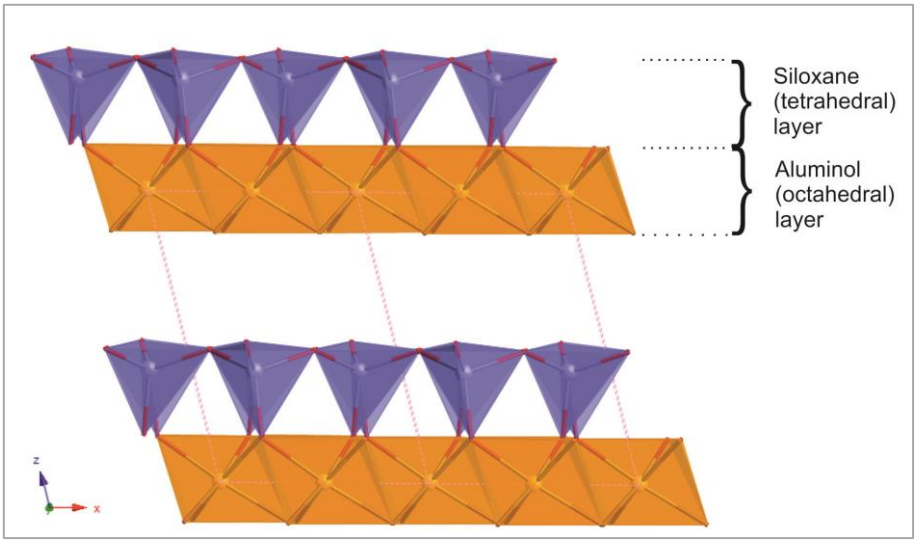

Figure 5.1 Detail of the kaolinite crystal structure perpendicular to the <010> direction. Two 1:1 layers are shown in the drawing, with siloxane and aluminol layer highlighted in the upper one. Cleary visible are the distinct nature of both upper and lower crystal termination.

5.2 Materials and Methods

5.2.1 Oriented kaolinite samples preparation

In order to study the adhesion over a particular kaolinite face, it was imperative to prepare films of oriented kaolinite crystals (KGa-1b from the Clay Minerals Society Source Clay Repository). To this end, a modified version of the method originally developed by Gupta and Miller [11] was used. This method is based on the fact that the negatively charged surface of the siloxane face is attracted to a positively charged surface (for example, sapphire) whereas the positively charged alumina face is attracted to a negatively charged surface (like muscovite mica). The effectiveness of this method on producing orientated samples has been verified by Alagha et al. [27]. For both preparations, a suspension of

kaolinite crystals was prepared by adding 10 mg powdered kaolinite to 10 ml Milli-Q water. The suspension was then homogenously dispersed using a QSonica sonicator probe (Q125) at 20% amplitude for a total of 14 min sonication time (with a 2s : 5s sonication/rest cycle). After sonication, the solution was left for 30 min to settle the larger, agglomerated crystals. Finally, a few droplets of the solution were taken from the upper part of the vial with a glass pipette and were deposited on the prepared substrate. The substrate was then introduced in an oven to dry at 70 °C for one hour, followed by rinsing with Milli-Q water (to remove any potentially loose crystals) and further drying (20 min) in the oven (70 °C). For samples oriented with the siloxane face up, freshly cleaved muscovite mica sheets of 11mm x11mm (Agar scientific) were used. For samples with the aluminol face oriented up, polished sapphire substrates (Valley Design Corp.) were used. The sapphire was cleaned by washing with ethanol and acetone, followed by 30 min in a UV/ozone cleaner [12]. Prior to performing the AFM experiment, the substrate was glued to a glass slide using an epoxy glue and then it was introduced in the fluid cell.

5.2.2 Chemical force microscopy

Chemical force microscopy measurements were performed using a Nanowizard 3 AFM (JPK Instruments AG). Scanning of the kaolinite samples was done using the Force Mapping mode, were the AFM probe is brought up and down (i.e. into contact and out of contact with the substrate/sample) in a regular, user-defined fashion, creating a so-called force-distance curve (FD) at every pixel of the image (Figure 5.2a). From these force distance curves a multitude of information concerning the adhesion and other mechanical properties of the sample can be extracted [28], therefore creating a “map” of these properties, which can be superimposed onto the topographical information, also registered during the scanning.

Experiments were started by scanning the sample in Milli-Q water using a proprietary, fast Force Mapping mode (Quantitative Imaging™), at low resolutions (32 x 32 pixels), and low applied force (≈ 0.3nN), in order to find an adequate crystal to perform the CFM experiment. The main characteristics that were looked after were that the crystal was flat and single (not an agglomerate), that was stable (i.e. did not move) during scanning, and that had a size close to or larger than 1um across. Scanning at this stage was performed using a PNP-TR probe (NanoWorld AG), which has a nominal spring constant of 0.67 N/m. Once an adequate crystal was found, it was scanned with a resolution of 64x64 pixels (Figure 5.2c and 5.2d), so any possible contamination on the surface of the crystal that could hinder the CFM measurements could be observed.

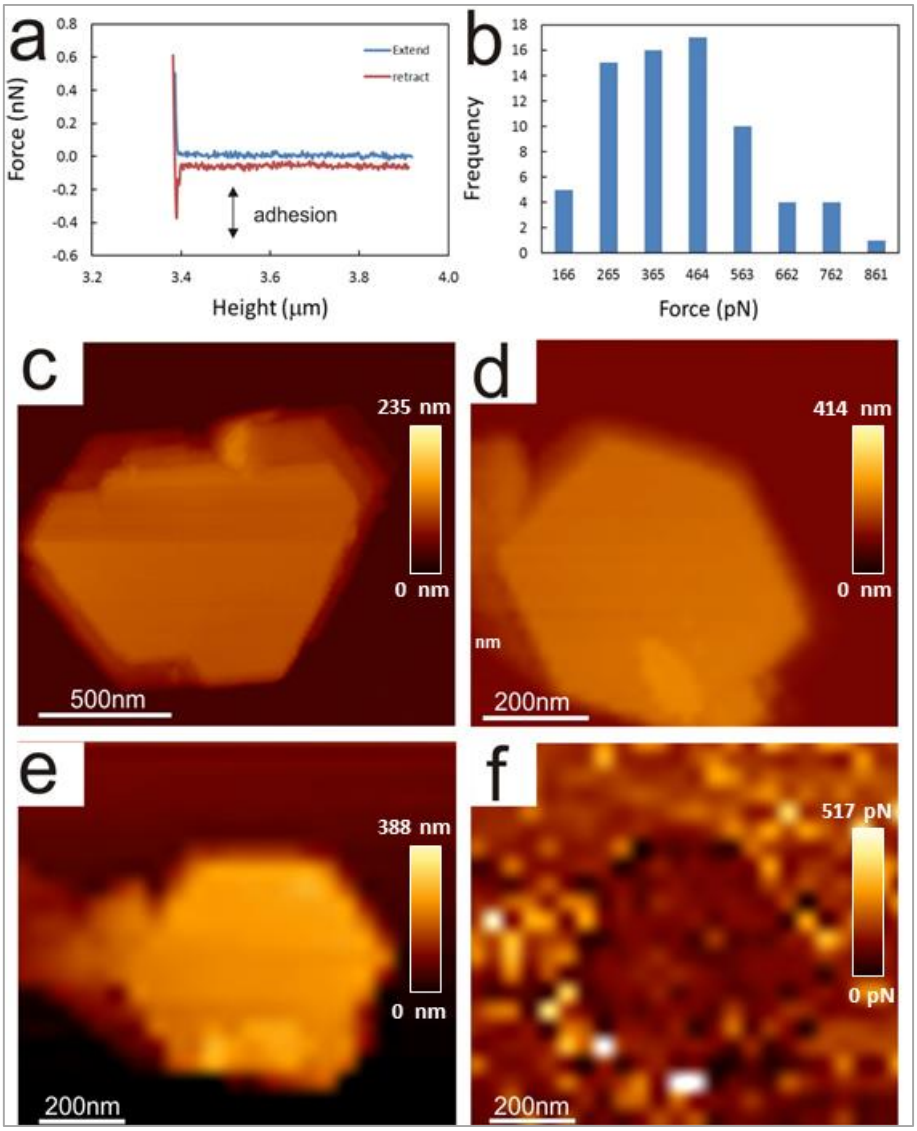

Figure 5.2 Representative force-distance curve measured over a kaolinite crystal (a). Extend and retract curve (blue and red, respectively) are shown. Adhesion region highlighted in plot. b) Representative histogram showing the spread of adhesion measurements over a kaolinite crystal. c) Height image (64x64 pixels) of a representative kaolinite crystal. d) Height image (64x64 pixels) of the kaolinite crystal measured in experiment kao-Si-4. e) Low resolution (25x25 pixels) height image of the crystal shown in (d). f) Adhesion map of the crystal shown in (e).

The CFM experiment was started by substituting the "standard" probe with a commercial, -COOH and $-NH_2$ functionalised tip (ST-PNP, from Smart Tip Probe solutions). All cantilevers have a triangular shape and a tip radius of < 40 nm. The tip was initially calibrated (in water) by first measuring the cantilever sensitivity (V/nm) by performing a

force distance curve (either against a glass or sapphire substrate). After this, the tip was brought out of contact and calibration of the vertical spring constant was done using the thermal method [29] and the correction factors from Butt and Jaschke [30]. The value obtained was used to convert the measured deflection signal (in V) into force units (N). For the probes used, calculated vertical spring constant varied between 0.055 and 0.04 N/m. After calibration, the CFM experiment was started by introducing the first corresponding solution of the particular experiment followed by scanning the previously identified crystal in the force mapping mode. A first round of experiments was performed to investigate the effect of dwell time (time spent by the tip in contact with the sample after the initial approach) using 0, 0.5 and 1 s, and to compare the use of QI *vs.* standard Force Mapping. Table 5.1 details the solutions used in these experiments.

Table 5.1 Solution composition, order, pH and surface studied for different dwell times.

Exp.	**Tip Used**	**water**	**NaCl 0.001 M**	**NaCl 0.01M**	**NaCl 1M**	**$CaCl_2$ 0.001 M**	**$CaCl_2$ 0.01M**	**$CaCl_2$ 1M**	**pH**
T_kao-Si-1	COOH	1				3	2		5.5
T_kao-Si-2	COOH	1	2	3					5.5
T_kao-Al-3	COOH	1					2		6/7/8
T_kao-Si-4	NH_2	1	7	6	5	4	3	2	5.5
T_kao-Al-5	NH_2	1	2	3					6/7/8

The main set of experiments was done to measure the effect different brines on the adhesion between tip and crystal (Table 5.2). For this second set, two force mapping mode scans were done per each solution composition (or pH), the first with a 0 second delay time and the second with a 1 second delay (whilst in contact with the crystal surface). This was done to ensure that proper contact and bonding between the functional groups and the kaolinite crystal occurred, which leads to a more reliable measure of the adhesion forces, as shown on the results from the dwell-time experiments, and as has been shown by other authors [26]. Each scan was performed with a minimum resolution of 25 x 25 pixels (or 625 total FD curves). This relatively low resolution was chosen to minimize potential loss of functionalization by the tip due to its repeated contact with the mineral's surface. However, it still provides a relatively large number of sample points per kaolinite crystals (>100 pixels). Representative topography and adhesion maps from a CFM experiment are shown in Figure 5.2e and 5.2f, respectively. The rest of parameters used during the force mapping scanning were: set point of 0.4 nN, z range (piezo height away from the sample): 700 nm, approach (and retraction) speed of the probe: 10 nm/s. Experimental solutions were manually exchanged from the fluid cell for a total of 4 times, to ensure full removal of

the previous solution. During the exchange, the tip was rinsed several times with Milli-Q water and the new solution, and was not allowed to dry.

Table 5.2 Solution composition, order, pH and surface studied for the different brines.

Exp.	Tip Used	water	NaCl 0.001 M	NaCl 0.01M	NaCl 1M	$CaCl_2$ 0.001 M	$CaCl_2$ 0.01M	$CaCl_2$ 1M	pH
kao-Si-1	COOH	1				2	3	4	5.5
kao-Si-2	COOH	1				4	3	2	5.5
kao-Si-3	COOH	1				5	4/6	3/7	8
kao-Si-4	COOH	1				2			5/6/7/8/9
kao-Si-5	COOH	1				2			5/6/7/8/9
kao-Si-6	COOH	1				2			5/6/7/8/9
kao-Si-7	COOH	1	4	3	2				5.5
kao-Si-8	COOH	1	2						5/6/7/8/9
kao-Si-9	COOH	1/5	2	3	4	6	7	8	5.5
kao-Si-10	COOH	1	1			2	3	4	5.5
kao-Si-11	NH_2	1				2	3	4	5.5 / 8
Kao-Si-12	NH_2	1				2	3	4	8
Kao-Si-13	NH_2	1				2			5/6/7/8/9
kao-Al-1	COOH	1				2	3	4	5.5
kao-Al-2	COOH	1				2			6/7/8
kao-Al-3	COOH	1	2						6/7/8
kao-Al-4	NH_2	1	7	6	5	4	3	2	5.5
kao-Al-5	NH_2	1				2			6/7/8
kao-Al-6	NH_2	1					2		6/7/8
kao-Al-7	NH_2	1	2						6/7/8

5.2.3 Data processing

All data from the CFM experiments was analyzed using the JPK Data Processing software. To calculate the adhesion, each force distance curve was analyzed in the following way: 1) the baseline subtraction tool was used to "bring" the retract curve to a 0 N position (i.e. to remove the effect of hydrodynamic drag, as expressed by a difference in the laser position at zero load between approach and retract curves, as can be seen in Figure 5.2a), and also to remove any tilt of the baseline (out of contact) portion of the curve, ensuring a 0 N load at the point where the probe snaps out of contact and across the full extension of the baseline, 2) the minimum value tool was then used to locate the minimum value of force recorded (which corresponds to the adhesion), measured against the 0 N baseline. This procedure was applied to all the recorded FD curves using the batch analysis function. After

completion the software creates an image (adhesion map) with the calculated data. Using the adhesion map, it was then possible to measure the adhesion on the surface of each kaolinite crystal. This was done by selecting all data inside the crystal (minus edges, which tend to show a higher adhesion). The data was then saved as an ASCII file and analysed for average and standard deviation. In addition, data was statistically treated to determine the upper and lower inner bounds, which were then used to identify data outliers which were then removed from the data set. Figure 5.2b shows a representative histogram of the adhesion data as measured in the kaolinite crystal shown in Figure 5.2e. The relatively high spread in the data may reflect, to some extent, the heterogeneous distribution of surface charge in kaolinite that was recently described by Kumar et al. [12]. Moreover, the nature of CFM techniques is such that small areas are measured (nm). The observed absolute adhesion represents a small area that is very sensitive to measurement and contamination. It is necessary to analyse and show the data as average values which is more consistent for the whole surface.

All data shown in the figures (with the exemption of the dwell-time effect experiments) correspond to that measured with a 1s dwell time. Data was not normalized per contact area because of difficulties in measuring the tip radius without damaging the probe. This is due to the fact that in order to measure its radius, the probe has to be scanned against a roughness standard sample, which could lead to the loss of functionalization (due to high friction forces). Therefore, relatively large variations in the absolute values of measured adhesion are reported across different experiments, even in similar systems (same functionalization, same trigger force, same solution composition). These differences are probably due to variations in the contact radius, derived from the fabrication of the AFM probes, which need to be gold coated before functionalization (Chapter 4). For these reasons, the data reported here has to be considered in terms of the qualitative differences or changes observed within each experiment, and no conclusions are derived from comparing data across different experiments. Furthermore, tip degradation could affect data quality. This issue was controlled by considering the adhesion results. During the experiment, the first scan was performed in the water as background. The observed data was compared to the first scan that has full functionalization. If the adhesion is significantly lower in three consecutive scans, the experiment was re-checked in the water. If the adhesion was lower than the background adhesion (in the water), the experiment was identified as degradation of the functionalised tip, which impacted to the resulting in low data quality. In this case, the experimental data was not used.

5.2.4 Aqueous solutions

Experiments reported here were performed with solutions of either $CaCl_2$ or NaCl composition. These two cations (Ca^{2+} and Na^{+}) were chosen as representative of monovalent and divalent cations and because they are the most common ions in formation and seawater. In addition, the reduction of Ca^{2+} concentration has been observed to play a critical role in the low salinity effect [31, 32], and it forms the basis of the MIE mechanism as the main driver in the process. For both cations, solutions were prepared using Milli-Q water and reagent-grade NaCl and $CaCl_2$ (Sigma-Aldrich). A 1 M solution of each reactant was prepared and was later diluted to prepare the 0.01 M and 0.001 M solutions. pH was measured using a Jenway model 3520 pH meter, equipped with a Schott Instruments pH probe (blue line), which had been previously calibrated with pH 4.01, 7 and 10.01 standard solutions (Fisher Scientific). pH of the solutions was mostly not adjusted, and measured to be around 5.5. When adjusted, it was done so by means of HCl and NaOH solutions for the NaCl experiments, and with HCl and $Ca(OH)_2$ for those experiments performed with $CaCl_2$ solutions.

5.3 Results and Discussion

5.3.1 Effect of AFM experimental parameters: Dwell time

Previous studies have shown that the time that the functionalized tip is in contact with the studied surface will have an effect on the adhesion recorded [24]. For this reason, it was decided to perform adhesion measurements with different dwell times. Initial experiments were performed at 0, 0.5 and 1s and involved -COOH and $-NH_2$ functionalised tips. Results from two such measurements (experiments T_kao-Si-1 and T_kao-Si-2), performed with a -COOH functionalized tip, over a kaolinite siloxane face, and using $CaCl_2$ and NaCl solutions on siloxane face are shown in Figure 5.3a and b respectively. It can be seen that the measured adhesion increases significantly with 0.5 and 1s of dwell or stoppage time over the surface. In addition, no significant variation in adhesion is observed between the measurements performed using the QI mode *vs.* Force Mapping at 0s dwell time.

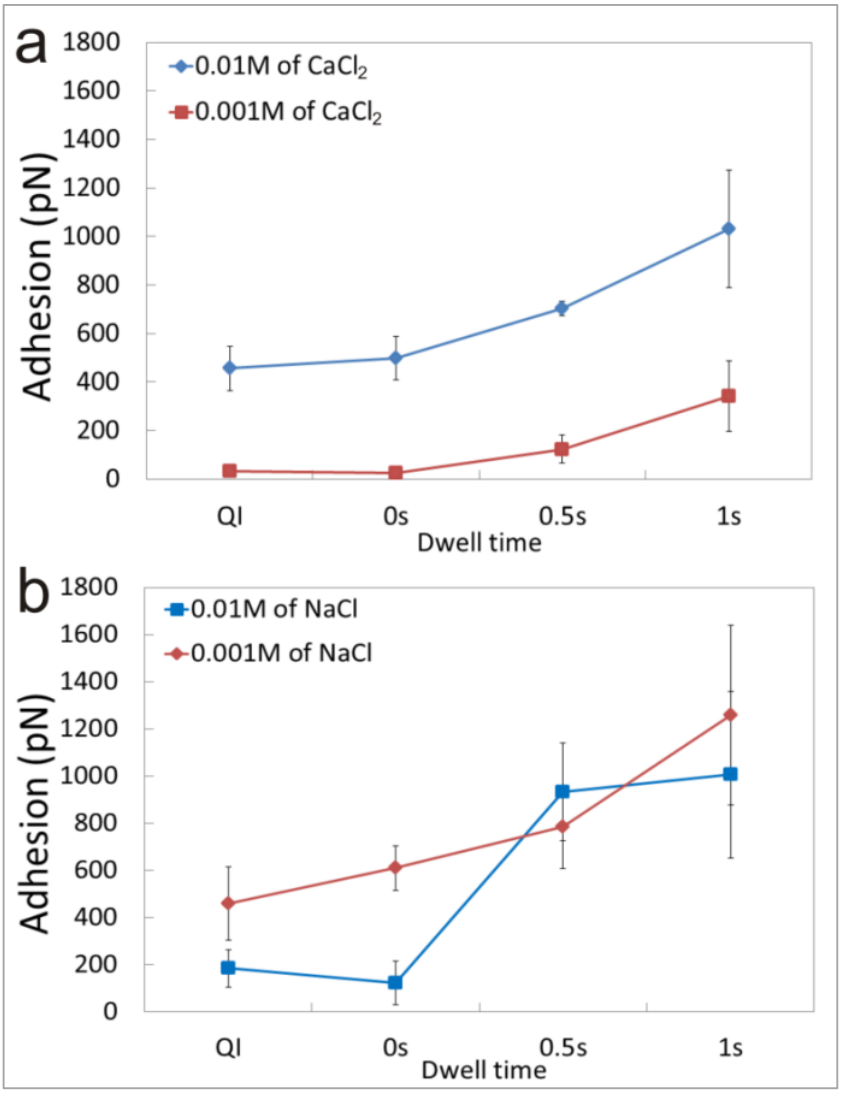

Figure 5.3 Graphs showing the measured adhesion using QI™ imaging (25 m/s) and Force Mapping at 0, 0.5 and 1s dwell times on the silixane face of kaolinite measured with a –COOH-functionalised probe in 0.01 and 0.001M of $CaCl_2$ (a) and in 0.01 and 0.001M of NaCl (b).

Similar experiments performed over the aluminol face using –COOH probes (T_kao-Al-3, Figure 5.4) and on a siloxane face using $-NH_2$ probes (T_kao-Si-4, Figure 5.5) show also a significant increase in adhesion when the dwell time was increased from 0 to 1s. Because the functionalized tip is composed of a number of a ligand molecules [33], with a "brush" type distribution, the very small contact time for the QI™ and 0s dwell time force mapping is not enough to allow the functionalized group to completely penetrate the hydration layer around the clay surface [24]. From these test experiments, it can be concluded that 1s dwell time is enough for a proper functional group-clay interaction to occur. In addition, as can be seen in Figures 5.4, 5.5a and 5.5b measurements with this dwell

time show more clearly the effects of changing the brine chemistry (in this case pH) and also produced more reproducible results across experiments when compared to 0s and QI™ measurements. For these reasons, it was decided to perform the measurements in the main set of experiments (Table 5.2) with a maximum dwell time of 1s.

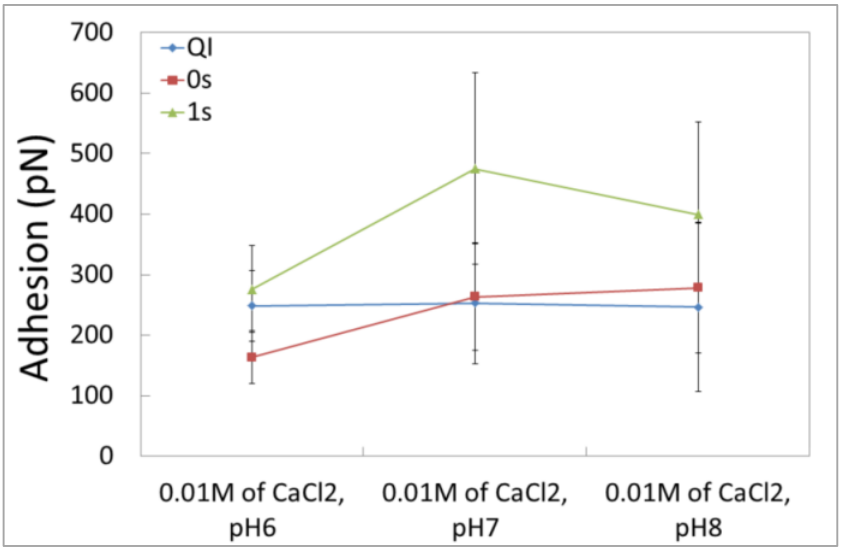

Figure 5.4 Graph showing the comparison of measured adhesion using QI™ imaging (25 m/s), Force Mapping 0 and 1s dwell times on an aluminol face of kaolinite measured with –COOH probe in 0.01M of $CaCl_2$ with pH 6, 7 and 8.

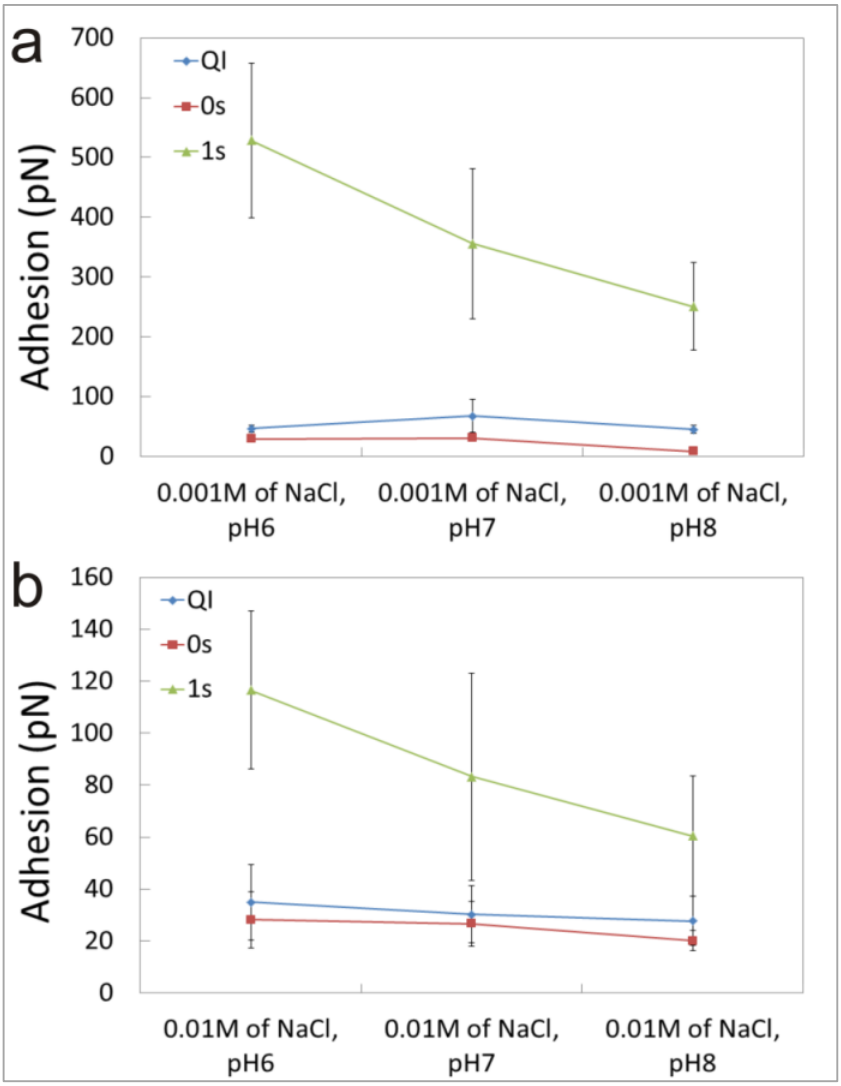

Figure 5.5 Graph showing the comparison of measured adhesion using QI™ imaging (25 m/s), force mapping 0 and 1s dwell times on aluminol face of kaolinite plane measured with $-NH_2$ probe in 0.001 of NaCl pH 6, 7 and 8 (a) and in 0.01 of NaCl pH 6, 7 and 8 (b).

5.3.2 Effect of concentration and pH on the measured adhesion on kaolinite siloxane face

The low salinity effect on the adhesion of different functional groups with the siloxane face of kaolinite was studied by performing experiments at different concentrations. The brines used were $CaCl_2$ and NaCl which represent the more prevalent divalent and monovalent cations in sea water. The tested concentrations were 0.001 M, 0.01 M, and 1 M. Experiments were performed by introducing the solutions in a sequence of high to low concentration, or vice versa. In this way, any possible effect of ion adsorption on the tip or tip weathering could be decoupled from the actual adhesion measurements. In this section results from

experiments performed with tips functionalized with –COOH and $–NH_2$ groups will be discussed.

5.3.2.1 Adhesion of –COOH groups to the siloxane face

The bulk of experiments shown in this study were performed over the siloxane face of kaolinite as this will probably be the most exposed face on the pore, at least in terms of the nanoparticles coating quartz grains, which are quite prevalent in real reservoir rocks [8, 22].

5.3.2.1.1 Effect of $CaCl_2$ concentration

The effect of the concentration of Ca^{2+} on the adhesion of –COOH groups on the siloxane face was studied at two different pH values: 5.5 (which is the typical value for sandstone reservoirs) and 8. This was done to try to disentangle a pure MIE mechanism from one combined with a variation in pH, as it has been reported that pH can play a large role in determining the oil adsorption capacity (or adhesion) [5, 7, 34]. Figure 5.6 shows the results from experiments kao-Si-1 and kao-Si-2. In Figure 5.6a it can be seen that the measured adhesion (at 1 s dwell time) increases significantly from ≈125 pN measured in water to ≈ 500 pN) when measured in a 0.001 M $CaCl_2$ solution. This is followed by a continuous decrease down to ≈ 220 pN when the solution composition was exchanged to 0.01 and 1 M. This result, therefore, indicates a decrease in adhesion with an increase in concentration, which is the opposite of the so-called low salinity effect. Two more experiments were performed using the same conditions and solution sequence (kao-Si-9 and kao-Si-10) and they both showed the same trend (Figure 5.7), indicating good reproducibility of the results. In addition, a separate experiment (kao-Si-2) was performed with the same solutions but the opposite sequence of introduction in the fluid cell, in order to see if this had any effect on the observed trend. Figure 5.6b shows results from this experiment. It can be seen that the adhesion increased as the Ca^{2+} concentration decreased from 1 M to 0.001 M, therefore confirming the result. At pH 8, however, the opposite picture emerged, as can be seen in Figure 5.8, which shows the results from experiment kao-Si-3, where the solution concentration was first decreased from 1 M to 0.001M and then increased back up to the original 1 M (Table 5.2). Results show a large adhesion measured at 1 M (≈ 520 pN) which then decreases in two steps down to ≈300 pN after addition of the 0.01 M and 0.001 M solutions. After this, the solutions with a concentration of 0.01M and 1 M were reintroduced in the fluid cell, which led to an increase in the measured adhesion reaching ≈500 and ≈610 pN respectively. This indicates that the trend in increased adhesion at higher concentration can be “recovered”, and therefore, that the measurements are not affected by other processes, or experimental factors, like tip

"weathering", which may affect the functionalisation and, consequently, the "sensitivity" of the probe.

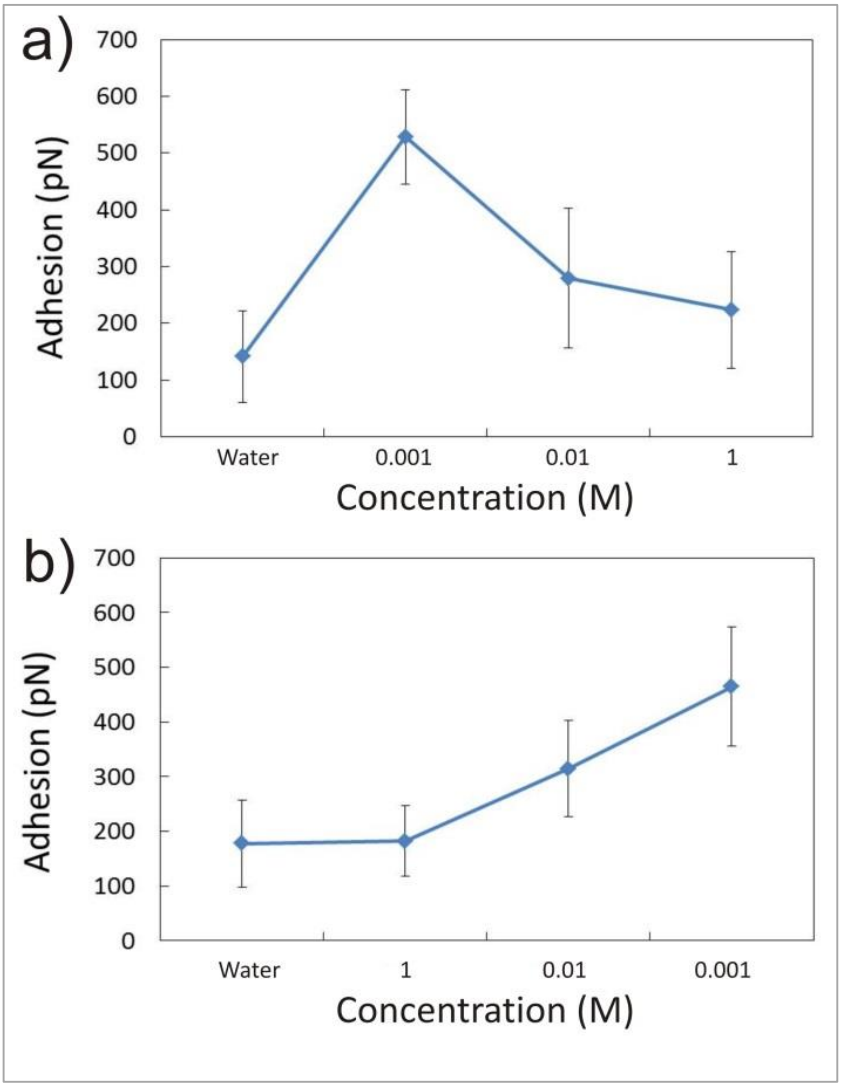

Figure 5.6 Graphs showing the measured adhesion for experiments kao-Si-1 (a) and kao-Si-2 (b) performed with a –COOH probe over the siloxane surface of kaolinite and in the presence of $CaCl_2$ solutions of different concentrations (0.001, 0.01 and 1 M) at pH ≈ 5.5. a) The solutions were introduced in the fluid cell following a sequence of low to high $CaCl_2$ concentration. b) The solutions were introduced in the fluid cell following a sequence of high to low $CaCl_2$ concentration. In both experiments an increase in the adhesion with lower $CaCl_2$ concentration is observed.

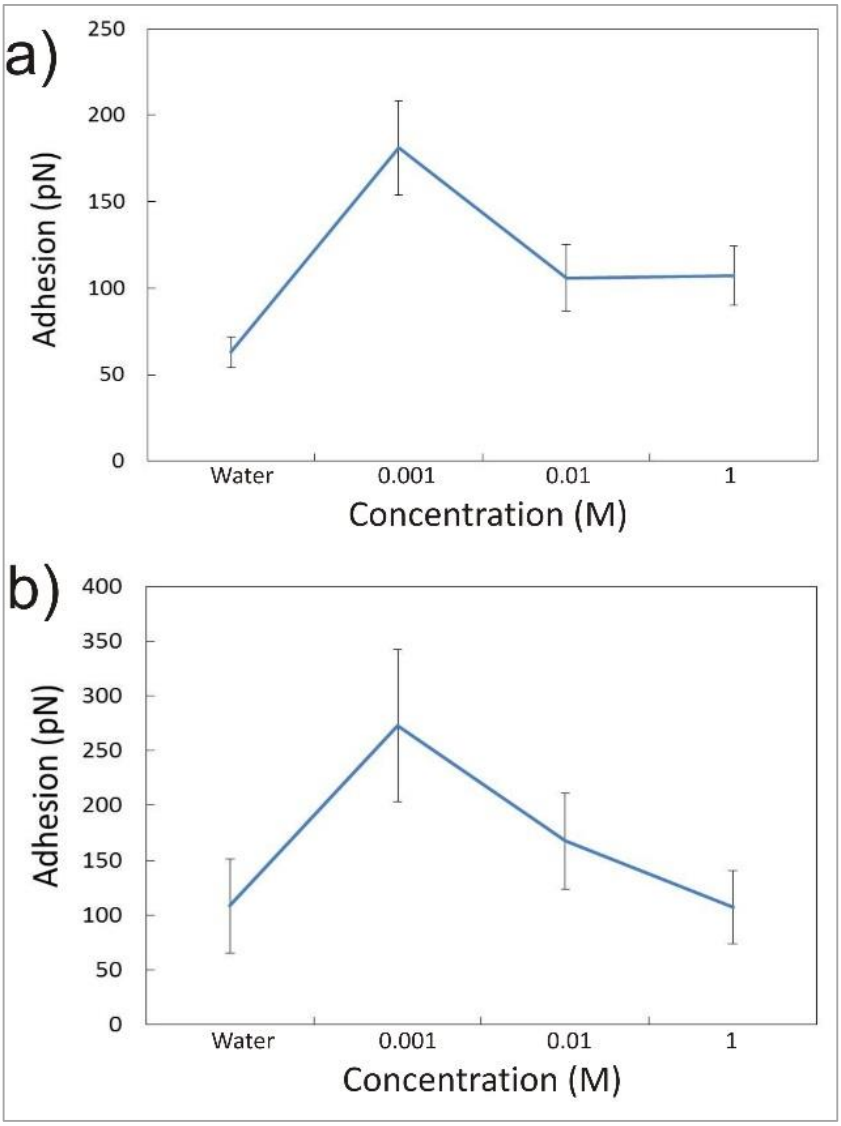

Figure 5.7 Adhesion graphs for experiments kao-Si-9 (a) and kao-Si-10 (b), performed with a –COOH probe over the siloxane face of kaolinite and in the presence of $CaCl_2$ of various concentrations (0.001, 0.01 and 1M). Both graphs show a decrease in adhesion as the $CaCl_2$ is increased.

The results reported at low pH seem to run against the basic understanding of the MIE mechanism, were –COOH groups will be bound to the mineral surface via a divalent cation bridge or through the formation of an organo-metallic complex [31]. In this model, a reduction in Ca^{2+} concentration would result in a smaller amount of bridging and therefore to less adhesion. Authors have, however, usually linked the MIE mechanism to a variation in pH as well [5, 34] as, in their experiments, this parameter was allowed to vary, or it's varied in a controlled manner. In the case of the experiments shown here, the pH was maintained constant throughout its duration, and only the concentration was changed. These conditions are also ideal to test the double layer expansion mechanism, which

generally predicts an increase in the width of the double layer extending away from the surface of the mineral, when the ionic strength of the solution is reduced [3, 4]. This expansion then is linked to an increase in the range of repulsion forces, and therefore to a decrease in the overall adhesion of the organic molecules to the mineral surfaces. For the experiments reported in Figure 5.6, and using the standard equation to measure the double layer width (or Debye length):

$$k^{-1} = \left(\frac{\varepsilon\varepsilon_0 kT}{Ie^2 N_A \times 10^3}\right)^{1/2} \qquad \text{(Equation 5.1)}$$

Where k^{-1} is the Debye length, Ɛ is the permittivity of vacuum, $Ɛ_0$ is the relative permittivity of the solution, k is the Boltzmann's constant, T is the temperature, I is the ionic strength of the solution, e is the charge of an electron and N_A is the Avogadro's number. Using this equation the Debye length was calculated for each $CaCl_2$ solution used in the low pH experiments, giving lengths of 5.53, 1.75 and 0.184 nm for concentrations of 0.001, 0.01 and 1 M, respectively. These calculations predict a large decrease in the double layer width as concentration was increased, but the related decrease in adhesion was not observed, instead the opposite was true. Therefore, neither the standard double layer expansion mechanism, nor a basic MIE mechanism can be invoked to explain our results, however, a closer look at the surface complexation and deprotonation reactions may offer a better explanation.

At the experimental conditions (constant pH), the protonation state of the –COOH will remain unchanged and, therefore, should be critical in determining the adhesion to the kaolinite surface. In addition, as has been established by numerous authors, the overall charge of the kaolinite siloxane surface is negative, although some authors have found it to vary, to some extent, as a function of pH [10, 11], and to also be affected by the ionic strength of the electrolyte on which its immersed, although always maintaining its negative value [13].

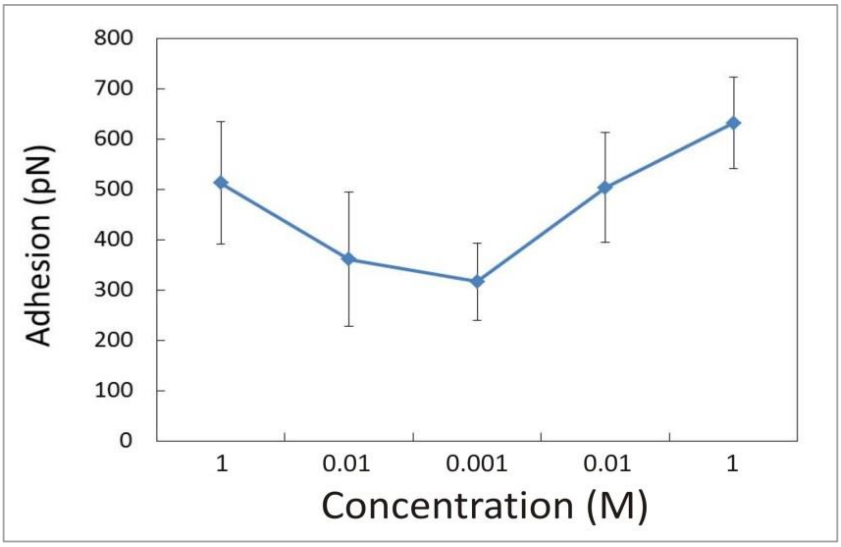

Figure 5.8 Graph showing the measured adhesion for experiment kao-Si-3, performed with a –COOH probe over the siloxane surface kaolinite and in the presence of $CaCl_2$ of various concentrations (0.001, 0.01 and 1 M) at pH = 8. Solutions were introduced in a sequence of high to low to high concentration. A drop in the measured adhesion is observed as the $CaCl_2$ decreases, followed by an increase as the concentration is increased again.

The protonation state of –COOH groups bound to AFM probes is known to be affected by the pH in a similar way to its unbound counterparts in solution, and has been reported to have a $pK_a = 5.5 \pm 0.5$, according to CFM measurements performed by Vezenov [35]. Therefore, on the experiments performed at a pH ≈ 5.5 it can be expected that the AFM probe will contain a similar number of –COOH and $–COO^-$ groups, and therefore has an overall negative charge. Strand et al. and Austad et al. explained the observed high affinity of organic matter to clay surfaces at near-to-neutral pH through the formation of hydrogen bonds between the carbonyl oxygen and protons adsorbed to the clay surface, in addition to bonds between the hydrogen in the -COOH molecule and the negative charge on the clay mineral [5, 7]. The presence of Ca^{2+}, however, complicates this picture as there will be competition with protons for surface sites, which may lead to the development of cation bridging (Figure 5.9a). Sorption reactions on the clay surface can be defined by the general equation:

$$\equiv SX \leftrightarrow \equiv S^- + X^+ \qquad \text{(Equation 5.2)}$$

Where $\equiv S^-$ represents a surface site in the siloxane surface, X^+ represents a cation (H^+, Ca^{2+}, Na^+) near the surface and $\equiv SX$ a cation bound to a surface site. Several authors have reported a much larger affinity for H^+ for clay surfaces [5, 36, 37], as demonstrated by pK values (for reaction 2) for H^+ and Ca^{2+}, of 5.3 and 1.5, respectively [37]. The concentration of species at the mineral surface $[X^+]$ would be given by the well-known Boltzman distribution:

$$[X^+] = [X^+]_\infty e^{\left(-Z_i e\Psi_0 / kT\right)} \qquad \text{(Equation 5.3)}$$

Where $[X^+]$ is the cation concentration near the surface, $[X^+]_\infty$ is the bulk cation concentration, Z_i is the cation valency and Ψ_0 is the surface potential. For the lower Ca^{2+} concentration (0.001 M) and pH ≈ 5.5 conditions we can assume a surface potential in the order of -70 – 40 mV [11, 13], leading to relative concentrations of $[H^+]$ over $[Ca^{2+}]$ of approximately 3 orders of magnitude apart. Considering this and the relative pK values for reaction 2 only a relatively small amount of surface sites will be expected to be complexed with Ca^{2+} as opposed to those bound to H^+. At these conditions, the protonated -COOH molecules will bind to the surface, and a small amount of $-COO^-$ may form bridging bonds through adsorbed Ca^{2+}, resulting in a large measured adhesion. At high Ca^{2+} concentrations (1 M), however, the number of surface-bound Ca^{2+} ions will increase significantly, resulting in smaller number of sites available for hydrogen bonding with -COOH molecules and only cation bridging will occur resulting in a smaller adhesion.

For the experiments performed at pH ≈ 8, the surface chemistry characteristics of the system will be different (Figure 5.9b). At this pH, the –COOH groups in the AFM probe will be completely deprotonated ($-COO^-$) and therefore any bonding with the clay surface will be expected to occur via cation bridging. In addition, the higher pH will be translated onto a much smaller concentration of H^+ bound to the siloxane surface compared to that of $[Ca^{2+}]$. Assuming just these two sorption reactions (equation 2), for the low Ca^{2+} concentrations (0.001M) we would expect a difference close to an order of magnitude in adsorbed species, in favour of Ca^{2+}. Increase in the Ca^{2+} will significantly reduce the number of H^+-bound sites, increasing the amount of bridging, and therefore the measured adhesion, as was observed in the experiment. Finally, some authors have suggested that high Ca^{2+} may induce a charge reversal on negatively charged surfaces [37]. For the experiments reported here, the simple surface speciation model described above seems to point in this direction and which would also explain the increase in adhesion with concentration at pH 8. However, we could not see definitive experimental evidence for this in our experiments, like the observation of long-range attraction forces on the force-distance curves.

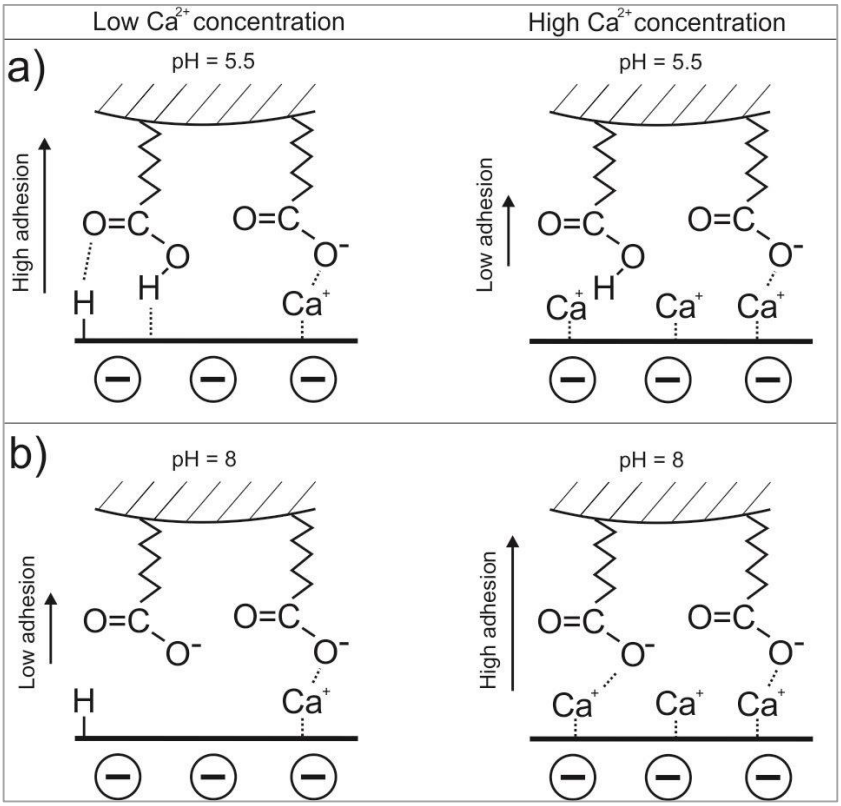

Figure 5.9 Idealized schematic cartoon showing the protonation state of the –COOH groups on the AFM probe as well as complexation on the kaolinite siloxane surface at high and low concentrations of $CaCl_2$ and two pH conditions, ≈ 5.5 (a) and 8 (b).

5.3.2.1.2 Effect of pH in the presence of 0.001 M $CaCl_2$

As noted above, pH has been invoked in several studies as an important factor in determining the effectiveness of LSEOR as well as in establishing the most important underlying mechanisms. Austad et al. have shown experimental data where an increase in the pH of the effluent solution is observed after injection of low salinity water [5]. In addition, Shi et al. [34] observed a small decrease in the measured adhesion for CFM experiments performed on sandstone grains using -CH_3 and -COOH functionalised AFM probes. For these reasons, it was decided to perform a series of experiments were the Ca^{2+} solution composition was kept constant (at 0.001M), but the pH was varied. The low Ca^{2+} concentration was chosen as we were more interested in the low-salinity effect. Three different experiments were carried out (kao-Si-4, kao-Si-5 and kao-Si-6) and the results are reported in Figure 5.10. As can be seen in the figure, for all three experiments an overall increase in the measured adhesion was observed when the pH was increased from 4 to 9. However, the actual magnitude of variation of the measured adhesion varied considerably across experiments. Experiments kao-Si-4 and kao-Si-6 (Figure 5.10a and 5.10b,

respectively), show a continuous, but smaller increase in adhesion, from pH 5 to 8, followed by a larger increase when the pH was increased to 9, as can be seen in the drastic change of the slope of the trend line connecting the data points. Experiment kao-Si-5, on the contrary, shows a different pattern, with a large increase in adhesion after pH 5, followed by a decrease at pH 8 and a larger increase after pH 9. This relatively lack of reproducibility in the measurements may have been due to different experimental factors such as tip shape, modification of the tip shape during the experiment or contamination when changing the solutions. It may also be due to variation of the surface charge across different crystals, something we cannot discount, based on recent reports of important variations of this property across individual crystals [12]. In any case, the observed general trend of smaller increase in adhesion at neutral pH followed by a faster increase at higher pHs is supported by the three experiments.

The observed increase in measured adhesion with increasing pH, however, is not in agreement with either CFM measurements performed on sandstone samples [34], nor with the studies on the adsorption of benzoic acid [38] and crude oil [39] by kaolinite. In the former experiments the presence of organic groups in the surface was invoked to explain the results, so a direct comparison to the results shown here is not appropriate. In the latter studies bulk kaolinite was used, as opposed to the specific adhesion measurements on the siloxane surfaces reported here, and the experiments were not performed in the presence of Ca ions, either. These could indicate the adhesion on the aluminol face (and on crystal edges) may have a larger role in shaping the shaping the increase in adhesion reported by those authors. This point is further discussed below in Section 3.2.2, where measurements on the aluminol face are discussed.

The observed increase in the measured adhesion can be explained by looking again at the protonation state of the –COOH molecules and the surface complexation of the kaolinite surface, as they both vary with pH. At the lower pH studied (5) the probe will be mostly composed of protonated –COOH groups and a large majority of surface-complexed sites will be bound to H^+ (but still maintaining an overall negative charge), which would result in bonding through the aforementioned hydrogen bonding mechanism. As the pH is increased, the –COOH groups will become deprotonated, decreasing the amount of hydrogen bonding. However, at the same time the relative amount of Ca^{2+} bound to the surface will increase steadily, as the H^+ concentration in solution (and near the surface) decreases, whereas that of Ca^{2+} in solution stays the same (and varies little near the surface), therefore increasing the number of bonds that will occur through cation bridging and resulting in an overall increase of the measured adhesion. The role of bridging Ca^{2+} in modifying the measured adhesion was explored in a separate experiment which measured

the adhesion of -COOH functionalised probes in the absence of any cations (MQ water) at pH ≈ 7 and pH ≈ 4 (HCl). In this case, a large increase (≈110%) in the measured adhesion was observed at the lower pH value, i.e the opposite of what was measured in the presence of Ca^{2+} (Figure 5.10). This result therefore, indicates that sorption of Ca^{2+} on the kaolinite surface (and therefore cation bridging) is critical in determining the –COOH adhesion behaviour.

Finally, the observed larger increase in adhesion from pH 8 to 9, may not respond completely to the increase in Ca^{2+} complexed to the surface but to a combination with another mechanism. This is because at pH 7-8 the vast majority of –COOH groups will be deprotonated and this number would not be expected to change with an increasing pH, therefore an increase in adhesion solely through an increase in cation bridging seems unlikely. An additional mechanism that could contribute to the large increase in adhesion may be related to a decrease in the electric double layer repulsive forces. Recently, Gupta et al. [11] measured the change in surface charge and potential of siloxane and alumina surfaces and reported a decrease on both quantities when solution pH increased from 8 to 9. Although their experiments were conducted with a KCl electrolyte its feasible to assume a similar reduction on our experiments with Ca^{2+}, and even expect a larger decrease in surface potential due to the larger affinity of Ca^{2+} for the siloxane surface. A reduction in surface potential will have the effect of decreasing the amount of Ca^{2+} near the crystal surface (when compared to a pH 8 solution), affecting the amount of complexed-Ca; but the decrease in proton concentration at pH 9 will partially offset this (when considering the surface complexation model). On the other hand, the reduction of surface potential will lead to a reduction on the repulsion forces between depronotated, anionic, $-COO^-$ groups and the negatively charged kaolinite surface with the net effect of substantially increasing the measured adhesion in the CFM experiments.

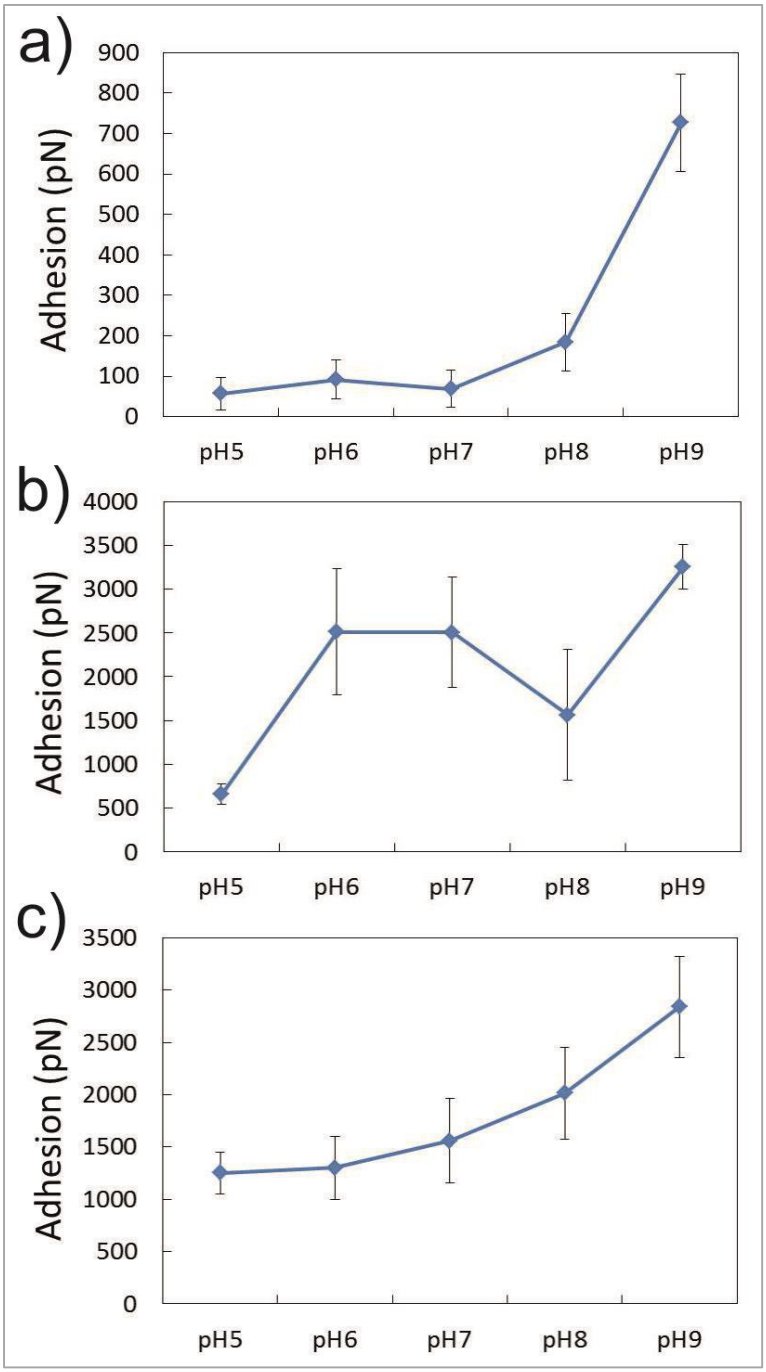

Figure 5.10 Graphs showing the measured adhesion from experiments kao-Si-4 (a), kao-Si-5 (b) and kao-Si-6 (c), where the overall effect of pH on the adhesion of a –COOH functionalised probe was measured in the presence of a 0.001 M $CaCl_2$ solution. An overall increase in adhesion as pH is increased can be observed.

5.3.2.1.3 Effect of NaCl concentration and pH

A series of experiments were carried out with NaCl solutions to understand the effect of this monovalent ion in determining the adhesion of –COOH groups to the siloxane surface of kaolinite crystals (Table 5.2). In two experiments, kao-Si-7 and kao-Si-9 the pH was kept constant at around 5.5 and the concentration was varied from 0.001 to 1M. A third experiment, kao-Si-8 was performed to study the effect of changing the pH on the measured adhesion. Figure 5.11a shows the results from experiment kao-Si-7 where solutions where introduced in the fluid cell with decreasing NaCl concentration. In the figure it can be seen that the measured adhesion decreased when the Na^+ concentration changed from 1 to 0.01 M, only to increase again (although to a lower total adhesion value than that measured at 1 M) when the solution composition decreased further to 0.001 M. Although the changes in the average measured adhesion are relatively significant (50 and 40%, respectively) the relatively large standard deviations diminishes their statistical importance. A similar result was observed in experiment kao-Si-9 (Figure 5.12) where the order of introduction of solutions to the fluid cell was reversed, and even less variation in adhesion across the different solutions was measured. From these observations it can be said that a variation in the Na^+ did not lead to a clearly defined trend in the variation of the measured adhesion. This result indicates that double layer interactions does not appears to be the determining factor in controlling the adhesion response when Na^+ is present in the solution. This is because the large change in concentration, which would considerably affect the size of the double layer (calculated to decrease from 9.5 nm at 1M to 0.3 nm at 0.001 M), does not produce the expected trend of increasing adhesion of -COOH groups to kaolinite at large concentrations. On the other hand, if we attend at the predicted surface complexation (and considering a pK_a of 0.5 for Na^+ binding to surface site, as per reaction 2), we will expect a large predominance of H^+ bound to the surface compared to Na^+ ions, even at the highest Na^+ concentration of 1M, favouring hydrogen bonding with the –COOH groups. At the same time, however, an overall decrease in the total amount of H-bound sites will occur with increasing concentration which may lead to a decrease in hydrogen bonding and adhesion, but this may probably be compensated by the decrease in the double layer size (due to the increase in concentration), resulting in the lack of a characteristic trend in the measure adhesion. This explanation also reinforce the role of monovalent *vs* divalent cations (MIE theory) in determining adhesion as a clear difference in behaviour is observed when comparing experiments performed in the presence of Ca^{2+} with those with Na^+.

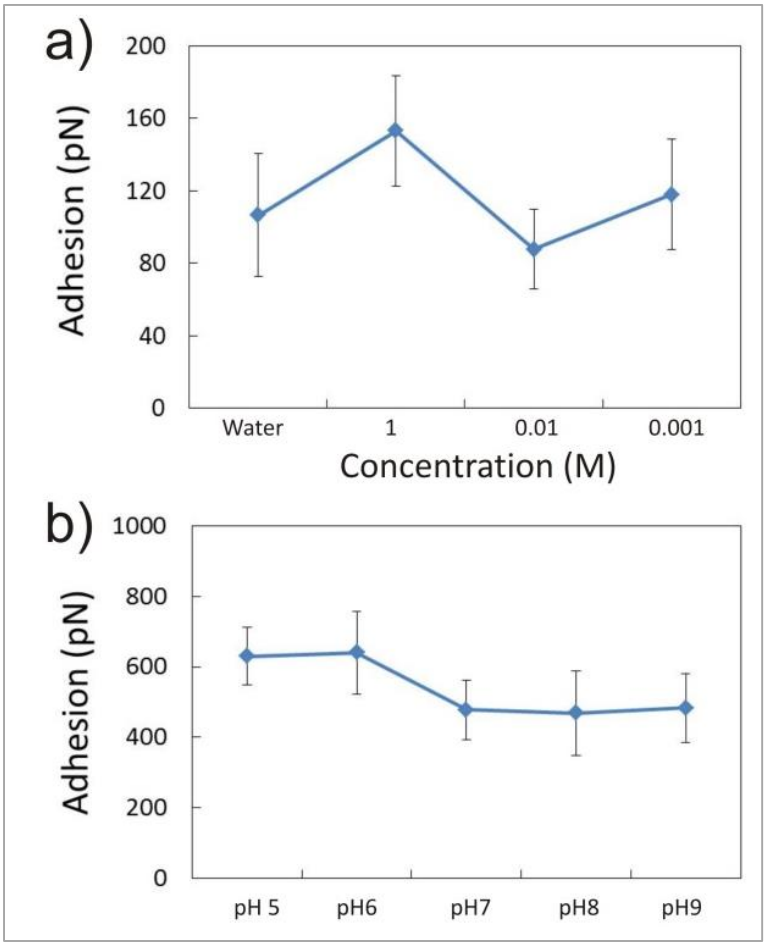

Figure 5.11 a) Graph showing the role of NaCl concentration in modifying the measured adhesion of a -COOH functionalised prove over the kaolinite siloxane surface (kao-Si-7). b) Graph showing the effect of pH on the measured adhesion of –COOH groups to a kaolinite siloxane surface in the presence of 0.001 M NaCl solution (kao-Si-8).

The effect of pH on the adhesion of –COOH groups to kaolinite in the presence of Na^+ with a concentration of 0.001 M was studied on experiment kao-Si-8, whose results are shown in Figure 5.11b. In the figure it can be seen that the adhesion at pH of 5 and 6 is very similar (≈630 pN), but then it decreases by about 25 %, to ≈ 480 pN, after pH 7, and stays around this valued for pH 8 and 9. This results agree, to some extent, with previous observations that acidic organic molecules bind better to kaolinite surfaces in the presence of NaCl than just deionised water [38]. They also indicate that Na^+ plays a smaller role in determining the organic matter adhesion than Ca^{2+}, as can be seen from comparing Figures 5.11b and 5.10. The trend observed can be explained by looking into the protonation of –COOH groups, at pH 5-6, a large number of groups in the tip will be protonated, and therefore able to bond to the kaolinite surface by the aforementioned hydrogen bonding mechanism, on

the contrary, at pH ≥ 7 most carboxylate groups will be deprotonated and will not form strong bonds in the absence of bridging cations such as Ca^{2+}. Neither the variation in the relative amount of H^+ to Na^+ –surface bound ions nor the previously reported decrease in surface potential [11] above pH 8 show any effect in modifying the adhesion. The contrast between this result and that observed from the Ca^2 experiments once again reinforces the critical role of Ca^{2+} in controlling -COOH adhesion.

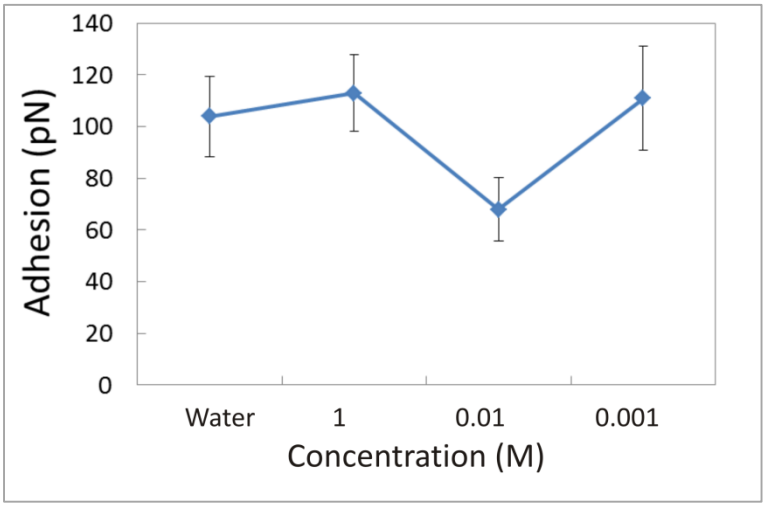

Figure 5.12 Adhesion graph for experiments kao-Si-9 (a) performed with a –COOH probe over the siloxane face of kaolinite and in the presence of NaCl of various concentrations (0.001, 0.01 and 1M). No clear trend on the measured adhesion is observed when varying the NaCl concentration.

5.3.2.2 Adhesion of –NH_2 groups to the siloxane face

A number of experiments were performed using NH_2 functionalised tips focusing on the effects of $CaCl_2$ concentration and pH.

5.3.2.2.1 Effect of $CaCl_2$

Figure 5.13 shows the results from experiment kao-Si-11, where the effect of varying the $CaCl_2$ concentration on the measured adhesion was measured at pH 8 and pH 5.5. Measurements from three different crystals are presented in Figure 5.13. At pH 5.6 two of the crystals display an increase in the measured adhesion with increasing $CaCl_2$ concentration (Figure 5.13a and 5.13b), whereas the third crystal (Figure 5.13c) shows almost no variation in adhesion across the three concentrations. With regard to the measurements at pH 8, all crystals showed an increase in adhesion when the solution was changed from 0.001M to 0.01M $CaCl_2$ (although for the first crystal as shown in Figure 5.13a is almost statistically insignificant). This was followed by a decrease in adhesion after introduction of the 1M solution, which in the case of two crystals (Figure 5.13a and 5.13b)

is quite significant, resulting in the lower adhesion value measured for the three solutions. Once again, direct comparison of absolute values even between crystals measured on the same experiments is complicated, this highlights the role of crystal heterogeneity (in terms of surface charge distribution or even the presence of contaminants) as was mentioned above. For this reason, a new experiment was performed where the adhesion was measured as a function of $CaCl_2$ concentration at pH 8 (kao-Si-12). Results from this experiment are shown in Figure 5.14 and indicates a clear trend of decreasing adhesion with increasing concentration. Therefore, two trends appear to be relatively clear from the two experiments: 1) a low salinity effect is mostly observed at pH 5.6 (low adhesion at low $CaCl_2$ concentration followed by a high adhesion at high salinity concentration) and 2) an inverse low salinity effect is observed at pH 8 (lower recorded adhesion at high $CaCl_2$ concentration).

The observation of the low salinity effect at pH 5.6 seems to contradict previous results of adsorption of amine-containing organic molecules on kaolinite, such as the results highlighted by Strand et al. which showed a decrease in quinoline sorption with increased $CaCl_2$ at a given pH [5]. Nevertheless, it is important to point out that the experiments looked at bulk kaolinite, i.e. included the effects of sorption on the aluminol face and edge sites. Our results however, do match those published by Desmond et al. [40] where they show the results of CFM measurements performed with $-NH_2$ functionalised tips on amorphous silica. Their results showed a low salinity effect when $CaCl_2$ was present during the adhesion measurements. They explained this by looking at the possible surface species formed over the silica surface and their relative proportion as a function of the $CaCl_2$ concentration. They identified the formation of a $\equiv O\text{-}Ca^{2+}\text{-}Cl^{-}_2$ ion pair in the surface as the likely adhesion-determining group. In our case, it is easy to expect the formation of a similar group as the negatively charged kaolinite surface will attract Ca^{2+} as has been described before. At low Ca^{2+} concentration, most of the kaolinite surface sites will be protonated (with a small amount of Ca^{2+}) whereas the tip will show a mixture of protonated $-NH_3^+$ and $-NH_2$ groups. Formation of hydrogen bonds and small electrostatic interactions with negatively charged surface sites will be expected at these conditions. At higher Ca^{2+} the relative amount of Ca^{2+} complexed to the surface will increase significantly, leading to the formation of a large number of $\equiv O\text{-}Ca^{2+}\text{-}Cl^{-}_2$ complexes which would increase the number of electrostatic interactions with the $-NH_3^+$ groups at the tip, leading to the observed increase in adhesion. At pH 8, the probe will mostly consist of $-NH_2$ groups, leading to a reduction of electrostatic interactions. At low Ca^{2+} concentration the lower concentration of charge balancing cations (protons and Ca^{2+}) will facilitate the formation of hydrogen bonding between the $-NH_2$ groups and $\equiv Si\text{-}O\text{-}Si\equiv$ surface sites [41]. At higher $CaCl_2$,

however, the surface will contain a larger amount of charge balancing Ca^{2+} ions, leading to a reduction of the hydrogen bonding and therefore a decrease in the measured adhesion.

An additional experiment (kao-Si-13) was performed to study the effect of pH on the measured adhesion of $-NH_2$ functionalised probes. The experiment was performed in a solution with a concentration of $CaCl_2$ of 0.001M as we were interested on the phenomena occurring at low salinity conditions. Results from this experiment are shown in Figure 5.15. It can be seen that the measured adhesion decreases as the pH increases from 5 to 9. This decrease in adhesion can be explained by looking at the protonation state of the $-NH_2$ functional groups as well as the surface complexation. At pH 5, a significant amount of functional groups will be in the protonated form $-NH_3^+$, in addition the surface will be protonated and also contain a relatively small number of Ca^{2+}. A number of negatively charged sites $\equiv Si\text{-}O^-$ are also expected to be present at the surface. At this stage adhesion into the surface will occur though electrostatic interactions between negatively charged sites and protonated NH_3^+ molecules on the tip, but also through hydrogen bonding on $\equiv Si\text{-}O\text{-}Si\equiv$ surface sites [41]. As the pH is increased the number of protonated $-NH_3^+$ molecules on the probe will be severely reduced, decreasing in turn the electrostatic interactions with negatively-charged sites significantly, which would lead to a decrease in adhesion.

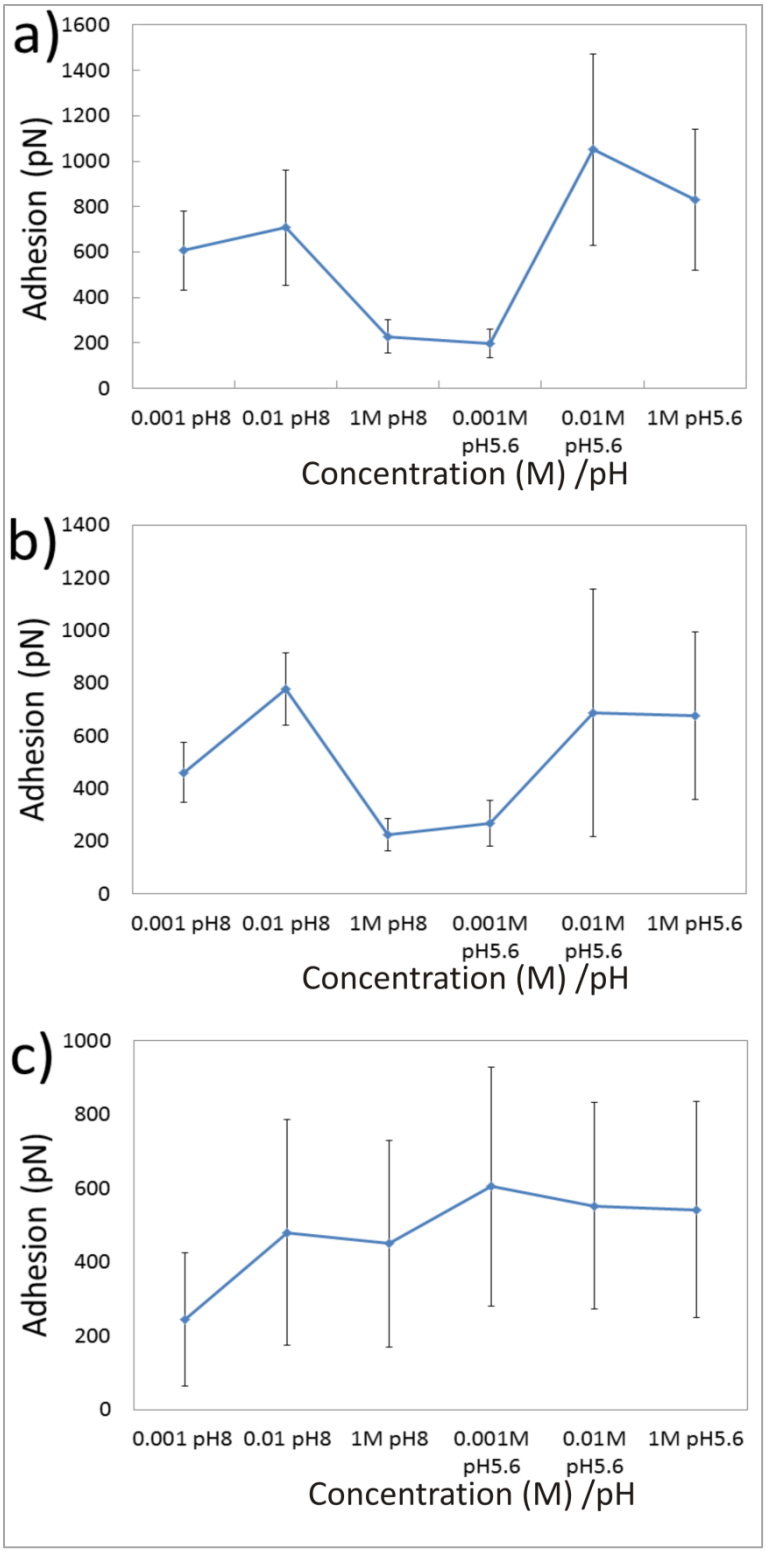

Figure 5.13 Graphs showing the effect of increasing the $CaCl_2$ concentration on the adhesion between -NH_2 groups and the kaolinite siloxane surface at pH 5.6 and 8 (kao-Si-11). Each graph represent measurements in a different kaolinite crystal.

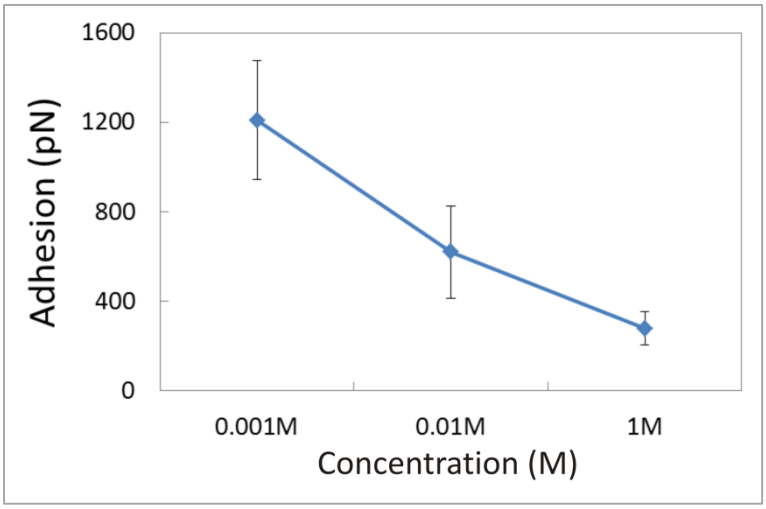

Figure 5.14 Graph showing the effect of decreasing the $CaCl_2$ concentration on the adhesion between -NH_2 groups and the kaolinite siloxane surface at pH 8 (kao-Si-12).

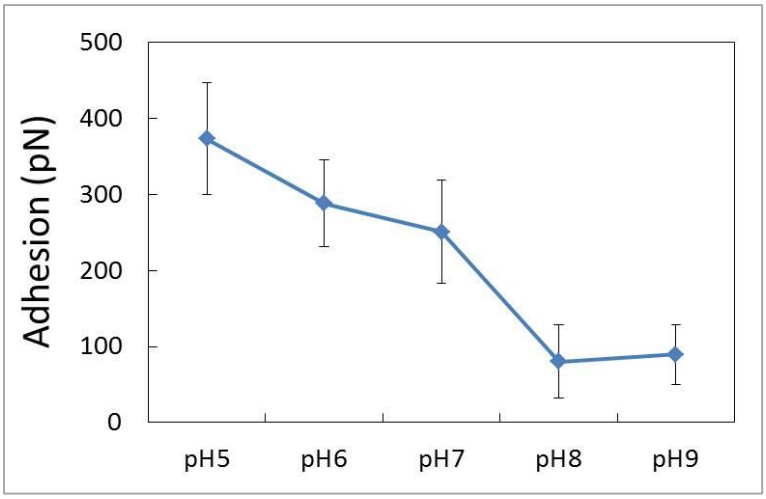

Figure 5.15 Graph showing the effect of decreasing the pH of a 0.001M $CaCl_2$ solution on the adhesion between -NH_2 groups and the kaolinite siloxane surface (kao-Si-13).

5.3.3 Low salinity effect on kaolinite aluminol hexagonal face

A series of experiments were performed on the aluminol face of kaolinite to determine any differences in the adhesion response to solution composition and pH to those observed in the silanol face (Table 5.2).

5.3.3.1 Adhesion of –COOH groups to the aluminol face

5.3.3.1.1 Influence of $CaCl_2$ concentration

An experiment was performed to assess the influence of the $CaCl_2$ concentration in the adhesion at a pH ≈ 5.5 (kao-Al-1) as this cation type produced the most interesting results in the CFM experiments performed over the aluminol face. Two different crystals were scanned at the same time (within the same image) and the results from the measurements are reported in Figure 5.16. It can be seen that the measured adhesion shows the same behaviour on both crystals, with a significant reduction in the recorded values as the Ca^{2+} concentration was increased. This behaviour is the same as that observed for the experiments performed on the siloxane face at the same pH (Figure 5.6 and Figure 5.7) and can be explained by looking into the protonation state of the –COOH groups and the surface charge of the kaolinite surface. At a pH ≈ 5.5 the overall surface charge of the alumina surface will be positive [11], whereas the tip, having a pK_a ≈ 5.5 [35], will be composed of approximately the same amount of protonated –COOH groups and deprotonated $–COO^-$ groups (i.e. it will have an overall negative charge). At low $CaCl_2$, only a relatively amount of Cl^- counter ions will be present at the surface and, therefore, electrostatic attraction between tip and surface will occur. We can also expect to see an increase in proton exchange with Ca^{2+} ions in solution that could potentially restrict the number of hydrogen bonds between surface AlOH groups and the -COOH groups at the surface. At higher concentrations of Ca^{2+}, further exchange reactions will occur; diminishing the number of hydrogen bonds that can potentially form, in addition, a decrease in the surface charge will be expected owing to the further presence of Cl^- counterbalancing anions. In fact, a decrease in surface charge density at the aluminol face was observed by Liu et al. [13], when a KCl concentration was increased over 70 mM (they observed an increase from 1-70 mM).

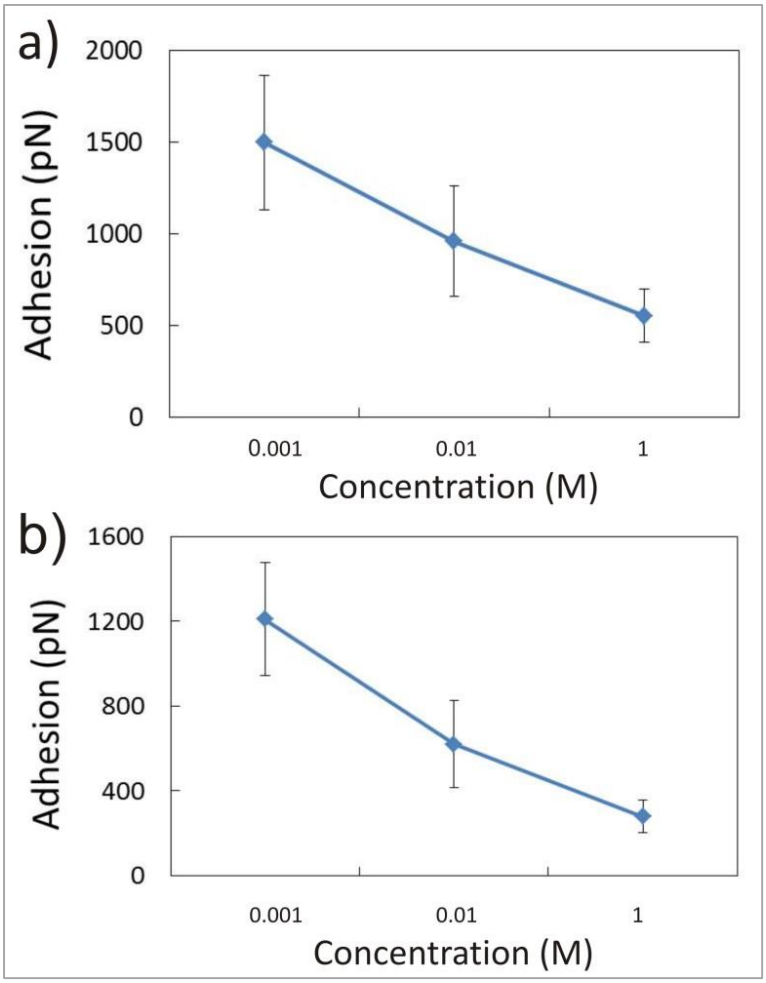

Figure 5.16 Effect of $CaCl_2$ concentration on the measured adhesion of –COOH groups over the aluminol face of two different kaolinite crystals, (a) and (b) (kao-Al-1).

5.3.3.1.2. Influence of pH

Given the results observed in the experiments performed with varying pH on the siloxane surface, further tests were performed on the aluminol face of kaolinite crystals to measure the adhesion of –COOH functionalised probes in the presence of $CaCl_2$ and NaCl at a pH varying from 6 to 8 (Table 5.2). This pH range was chosen as it has been shown that the aluminol surface changes surface potential from positive to negative between these values [11], with a point of zero charge around pH 7. Results from these experiments are shown in Figure 5.15. For the experiment performed with a $CaCl_2$ concentration of 0.001 M (kao-Al-2) it can be seen that the measured adhesion decreases substantially when increasing the pH from 6 to 8 (Figure 5.17). At a pH of 6 the aluminol surface is still positively charged (due to H^+ sorption on aluminol sites) whereas probably a majority of carboxylate groups are deprotonated, in the form of $–COO^-$, with the rest in the protonated form (-COOH). At these conditions, it can be expected that a strong electrostatic attractive force will occur

between tip and sample, a fact that is corroborated by the appearance of a small adhesion peak on the approach section of the force-distance curves measured over the kaolinite crystals. In addition, the formation of hydrogen bonding between the deprotonated –COOH groups and the surface hydroxyl groups on the aluminol surface, will likely occur as well. Both processes would lead to a large measured adhesion. After pH 7, however, the aluminol surface becomes negative due to the deprotonation of the aluminol surface groups [11], whereas the –COOH groups at the tip will be almost fully deprotonated, leading to a negatively charged tip. This situation should, in principle, lead to the formation of bridging through surface bound Ca^{2+} ions, as has been reported elsewhere for gibbsite crystals in contact with 0.01 M $CaCl_2$ solutions and hexanoate [42], but if these interactions exist they do not lead to an overall increase in adhesion. This may be due to the low concentration of Ca^{2+} in the solution and the relative proximity to the point of zero charge of the aluminol face. Finally, the observed decrease in adhesion with pH is more in line with the previously reported results on organic molecules sorption to kaolinite [38, 39] and may explain the discrepancies observed with the results observed on the siloxane face (Figure 5.10) (i.e. if more sorption occurs through this face), although the presence of Ca^{2+} may be a determining factor as well.

Results from the experiments performed with 0.001 M NaCl (kao-Al-2) show a similar decrease in adhesion with increasing pH (Figure 5.17b), which seems to indicate that, at these experimental conditions, there is not a large effect of the cation type on the underlying mechanism controlling adhesion at this face. This is in contrast with results from hexanoate sorption experiments performed by Wang et al. [42], which showed a notable increase in adhesion of the organic molecule on gibbsite crystals when the aqueous solutions contained Ca^{2+} ions compared to when contained Na^{+} only. In our case, we do see a much larger measured adhesion (almost 3 times) on the Ca^{2+} experiments (Figure 5.17a) when compared to the experiments performed with Na^{+}, but as mentioned before, as the experiments were performed with different tips we cannot establish this relationship

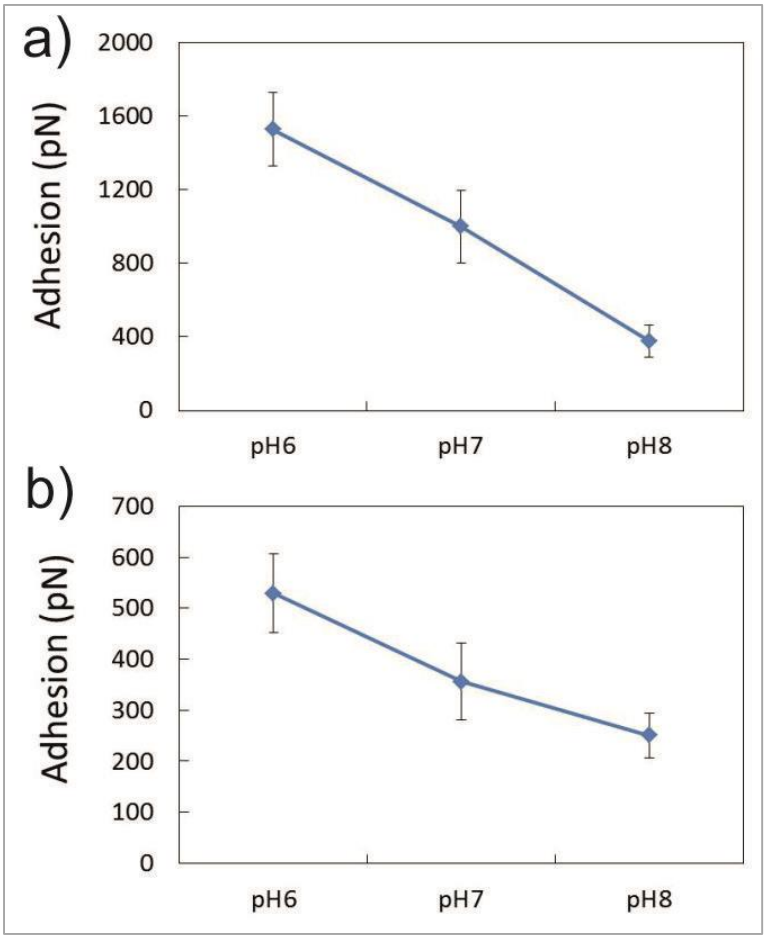

Figure 5.17 Graphs showing the results for experiments kao-Al-2 and kao-Al-3, where the effect of pH on the measured adhesion of a –COOH functionalised probe on the aluminol face of kaolinite was measured in the presence of a $CaCl_2$ concentration of 0.001M (a), and a NaCl concentration of 0.001M (b).

5.3.4 DLE vs. MIE mechanism

Results shown in this study suggest a complex picture on the role of cation type, composition and pH on the adhesion of acidic functional groups to kaolinite surfaces. This is in contrast to some previous studies which have attempted to explain results via a single theory such as double layer expansion or multicomponent ion exchange mechanisms. Recent studies on the sorption of $-CH_3$ and –COOH groups on sandstone surfaces acknowledge the deficiencies of accounting for changes in adhesion by solely relying on the double layer expansion model, and, in particular on the use of DLVO theory, which allows for the calculation of electric double layer force, to address the complex adhesion behaviour shown by sandstone surfaces [34]. One of the main problems highlighted is the assumption that the surface charge density does not depend on the ionic strength, or salinity, of the solution. In fact, as has been mentioned previously in this paper, kaolinite charge density

(across both faces) has been shown to be influenced by the concentration of the electrolyte to which is in contact [13]. A more robust way of dealing with these problems is the use of charge regulation theory where surface charge (and surface potential) are a function of sorption and desorption reactions at the interface [12, 43]. However, this approach has only been applied to relatively simple single mineral systems and their use on more complex "natural" surfaces where organic material may be involved remains to be seen. This said, it is clear from our results that distinct differences in behaviour are observed when comparing the experiments performed in the presence of Ca^{2+} with those performed with Na^{+}, and these can be attributed in some cases to the presence of cation bridging and/or the larger affinity of siloxane surfaces for Ca^{2+} ions, therefore, it is clear that cation type definitely plays a critical role in controlling the adhesion of –COOH as has been recently been acknowledge on work performed using contact angle and quartz microbalance measurements [42]. In addition, we have observed that pH is also a crucial parameter in defying the adhesion behaviour, due to its role in varying the protonation state of relevant functional groups, in agreement with recent studies. Therefore, it seems crucial, that in order to fully understand and develop adequate theoretical frameworks to predict the behaviour of low salinity solutions a greater emphasis should be given to determine the surface complexation reactions (and associated reaction constant) as well as those controlling the protonation state of relevant functional groups.

Measurements taken using NH_2 functionalised probes on the siloxane faces, also show a complex picture with a reversal of the effect of varying concentrations on determining the adhesion force. Due to time constrains and other technical difficulties only a limited set of experiments were performed on this thesis, but more will be required to gain a better picture on the underlying mechanism controlling the adhesion of this functional group on kaolinite crystals.

Overall, this experiment clearly observed cation bridging phenomena at high pH (8-9), due to the fully protonation of the carboxylic acid. However, the polar fraction in nature crude oils, which are slightly acidic (pH 5-6), could relate to cation bridging by partial protonation (pH 4-6) of carboxylic acids as can be seen in the study of Vezenov et al.[35].

5.4 Conclusions

In this study we have measured the adhesion between –COOH functional groups and the siloxane and aluminol faces kaolinite by means of chemical force microscopy as a function of pH, salinity (0.001 to 1 M) and cation identity (Na^{+} vs. Ca^{2+}). In addition, a reduced number of experiments was performed on siloxane surfaces using -NH_2 functional groups and $CaCl_2$ solutions. Results from measurements on the siloxane face show that, Ca^{2+}

displays a reverse low-salinity effect (with adhesion decreasing at higher concentrations) at pH 5.5, and a low salinity effect at pH 8. This contrasting behavior at different pH values, cannot be explained by recurring to a double layer expansion mechanism, but can be described by looking at the variations in complexation at the surface and the deprotonation of the –COOH groups when the pH is varied. At a pH of 5.5 the tip still possess a large number of protonated –COOH groups that will form hydrogen bonds with surface-bound H^+, and any sorbed Ca^{2+} may form cation bridges with deprotonated $–COO^-$ groups. As the Ca^{2+} concentration is increased, Ca^{2+} will substitute H^+ at the clay surface reducing the number of hydrogen bonds and therefore decreasing the adhesion. At pH 8.8 a different situation develops with the –COOH groups at the probe now fully deprotonated and the source of adhesion only due to cation bridging, therefore a decrease in concentration would lead to a decrease in this mode of bonding and a lower measured adhesion.

At constant Ca^{2+} concentration of 0.001 M, however, an increase in pH (from 5 to 9) leads to larger adhesion. Again, this behaviour is explained by changes in the protonation state of the tip with varies between being fully protonated at pH 5 to being fully deprotonated at pH 9. The increase in adhesion is due to an increase in the number of Ca^{2+} bridging as the ratio of Ca^{2+}/H^+ bound to the surface increases with pH. The larger increase in adhesion recorded at the pH 8 to 9 intervals can be explained by this effect in combination with a reduction on the double layer width due to a decrease in surface potential. On the contrary, a variation in the Na^+ concentration did not show any discernible trend in varying the adhesion of –COOH groups to the siloxane face, which again points in the direction of a minimal effect on double layer expansion but an effect on the cation identity and complexation of the kaolinite surface.

Measurements performed with $–NH_2$ groups show a low-salinity effect at pH 5.6 and a reverse low-salinity effect at pH 8. Again, this result can be explained by looking at the surface complexation and the protonation of the functional group. At a pH of 5.6 and low $CaCl_2$ adhesion will occur through electrostatic interactions between the positively charged $–NH_3^+$ groups and negatively charged surface sites (in addition to some hydrogen bonding) At higher Ca^{2+} the relative amount of Ca^{2+} complexed to the surface will increase significantly, leading to the formation of a large number of $≡O\text{-}Ca^{2+}\text{-}Cl^-_2$ complexes which would increase the number of electrostatic interactions with the $\text{-}NH_3^+$ groups at the tip, leading to the observed increase in adhesion. At a pH 8, all $–NH_2$ groups on the probe will be de-protonated. At pH 8, the probe will mostly consist of $\text{-}NH_2$ groups, leading to a reduction of electrostatic interactions. At low Ca concentration the lower concentration of charge balancing cations (protons and Ca^{2+}) will facilitate the formation of hydrogen bonding between the $\text{-}NH_2$ groups and ≡Si-O-Si≡ surface sites. At higher $CaCl_2$, however,

the surface will contain a larger amount of charge balancing Ca^{2+} ions, leading to a reduction of the hydrogen bonding and therefore a decrease in the measured adhesion.

At a constant concentration of 0.001M the adhesion between $-NH_2$ groups and the siloxane surfaces decreased significantly when the pH was increased from 5 to 9. As above, this can be explained by changes in the protonation state of the $-NH_2$ groups and surface speciation. At low pH adhesion into the surface will occur though electrostatic interactions between negatively charged sites and protonated NH_3^+ molecules on the tip, but also through hydrogen bonding on ≡Si-O-Si≡ surface sites. As the pH is increased the number of protonated $-NH_3^+$ molecules on the probe will be severely reduced, decreasing, in turn, the number of electrostatic interactions with negatively-charged sites significantly, which would lead to the observed decrease in adhesion. Measurements on the aluminol face showed a reverse low-salinity effect at pH 5.5 and in the presence of Ca^{2+}, similar to what was observed on the siloxane face at the same pH. This result can be explained by a decrease in hydrogen bonding and electrostatic attraction by the accumulation of a larger number of counter ions on the kaolinite surface as the $CaCl_2$ is increased. An increase in pH with constant ion concentration resulted in a decrease in adhesion for both Ca^{2+} and Na^+, opposite to what was observed in the siloxane face, but which correlates better with the behaviour observed on reported experiments that looked at the sorption of acidic organic molecules to kaolinite. In this case, the change in the charge sign of the aluminol face seems to be the main driver of the observed trend. In summary the results presented here indicate a more complex relationship between different effects, but were cation identity and pH variation are the most important determining factors in varying the adhesion of –COOH molecules to kaolinite surfaces. Therefore these results align better with the multicomponent ion exchange mechanism (with pH variation) that has been invoked to explain the operation of low salinity water flooding in core experiments and field tests.

5.5 References

[1] I.E. Agency, World Energy Outlook, 2013.

[2] A. Muggeridge, A. Cockin, K. Webb, H. Frampton, I. Collins, T. Moulds, P. Salino, Recovery rates, enhanced oil recovery and technological limits, 2014.

[3] M.D. Jackson, J. Vinogradov, G. Hamon, M. Chamerois, Evidence, mechanisms and improved understanding of controlled salinity waterflooding part 1: Sandstones, Fuel 185 (2016) 772-793.

[4] J.J. Sheng, Critical review of low-salinity waterflooding, Journal of Petroleum Science and Engineering 120(0) (2014) 216-224.

[5] S. Strand, T. Puntervold, T. Austad, Water based EOR from clastic oil reservoirs by wettability alteration: A review of chemical aspects, Journal of Petroleum Science and Engineering 146 (2016) 1079-1091.

[6] A. Lager, K.J. Webb, I.R. Collins, D.M. Richmond, LoSal Enhanced Oil Recovery: Evidence of Enhanced Oil Recovery at the Reservoir Scale, Society of Petroleum Engineers, 2008.

[7] T. Austad, A. Rezaeidoust, T. Puntervold, Chemical Mechanism of Low Salinity Water Flooding in Sandstone Reservoirs, Society of Petroleum Engineers, 2010.

[8] R. Kareem, P. Cubillas, J. Gluyas, L. Bowen, S. Hillier, H.C. Greenwell, Multi-technique approach to the petrophysical characterization of Berea sandstone core plugs (Cleveland Quarries, USA), Journal of Petroleum Science and Engineering 149 (2017) 436-455.

[9] T.S. Arnarson, R.G. Keil, Mechanisms of pore water organic matter adsorption to montmorillonite, Marine Chemistry 71(3) (2000) 309-320.

[10] X. Yin, V. Gupta, H. Du, X. Wang, J.D. Miller, Surface charge and wetting characteristics of layered silicate minerals, Advances in Colloid and Interface Science 179-182(0) (2012) 43-50.

[11] V. Gupta, J.D. Miller, Surface force measurements at the basal planes of ordered kaolinite particles, Journal of Colloid and Interface Science 344(2) (2010) 362-371.

[12] J. Vevle, NMR measurements of wettability alternation in Berea Sandstone, The University of Bergen, 2011.

[13] J. Liu, J.D. Miller, X. Yin, V. Gupta, X. Wang, Influence of ionic strength on the surface charge and interaction of layered silicate particles, Journal of Colloid and Interface Science 432(0) (2014) 270-277.

[14] J. Jupille, Analysis of Mineral Surfaces by Atomic Force Microscopy, in: G.S. Henderson, D.R. Neuville, R.T. Downs (Eds.), Spectroscopic Methods in Mineralogy and Materials Science, The Mineralogical Society of America, Chantilly, Virginia, USA, 2014, p. 800.

[15] T. Hassenkam, L.L. Skovbjerg, S.L.S. Stipp, Probing the intrinsically oil-wet surfaces of pores in North Sea chalk at subpore resolution, Proceedings of the National Academy of Sciences of the United States of America 106(15) (2009) 6071-6076.
[16] J. Matthiesen, T. Hassenkam, N. Bovet, K.N. Dalby, S.L.S. Stipp, Adsorbed Organic Material and Its Control on Wettability, Energy Fuels 31(1) (2017) 55-64.
[17] T. Hassenkam, M.P. Andersson, E. Hilner, J. Matthiesen, S. Dobberschutz, K.N. Dalby, N. Bovet, S.L.S. Stipp, P. Salino, C. Reddick, I.R. Collins, Could Atomic-Force Microscopy Force Mapping Be a Fast Alternative to Core-Plug Tests for Optimizing Injection-Water Salinity for Enhanced Oil Recovery in Sandstone?, Spe J 21(3) (2016) 720-729.
[18] D.V. Okhrimenko, K.N. Dalby, L.L. Skovbjerg, N. Bovet, J.H. Christensen, S.L.S. Stipp, The surface reactivity of chalk (biogenic calcite) with hydrophilic and hydrophobic functional groups, Geochimica Et Cosmochimica Acta 128 (2014) 212-224.
[19] J. Matthiesen, N. Bovet, E. Hilner, M.P. Andersson, D.A. Schmidt, K.J. Webb, K.N. Dalby, T. Hassenkam, J. Crouch, I.R. Collins, S.L.S. Stipp, How Naturally Adsorbed Material on Minerals Affects Low Salinity Enhanced Oil Recovery, Energy & Fuels 28(8) (2014) 4849-4858.
[20] L.L. Skovbjerg, D.V. Okhrimenko, J. Khoo, K.N. Dalby, T. Hassenkam, E. Makoyicky, S.L.S. Stipp, Preferential Adsorption of Hydrocarbons to Nanometer-Sized Clay on Chalk Particle Surfaces, Energy & Fuels 27(7) (2013) 3642-3652.
[21] T. Hassenkam, A.C. Mitchell, C.S. Pedersen, L.L. Skovbjerg, N. Bovet, S.L.S. Stipp, The low salinity effect observed on sandstone model surfaces, Colloids and Surfaces A: Physicochemical and Engineering Aspects 403(0) (2012) 79-86.
[22] T. Hassenkam, C.S. Pedersen, K. Dalby, T. Austad, S.L.S. Stipp, Pore scale observation of low salinity effects on outcrop and oil reservoir sandstone, Colloids and Surfaces A: Physicochemical and Engineering Aspects 390(103) (2011) 179-188.
[23] J. Wu, F. Liu, H. Yang, S. Xu, Q. Xie, M. Zhang, T. Chen, G. Hu, J. Wang, Effect of specific functional groups on oil adhesion from mica substrate: Implications for low salinity effect, J Ind Eng Chem 56(Supplement C) (2017) 342-349.
[24] K.M.S. Juhl, C.S. Pedersen, N. Bovet, K.N. Dalby, T. Hassenkam, M.P. Andersson, D. Okhrimenko, S.L.S. Stipp, Adhesion of Alkane as a Functional Group on Muscovite and Quartz: Dependence on pH and Contact Time, Langmuir 30(48) (2014) 14476-14485.
[25] S.A. Farzaneh, M. Sohrabi, Experimental investigation of CO2-foam stability improvement by alkaline in the presence of crude oil, Chem. Eng. Res. Des. 94 (2015) 375-389.
[26] K.M.S. Juhl, N. Bovet, T. Hassenkam, K. Dideriksen, C.S. Pedersen, C.M. Jensen, D.V. Okhrimenko, S.L.S. Stipp, Change in Organic Molecule Adhesion on alpha-Alumina

(Sapphire) with Change in NaCl and CaCl2 Solution Salinity, Langmuir 30(29) (2014) 8741-8750.

[27] L. Alagha, S. Wang, L. Yan, Z. Xu, J. Masliyah, Probing Adsorption of Polyacrylamide-Based Polymers on Anisotropic Basal Planes of Kaolinite Using Quartz Crystal Microbalance, Langmuir 29(12) (2013) 3989-3998.

[28] D.V. Vezenov, A. Noy, P. Ashby, Chemical force microscopy: Probing chemical origin of interfacial forces and adhesion, Journal of Adhesion Science and Technology 19(3-5) (2005) 313-364.

[29] J.L. Hutter, J. Bechhoefer, Calibration of atomic-force microscope tips, Review of Scientific Instruments 64(7) (1993) 1868-1873.

[30] H.J. Butt, M. Jaschke, Calculation of thermal noise in atomic force microscopy, Nanotechnology 6(1) (1995) 1-7.

[31] A. Lager, K.J. Webb, C.J.J. Black, M. Singleton, K.S. Sorbie, Low Salinity Oil Recovery - An Experimental Investigation1, (2008).

[32] K.S. Sorbie, I. Collins, A Proposed Pore-Scale Mechanism for How Low Salinity Waterflooding Works, Society of Petroleum Engineers, 2010.

[33] A. Berquand, N. Xia, D.G. Castner, B.H. Clare, N.L. Abbott, V. Dupres, Y. Adriaensen, Y.F. Dufrene, Antigen Binding Forces of Single Antilysozyme Fv Fragments Explored by Atomic Force Microscopy, Langmuir 21(12) (2005) 5517-5523.

[34] L. Shi, M.H.M. Olsson, T. Hassenkam, S.L.S. Stipp, A pH-Resolved View of the Low Salinity Effect in Sandstone Reservoirs, Energy Fuels 30(7) (2016) 5346-5354.

[35] D.V. Vezenov, A. Noy, L.F. Rozsnyai, C.M. Lieber, Force Titrations and Ionization State Sensitive Imaging of Functional Groups in Aqueous Solutions by Chemical Force Microscopy, Journal of the American Chemical Society 119(8) (1997) 2006-2015.

[36] R. Kleven, J. Alstad, Interaction of alkali, alkaline-earth and sulphate ions with clay minerals and sedimentary rocks, Journal of Petroleum Science and Engineering 15(2) (1996) 181-200.

[37] F. Mugele, B. Bera, A. Cavalli, I. Siretanu, A. Maestro, M. Duits, M. Cohen-Stuart, D. van den Ende, I. Stocker, I. Collins, Ion adsorption-induced wetting transition in oil-water-mineral systems, Scientific Reports 5 (2015) 10519.

[38] L. Madsen, L. Ida, Adsorption of Carboxylic Acids on Reservoir Minerals From Organic and Aqueous Phase, SPE Reservoir Eval. Eng. 1(1) (1998) 47-51.

[39] A. Fogden, Removal of crude oil from kaolinite by water flushing at varying salinity and pH, Colloids Surf. Physicochem. Eng. Aspects 402(Supplement C) (2012) 13-23.

[40] J. Desmond, K. Juhl, T. Hassenkam, S.L.S. Stipp, T. Walsh, P. Rodger, Organic-silica interactions in saline: elucidating the structural influence of calcium in low-salinity enhanced oil recovery, Sci Rep-Uk 7(1) (2017) 10944.

[41] Y.-L. Wu, N.E. Horwitz, K.-S. Chen, D.A. Gomez-Gualdron, N.S. Luu, L. Ma, T.C. Wang, M.C. Hersam, J.T. Hupp, O.K. Farha, G-quadruplex organic frameworks, Nature Chem. 9(5) (2017) 466.

[42] W.G. Anderson, Wettability literature survey-part 4: Effects of wettability on capillary pressure, J Petrol Technol 39(10) (1987) 1,283-1,300.

[43] M.J. Fernández-Gómez, M. Díaz-Raviña, E. Romero, R. Nogales, Recycling of environmentally problematic plant wastes generated from greenhouse tomato crops through vermicomposting, International Journal of Environmental Science and Technology 10(4) (2013) 697-708.

6

The effect of salinity and pH of formation water and injected water on wettability alteration of kaolinite films studied by contact angle measurement and environmental scanning electron microscopy

Low-salinity enhanced oil recovery (LSEOR) has shown great effectiveness in improving the oil recovery ratio and extending the life of mature oil reservoirs. This effectiveness is related to the ability of low salinity injection water to change the wettability state of the reservoir to more water-wet. However, the complexity of the chemical relationship between brine, oil and rock is such that no single mechanism has been identified for being responsible for this change in wettability. This said, the role of clay minerals (which are widely present in the pore space of clastic reservoirs) in their interaction to oil molecules has been regarded as critical. In this chapter, we show results from the study on the effect of formation water (varying composition), model oil (decanoic acid/dodecane) aging and salinity treatment (with varying degrees of concentration, cation identity, and pH) on clay mineral wettability, as studied by contact angle measurements. To this end, we have developed a method to prepare smooth, oriented, kaolinite films (with the siloxane face exposed to the solution/oil) of several square cm and a submicron roughness. Contact angles of model oil droplets over the clay films were measured using the captive bubble method and environmental scanning electron microscopy (ESEM). Results from the contact angle measurements show that formation water containing Na^{+} does not result in large contact angle (wettability) variation, but the presence of Ca^{2+} does lead to larger disparities. Increasing pH from 6.5 to 8 leads to an overall increase in the measured contact

angle, i.e. to decreased oil sorption (or increasing water-wetness) by the kaolinite film. This effect can be explained by the protonation state of the polar molecules (decanoic acid) as well as the surface complexation (which would lead to the formation of cation bridges in the case of Ca^{2+}). Treatment (washing) of oil-aged films by brines of different concentrations (and either $CaCl_2$ or NaCl composition) showed no clear trends in the modification of contact angle but, in general, increasing $CaCl_2$ concentrations leads to lower contact angles, i.e. less oil desorption (oil wet surface). On the other hand most treatment with NaCl led to higher contact angles, or increased water-wetness of the kaolinite films. The results of ESEM were limited in this study due to the narrow range wetting properties.

6.1 Introduction

Enhanced oil recovery (EOR) techniques have shown great potential in improving the oil recovery ratio and extending the life of mature oil reservoirs to supply a constant increase in global energy demand. One of the most interesting EOR techniques is low salinity enhanced oil recovery (LSEOR), which mainly utilize desalinated sea water for injection. This is beneficial not only for effectiveness, but also for cost reduction, and environment-friendly initiatives [1, 2]. In particular, the application of LSEOR to sandstone reservoirs has shown larger potential than to other lithologies [3].

LSEOR in sandstone reservoirs has been intensively studied at pilot, commercial and laboratory scale [3]. Most authors have observed that the low salinity effect operates when a series of conditions are true in the rock/reservoir. This include: 1) presences of clay minerals [4], 2) presence of polar components in the crude oil [4, 5], 3) presence of formation water. Lager et al. and Ligthelm et al. proposed that the adsorption of crude oil molecules on pore-lining, clay minerals could be controlled by cations dissolved in formation water [6, 7]. Then, the different chemical properties of the low salinity injection (cation identities, concentration, pH, etc.) would promote the desorption of the crude oil from the mineral surfaces [7-9]. This desorption would then alter the clay mineral surface from oil-wet to more water-wet, resulting in an increase in oil production. Therefore, wettability alteration has been typically been invoked as the microscopic mechanism underlying LSEOR [2, 8, 10].

Wettability alteration as a function of salinity has been studied widely on core flooding experiments and Amott imbibition tests [10-16]. However, several authors reported important issues with experiment reproducibility [10, 12, 15, 16]. This can be problematic and may be due to experimental artefacts such as the capillary end effect described in detail by Chang et al. [17]. Therefore, to study the mechanisms behind wettability alteration at a fundamental/microscopic level, the use of idealized systems

(smooth mineral substrates, model oils, prepared solutions) and direct assessment, has been used as an alternative to core scale investigations.

Wettability studies on model/ideal system have focused on pore-lining clay minerals, such as kaolinite, that are common in sandstone rocks [18] and are, therefore, involved with oil migration [19-21]. Lebedeva et al. and Lebedeva and Fogden studied the effects of concentration and pH of initial brine effect on the wettability of kaolinite films using the captive bubble method [22, 23]. Other authors, such as Berg et al. and Mahani studied the effect of salinity of an injection brine on wettability [16, 24]. In both studies, the authors exposed a clay film to oil-wetting conditions in high salinity brine, and then implanted drops of crude oil on it. Afterwards, they flowed brines of different concentration through the fluid cell to study their effect on oil wettability. These experiments provided direct, visual evidence, on oil release, as well as on the variation (kinetics) of contact angle at the oil-brine-mineral interface. Although the techniques they used provide an interesting insight, their studies were limited to single solutions (either the initial brine or the flooding brine waters). Therefore, the study did not address (through a direct measurement), the effect of a combination of parameters such as formation water, low-salinity injection brine composition, and their role as critical factors in determining wettability in LSEOR process.

The purpose of this study is 1) to develop a method to prepare oriented kaolinite films (exposing either the siloxane or the aluminol face) with a consistent and reproducible roughness. 2) to study the effect of brine concentration on captive bubble analysis to further develop the technique. 3) to understand the wettability alteration on kaolinite surfaces as a function of several parameters of the formation (aging) water and flooding water (cations identity, concentration, and pH), as well as the relationship between initial water and treatement water in the low salinity effect. Establishing a relationship between formation water composition and the low salinity effect of flooding water could lead to an improved selection of flooding water composition to achieve maximum wettability alteration, and therefore, maximum oil-release rates. Contact angle measurements (captive bubble method) were performed over smooth, oriented, kaolinite films; as a representative of pore-lining minerals, aged in NaCl and $CaCl_2$ solutions and decanoic acid/dodecane mixtures The captive bubble method was chosen due to its reliability to study this type of system [24, 33]. Results provide an insight into the change of wetting as a result of different aging and flooding parameters. Moreover, environmental electron microscopy (ESEM) was used to try to obtain a microscale view of the wettability alteration and to compare with the contact angle measurements.

6.2 Materials and methods

6.2.1 Kaolinite film preparation

Kaolinite standard (KGa1b from The Clay Minerals Society clay mineral repository, Washington County, Georgia, USA) was mixed with Milli-Q® water which was adjusted to a pH of 9.8 using 0.1M NaOH, to prepare three different suspension of kaolinite with concentrations of 1, 2.5, 5 %w/w (0.3 g of kaolinite in 29.7 ml of Milli-Q® water, 0.75 g of kaolinite in 29.25 ml of Milli-Q® water, 1.5 g of kaolinite in 28.5 ml of Milli-Q® water). The suspensions were sonicated using a sonicator probe (Q-Sonica Q125, 125 W) at 40% amplitude with 2 seconds sonication burst followed by 5 seconds of rest both 8 min and 16 min. The suspension was then allowed to rest for 15 min to settle the largest particles down. Then, the suspension was centrifuged (LMC-3000 from Biosan) at 3000 rpm for 5 min to eliminate the large and medium-sized kaolinite from the solution.

The suspension was used to produce a kaolinite film using four different approaches: 1) 1 ml of suspension was dropped on a glass slide (VWR®), and dried in an oven (Panasonic electric oven Model No. MOV-112-PE) at 70 °C for 24 h. 2) 1ml of the suspension was dropped on a microscope slide (VWR®) and the droplet was dried by spin coating at 200 rpm for 2min. Spin coating is a basic technique to create uniform thin films of liquid for solidification into a coating ranging from nanometres to microns depending on the velocity of spinning [25]. 3) 1ml of the suspension was dropped on a microscope slide (VWR®) and the droplet was dried by means of a heat gun for 2 min. 4) A cleaned microscope slide (VWR®) was placed upright into the tube holding the suspension and then left to dry inside an oven for 48 h at 70 °C. In the four cases, all dried samples were rinsed a couple times using 5 ml of Milli-Q® water (to remove any “loose” kaolinite crystals) and the dried in the oven (70 °C) for 20 min. All parameters for the four preparation methods are shown in Table 6.1. Samples of films made with each method were later imaged using a FEI Helios Nanolab Mk2 Scanning Electron Microscope (SEM). The method that produced the kaolinite films with the best coverage and more consistent roughness values was then followed to prepare the films used for the contact angle measurements.

Samples imaged by SEM were prepared by for imaging by covering them with a 25 um layer of gold and were imaged at 5 kV and a working distance of 4 mm. Roughness measurements (Sa) were performed using a non-contact optical 3D profiler (Zygo NewView 5000 white light phase shifting interferometer). Analyses were performed on three different kaolinite films (and 2 different areas per film) to observe any variability across different films and different areas of the same film. Areas of 0.5 mm x 0.5 mm (with a lateral resolution of 1 um) were scanned so the measured value would be as

representative as possible of the area were a droplet (2 mm in diameter) would sit during the contact angle measurements. Extracted surface roughness maps were obtained after applying a 0.25 mm filter to the raw height data.

Table 6.1 Parameters for kaolinite film preparation.

Procedures	Review on Lebedeva and Fogden [23]	Testing parameters
1.% of Kaolinite	6.3%	-1% -2.5% -5%
2. Solutions	QI water pH 9.8	-QI water pH 9.8
3. Sonication Time	Don't mention	-8 min -16 min
4. Substrate	microscope glass slide (76mm ×2 6 mm)	-microscope - glass slide (76x26mm) -mica sheet(11x11mm)
5. Drying	120 °C by heat gun	-drop and dry by 70 °C oven -unknown T by Heat gun -spin coating -charge attachment and dry by 70 °C oven

6.2.2 Effect of immersion brine composition on contact angle measurements on glass and kaolinite substrates.

Before the study on the effect of formation water and "treatment" brines on contact angles, a series of test were performed to study the effect of the concentration "immersion" solution on the measured contact angle over a model surface (glass) and a clay film. The glass substrate consisted of cleaned microscope glass slides (7.6 cm ×2.6 cm from VWR®). The measurements were conducted using PVC rounded standings (radius 2 cm. height 2 cm.), which were placed into a transparent quartz tank (size 5 cm x 6 cm x 10 cm). The tank was then filled with 100 ml of a brine solution of 0.001M of $CaCl_2$ or NaCl. The glass slide was placed over the round stands using clean tweezers (Figure 6.1). Eventually, the model oil (decanoic acid dissolved into dodecane) droplet were placed on the substrate using an U-shape needle (outer diameter 0.362 mm, inner diameter 0.184 mm, wall thickness 0.089 mm) attached to a 1ml syringe (BD syringe, size 1ml), for a total of four droplets on the substrate (Figure 6.1).

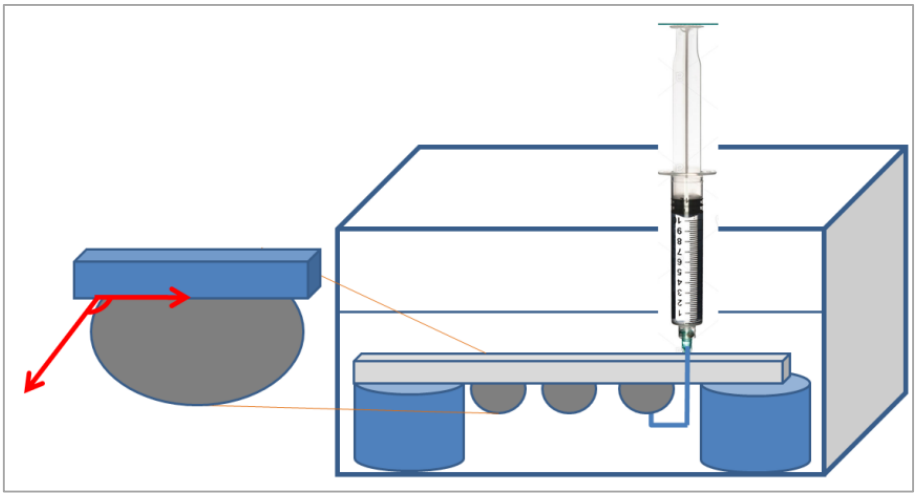

Figure 6.1 Schematic diagram of the contact angle experiment and the procedure to measure the angle.

All droplets were individually measured 10 times every 30 s using using a contact goniometer Model 260 from Ramé-hart Instrument Co. and the DropImage Advanced software (Experiment Wizard mode, contact angle) After the initial set of measurements, the concentration of the solution was modified increased to 0.01M by adding a few droplets of 1 M or 2 M of $CaCl_2$ or NaCl solutions into the quartz tank (priot to this, the same volume of solution was removed to keep the 100 ml of solution inside the tank constant). Using this methodology it would be possible to measure any effect of the solution on the contact angle for the same oil droplet (constant volume) over the same area of substrate (no change in surface roughness. Eventually, the contact angle was re-measured in the new solution on the same way as with the previous solution. The concentration was increased in this way from 0.001M to 0.01M, to 0.1, and finally to 1M (Figure 6.2). The volume of solution to be added to the tank to change the concentration was calculated following Equation 6.1. This experiment was performed both NaCl and $CaCl_2$ solutions at pH 6.5 (The adjustment of brine at pH 6.5 are given in Section 6.2.3.1).

$$V_{ad} = \frac{V_i\,[\,]_f}{[\,]_{ad} - [\,]_f} \qquad \text{(Equation 6.1)}$$

Where V_{ad} is volume of added solution; V_i is volume of initial solution; $[\,]_{ad}$ is concentration of final solution; $[\,]_f$ is concentration of final solution.

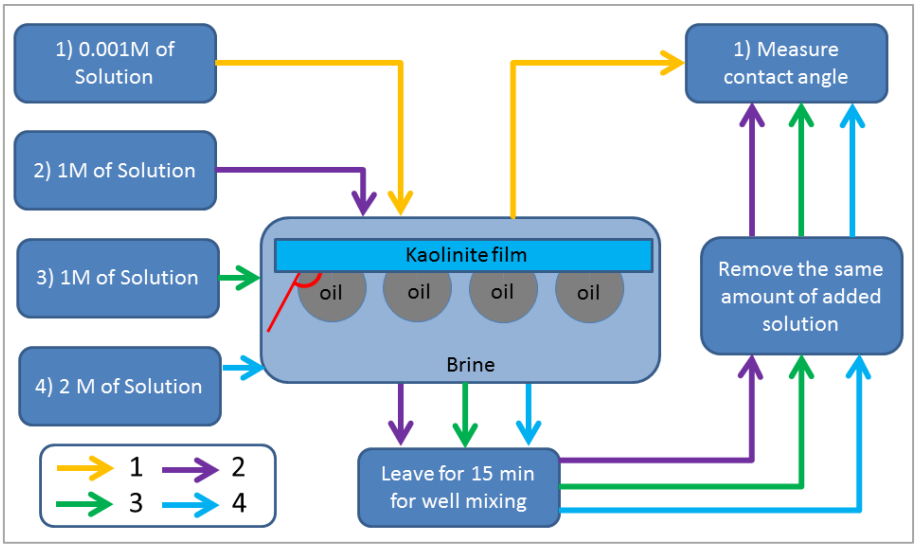

Figure 6.2 Flow diagram showing the procedure followed to measure the same droplet whilst changing the "immersion" solution.

6.2.3 The study of wettability of kaolinite-coated substrates through contact angle measurements

6.2.3.1 Kaolinite-film aging

The study of wettability alteration on kaolinite-films was performed following three procedures (designed to replicate certain reservoir conditions), which were initial brine aging (pre-migration/formation water), oil aging (migration), and salinity washing (oil production). Contact angle measurements were performed on different films after each stage of treatment.

Formation water (pre-migration) aging: Kaolinite films were aged on solutions of either $CaCl_2$ or NaCl with three different concentrations (1, 0.01 and 0.0001 M) and pH of either 6.5 or 8, for a total of 12 different solution chemistries. $CaCl_2$ and NaCl solutions were prepared using $CaCl_2$ and NaCl salts (Sigma-Aldrich, reagent grade) respectively, and Milli-Q® water. All solutions were adjusted to pH 6.5 and 8 using 0.1M of NaOH and 0.1 M of HCl for NaCl solutions, and using 0.1M of CaOH and 0.1 M of HCl for $CaCl_2$ solutions. All solutions are listed in Table 6.1. For each solution, 8 petri dishes were prepared with 25 ml of solution, and then the kaolinite films were immersed into each petri dish using cleaned tweezers. The petri dishes were sealed using ParaFilm® to avoid contamination and the samples kept into the oven 70°C for 24 h to imitate reservoir conditions. All samples were retrieved from the brine. One out of eight samples was used to study the effect of initial-brine (formation water) aging. The other seven samples were placed in new individual petri dishes and filled with 25 ml of 1 M of decanoic acid ($CH_3(CH_2)_8COOH$) which was

prepared by dissolving 176.26 g of decanoic acid (Sigma-Aldrich) into 1 liter of dodecane (ReagentPlus® ≥ 99% supplied by Sigma-Aldrich).

Oil aging: The samples were aged in the polar model oil at 70 °C for 24 h. All samples were then brought out from the model oil mixture. One of seven samples was kept to study the effect of oil-aging in the contact angle.

Brine treatment: The remaining six kaolinite-coated substrates were separately placed in petri dishes that contained 25 ml of 1, 0.01, and 0.001 M of $CaCl_2$ or NaCl (with same pH as the initial aging brine) to simulate the oil-recovery phase. These solutions were prepared in the same way (and using the same reagents) as the initial brine. The samples were kept in the oven 70°C for 24 h. After this, they were removed from solution and used for contact angle measurements. The work-flow for the aging sequence is displayed in Figure 6.3. Prior to performing the contact angle measurements, the retrieved substrate was immersed into the brine directly.

Table 6.2 Used solutions for the initial brine and flooding salinity

Solutions No.	Concentration	pH
1	1M of $CaCl_2$	6.5
2	0.01M of $CaCl_2$	6.5
3	0.001M of $CaCl_2$	6.5
4	1M of NaCl	6.5
5	0.01M of NaCl	6.5
6	0.001M of NaCl	6.5
7	1 M of $CaCl_2$	8
8	0.01M of $CaCl_2$	8
9	0.001M of $CaCl_2$	8
10	1M of NaCl	8
11	0.01M of NaCl	8
12	0.001M of NaCl	8

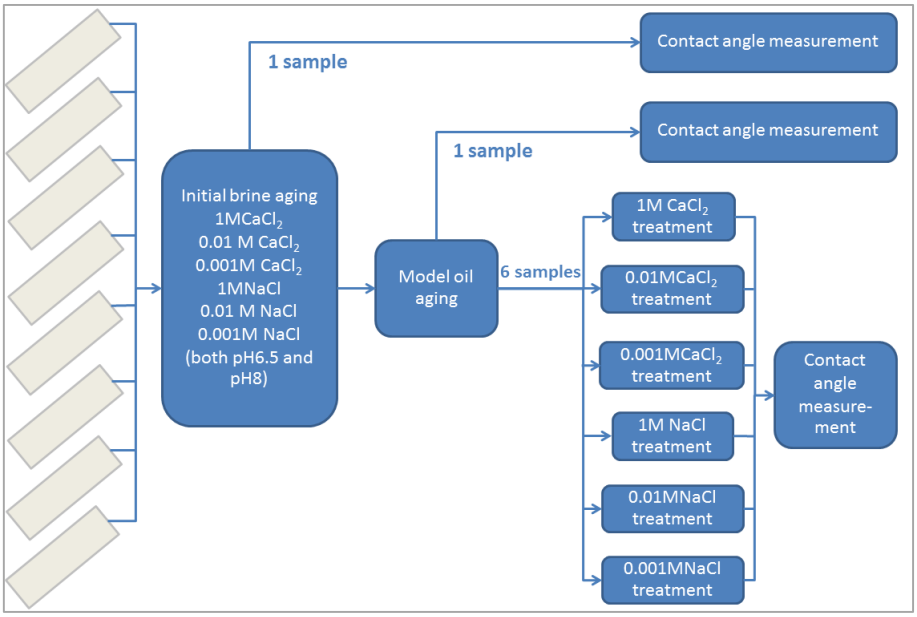

Figure 6.3 Diagram showing the sequential aging (initial brine aging, polar oil mixture aging, and salinity washing).

6.2.3.2 Contact angle measurements

Contact angle measurement was performed using a contact goniometer Model 260 from Ramé-hart Instrument Co. (Figure 6.4). Experiments were started by calibrating the instrument (x and y dimensions), using 4 mm metallic spheres. After this, the kaolinite-coated substrates were placed, upside down, on a PVC stand, inside a transparent quartz tank filled with 100 ml of a brine solution of equal concentration (and pH) to the last aging step (Figure 6.6). Subsequently, a series of droplets (5.5 ± 1 µl) of the model oil mixture, contained on a syringe (BD syringe, size 1ml) equipped with U-shape needle (outer diameter 0.362 mm, inner diameter 0.184 mm, wall thickness 0.089 mm), were placed on the kaolinite film, as shown in Figure 6.6. Contact angle measurements were performed over optical images of the droplets using the DropImage Advanced software (Experiment Wizard mode, contact angle) (Figure 6.5). The contact angle values reported for each oil droplet were the average angle from 10 measurements taken every 30 s for both left and right angle, as shown by the red line of Figure 6.6. The contact angle was measured against the oil droplet, meaning that high values correlate with an increase in water-wetness, whilst lower angles indicate more oil-wetness (Figure 6.6). All experiments were conducted at ambient conditions (ca. 25 ± 2 °C). To check for repeatability of measurements, three individual droplet measurements were performed on each kaolinite film, and the final average is reported.

Figure 6.4 An image of goniometer.

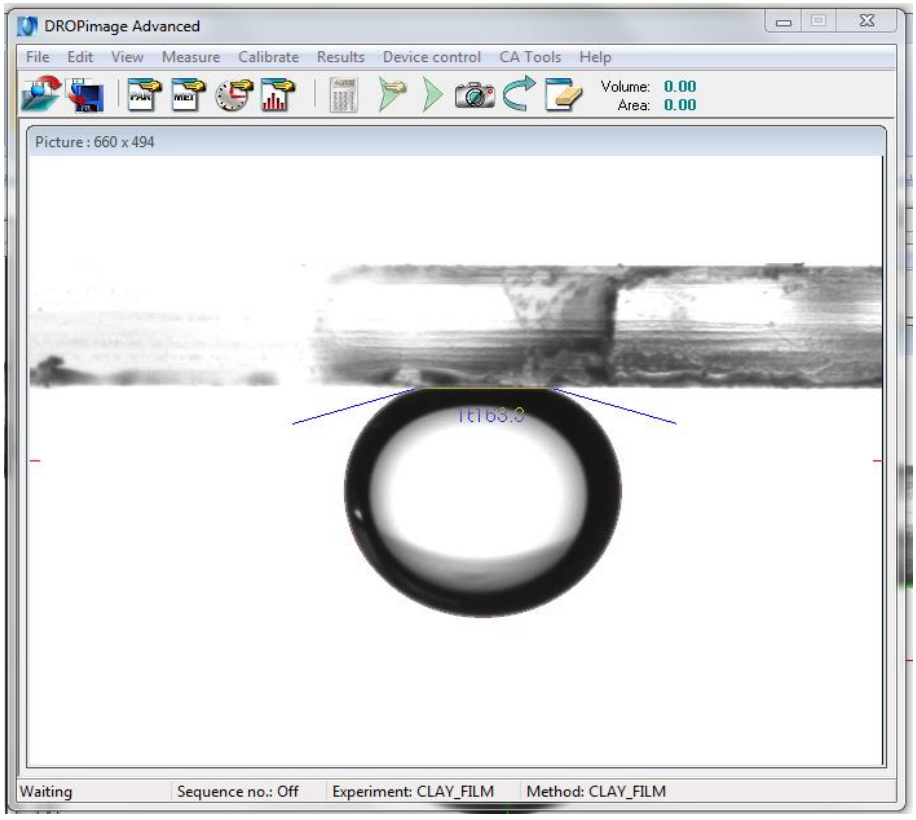

Figure 6.5 Contact angle measurement on clay film by DROPimage Advanced software.

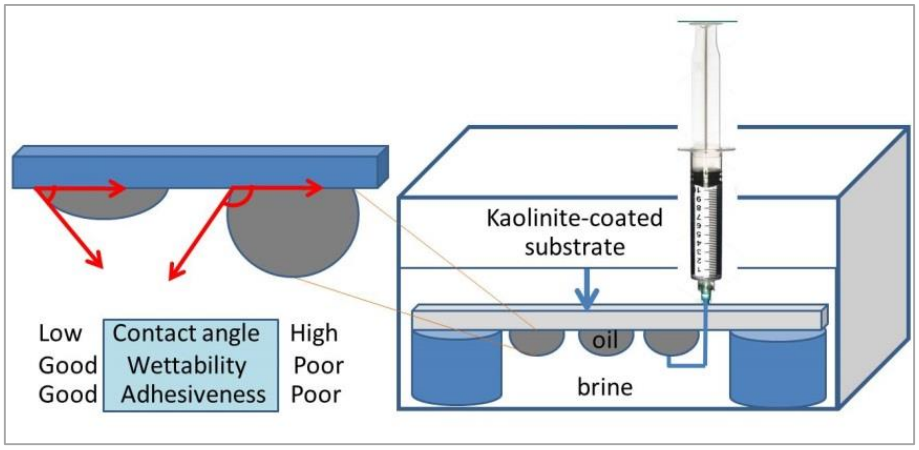

Figure 6.6 Schematic diagram of a contact angle experiment.

6.2.4 The study wettability of kaolinite-coated Berea sandstone by ESEM

6.2.4.1 Sample preparation

Due to the low thermal conductivity of glass, it was not possible to conduct water saturation experiments over kaolinite films (on glass slides) using ESEM. Instead, rock chips of Berea sandstone were coated with kaolinite films (the rough surface of the sandstone would allow the observations of droplets at the right angles to adequately measure contact angles). Berea sandstone was broken onto small chips a size of approximately 5 x 5 x 2 mm, with flat surface. Before kaolinite coating, the chips were cleaned immersing them in Milli-Q® water overnight (24 h) to remove ions. Chips were then sonicated in an ultrasonic bath (Ultrawave U50 Ultrasonic cleaner) with 100% power at room temperature for 1 h to remove the clay minerals at the surface and pores. The cleaned rock chips were placed in a petri dish and dried in the oven 70 °C for 1 h. After that, a suspension was prepared using the same procedure as for the contact angle experiments on glass slides. 30 ml of suspension were added to the petri dish containing the rock chips and then placed into the oven at 70 °C for 48 h. After this all samples were rinsed with Milli-Q® water three times to remove the unattached kaolinite crystals. The prepared samples were imaged using an SEM (FEI Helios Nanolab Mk2 Scanning Electron Microscope) to confirm the coating by kaolinite crystals.

6.2.4.2 Treatment of samples

The ESEM study looked at the effect of formation water aging (1M of $CaCl_2$ and 1M of NaCl at pH 6.5) and brine treatment (1 and 0.001M of $CaCl_2$ at pH 6.5) on determining the microscale wettability of the kaolinite crystals. The adjustment of brine at pH 6.5 and the rock chips aging was done in the same manner as the kaolinite films (Section 6.2.3.1). Three chips of the kaolinite-coated Berea sandstone were placed into a vial, for a total of two vials.

5 ml of 1M of $CaCl_2$ was added to first vial, and the same amount of 1M of NaCl was added to the second vial. The vials were then kept for 24 h at 70 °C in the oven. The samples from the two vials were placed in a two new vials using clean tweezers and then they were aged in a 1M model oil mixtures for 24hrs at 70 °C. After this, one rock chip sample out of the three (per vial) was kept in a cleaned vial, another one was treated in 0.001M of $CaCl_2$ (24h at 70 °C), and the last chip was treated in 1M of $CaCl_2$ (24h at 70 °C). The first samples were used to study the effect of formation water, whereas the other two samples were used to observe the effect of brine treatment with 0.001M and 1M of $CaCl_2$. Prior to ESEM analysis, all rock chips were rinsed with a small amount of Milli-Q® water (to remove any leftover salt) and left to dry for 15 min, as a dried surface is needed in order to observe the formation of water droplets inside the chamber of the ESEM.

6.2.4.3 Environmental scanning electron microscope (ESEM)

The ESEM study was performed at the electron microscopy facility at School of Energy, Geoscience, Infrastructure and Society, Heriot-Watt University. The equipment use was a Philips XL30 ESEM, quipped with LAB6 gun and operated in wet ESEM mode. This instrument is equipped with a 500 micron diameter gaseous secondary electron detector (GSED) to produce the images [26]. The experiment was started by placing the sample on a thin silver holder, and placed on the Peltier stage inside the instrument. After this, the sample was pre-cooled to approximately 5 °C. After closing the ESEM, the paltrier stage was controlled the temperature at 5 °C and the chamber was evacuated to 6 Torr and then flooded with water vapour from 6 to 10 Torr. These conditions produced a suitable atmosphere for inducing the condensation of water droplets which is required for the experiment and to prevent sample dehydration [26-28]. Once these conditions were established, the sample was moved using the stage controller in order to find a kaolinite-coated area. Eventually, the suitable area was double-checked by performing and EDX analysis in order to confirm the presence of kaolinite. The pressure in the chamber was then reduced to 4.5 Torr, and then incrementally increased to 0.5 Torr until the condensation of water droplets over the surface was observed. The increase in pressure should not be over than 6.5 Torr, as at this pressure 100% of relative humidity is achieved and water condensation can cause the flooding of the samples as explained in Chapter 4 (ESEM). In this situation no individual droplets would be able to be seen.

6.3 Results and Discussions

6.3.1 Influence of preparation parameters on kaolinite film quality: concentration of kaolinite, sonication time, and drying procedure

Figure 6.7 shows medium and high resolution SEM images of kaolinite films (by drop and dry) prepared using three different concentration of the kaolinite suspension (1%, 2.5% and 5%) and two different sonication times (8 and 16 min). It can be observed on the images that the films prepared from a suspension prepared by 8 min of sonication show particle aggregation and inconsistent coverage for all three kaolinite concentrations. At high magnification (over x24000), the kaolinite film displays a narrow size-distribution and parallel orientation (to the glass slide substrate) on those substrates prepared with 1% and 2.5% kaolinite suspension. The 5% suspension, however, led to the formation of particle stacks, culminated with crystals in random orientations. Moreover, at low magnification (x600), it can be observed that all suspensions led to the formation of "clumps" of kaolinite crystals of various sizes, and unevenly dispersed over the glass slides, as shown in Figure 6.7. These features render the films unusable for contact angle measurements; as these require a smooth, homogenous and stable surface [29-32]. When the sonication time was increased from 8 min to 16 min, the SEM images show that kaolinite films at 1 and 2.5% have a better overall coverage, whereas those derived from the 5% are rather "patchy" This probably is because at the 5% of suspension the kaolinite crystals are too close to each other and repulsive forces lead to an unstable surface, which is also easily washed out. Higher magnification images show very good orientation of the kaolinite crystals at 1 and 2.5% solutions. This indicates that the higher sonication time is better for film preparation, and also that the concentration of kaolinite in the suspension needs not to be higher than 2.5% w/w, which is lower values reported by other authors [23, 33]. Nevertheless, even though the SEM images suggests 16 min sonication of suspension with 1% or 2.5% of kaolinite as the best parameters to disaggregate the particles, the kaolinite coating is still relatively uneven covering continuous areas of only 0.25 mm x 0.25 mm (at best), which were still inadequate to perform the contact angle measurements.

After the optimum parameters of dispersion time (sonication) and kaolinite concentration of the suspension were confirmed, the next step was to look at various deposition techniques to achieve the maximum size of even and continuous coating. Initially, two deposition methods were tried, as reported in the literature: drop and dry by oven and drop and dry by heat gun, which have been used by Sheng et al. and Lebedeva and Fogden [23, 33]. Both methods involved the deposition of a large droplet of suspension over a glass slide followed by drying by either oven or heat gun. Either method, however, did not

show enough large area and even coverage (Figure 6.8). Although reasons for the discrepancies with literature results are not obvious, for the oven drying samples it may be that the evaporation rate was too fast which may have lead the particles no to settle down fast enough to cover the whole surface. With respect to the heat gun, it is use may have led to particles being "blown off" from the surface. . The third technique attempted was spin coating, which is a basic technique used to create uniform thin films of organic chemicals [25]. Results from the use of this technique shows that kaolinite crystals deposit as "streaks" over the surface (Figure 6.8). Therefore, not covering all the glass slide evenly. From these attempts, it was determined that a procedure with slow drying and uniform deposition rate over the glass slide surface was required. This leads to the use of the last method, which is based, in charge interaction or "attachment".

In the charge attachment method, the glass slides were placed in an upright position inside a vial containing the suspension. This allowed the larger kaolinite crystals to "fell" to the bottom of the vial without adhering to the glass slide and allowed the colloid-size particle to spontaneously deposit onto the glass slide. At the same time, the water was evaporated by placing the vials inside an oven at 70 °C. The result from this method was the evenly coating of the glass slide by kaolinite crystals in an area approximately 25 mm x 75 mm, which is much larger than that reported in the literature (~7.5 mm × 12 mm) [23]. From the SEM images it can be seen that the kaolinite film looks smooth and homogenous and that the crystal showed a very consistent orientation with its faces parallel to the glass slide substrate. Two different suspension concentrations were tried with this method, 1 and 2.5%. Both suspensions led to good coatings, Therefore, this film preparation method, along 1% suspensions (with 16 min of sonication time) was used for this study (Figure 6.9).

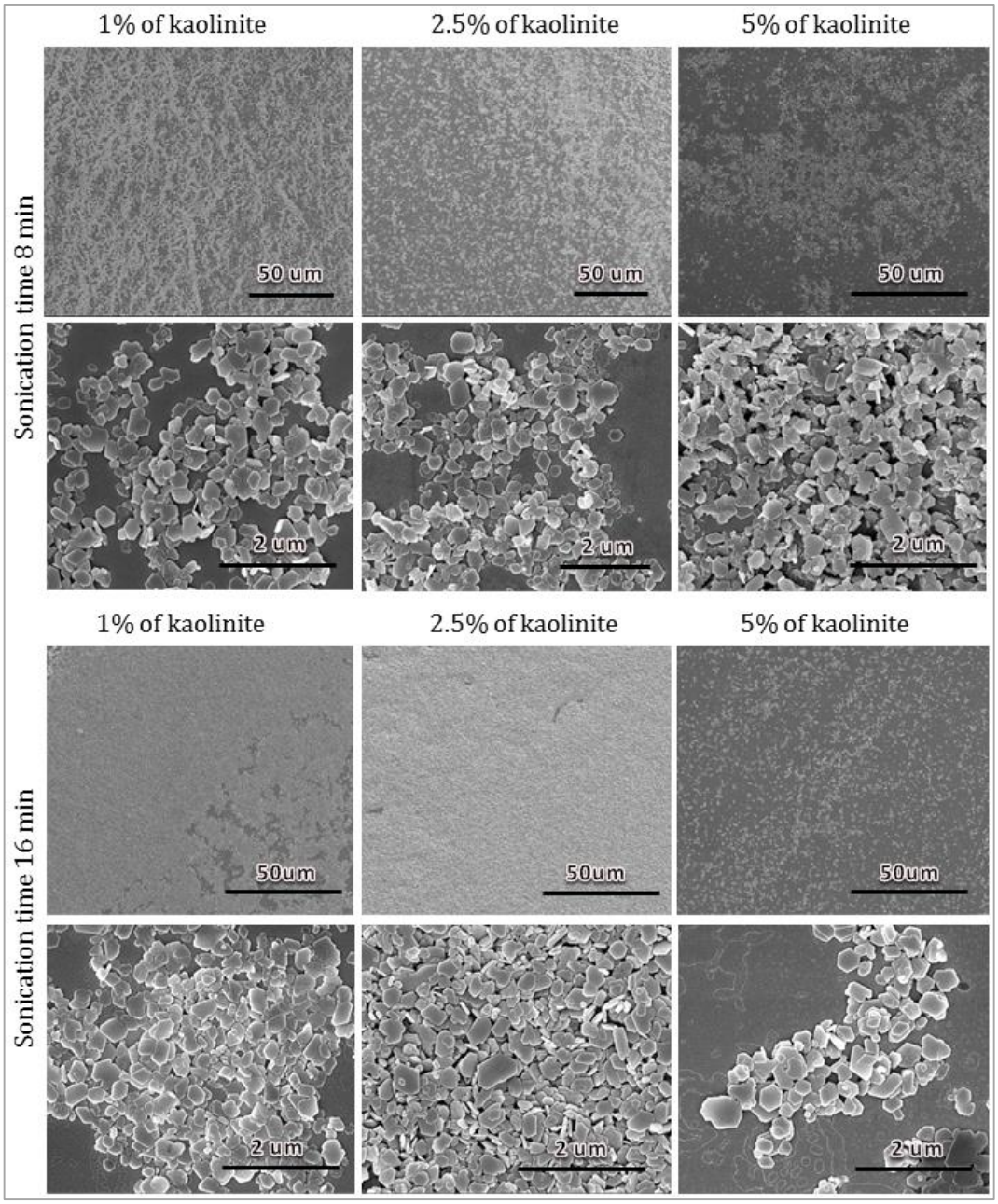

Figure 6.7 SEM photomicrographs of kaolinite films specimens prepared with suspension of various concentrations and two different sonication times.

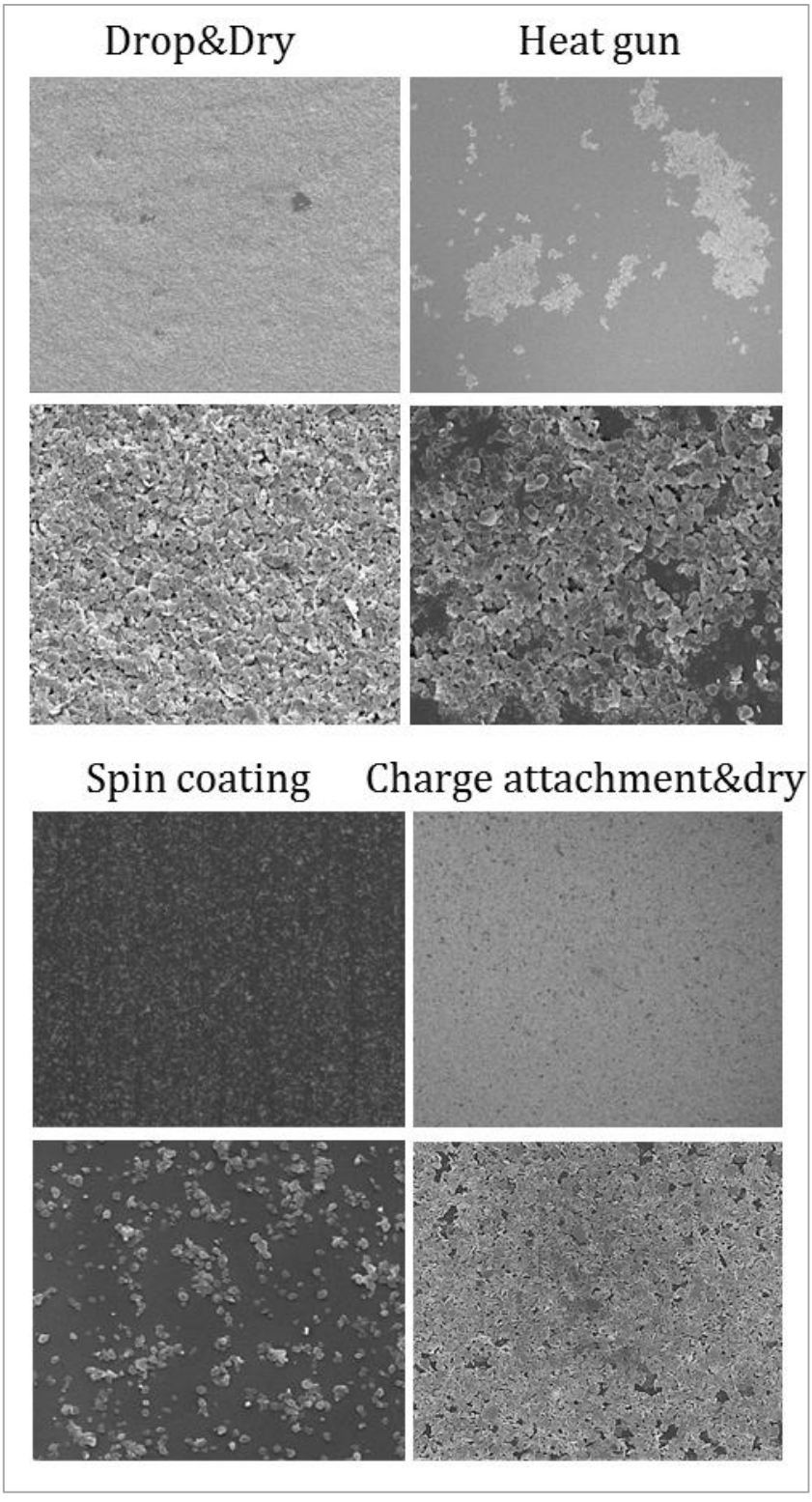

Figure 6.8 SEM images showing kaolinite films prepared with found different methods: drop and dry, drop and dry by heat gun, spin coating, and charge attachment and evaporation.

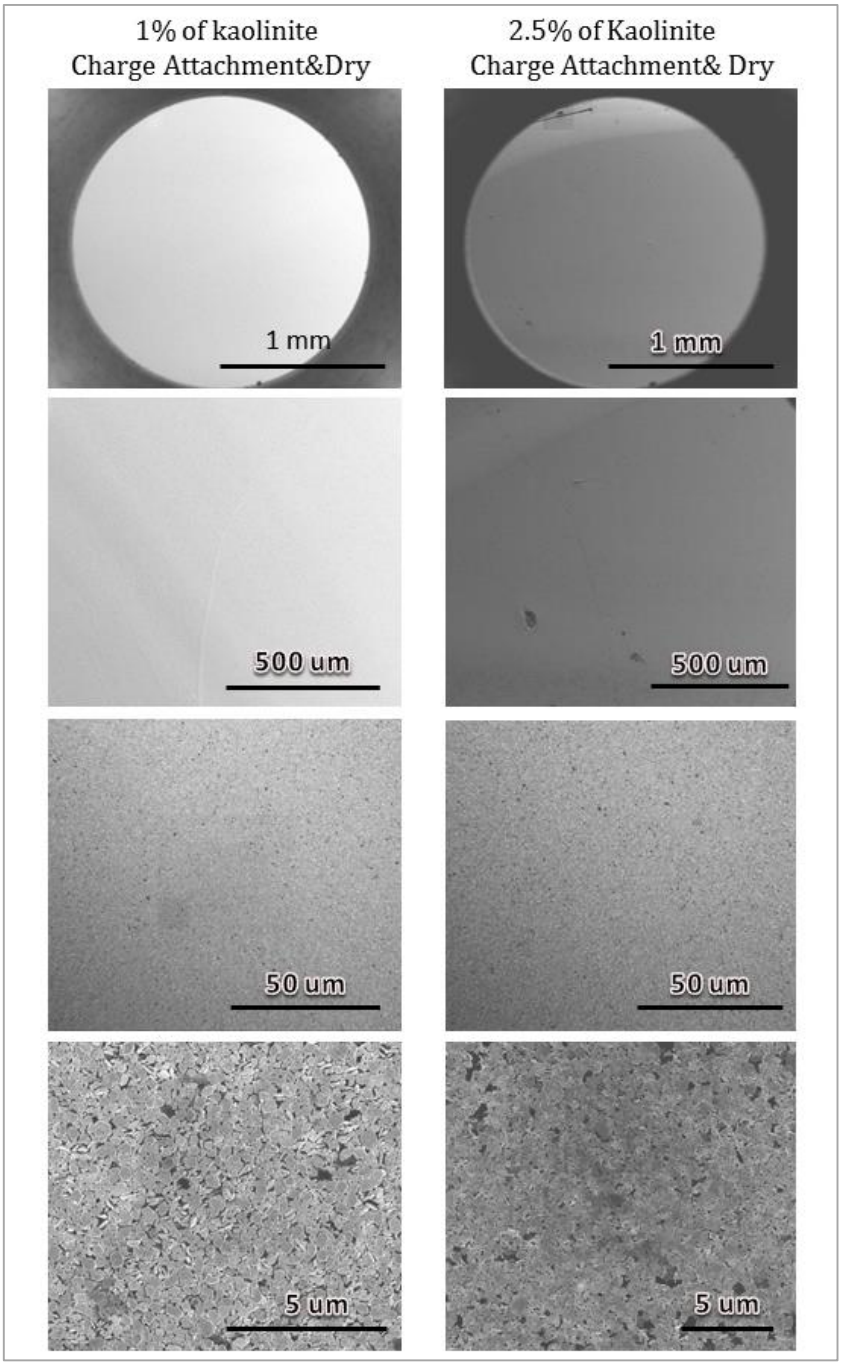

Figure 6.9 SEM images showing kaolinite films prepared by charge attachment and evaporation with 1% and 2.5% suspensions of kaolinite.

6.3.2. Kaolinite film characterisation

Prior to contact angle measurements, a few kaolinite films were characterised by means of SEM and white light interferometry. SEM images at low magnification (up to x600) show a smooth and homogeneous coating of kaolinite crystals (Figures 6.10a and 6.10b). Higher magnification (x20000 to x50000) show that kaolinite crystals on the film have a relatively well constrained size, and also that they are very well oriented within the film, with the

majority of crystals lying flat on the (011) face (Figures 6.10c and 6.10d). Roughness measurements (Sa) across the 3 different slides (and 2 different areas per slide) show values ranging from 0.181 to 0.206 μm. Figure 6.11 shows maps of the extracted surface roughness for the 6 different areas studied. From these values, as well as the SEM observations, it can be concluded that the clay-film preparation method is robust and leads to a smooth and reproducible, low roughness clay-coated substrate, as required for contact angle measurements [24-26].

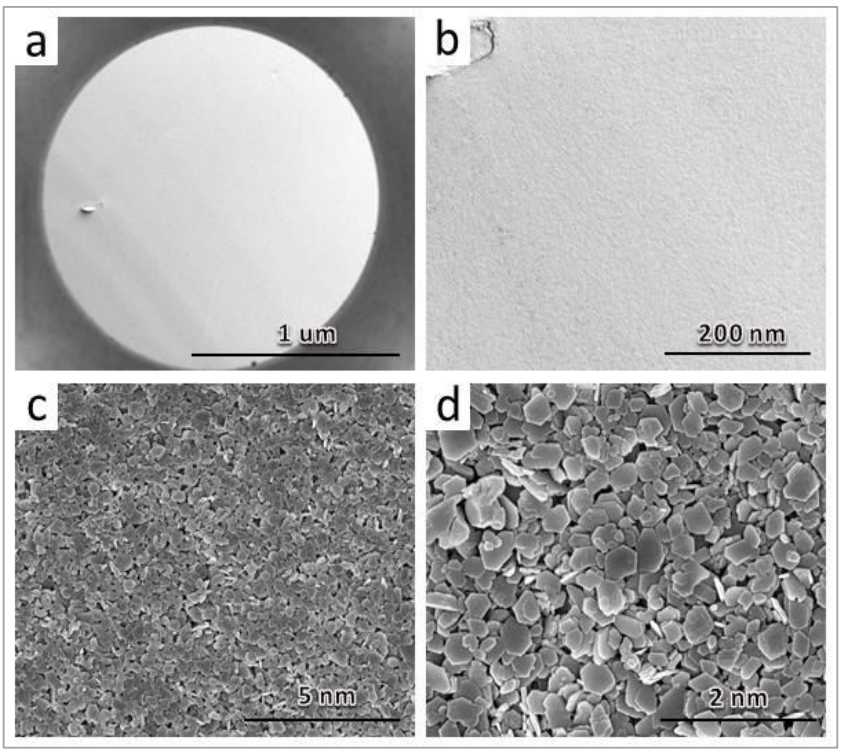

Figure 6.10 SEM micrographs of the clay film samples at various magnifications (a: x66, b: x493, c: x20000 and d: x50000).

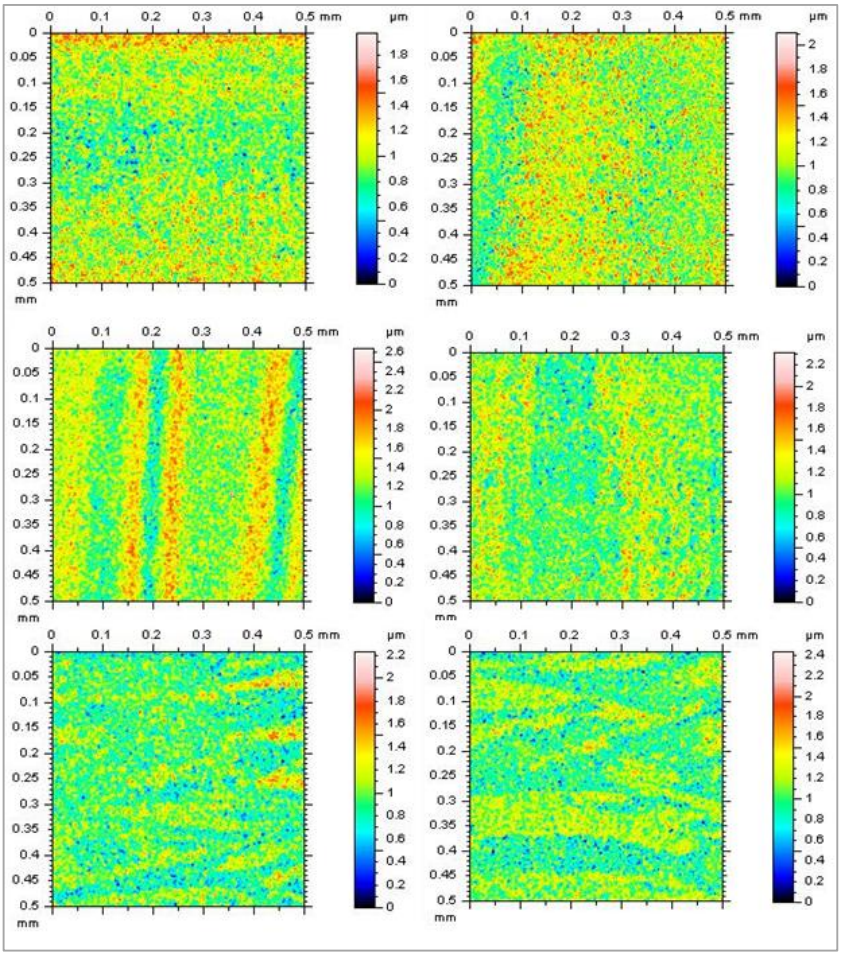

Figure 6.11 Extracted surface roughness measurements on the six random clay films.

6.3.3 Effect of concentration on oil droplet contact angles as measured on glass and kaolinite films

With the goal of observing the effect of brine concentration on the measured contact angle of oil droplets, a series of experiments were performed were the same droplets (located on the same spot on the surface) where measured whilst the solution concentration was changed. Solutions of both $CaCl_2$ and NaCl were tested with concentrations of 0.001, 0.01, 0.1, and 1 M at pH 6.5. The contact angle of oil droplets on a glass slide was observed to decrease from average values around 146° to 140° (moderately water-wet), when the concentration of $CaCl_2$ increased. On the contrary when the droplets were measured on NaCl, the average contact angle increased from 150 to 161° (significantly water-wet) with increasing concentration, as can be seen in Figure 6.12. For the kaolinite film, the average measured contact angle decreased from a value of 159°-153° (significantly water-wet) when in contact with $CaCl_2$ of increasing concentration (Figure 6.12). However, when measured on NaCl solutions, the contact angle was more stable varying only from 157° to 159° (significantly water-wet) (Figure 6.12). The observed variation in contact angle as the

solution concentration was varied must be due to a variation in the interfacial tension (or energy) on oil-solution and solid-solution interface, as the interfacial tension between the oil and solid should not be affected (as the oil droplet stays in the same position through the duration of the experiment). The relationship of the different interfacial tension on the measured contact is given by Young's equation:

$$\sigma_{sw} = \sigma_{os} + \sigma_{ow}\cos\theta \qquad \text{(Equation 6.2)}$$

Where σ_{os} is Interfacial tension (energy) between oil and solid (J/m_2); σ_{ws} is interfacial tension between water (brine) and solid (J/m_2); σ_{ow} is Interfacial tension between oil and water (brine) (J/m_2); θ is contact angle at the oil-brine and solid boundary (°). [34]. The interfacial tension of the water-solid interface is known to decrease as salt content increases [35] which would lead to an increase in the measured contact angle if this was the only parameter changing in the equation. However, the interfacial tension between oil and a solution is also known to increase significantly when the ionic strength of the solution increases [36]. The interplay between these two factors will lead to a small variation in the contact angle, than in our case is reflected by a small decrease. The most important conclusion of the measurements, however, is that the measured contact angle is not significantly affected by the change in solution concentration (ionic strength). Therefore any of the larger contact angle variations reported in the kaolinite-film experiments are due to additional factors.

The results also show that the glass slide tends to be more oil-wet than the kaolinite film when in the presence of a $CaCl_2$ solution, whereas both materials show the same wetting properties on the presence of NaCl (Figure 6.12). This result must be related to the specific effect on each cation type on determining the initial oil-surface interfacial tension. As the oil droplet is brought into contact after the slide has been immersed in the brine, the cations in it would have already interacted with the solid surface, and then they would also interact with the model oil mixture. The difference in contact angle between the glass slide and kaolinite fim (in the presence of $CaCl_2$) is probably related to the formation of a much larger amount of cation "bridges" between the glass and oil face than between the kaolinite crystals and oil. This is something to be expected when considering the relative amounts of Ca^{2+} that would bind to each type of surface, which in turn is related to the surface charge of each material. The surface charge of kaolinite would be slightly negative at the pH 6 of the brine solution, whereas that of the glass slide is expected to be at least twice as large [37]. Therefore more Ca^{2+} will be bound to the glass surface (to counter balance the charge)

and more cation bridges will form with the oil molecules, leading to a more oil-wet surface, as reflected in the contact angle measurements (Figure 6.12).

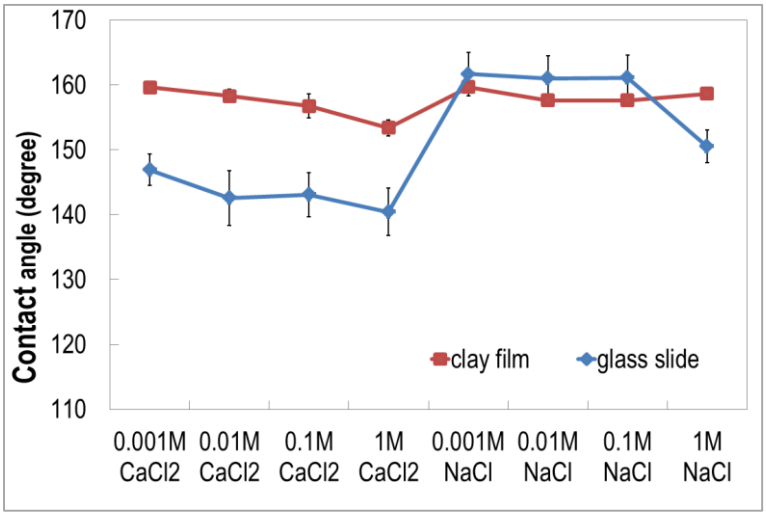

Figure 6.12 The effect of different brine on wettability of ideal materials (glass slide and kaolinite film).

6.3.4 Formation water / oil aging effect on contact angle

A series of contact angle measurements were taken on kaolinite films after they were aged on the initial brine (representative of formation water). As per Figure 6.3, the aging brines contained either $CaCl_2$ or NaCl with concentrations of 1, 0.01 or 0.001 M and pH values of 6.5 or 8. Contact angle measurements were taken by placing a drop of model oil over the kaolinite surface in the presence of a solution identical to that were the aging took place. A separate series of measurements were done over samples aged in the initial brine and the 1 M decanoic acid solution (Figure 6.3). In this case, the measurements were performed under a brine of equal composition as to that used for the initial aging.

Figure 6.13a shows contact angle values as a function of brine composition for the experiments aged in formation brine only. It can be seen in the Figure 6.13 that both pHs show different trends on contact angle variation as a function of concentration and cation identity. Films aged on $CaCl_2$, pH 6.5 solutions, show a small decrease in contact angle (3°) with an increase in concentration. However, films ages on NaCl, pH 6.5, solutions do not show any trend, with the variation in contact angle between different concentrations being relatively small (about 1 °, or less than 1%). The observed reduction of contact angle means that kaolinite is more-oil wet when the Ca^{2+} content in the formation water is the largest. This observation is consistent with previous studies on oil sorption in the presence of brine solutions performed on cores [38], and clay films [24]. Berg et al. reported that connate

water containing high concentrations of divalent cations of Ca^{2+} and Mg^{2+} is favourable condition for oil and clay binding [24]. Experiments performed at pH 8 show a different picture, as no discernible trend is observed in the contact angle measurements taken at different $CaCl_2$ concentrations, whereas there is an increase in contact angle as the concentration of NaCl is increased.

When comparing the contact angle measurements performed at the two different pHs, it can be seen that the measured contact angle in solutions with a pH 8 is consistently smaller (by 6 to 10°) than the values measured for similar solutions with the same composition but pH of 6.5°. This indicates that an increase in formation water pH leads to an increase in the oil-wetness of the kaolinite films. This result is in agreement with the adhesion measurements performed by Santha et al. over kaolinite surfaces using chemical force microscopy (Chapter 5) [39]. In addition, the results are consistent with the study done by Lebedeva and Fogden who found a decrease in oil-clay adhesion when the pH was decrease from 9 to 4 [22]. The influence of pH on the wettability of the clay surfaces may be explained by attending to the protonation state of the carboxylic acids. At pH 8 condition, the carboxylic groups on the model oil will be fully deprotonated into $-COO^-$ groups [40], and can strongly interact with the negatively charge of clay through cation bridging. On the contrary, at pH 6.5 a significant number of carboxylic groups will be protonated and therefore unable to interact with the clay surface via cation bridging.

For the experiments performed with double aging (initial brine and model oil), the variation in contact angle with brine chemical parameters shown a different behaviour (Figure 6.13b). At a first glance, it can be seen that the error bars for the measurements of this experiments were larger than what is shown in Figure 6.13a. This may reflect local variation in oil-sorption across the film that will increase the spread in the measured values across the three droplets studied per sample. For the experiments performed with pH 8 solutions, it can be seen that an increase in $CaCl_2$ concentration leads to a decrease in the measured contact angle, and therefore an increase in the oil-wetness of the sample (from significantly to moderately water-wet). On the contrary, no clear trend was observed on the samples initially aged in NaCl solutions, but they do show, in general a larger contact angle (are more water wet). This observation follows the results from chemical force microscopy experiments reported by Santha et al. were no clear trends in oil adhesion were observed on NaCl solutions [39].

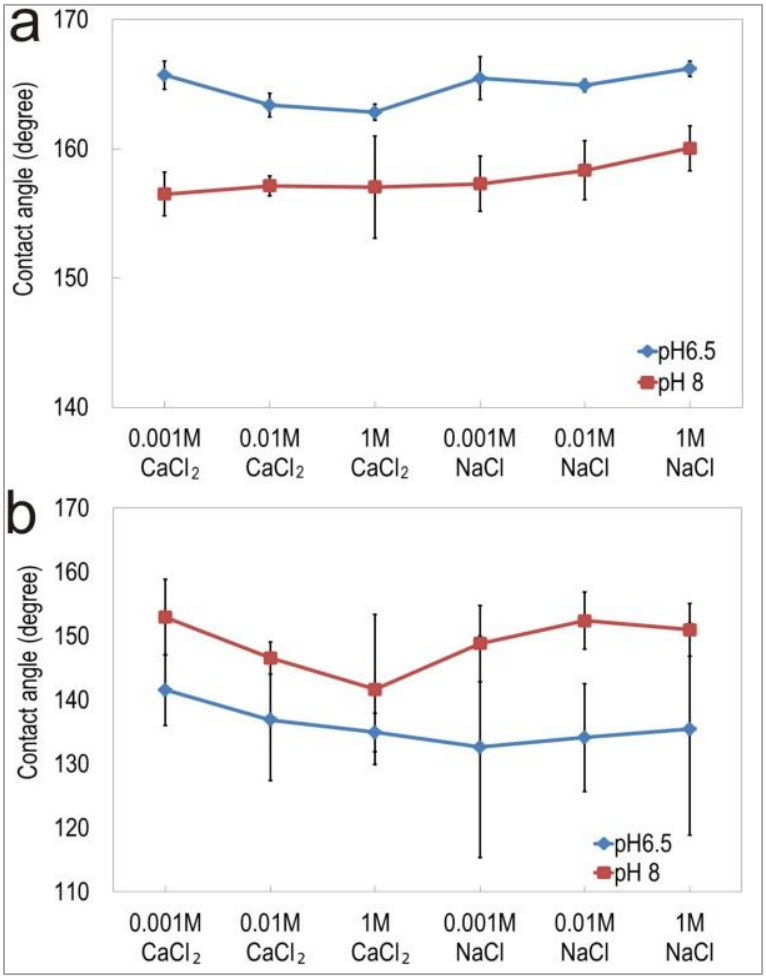

Figure 6.13 Wettability alterations on the kaolinite-coated substrate a) after initial aging; b) after initial brine and model oil aging.

For the experiments performed at pH 6.5 a similar trend is observed for the films aged in $CaCl_2$ where a decrease in contact angle was measured as the concentration increased. However, the samples aged in NaCl show this time a slight trend of increasing wetness with an increase in concentration, as opposed to the experiments performed on pH 8 solutions. Further insight onto the observed trends may be gaining from looking at the surface of films after aging on both types of solutions. Figure 6.14 shows SEM micrographs taken on films aged on $CaCl_2$ formation water only (Figures 6.14a and 6.14c) and those also aged on oil (Figure 6.14c and 6.14d). For those films aged only on brine the same overall particle distribution is observed irrespective of the type of cation of the concentration on which it was aged, however this is not the case for the films aged in oil. Figure 614b shows details of a kaolinite film aged on a 0.001 M $CaCl_2$ solution and model oil. The surface looks rather different than that shown in Figure 6.14a, where the film was aged only on a 0.001 M

$CaCl_2$.The oil-aged film shows a smoother surface, and is harder to visualize individual kaolinite grains. This may be indicative of the presence of an oil film. For those clay films aged in 1 M $CaCl_2$ the surface shows even less detail and what appears to be some sort of coating over the kaolinite crystals with a series of "cracks" running around some parts of the surface. Again, this probably reflects the formation of a layer of oil after aging, with this layer growing in thickness as the concentration of $CaCl_2$ in the initial aging brine is increased.

Finally, when comparing the contact angle values measured at pH 8 versus those at pH 6.5 is clear that the latter experiments show a consistently smaller contact angle (more oil-wet). This is in contrast to what was reported for the brine-only experiments, were oil wetness increased with pH. This behaviour may be explained by attending to oil-oil interactions rather than oil-mineral. As the films are taken from the oil-containing petri dish and introduced into the measuring cell (containing a brine), and also following the SEM observations (Figure 6.14) it can be assumed that an oil film is covering the clay-layer surface, in this case then the oil droplet placed over the surface to measure the contact angle will come into contact with this oil-film so the contact angle will be determined by oil-oil interactions. Shi et al. studied oil-oil interaction using Atomic Force Microscopy and observed that a decrease in pH led to a decrease in negative repulsive forces among droplets [41]. In addition the presence of Ca^{2+} ions was found to also lead to an increase in the coalescence of oil drop lets. Both results are in agreement with the contact angle measurements shown in this study.

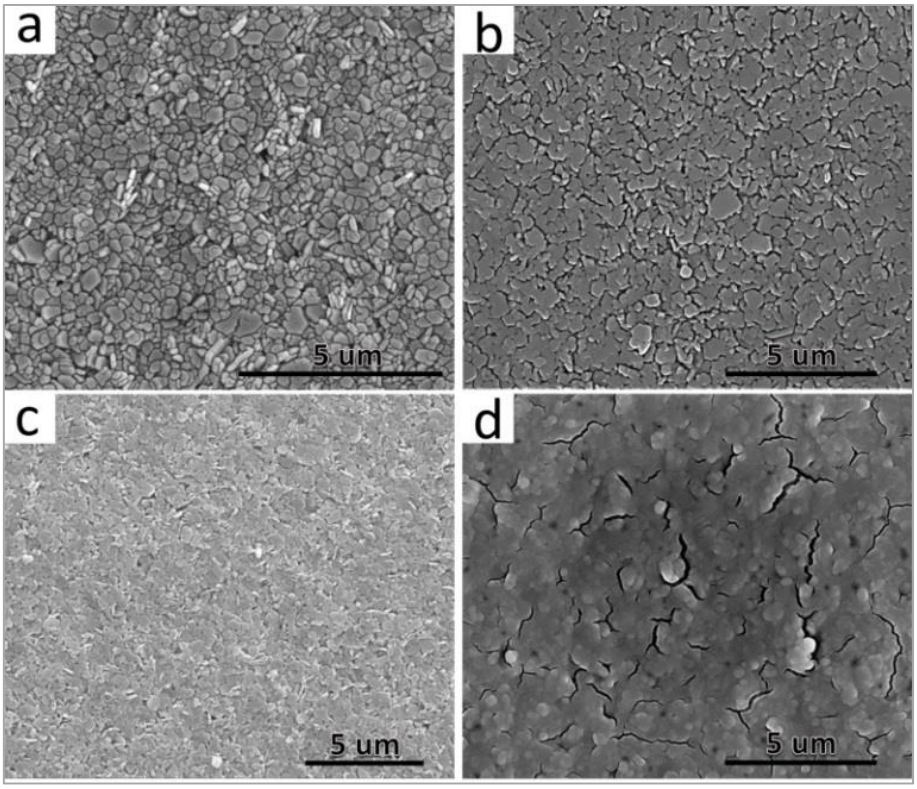

Figure 6.14 SEM micrographs of the aged clay film with different brines; a) aging in 0.001M of $CaCl_2$, b) aging in 0.001M of $CaCl_2$ and model oil, c)aging in 1M of $CaCl_2$, d) aging in 1M of $CaCl_2$ and model oil, e) aging in 0.001M of NaCl, f) aging in 0.001M of NaCl and model oil, g) aging in 1 M of NaCl, h) aging in 1M of NaCl and model oil.

6.3.5 Brine treatment effect on contact angle

After the kaolinite films were aged on initial brine and model oil, they were subsequently placed in a brine solution (of different composition and pH) for 24 h (Figure 6.3). Then, the contact angle of oil droplets placed on the kaolinite film were measured under the same brine composition. Below are the results of such measurements, separated by the composition of the initial/formation brine.

6.3.5.1 Initial brine: $CaCl_2$ pH 6.5

The measured contact angles for the samples aged on a $CaCl_2$ pH 6.5 brine, followed by oil aging and treatment with different brines shown in Figure 6.15. The first data point in all three graphs represent the value measured after the initial aging, and shows value ranging from 164°-166°(significantly water-wet), indicating water-wet behaviour. After oil aging, the measured contact angle decreased for all three initial brine compositions, to values ranging from 135°-142° (moderately water-wet), reflecting a change in wettability to a

more oil-wet state (these data points are the same as those displayed in Figure 6.13). After brine treatment the graphs show a somewhat different behavior but for all three initial brine composition, the wettability state changed clearly to more water-wet after the 24 h. brine treatment. For all three initial brine compositions, treatment with $CaCl_2$ solutions led to a similar behavior: treatment with 0.001M resulted in the largest increase in contact angle (when compared to the values measured after oil aging), whereas treatment with 1M led to the smallest increase (the total magnitude varied across experiments), with one experiment (sample initially aged in 0.01M $CaCl_2$) showing almost no increase in contact angle. In all cases, treatment with 0.01M solution lead to an intermediate value of contact angle increase, resulting on a linear trend of contact angle variation, as observed in the graphs in Figure 6.15. Overall, this means that 0.001M was the most effective concentration in changing the wettability of the kaolinite films to a more water-wet state. Treatment with NaCl solutions lead to a more varied behaviour across experiments, but in all cases resulted in an significant increase (15°-30°) in the measured contact angle (with respect to that measured on the oil-aged films). In most cases, as well, the increase in contact angle was larger than that measured for an equivalent $CaCl_2$ solution. For two of the initial brine compositions (0.001 and 1M) the largest increase in contact angle was produced by the lowest NaCl concentration in the treatment brine, whereas for the films aged in 0.01M $CaCl_2$ the largest increase occurred after treatment with a 0.01M NaCl solution. In any case, for each initial brine composition, the lowest increase in contact angle was observed when the samples were treated with 1M NaCl, but the total variation changed across experiments. Overall, 0.001M NaCl probed to be the most effective at changing the wettability state to more water-wet and 1M NaCl was the least effective.

6.3.5.2 Initial brine: NaCl pH 6.5

Figure 6.16 shows the measured contact angles for the samples aged on a NaCl pH 6.5 brine, followed by oil aging and treatment with different brines. The first data point in all three graphs represent the value measured after the initial aging, and shows value ranging from 165°-166° (significantly water-wet), indicating water-wet behaviour. After oil aging, the measured contact angle decreased for all three initial brine compositions, to values ranging from 132°-135° (moderately water-wet), reflecting a change in wettability to a more oil-wet state. The change in contact angle between the initial brine treatment and the oil aging was larger than on the experiments performed with $CaCl_2$, but the data shows a larger spread, as indicated in the error bars. Treatment of the kaolinite films with the different brines resulted in a large increase in contact angle (between 21° and 27°), i.e. on a change to a more water-wet state. In comparison with the kaolinite films aged in $CaCl_2$ (pH 6.5), the

brine treatment was more effective in modifying the wettability state (especially for the more concentrated brines).

Treatment with $CaCl_2$ showed similar trends to those observed on the films aged in $CaCl_2$ with the lower concentration (0.001M) resulting in the largest change in wettability (to a more water-wet state). Subsequently higher concentration led to a smaller increase in contact angle, with the 1M being the least effective in modifying the wettability state. Treatment with NaCl led, in all cases, to a significant increase in the measured contact angle. As with the previously discussed experiments, no clear trend of contact angle change with concentration was observed, with values varying across the treatment concentrations and initial aging concentration. Average contact angle values are, however, slightly larger than those measured after $CaCl_2$ treatment, especially at larger concentrations. This indicates that NaCl is, in general, more effective in changing the wettability state. This is relevant to the study of wettability alteration on silica face of kaolinite using molecule dynamics simulation [31].

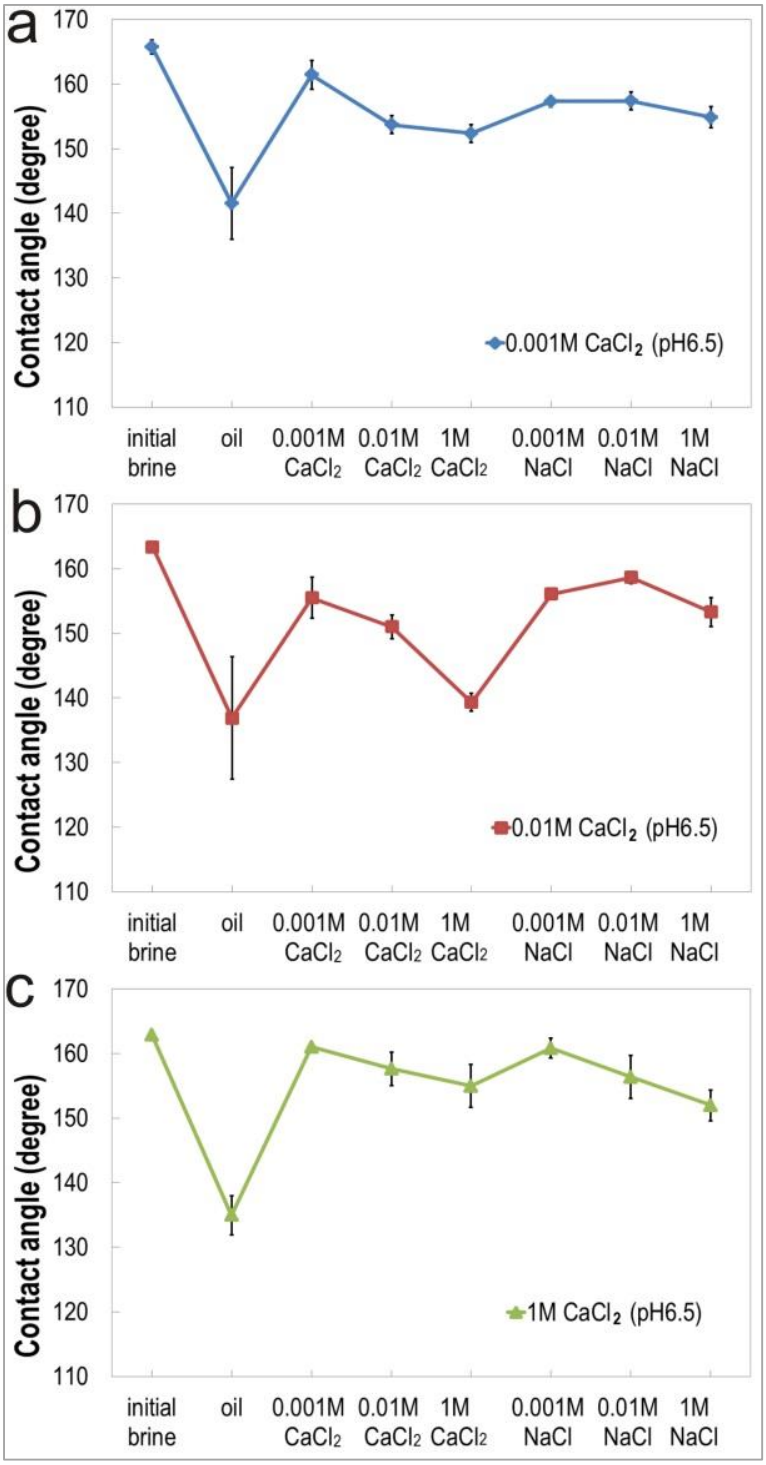

Figure 6.15 Graphs showing contact angle measurements on clay films, initially aged with $CaCl_2$ solutions (pH 6.5): a) 0.001M, b) 0.01M, c) 1M; and treated with six different brine composition (0.001, 0.01, 1 M of $CaCl_2$ and NaCl pH 6.5). Each data point represents a single experiment (unique kaolinite film).

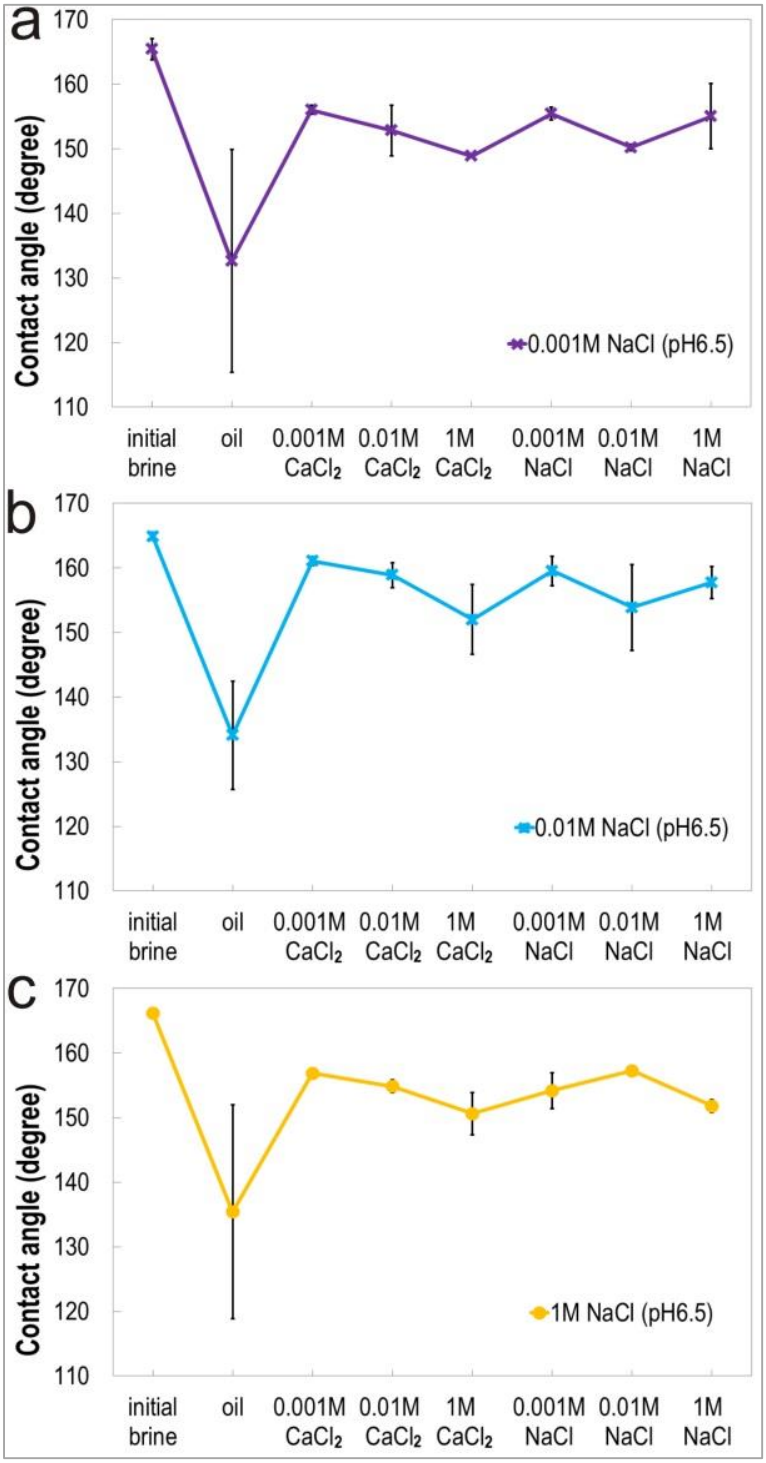

Figure 6.16 Graphs show in contact angle measurements on clay films, initially aged with NaCl solutions (pH 6.5): a) 0.001M, b) 0.01M, c) 1M, and treated with six different brine composition (0.001, 0.01, 1 M of $CaCl_2$ and NaCl pH 6.5). Each data point represents a single experiment (unique kaolinite film).

6.3.5.3 Initial brine: $CaCl_2$ pH 8

Figure 6.17 shows the measured contact angles for the samples aged on a $CaCl_2$ pH 8 brine, followed by oil aging and treatment with different brines. The experiments show similar trends as the two previously discussed cases, although, in this case, the initial measured contact angles (after the initial aging in brine) show values varying from 156°-157° (significantly water-wet), which are 5° to 9° less than what was measured on the experiments aged in $CaCl_2$ and pH of 6.5. In addition, although the oil-aging led also to a decrease in the measured contact angle (i.e. it led to more oil-wet conditions), the decrease was always smaller than on the previously discussed experiments (132°- 141°), with values varying between 141°-152° (moderately water-wet). Treatment with the $CaCl_2$ and NaCl brines led, in general, to an increase in the contact angle, but trends across samples aged with different brine concentrations were more varied than in previous experiments. In great part, differences across experiments were due to the fact that the contact angle after oil again did not decrease as much as in the pH 6.5 experiments. This was the case, in particular for the films aged in 0.001M and 0.01M $CaCl_2$ solutions. Treatment with brines on these experiments leads in general to an increase in the contact angle, but in some occasions the measured angle was smaller. The experiment performed with 1M $CaCl_2$ did not exhibit this behaviour, although the spread on the contact angle measurements after oil-aging is relatively high, as evidenced by the error bars in the graph (Figure 17c). This set of experimental results was slightly limited in the interpretation, due to no different effects of salinity treatment. It is possible that the results are primarily controlled by the loss of oil deposited in the 24 hour period, irrespective of the aqueous fluids used in the treatment. This could be improved for the further studies by extension of oil-aging time.

Treatment with the different solutions led, again, to similar trends as observed in the pH 6.5 experiments. Treatment with 0.001M $CaCl_2$ led to an increase in the contact angle (more water-wet state). As the concentration of the treatment brine decrease so it did the measured contact angle, in some cases, reaching values lower than those measured on the oil-aged films, as mentioned before. Treatment with NaCl resulted in a similar trend, with the largest contact angles measured on films treated with the lower concentration of NaCl brines. However, only on the films ages with a 0.01M $CaCl_2$ brine did the treatment with NaCl lead to consistently higher contact angles than when the sample was treated with $CaCl_2$. For the other two aging concentrations, $CaCl_2$ was, in general, more effective in moving the wettability state to a more water-wet condition.

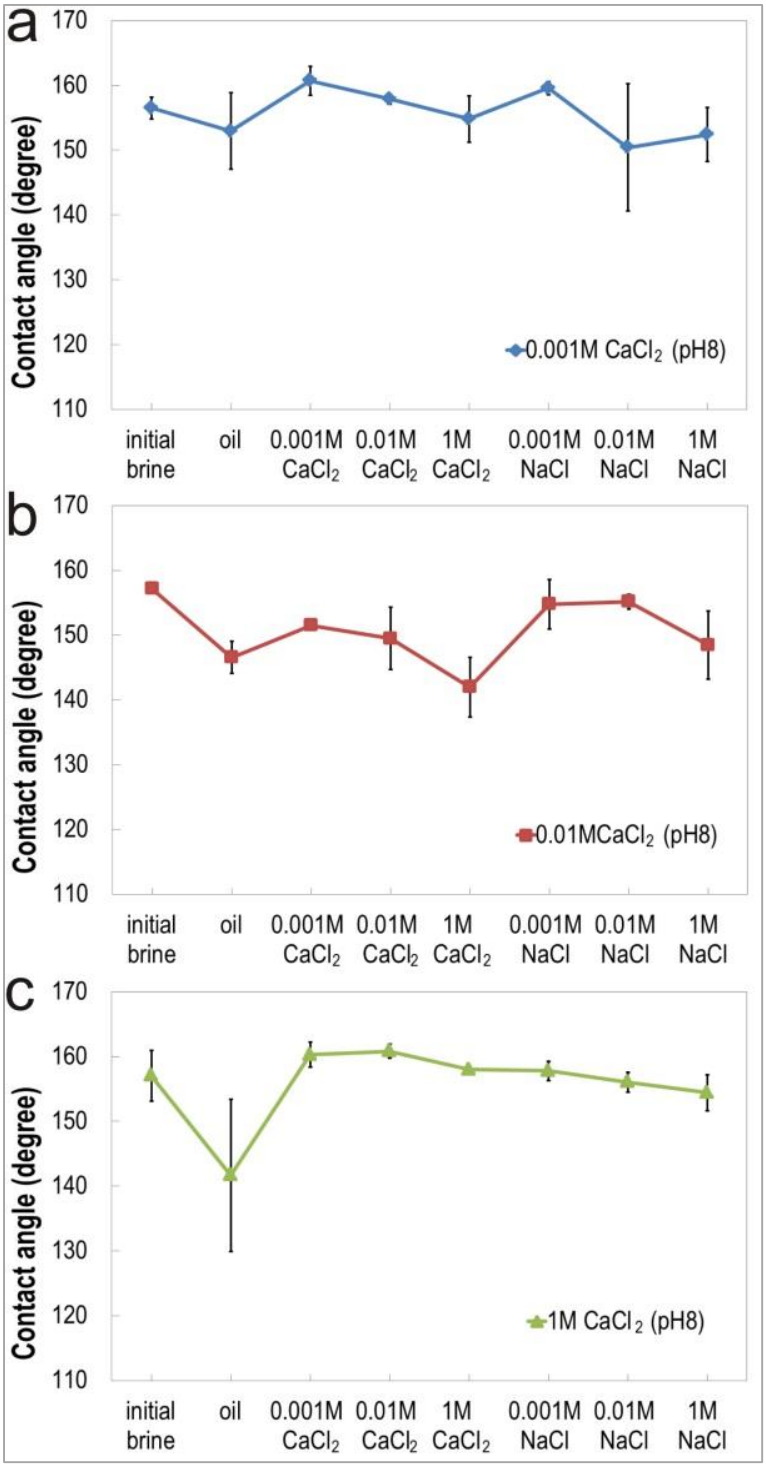

Figure 6.17 Graphs showing contact angle measurements on clay films, initially aged with $CaCl_2$ solutions (pH 8):a) 0.001M, b) 0.01M, c) 1M; and treated with six different brine composition (0.001, 0.01, 1 M of $CaCl_2$ and NaCl pH 6.5). Each data point represents a single experiment (unique kaolinite film).

6.3.5.4 Initial brine: NaCl pH 8

The measured contact angles for the samples aged on a NaCl pH 8 brine, followed by oil aging and treatment with different brines as shown in Figure 6.18. The initial measured contact angles (after the initial aging in brine) show values varying from 157°-158° (significantly water-wet), which are similar to those recorded with the pH 8 $CaCl_2$ brine, but still smaller to those observed when the aging brine had a pH of 6.5. Following aging with oil, contact angles decreased to values ranging from 149° to 152° (moderately water-wet), indicating a more oil-wet state. This decrease was similar to that observed in the experiments performed with $CaCl_2$ with the same pH but significantly smaller than that observed for the pH 6.5 aging. Treatment with $CaCl_2$ brine resulted in similar trends to those reported on the previous sections, but in this case, all three experimental series showed lower contact angles when the concentration of the treatment brine was 1M $CaCl_2$. It was only the 0.001M concentration that showed a significant increase in contact angle. All three experiments showed a linear decrease in contact angle with increasing $CaCl_2$ concentrations. NaCl treatment resulted, in general, in higher contact angle, when compared to $CaCl_2$ of the same concentration. In general, no clear trend was observed in contact angle evolution when the NaCl was increased, but smaller concentration tended to lead to larger contact angles. Therefore, it can be said NaCl was better in inducing a change in the wettability state of the kaolinite films.

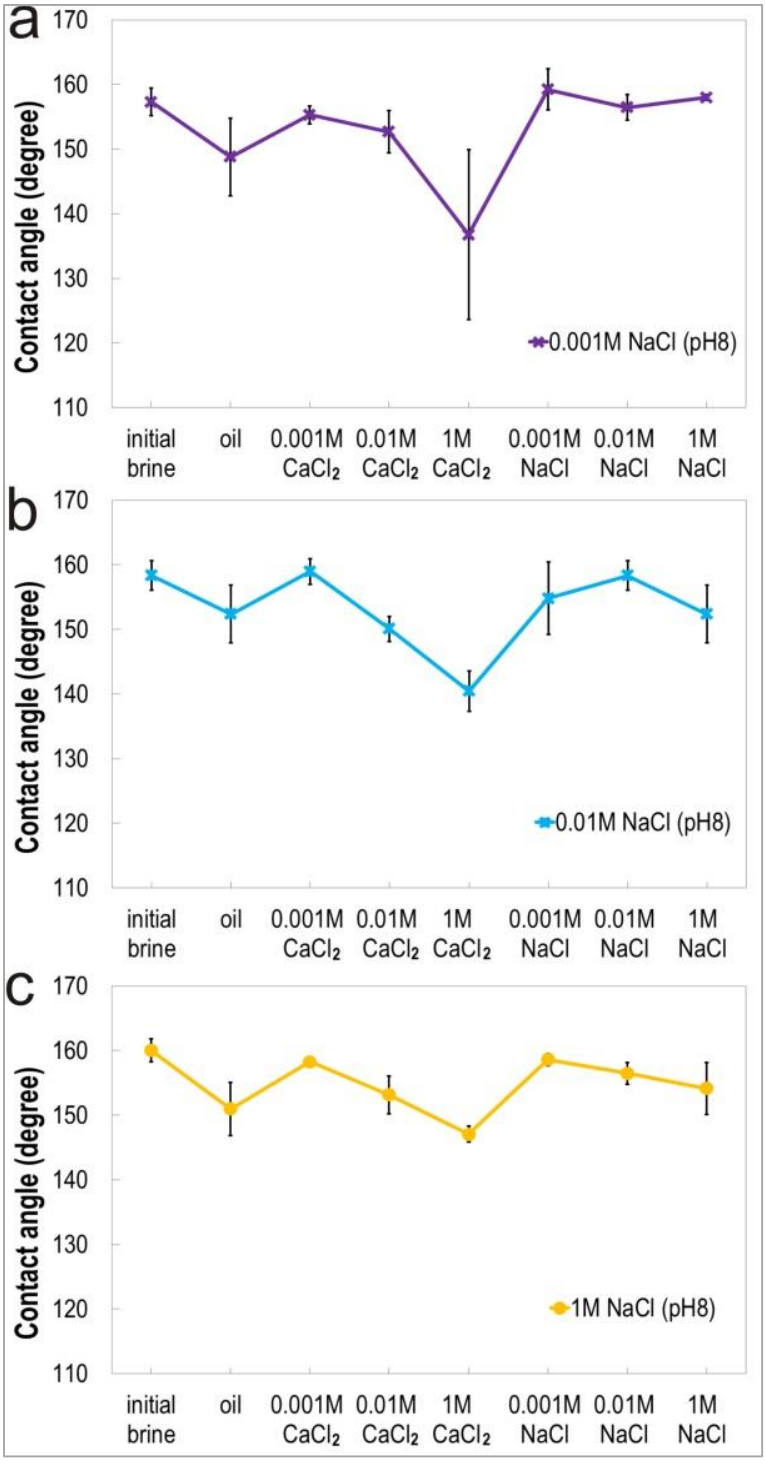

Figure 6.18 Graphs showing contact angle measurements on clay films, initially aged with $CaCl_2$ solutions (pH 8); a) 0.001M, b) 0.01M, c) 1M; and treated with six different brine composition (0.001, 0.01, 1 M of $CaCl_2$ and NaCl pH 6.5). Each data point represents a single experiment (unique kaolinite film).

6.3.5.5 Brine treatment effect on contact angle: pH

Figure 6.19 shows 4 plots of all the different experiments performed and grouped according to pH and cation identity. Summarizing the results from all experimental runs, it can be said that, similar trends were observed across experiments with the same aging and treatment pH. When this was 6.5 almost every brine treatment resulted in an increase in the contact angle measured (more water-wet). When using $CaCl_2$, a clear relationship between the increase in contact angle and concentration was observed, with the lowest $CaCl_2$ concentration (0.001M) always inducing the greater change in wettability and the higher concentration (1M) always results in the smaller change. NaCl treatment showed varying trends but in general tended to produce larger increases in contact angle than the corresponding $CaCl_2$ concentration (except for some experiments where the lower $CaCl_2$ concentration was slightly more effective). For the experiments performed at pH 8 the trends observed were similar across the experimental series, but varied, with respect to the pH 6.5 experiments, in one significant way. In all the experiments a decrease in the contact radius was observed after oil aging, but this decrease was significantly smaller at pH 8 than on the experiments performed with pH 6.5 solutions (Figure 6.19). Treatment with brine resulted in an increase in the contact angle, into a more water-wet state, but only for the lower concentration solutions (for both $CaCl_2$ and NaCl). For higher concentrations of the treatment brine, particularly for $CaCl_2$, the contact angle decreased below the measured value after oil-aging on 4 of the 6 experiments (Figures 6.17 and 6.18 and 6.19). This behavior was not observed on the experiments performed with pH 6.5 solutions, where the contact angle was always higher after brine treatment. As indicated below, this behavior may be explained by looking at the differences between oil-oil and clay-oil interactions. At the same time, the same overall trend was observed with respect to the change in contact angle with $CaCl_2$ concentration. In all cases, a continuous decrease in contact angle was observed. For NaCl, no clear trend was observed across experiments, as was the case in the pH 6.5 tests, but, in general, the final wettability state tended to be more water-wet than a comparable value obtained with the same concentration (and pH) of $CaCl_2$ brine.

The observed discrepancies in behavior between the experiments performed at different pHs can be explained by attending at the differences in behavior between oil-oil and clay-oil interactions. As was explained above (Section 6.3.4), the differences in the measured contact angle between the two studied pHs are probably due to its control by oil-oil interactions. Shi et al. established that low pHs lead to stronger oil to oil interactions, as well as the presence of Ca^{2+} ions in the water film separating oil droplets. As the contact angle is measured by placing a droplet of oil over the clay film covered in oil, oil to oil interaction across the brine film (on which the sample is immersed) will play an important

role in determining the contact angle. As such, it can be expected that lower contact angles from significantly to moderately water-wet (more oil-wet) will occur at low pH conditions where oil to oil interactions are enhanced and higher values at higher pH. However, once the kaolinite films have been treated with a brine for a full day, it can be expected that a relatively larger amount of unbound (to the clay surfaces) will be lost, therefore, the subsequent contact angle measurements will be reflective of mostly oil to clay interactions (between the clay film and the oil droplet). On these conditions, it can be expected that increases in pH will lead to a higher adhesion of oil to the clay surfaces as has been observed by other authors [39]. An increase in adhesion will also be expected from an increase in the Ca^{2+} concentration [6, 7, 38, 39]. This would then explain why the measured contact angles will be smaller at the higher after treatment with the higher Ca^{2+} concentrations than after gaining in oil.

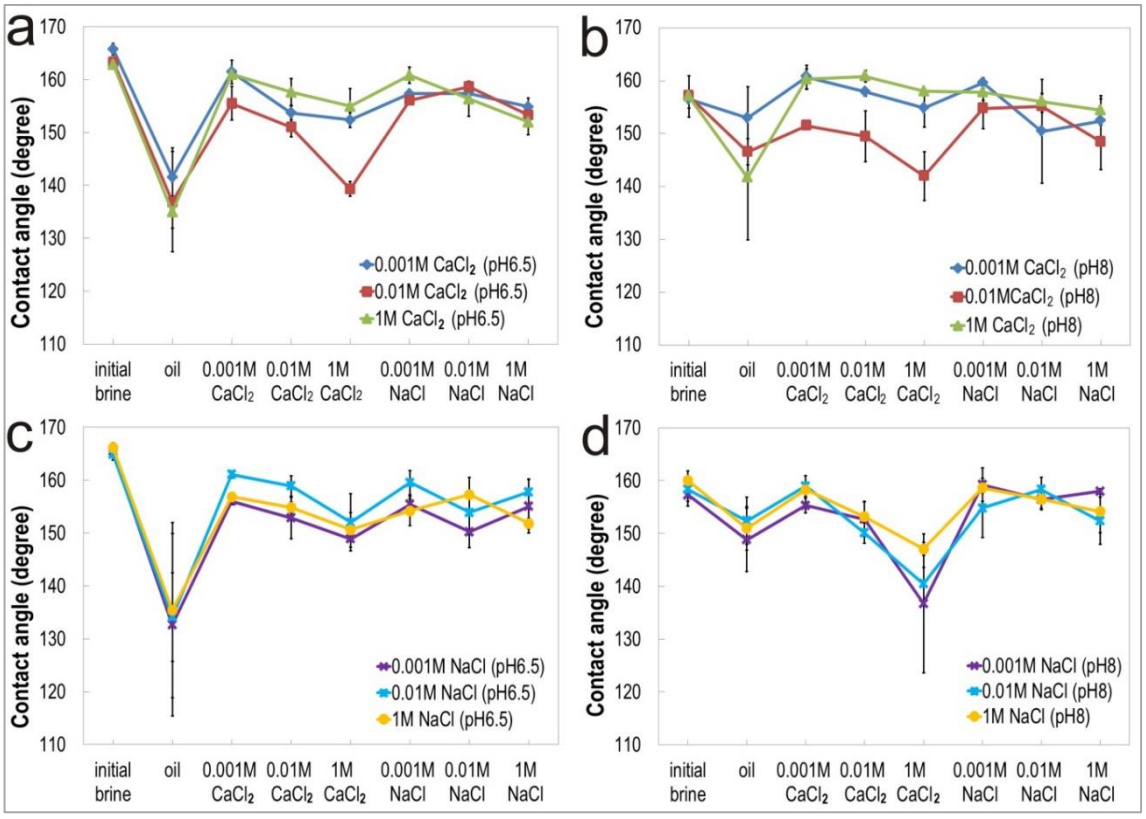

Figure 6.19 Graph comparing the contact angle alteration on brine washing between pH 6.5 (a and c); pH 8 (b and d).

6.3.6 The study of wettability by ESEM

Prior to performing the ESEM measurement, the kaolinite-coated Berea sandstone chips were observed using conventional SEM. Figure 6.20 shows the comparison between SEM images of kaolinite-coated and uncoated samples. Low resolution images showed a non-

uniform deposition of kaolinite over the sandstone surface (Figure 6.20a). In the areas where a kaolinite film could be observed, it showed a rather smooth upper layer, with kaolinite crystals showing a high degree of preferential orientation on their flat faces (Figure 6.20c). The sizes of these smooth kaolinite films reached values of more than 100 x 100 μm^2, which made them of a large enough size to perform water condensation experiments on the ESEM.

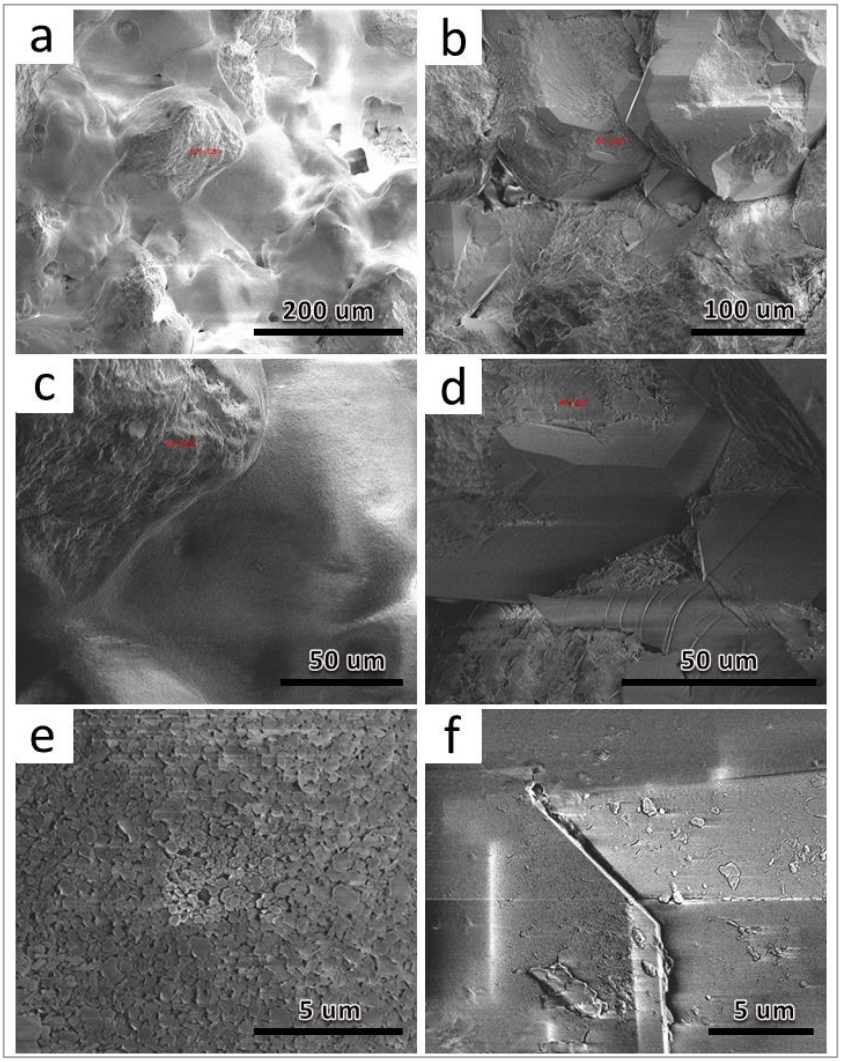

Figure 6.20 Representative SEM photomicrographs of kaolinite-coated Berea sandstone (a, c, e) and non-coated Berea sandstone (b, d, f).

6.3.6.1 Aging brine effect on the wettability

Prior to the ESEM measurements, the kaolinite-coated Berea sandstone chips were aged in either, 1M $CaCl_2$ or 1 M NaCl solutions. After this they were aged in the model oil mixture. After this, the majority of samples were "washed" with brines, but a few were scanned after oil aging to determine their wettability. Figure 6.21 shows a time series of ESEM images of

two such samples (one aged with $CaCl_2$, the other with NaCl), taken during the water condensation process. For either sample no formation of actual water droplets over the surface was observed. Instead, "creeping" of a thin water film can be deduced to occur from the gradual loss of "sharpness" on the images. This would indicate a relatively high degree of water-wetness on both samples at this stage, although the lack of droplets makes it impossible to be more precise.

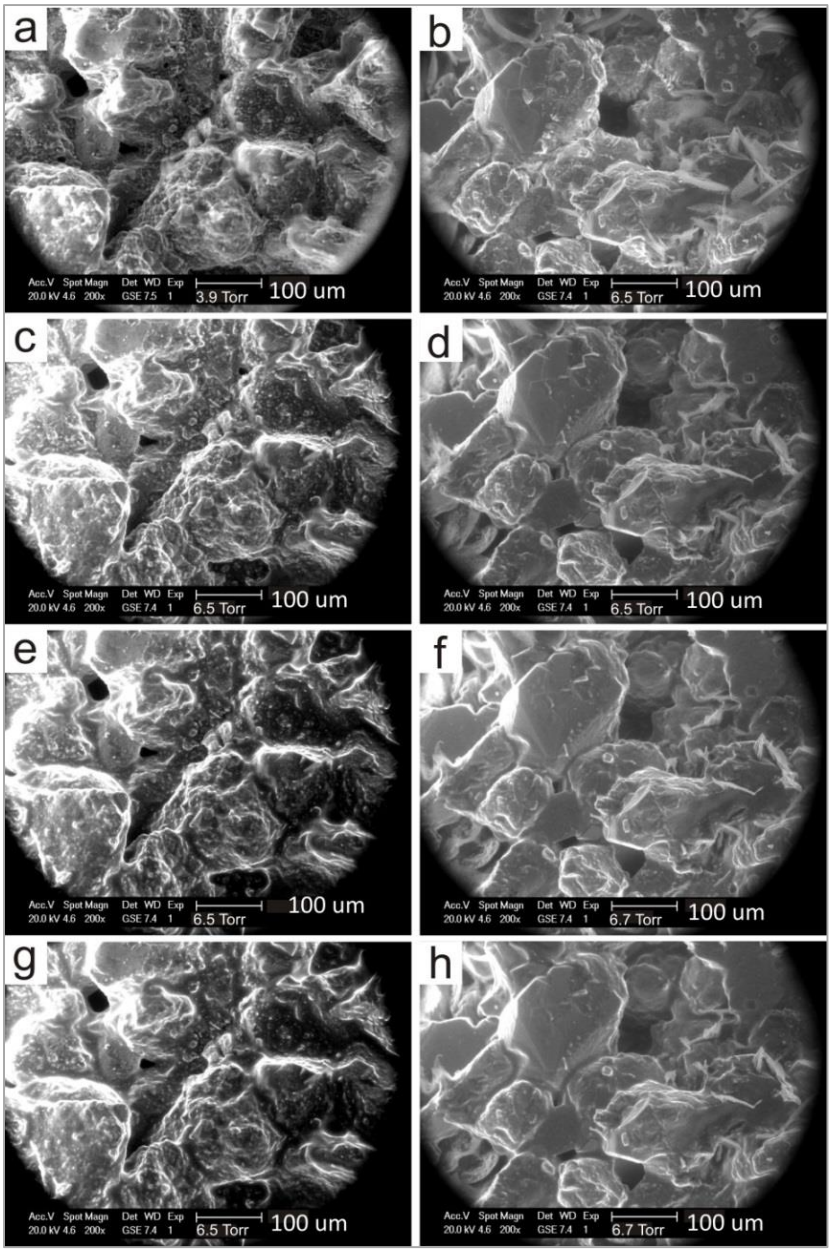

Figure 6.21 Time sequence of ESEM micrographs of kaolinite-coated Berea sandstone aged in variation of initial brine 1M of $CaCl_2$ (a, c, e, g) and 1M of NaCl (b, d, f, h) at pH 6.5.

6.3.6.2 Brine treatment effect on the wettability

A number of rock chips were "treated" with 0.001 M or 1 M brines of $CaCl_2$in order to observe a possible low salinity effect. Rock chips were removed from the vial containing the brine and quickly washed with a small amount of water, then left to dry in open air for 15 min. Figure 6.22 shows a time-series of ESEM images taken during the water condensation process on samples aged with 1M $CaCl_2$ and oil. For the samples treated with 1M $CaCl_2$ the development of a water film "creeping" into the sample can be seen after the pressure chamber 6.5 Torr (Figure 6.22c). Further images show the film "raising" up until almost completely covering the whole scanned area (Figure 6.22g), with only a few "patches" of sample left exposed (and even this appear to have some water, due to their "blurred" appearance. As was the case with non-washed samples (Figure 6.21) no individual water droplets were observed, but in this case, the water film developed over the surface was very significant, indicating probably an increase in the water wetness of the sample after treatment with the brine. For the sample treated with the 0.001M CaCl2 solution, ESEM pictures indicate a slightly different picture. In this case, an increase in the pressure up to 6.5 Torr did not led to the formation of a film of water (Figure 6.22d). This was only started to be visible after the pressure reached 6.6 Torr, and after a few minutes the surface got completely covered in a film of water (Figure 6.22h). Unfortunately, since the increase of the pressure was performed manually, it was not possible to compare the rate of advancement of the water film between the two types of samples, however the observed behaviour indicates a similar degree of water-wetness of the treated sample. The fact that both "washed" samples appear to be more water-wet than the oil treated sample, conforms with the contact angle measurements reported on the previous sections, where oil-aged samples always showed a lower contact angle compared to the "washed" or treated sampled.

A similar set of observations were carried out on the sample aged with 1M of NaCl (and model oil) and treated with either 1M of $CaCl_2$ or 0.001 M of $CaCl_2$ pH6.5. A time-series of ESEM micrographs for these experiments are shown on Figure 6.23. In this case, both samples show a very similar behaviour, with a change in the surface features starting after 6.3 and 6.5 Torr, indicating the formation of a water film over the sample (Figures 6.23c and 6.23d). Further images show the increase in size of the water film until reaching the point of almost completely covering the initial sandstone surface. As with all previous experiments, no development of individual droplets over the substrate was observed. However, the formation of the continuous water film indicated that the surface is rather water-wet. Unfortunately, results from the ESEM study were not conclusive, as none of the samples showed the development of individual droplets over which contact angle

measurements could have been taken. This may be because, in fact, the difference in wettability between the different samples was not as large as to be able to be observed with this technique or perhaps the kaolinite coating was too porous to allow for the development of droplets. Due to time and budgetary constraints, it was not possible to further explore the use of ESEM on kaolinite films.

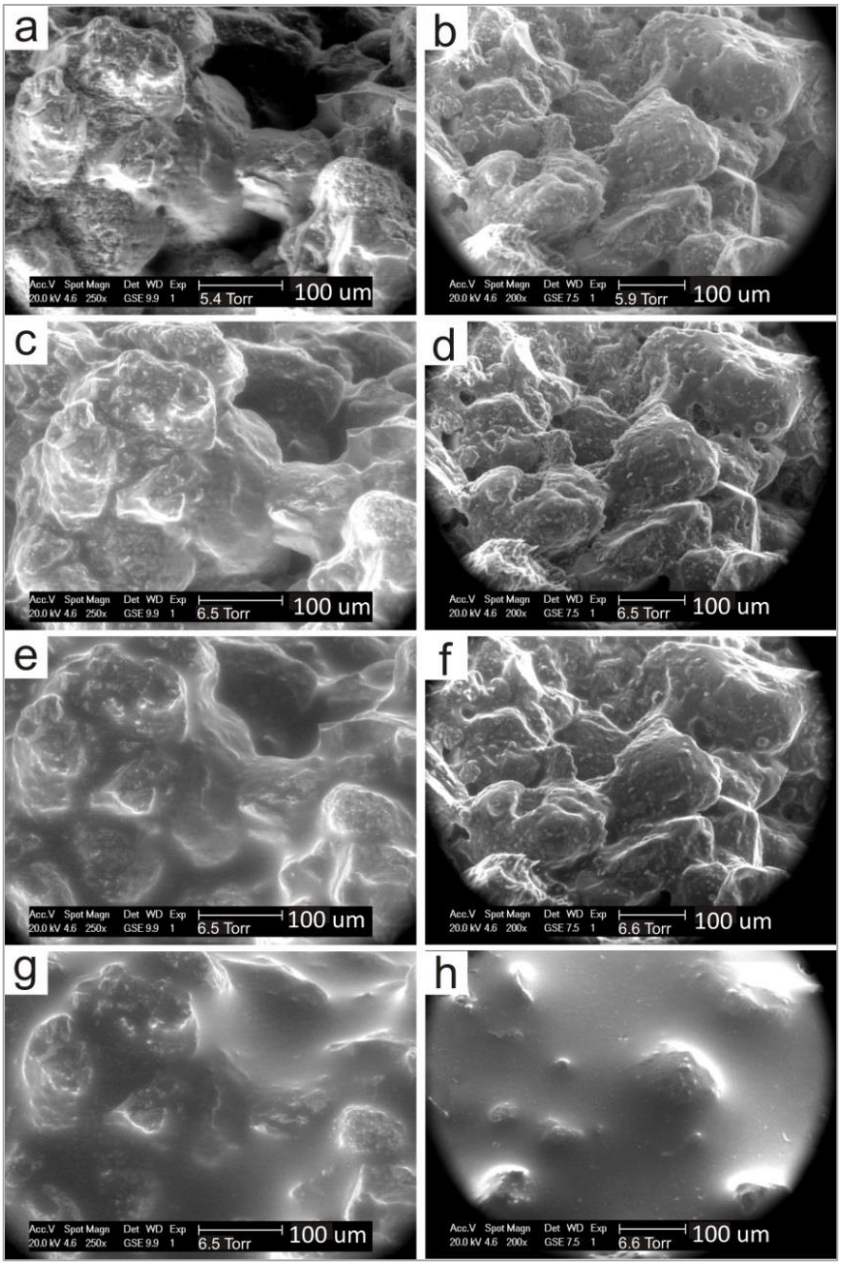

Figure 6.22 Time series of ESEM micrographs taken during the water condensation process (as evidenced by the increase in pressure inside the chamber) kaolinite-coated Berea sandstone aged in 1M of $CaCl_2$ at pH 6.5, and treated by 1 M (a,c,e,g) and 0.001M $CaCl_2$ (b, d, f, h) brines at pH 6.5.

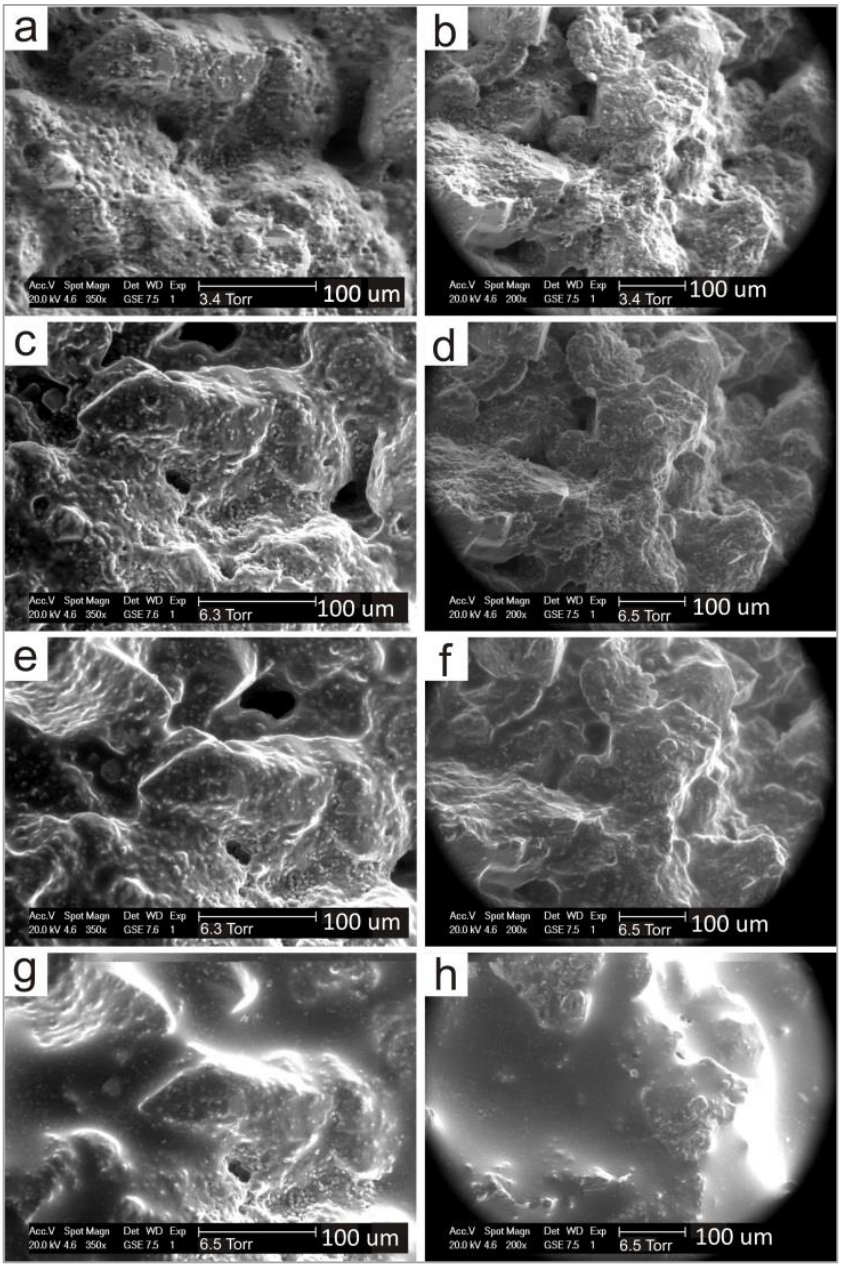

Figure 6.23 Time series of ESEM micrographs taken during the water condensation process (as evidenced by the increase in pressure inside the chamber)kaolinite-coated Berea sandstone aged in 1M of NaCl at pH 6.5, and treated by 1 M (a,c,e,g) and 0.001M $CaCl_2$ (b, d, f, h) brines at pH 6.5.

6.4 Conclusions

Results from the experiments discussed in this paper show that:

1) The best experimental parameters for kaolinite film preparation are 1% w/w concentration, 16 min of sonication time and charged-attachment and drying.
2) The wettability alteration of clay film treatment is ranged into moderately to significantly water-wet.
3) Formation water's pH has an important effect on determining the wettability state of kaolinite surfaces after aging in oil, with lower pHs (6.5) leading to a more oil-wet state than higher (pH 8) values. This is because; the contact angle after oil aging is determined mostly through oil-oil interactions (in the presence of a brine phase) and at therefore lower pH reduces the repulsion between the oil film and the oil droplet.
4) Cation identity (Na^+ *vs.* Ca^{2+}) and concentration is less important in determining oil absorption (after aging) than pH, with very small differences observed when the pH was the same.
5) A combination of the treatment/washing brine (post oil aging) pH and concentration is crucial in determining the wettability of oil-aged kaolinite surfaces. Films treated with brines at pH 6.5 showed a marked increase in contact angle (water wetness) across all Ca^{2+} (or Na^+) concentrations. For those films treated with brines at pH 8, only solutions with concentrations of 0.01M or smaller, led to increase in the contact angle of the kaolinite surfaces. Higher Ca^{2+} (and in some cases, Na^+) concentrations actually led to an increase in the contact angle, this is because oil-clay interactions prevail at the conditions operating during the brine treatment and therefore a higher pH leads to higher oil adsorption over kaolinite.
6) For all experiments, the measured contact angle showed an inverse relationship with Ca^{2+} concentration, whereby higher more Ca^{2+} in solution led to lower contact angles which reflects from significantly to moderately water-wet (more oil-wet surfaces).
7) Variation of the Na^+ concentration on treatment brines led to no discernible trends with respect to the contact angle variation, but in general, the measured contact angle tended to be larger than the corresponding value measured on the same Ca^{2+} concentration and also tended to be larger the smaller the Na^+ concentration. These results confirm that using low Ca^{2+} concentration during EOR operations would lead to a change of the clay minerals in the formation to a more water-wet state, and therefore to an increase in oil recovery.

8) The study by ESEM on the kaolinite-coated Berea sandstone was limited but results seem to indicate an increase in water-wetness after sample treatment with brines.

6.5 References

[1] M.D. Jackson, J. Vinogradov, G. Hamon, M. Chamerois, Evidence, mechanisms and improved understanding of controlled salinity waterflooding part 1: Sandstones, Fuel 185 (2016) 772-793.

[2] J.J. Sheng, Critical review of low-salinity waterflooding, Journal of Petroleum Science and Engineering 120(0) (2014) 216-224.

[3] V. Alvarado, E. Manrique, Enhanced oil recovery: an update review, Energies 3(9) (2010) 1529-1575.

[4] G.-Q. Tang, N.R. Morrow, Influence of brine composition and fines migration on crude oil/brine/rock interactions and oil recovery, Journal of Petroleum Science and Engineering 24(204) (1999) 99-111.

[5] B. Suijkerbuijk, J. Hofman, D.J. Ligthelm, J. Romanuka, N. Brussee, H. van der Linde, F. Marcelis, Fundamental investigations into wettability and low salinity flooding by parameter isolation, SPE Improved Oil Recovery Symposium, Society of Petroleum Engineers, 2012.

[6] A. Lager, K.J. Webb, C.J.J. Black, M. Singleton, K.S. Sorbie, Low Salinity Oil Recovery - An Experimental Investigation1, Petrophysics 49(01) (2008) 8.

[7] D.J. Ligthelm, J. Gronsveld, J. Hofman, N. Brussee, F. Marcelis, H. van der Linde, Novel Waterflooding Strategy By Manipulation Of Injection Brine Composition, EUROPEC/EAGE Conference and Exhibition, Society of Petroleum Engineers, Amsterdam, The Netherlands, 2009.

[8] A. Lager, K.J. Webb, I.R. Collins, D.M. Richmond, LoSal Enhanced Oil Recovery: Evidence of Enhanced Oil Recovery at the Reservoir Scale, Society of Petroleum Engineers, 2008.

[9] T. Austad, A. RezaeiDoust, T. Puntervold, Chemical mechanism of low salinity water flooding in sandstone reservoirs, SPE improved oil recovery symposium, Society of Petroleum Engineers, 2010.

[10] Y. Zhang, N.R. Morrow, Comparison of Secondary and Tertiary Recovery With Change in Injection Brine Composition for Crude-Oil/Sandstone Combinations, SPE/DOE Symposium on Improved Oil Recovery, Society of Petroleum Engineers, Tulsa, Oklahoma, USA, 2006.

[11] P. Jadhunandan, N.R. Morrow, Effect of wettability on waterflood recovery for crude-oil/brine/rock systems, SPE reservoir engineering 10(01) (1995) 40-46.

[12] H.O. Yildiz, N.R. Morrow, Effect of brine composition on recovery of Moutray crude oil by waterflooding, Journal of Petroleum science and Engineering 14(3-4) (1996) 159-168.

[13] R. Zhang, N. Qin, L. Peng, K. Tang, Z. Ye, Wettability alteration by trimeric cationic surfactant at water-wet/oil-wet mica mineral surfaces, Applied Surface Science 258(20) (2012) 7943-7949.

[14] J. Yang, Z. Dong, M. Dong, Z. Yang, M. Lin, J. Zhang, C. Chen, Wettability alteration during low-salinity waterflooding and the relevance of divalent ions in this process, Energy & Fuels 30(1) (2015) 72-79.

[15] H. Yildiz, M. Valat, N. Morrow, Effect of brine composition on wettability and oil recovery of a Prudhoe Bay crude oil, Journal of Canadian Petroleum Technology 38(01) (1999).

[16] H. Mahani, S. Berg, D. Ilic, W.-B. Bartels, V. Joekar-Niasar, Kinetics of low-salinity-flooding effect, SPE-169143-PA 20(01) (2015) 8-20.

[17] Y. Chang, K. Mohanty, D. Huang, M. Honarpour, The impact of wettability and core-scale heterogeneities on relative permeability, Journal of Petroleum Science and Engineering 18(1-2) (1997) 1-19.

[18] M. Wilson, L. Wilson, I. Patey, The influence of individual clay minerals on formation damage of reservoir sandstones: a critical review with some new insights, Clay Minerals 49(2) (2014) 147-164.

[19] N. Hancock, A. Taylor, Clay mineral diagenesis and oil migration in the Middle Jurassic Brent Sand Formation, Journal of the Geological Society 135(1) (1978) 69-72.

[20] Ø. Marcussen, T.E. Maast, N.H. Mondol, J. Jahren, K. Bjørlykke, Changes in physical properties of a reservoir sandstone as a function of burial depth–The Etive Formation, northern North Sea, Marine and Petroleum Geology 27(8) (2010) 1725-1735.

[21] K. Bjørlykke, Relationships between depositional environments, burial history and rock properties. Some principal aspects of diagenetic process in sedimentary basins, Sedimentary Geology 301 (2014) 1-14.

[22] E.V. Lebedeva, A. Fogden, Adhesion of oil to kaolinite in water, Environ. Sci. Technol. 44(24) (2010) 9470-9475.

[23] E.V. Lebedeva, A. Fogden, Wettability alteration of kaolinite exposed to crude oil in salt solutions, Colloids Surf. Physicochem. Eng. Aspects 377(1-3) (2011) 115-122.

[24] S. Berg, A.W. Cense, E. Jansen, K. Bakker, Direct Experimental Evidence of Wettability Modification By Low Salinity, Petrophysics 51(05) (2010) 9.

[25] L. Scriven, Physics and applications of dip coating and spin coating, MRS Online Proceedings Library Archive 121 (1988).

[26] J. Buckman, A. Todd, P. Hill, Observations on Reservoir Rock Wettability Using an Environmental SEM, Microscopy and Analysis (2000) 35-38.

[27] M.A. Al-Shafei, T.M. Okasha, Wettability studies at the pore level of Saudi Aramco reservoirs, SPE Saudi Arabia Section Technical Symposium, Society of Petroleum Engineers, 2009.

[28] E.J. Polson, J.O. Buckman, D.G. Bowen, A.C. Todd, M.M. Gow, S.J. Cuthbert, An environmental-scanning-electron-microscope investigation into the effect of biofilm on the wettability of quartz, Spe J 15(01) (2010) 223-227.

[29] J.S. Buckley, Microscopic investigation of the onset of asphaltene precipitation, Fuel Science & Technology International 14(1-2) (1996) 55-74.

[30] J.S. Buckley, C. Bousseau, Y. Liu, Wetting alteration by brine and crude oil: from contact angles to cores, SPE-169143-PA 1(03) (1996) 341-350.

[31] A. Bera, K. S, K. Ojha, T. Kumar, A. Mandal, Mechanistic Study of Wettability Alteration of Quartz Surface Induced by Nonionic Surfactants and Interaction between Crude Oil and Quartz in the Presence of Sodium Chloride Salt, Energy Fuels 26(6) (2012) 3634-3643.

[32] Y. Yuan, T.R. Lee, Contact angle and wetting properties, Surface science techniques, Springer2013, pp. 3-34.

[33] J. Shang, M. Flury, J.B. Harsh, R.L. Zollars, Comparison of different methods to measure contact angles of soil colloids, J. Colloid Interface Sci. 328(2) (2008) 299-307.

[34] O. Vizika, J. Lombard, Wettability and spreading: two key parameters in oil recovery with three-phase gravity drainage, SPE Reservoir Engineering 11(01) (1996) 54-60.

[35] R.M. Pashley, J.N. Israelachvili, Dlvo and hydration forces between mica surfaces in Mg2+, Ca2+, Sr2+, and Ba2+ chloride solutions, J. Colloid Interface Sci. 97(2) (1984) 446-455.

[36] E. Lima, B. De Melo, L. Baptista, M. Paredes, Specific ion effects on the interfacial tension of water/hydrocarbon systems, Brazilian Journal of Chemical Engineering 30(1) (2013) 55-62.

[37] V. Gupta, J.D. Miller, Surface force measurements at the basal planes of ordered kaolinite particles, Journal of Colloid and Interface Science 344(2) (2010) 362-371.

[38] A.M. Shehata, H.A. Nasr-El-Din, Reservoir Connate Water Chemical Composition Variations Effect on Low-Salinity Waterflooding, Abu Dhabi International Petroleum Exhibition and Conference, Society of Petroleum Engineers, 2014.

[39] N. Santha, P. Cubillas, A. Saw, H. Brooksbank, C.H. Greenwell, Chemical Force Microscopy Study on the Interactions of COOH Functional Groups with Kaolinite Surfaces: Implications for Enhanced Oil Recovery, Minerals 7(12) (2017).

[40] D.V. Vezenov, A. Noy, L.F. Rozsnyai, C.M. Lieber, Force Titrations and Ionization State Sensitive Imaging of Functional Groups in Aqueous Solutions by Chemical Force Microscopy, Journal of the American Chemical Society 119(8) (1997) 2006-2015.

[41] C. Shi, L. Zhang, L. Xie, X. Lu, Q. Liu, C.A. Mantilla, F.G. van den Berg, H. Zeng, Interaction mechanism of oil-in-water emulsions with asphaltenes determined using droplet probe AFM, Langmuir 32(10) (2016) 2302-2310.

7

Adsorption of oil compounds on kaolinite and pyrophyllite as studied by thermogravimetric analysis and mass spectrometry

It is a well-known fact that low salinity enhanced oil recovery (LSEOR) techniques work by altering the wettability of pore-lining minerals in an oil reservoir towards a more water-wet state. Therefore, to gain an understanding of the nanogeochemical mechanisms behind LSEOR, it is crucial to establish what drives this wettability change, particularly on clay minerals, which are the most common minerals in the pore space. In this work, we aim to understand how physical pre-treatment (as-received, baked, water-aged and dried, water-aged and wet) as well as different chemical parameters (pH, salinity, cation type, Na^+:Ca^{2+} ratio, ionic strength [IS]) of aging water (representing formation water) affects the wettability of two clay minerals (kaolinite and pyrophyllite) with respect to a model oil mixture (decanoic acid / dodecane). To this end, we used thermogravimetric analysis coupled to mass spectrometry (TGA-MS) to quantify and understand the type of adsorption and desorption of organic matter on these minerals, which is indicative of the wetting state. Results highlight the hydrophilic character of kaolinite and the hydrophobic nature of pyrophyllite, as they showed a large amount of water sorption for kaolinite and a great amount of oil sorption in pyrophyllite. Moreover, changing the cation type also lead to variations in the oil sorption, with $CaCl_2$ inducing a larger amount of oil to be sorbed on the clays than an equivalent (in concentration) NaCl solution. In addition, there was a more pronounced concentration effect on the experiments performed with $CaCl_2$ where higher concentrations lead, invariably, to a higher oil retention. This effect was less prevalent on the experiments performed with NaCl. The study of Na^+:Ca^{2+} ratios effect indicate that an increase in the relative amount of Ca^{2+} present in the mixture leads to increasing oil

sorption for both, kaolinite and pyrophyllite minerals. Finally, experiments performed with varying values of ionic strength (and a fixed Na^{+}:Ca^{2+} ratio) show partly effect on the kaolinite, but there was no effect on pyrophyllite. Overall, these results indicate that the cation bridging mechanism is the dominant process determining oil adhesion on kaolinite and pyrophyllite, with the double layer effect playing only a limited role.

7.1 Introduction

With primary and secondary oil production displacing only 30 to 50% of the original oil in place (OOIP) [1, 2] enhanced oil recovery (EOR) methods have gained a significant amount of global interest as a way of further extracting oil from currently used, or abandoned, reservoirs [3]. Among the many EOR methods, one of the most interesting is low salinity enhanced oil recovery (LSEOR) because it is effective, economical, ecologically-friendly and sustainable [4, 5].

LSEOR applied to sandstone rocks has been widely studied in both laboratory-based research and in oilfield operations [6]. Authors have concluded that there are a number of required parameters for LSEOR to be successful in clastic reservoirs, these include: the presence of clay minerals, polar crude oil, formation water and significant low salinity injection fluid (1000-2000 ppm) [6-8]. It has generally been acknowledged that LSEOR occurs due to low salinity-induced wettability alteration, in turn derived from the desorption of polar oil components from pore lining minerals (mostly clay minerals) [9-11]. However, in spite of the multiple studies published so far, researchers have been unable to pinpoint the main underlying mechanism responsible for oil adsorption/desorption at the micro or molecular scale.

The review of Sheng showed that oil chemical adsorption/desorption can be occur due to up to seventeen possible mechanisms [5]. Of these, two of most discussed as being the drivers behind LSEOR are: multicomponent ion exchange (MIE) [12-15] and the electric double layer (EDL) effect [16-19]. MIE includes three sub-type, organo-mineral binding mechanisms defined by Sposito [20]. including: cation bridging, ligand bridging and water bridging [8], as shown in Figure 7.1. Cation bridging occurs when divalent cation (Ca^{2+} or Mg^{2+}), act as an electrostatic bridge or an ionic bond between the negatively-charged clay surface and the negatively-charged polar oil molecule, leading to an ionic binding phenomenon; ligand bridging involves the formation of a covalent bond between the oxygen atom of an organic group and a divalent cation, which is also bonded to an tetrahedral clay oxygen; water bridging is the process by which a partially hydrated. The solvated multivalent cation balances the negative charge of the clay surface. At the same time, the solvation shell surrounding cations can binds to a functional group in the organic

molecule through a dipole−dipole interaction. Based on this knowledge, injection of low salinity water (disproportionately depleted of divalent cations), would lead to the replacement of the already present, bridging, divalent cations by monovalent cations at the negatively charged clay surface. As monovalent cations cannot sustain bridging, oil molecules would be released from the surface. A different phenomenon is electrical double layer (EDL) expansion [16], which refers to the increase or decrease of the electrical double layer width as function of the ionic strength (IS) of the solution in contact with a particular surface. At high concentration of ions, screening of the negatively charged surface of clay minerals will result in a reduction of the electric double layer width over the particle. The thin EDL then allows for oil molecules to approach and finally adsorb to the clay surface. This phenomenon can be described by the Gouy−Chapman−Stern theoretical model of an EDL layer on colloid surfaces [20]. The theory establishes that the interaction between a particle and a surface is related to ions controlling the width of the electrical double layer, or Debye length (see Chapter 3). If the counter ions concentration is small then the Debye length will be large, which leads to a repulsion force between negatively-charged molecules and the surface. On the other hand, if the counter ion concentration is large then, they will almost completely screen the surface charge, leading to a decrease in the Debye length, which will allow for attractive forces to develop between surface and molecules. Lager et al. points that the modification of the concentration of multivalent cations (in the formation brine) by the injected water is the main control of oil desorption and adsorption [8], whereas Ligthelm et al. claimed that the main factor relating to the double layer expansion effect is the total electrical charge of the brine [16], related to properties such as pH [18], concentration or ionic strength [17, 21] of the brine.

Double layer expansion effects are normally considered under the umbrella of DLVO theory [20]. DLVO takes into account electrostatic interactions between surfaces, ions and molecules and also van der Waals forces. The theory has been used to describe the dispersion or agglomeration of colloids and its dependence on the net charge of the material surface. Normally, van der Waals interactions induce an attractive force, while electrical double layer (EDL) leads to a repulsive interaction. Based on DLVO theory, oil interacts with a clay minerals' surface because the high concentration of ions of the connate water screen its negative charge resulting in a decrease of the width of the electric double layer. Whereas lower cation concentration, will result on less surface charge screening and a thicker double layer, resulting in the repulsion of the negatively charged polar oil molecules.

To address the validity of the different mechanisms, many authors have performed experiments exploring the various parameters that control the clay-oil sorption. These

include a variety of clay types, the chemical properties of connate water and injection water; and the clay-surface interactions controlled by those parameters. These interactions have been studied by computational chemistry simulations [22, 23] as well as laboratory investigations. The latter have included the use of various analytical techniques such as: X-ray absorption spectroscopies (XAS), nuclear magnetic resonance spectroscopy (NMR), fourier-transform infrared (FTIR) spectroscopy, thermal gravimetric analysis (TGA) [24, 25].

Recently, authors have studied the wettability alteration of calcite, quartz and kaolinite by various methods including gas and vapour adsorption isotherms and TGA. The results show that TGA is a suitable technique to study wettability as it can be related to contact angle measurements [26-30]. Also, TGA can provide a qualitative and quantitative measurement of organic matter adsorption and desorption on the solid surface [31], as such it has been used to study organic-mineral interactions on quartz, calcite and kaolinite [24, 26, 32]. However, the study of oil adsorption on clay minerals aged on different brines in the context of low salinity EOR, using TGA has never been reported.

The aim of this present work is to use TGA-MS to study the adsorption of polar and non-polar oil on kaolinite and pyrophyllite under the influence of a range of brine chemical parameters, including: concentration, cation charge (divalent vs. monovalent), ratio between monovalent and divalent ions, and ionic strength) These experiments were complemented with FTIR analysisis of selected samples to further investigate the oil-sorption mechanism The selection of kaolinite and pyrophyllite was undertaken in order to deduce differences in behaviour from the siloxane or aluminol faces in kaolinite, as this mineral possess both types (1:1 clay mineral type) but pyrophyllite only exposes the siloxane face (2:1 type clay) and has approximately the same charge (low as the siloxane in the surface of kaolinite). Kaolinite was selected as is the most common clay mineral in clastic reservoirs [33].

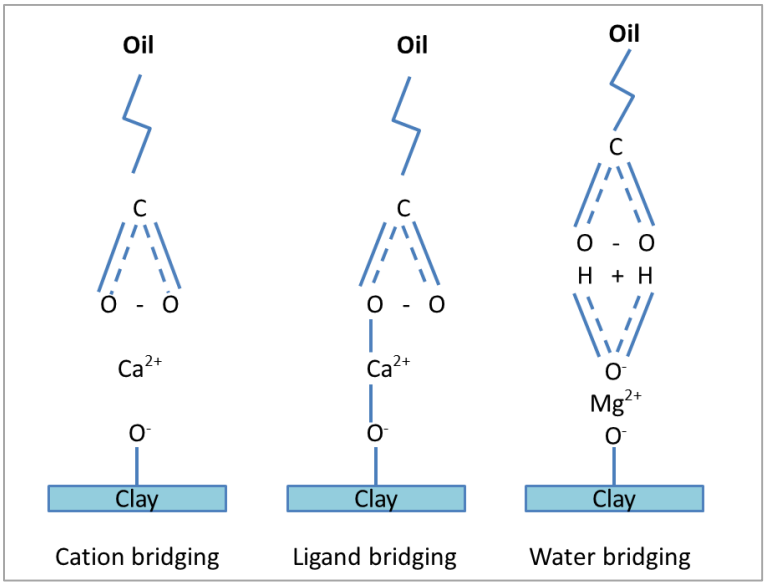

Figure 7.1 Schematic of the multicomponent ion exchange mechanism occurring between clay mineral surfaces and crude oil (based on Lager et al. [12]).

7.2 Materials

7.2.1 Model oils

Two model oil compounds were used for the experiments: 1) dodecane ($CH_3(CH_2)_{10}CH_3$) (ReagentPlus® ≥99% from Sigma-Aldrich), as the model non-polar oil, 2) a 1 M mixture of decanoic acid ($CH_3(CH_2)_8COOH$) in dodecane as the model polar oil. This latter oil was prepared by dissolving 176.26 g of decanoic acid (Sigma-Aldrich) into 1 liter of dodecane (ReagentPlus® ≥99% supplied by Sigma-Aldrich). The boiling points for dodecane and decanoic acid are 216 and 269 °C, respectively.

7.2.2 Clay minerals

Two types of clay minerals were used in the study: 1) kaolinite standard KGa-1b (from The Clay Minerals Society's clay mineral repository). 2) Pyrophyllite (from Goodfellow Cambridge Limited). Details of kaolinite and pyrophyllite crystal chemistry are given in Chapter 3.

7.2.3 Solutions

Milli-Q® deionized water was used to prepare all brines used in the study. The brines were prepared using $CaCl_2$ and NaCl reagents (99 % purity from Sigma-Aldrich). Brines were arranged into 2 sets. The first set was used to investigate the effect of concentration and cation identity. Six different concentrations were used: 1, 0.01, 0.001 M $CaCl_2$, and 1, 0.01, 0.001 M NaCl. Two initial pH values were used for all brines: 6.5 and 8. For the NaCl

solutions this was adjusted using 0.1 M of NaOH and 0.1 M of HCl, respectively. For the $CaCl_2$ solutions, it was adjusted using 0.1 M CaOH and 0.1 M of HCl solutions. All brines of the first set are shown in Table 7.1. The second set of brines was used to measure the influence of the Na^+:Ca^{2+} ratio and ionic strength. The different combinations used are shown in Table 7.2.

7.3 Experimental procedure

7.3.1 Standard samples analysis

Before the experiment, the as-received clays were analyzed to determine their morphology and size, as well as their surface area. The particles were imaged using a FEI Helios Nanolab Mk2 Scanning Electron Microscope (SEM). The samples were placed on double-sided carbon tape, and coated with a 25 nm layer of gold. The surface area analysis was performed by means of BET nitrogen adsorption using an Intelligent Gravimetric Analyser (IGA), supplied by Hiden Isochema Limited. The sample was weighed (0.8-1.5 g) and placed into the sample tube which was then fitted with a filler rod and isothermal jacket. The clay was degassed on the instrument at 70 °C (typically for ~4 h) by applying a vacuum. A nitrogen stream was flowed through the sample under isothermal conditions using liquid nitrogen (boiling point at −195.79 °C). The amount of adsorbed gas was calculated using the BET theory [34].

Table 7.1 Solutions used to study the effect of pH, concentration, and cation identity

Solution No.	pH	Concentration
1	6.5	1 M $CaCl_2$
2	6.5	0.01 M $CaCl_2$
3	6.5	0.001 M $CaCl_2$
4	6.5	1 M NaCl
5	6.5	0.01 M NaCl
6	6.5	0.001 M NaCl
7	8.0	1 M $CaCl_2$
8	8.0	0.01 M $CaCl_2$
9	8.0	0.001 M $CaCl_2$
10	8.0	1 M NaCl
11	8.0	0.01 M NaCl
12	8.0	0.001 M NaCl

Table7.2 Solutions used to study the effect of Na+: Ca^{2+} ratio and ionic strength.

Solution No.	Ionic Strength	Ratio Na^{+}: Ca^{2+}	NaCl Concentration (M)	$CaCl_2$ Concentration (M)
1	1.5	20:1	1.34	0.07
2	1.5	10:1	1.20	0.12
3	1.5	5:1	1.00	0.20
4	1.5	1:1	0.43	0.43
5	1	10:1	0.80	0.08
6	0.5	5:1	0.33	0.07
7	0.1	1:1	0.03	0.03

7.3.2 Oil sorption in the presence and absence of water: polar oil mixture and non-polar oil

Sample preparation: all experiments were performed using 0.5 g of clays, pre-treated at four different conditions namely baked, as-received, water aged and dry, and water aged and wet (Table 7.3). Baked samples were prepared by placing them in an oven (Laboratory Oven Panasonic (Sanyo) MOV-112-PE) at 70 °C for 24 h to remove any surface absorbed water. The as-received samples were directly used from the container; therefore, it was assumed that it will possess low water content due to absorption from ambient air. Additional samples were prepared using a water-aging method.

Water aging: 0.5 g of clay sample was introduced into a vial containing 5 ml of Milli-Q® water. The vials were placed in an oil bath at 70 °C and stirred (50 rpm) to ensure good mixing. The duration of the aging was 24 h, which has been deemed as a suitable time to establish equilibrium in this type of samples [26]. Then, two suspensions were centrifuged at 3000 rpm for 10 min, using a LMC-300 centrifuge from Biosan, and decanted. For water-aged and dried sample, the clay was then dried in an oven at 70 °C for 24 h. For water-aged and wet sample, the centrifuged clay sample was left at room temperature (24 h) inside a vial.

Table7.3 Type of clay pre-treatment.

Vials	Sample preparation	Water aging
1	Baked	-
2	As-received	-
3	As-received	Water-aged and dried
4	As-received	Water-aged and wet

Oil aging: after pre-treatment, samples were soaked in 5 ml of model oil (either non-polar or the polar mixture) and kept at 70 °C inside an oil bath and 50 rpm of stirring for 24 h. Afterwards, samples were centrifuged at 3000 rpm for 10 min and decanted to retrieve the clay from the model oil. Lastly, the samples were placed in an oven (70 °C) for 24 h, in order

to evaporate most of the intra-particle oil, before TGA-MS analysis. All experiments were repeated 3 times. A flow chart with all sample preparation procedures is shown in Figure 7.2.

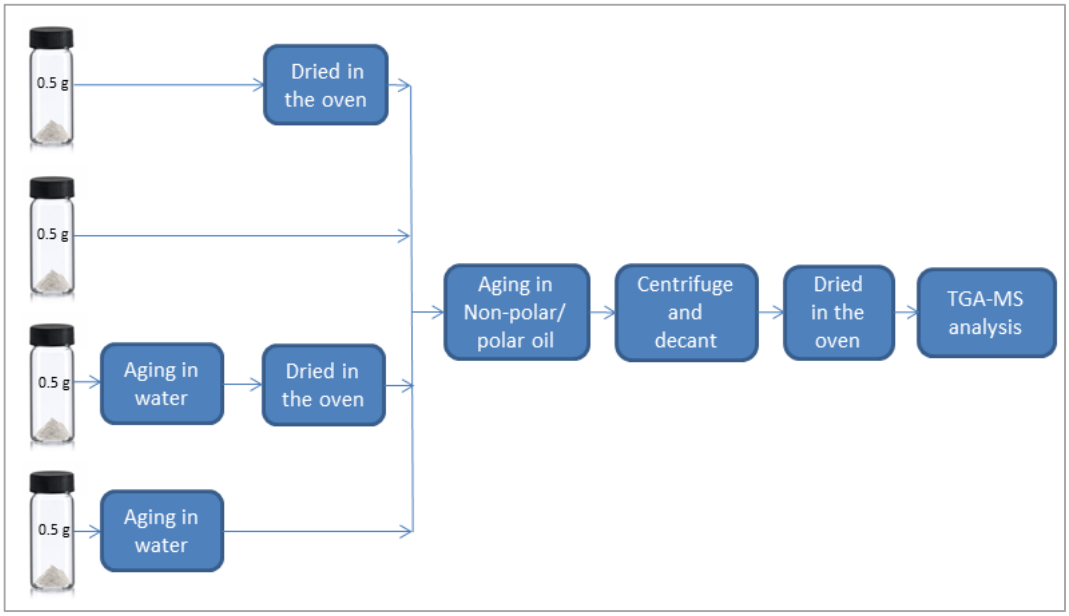

Figure 7.2 Flow diagrams showing the different sample preparation methods.

7.3.3 Control experiments

In addition to each oil-sorption test two types of control experiments were carried out (Table 6.4) to measure the amount of adsorbed water from the water-aging pre-treatment, before they were immersed in oil (Figure 7.3). In the first set, a clay sample was aged in water and then dried in the oven (70 °C and 24 hours) before being analyzed by TGA-MS. In the second set the clay samples was aged in water and then analyzed wet with the TGA-MS. The values of adsorbed water measured by the TGA-MS analysis were then subtracted from the measurements on the oil-aged experiments, where a mixture of water and oil was released during the earlier desorption phase, as explained in detail in the results section.

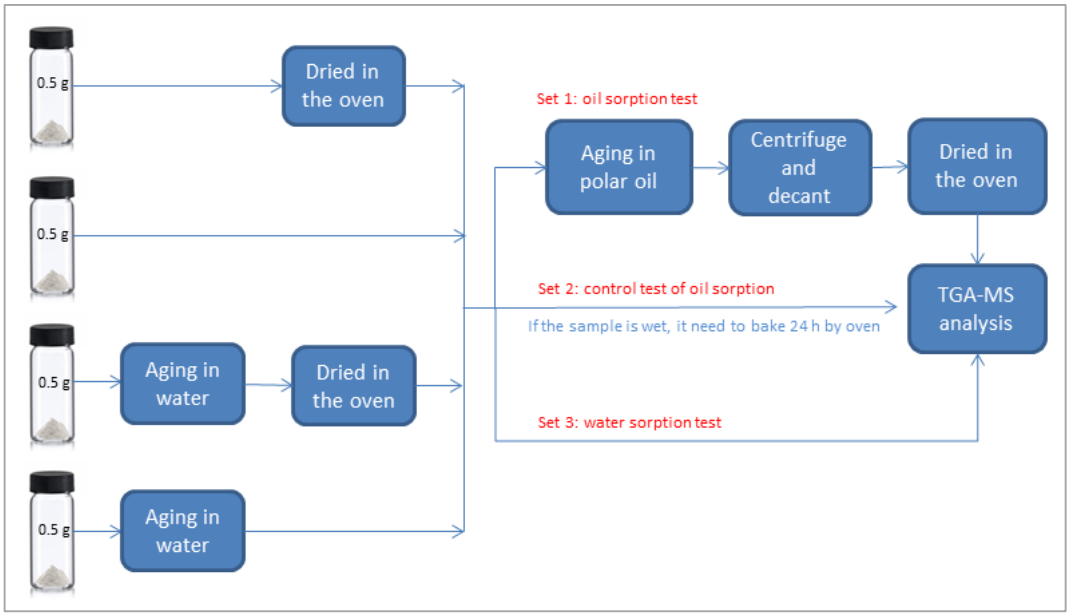

Figure 7.3 Flow diagram showing the methodology used for control-sample treatment.

7.3.4 Influence of brine chemistry pre-treatment

Sample preparation: 0.5 grams of as-received clay (kaolinite or pyrophyllite) were placed into vials. The samples were then organized into three groups. The first and the second batches consist of six samples, and the last contained seven samples. All experiments were performed three times for each condition.

Aging: 5 ml of 1, 0.01, 0.001 M of either $CaCl_2$ or NaCl, were individually added into each vial (containing the clay minerals). For batch 1, all solutions had a pH of 6.5, whereas for batch 2 they had a pH of 8 (Table 7.4). Batches 1 and 2 were used to investigate the effect of concentration, cation identity, and pH on oil adsorption. Batch 3 samples were used to study the effect of ratio Na^+: Ca^{2+} and ionic strength (IS). 7 vials of clays were filled with 5 ml of the solutions with the composition shown in Table 7.5. The brine aging was conducted at the same temperature (70 °C), time (24h) and stirring (50 rpm) rate as the experiments described in Section 7.3.2. After the samples were pre-treated in brine they were centrifuged (3000 rpm for 10 min), decanted and dried in the oven (70 °C for 24 h). After this, one sample was sent for TGA-MS analysis to determine the amount of adsorbed water after brine pretreatment (Figure 7.4). The rest of the samples (3) were aged in polar oil using the same procedure detailed in Section 7.3.2. No aging in dodecane was performed as the results from the water-aged experiments did not show a significant adsorption (Section 7.4.2). Finally, control experiments, to determine the water sorption, were performed in a similar matter to that described in Section 7.3.3.

Table7.4 Batch 1 and batch 2 experimental conditions.

Batch	Sample No.	pH	Concentration	Ca^{2+} or Na^{+} (ppm)	TDS (ppm)
1	1	6.5	1 M $CaCl_2$	40080	120240
	2	6.5	0.01 M $CaCl_2$	401	1202
	3	6.5	0.001 M $CaCl_2$	40	120
	4	6.5	1 M NaCl	22980	45960
	5	6.5	0.01 M NaCl	230	460
	6	6.5	0.001 M NaCl	23	46
2	1	8	1 M $CaCl_2$	40080	120240
	2	8	0.01 M $CaCl_2$	401	1202
	3	8	0.001 M $CaCl_2$	40	120
	4	8	1 M NaCl	22980	45960
	5	8	0.01 M NaCl	230	460
	6	8	0.001 M NaCl	23	46

Table 7.5 Batch 3 experimental conditions.

Ionic Strength	Ratio Na^{+}:Ca^{2+}	NaCl Concentration (M)	Na^{+} (ppm)	$CaCl_2$ Concentration (M)	Ca^{2+} (ppm)	TDS (ppm)
1.5	20:1	1.34	30678	0.07	2675	69381
1.5	10:1	1.20	27576	0.12	4810	69581
1.5	5:1	1.00	22980	0.20	8016	70008
1.5	1:1	0.43	9858	0.43	17194	71300
1.0	10:1	0.80	18384	0.08	3206	46387
0.5	5:1	0.34	7664	0.07	2673	23348
0.1	10:1	0.08	1834	0.008	320	4638
0.1	5:1	0.06	1533	0.013	535	4670
0.1	1:1	0.03	657	0.03	1146	4753

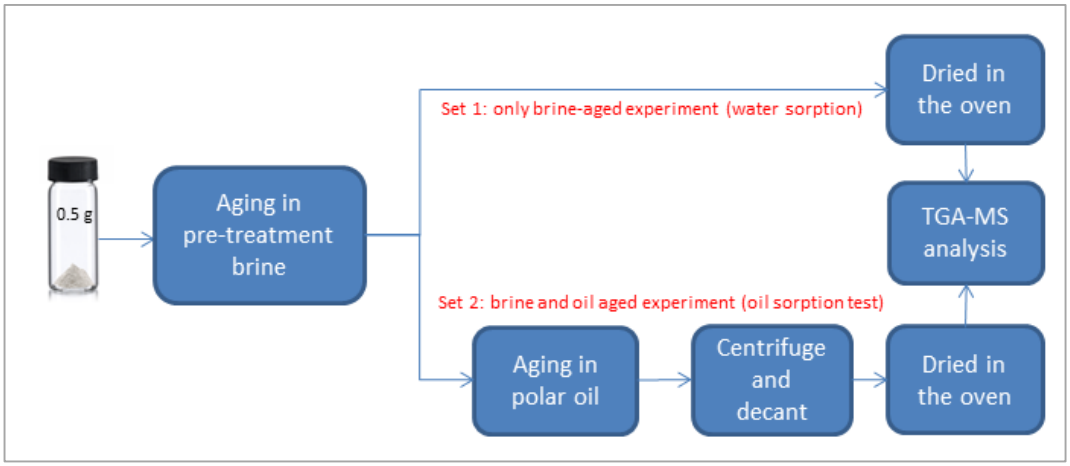

Figure 7.4 Flow diagram showing the methodology used in the brine pre-treated samples.

7.3.5 TGA-MS Analysis

TGA-MS analysis: Sample analysis was conducted by thermal gravimetric analysis (PerkinElmer Syns I) coupled with mass spectroscopy (Hiden HPR 20). The analyses were conducted by weighing 20 to 30 mg of sample on a standard ceramic pan. This was then placed into the pyrolysis oven which heated the sample at a rate of 10 °C/min, from ambient temperature to 1000 °C, under 30 ml/min of helium gas flow rate. This allows the investigation of the adsorption and desorption of organic matter on the minerals' surface as the weight loss can be directly related to the amount of adsorbed organic materials on a surface [7, 19, 21, 27, 30, 31]. During analysis by TGA, the vaporized gas expelled from the sample was transferred to the mass spectrometer (MS) by a helium carrier gas. Spectra were collected to determine the following species CO_2, (m/z = 44), CO (m/z =28), H_2O (m/z = 18) and decanoic acid (m/z = 43, 60, 73, 129). A full description of the techniques used is given in Chapter 4.

7.3.6 Data processing of TGA-MS

Data processing: Data analysis was performed using Pyris software, version 13, by PerkinElmer, Inc. The TGA data was manually separated into the different stages by considering the change of slope on the weight loss vs temperature diagram (calculated using the Delta Y Calc function of the Pyris software). Three different behaviors were recognized: 1) no or very small slope (less than 0.35 % weight in range 200 °C) a gradually deceasing slope, due to sample evaporation, or 3) abrupt change of slope, meaning boiling or decomposition [32]. MS data analysis was undertaken using the 7MASsoft (Professional Version 7) software from Hiden Analytical Limited.

The percentage of mass loss was considered to be due to the release of oil, water, or the decomposition (dehydroxylation) of the clay mineral. The amount of oil released was

calculated by subtracting the % weight loss observed by the amount of water released in the control experiments; the assumption being that a similar amount of water will be contained in the sample after oil sorption (i.e. it was implied that a small or no displacement of oil by water would occur during oil aging). The presence of water on the oil-aged samples was observed with MS (in addition to a simultaneous release of oil). The measured weight loss was recalculated to mg of oil or water released per surface area of initial clay (mg/m^2). The total initial clay surface area was calculated using the surface area value obtained from the BET analysis and the total amount of clay per sample, which was calculated by subtracting the amount of oil and water released from the initial sample weight introduced in the TGA oven.

7.3.6 FTIR analysis

Kaolinite and pyrophyllite samples were pre-treated with solutions of 0.001 M and 1M of either $CaCl_2$ or NaCl, with a pH of 6.5 or 8 and analysed by FTIR (FT-IT from The Frontier™)

7.4 Result and Discussion

7.4.1 Sample standard surfaces

Kaolinite and pyrophyllite samples were studied by SEM, as shown in Figure 7.5. It can be seen that the kaolinite sample shows a small variation in grain size, varying between 0.1 μm to 1.5 μm (Figure 7.5a and 7.5c). In addition, individual kaolinite crystals are euhedral with a hexagonal shape. In contrast, the pyrophyllite sample show a larger crystal-size variation (0.5μm to 5 μm) -and crystals display highly irregular shapes (Figure 7.5b, and 7.5d). The surface area of kaolinite and pyrophyllite was calculated from nitrogen adsorption isotherms using the Brunauer–Emmett–Teller (BET) method. The measured kaolinite surface area was of 11.33 m^2/mg, while pyrophyllite has a smaller surface area of 4.69 m^2/mg. The results found here are consistent with previous studies which report kaolinite's surface area values ranging from 11.7 to 16.1 m^2/g [35-37]. Reported values for the surface area of pyrophyllite varied from 0.27 to 12.61 m^2/g depending on milling time [38], whereas pyrophyllite from India (different source from this study) has a reported surface area 11.38 m^2/g [39].

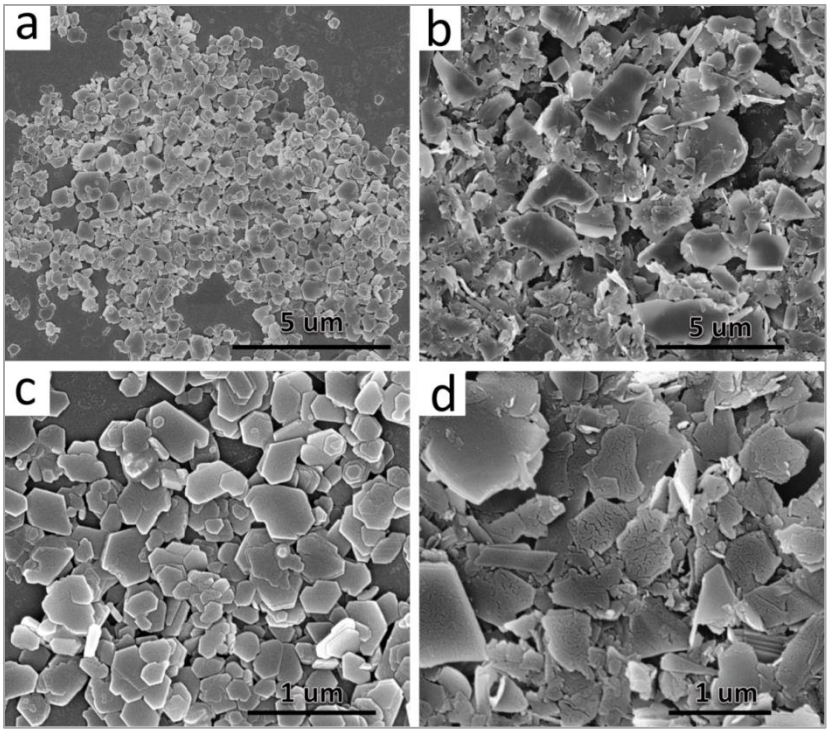

Figure 7.5 FEI SEM micrographs showing image of a, c) kaolinite and b, d) pyrophyllite.

7.4.2 Effect of water content on oil sorption

The first set of experiments was performed on samples with the four physical pre-treatment conditions (Table 7.3), which were then aged either in non-polar oil or polar oil mixture. Figures 7.6 and 7.7 shows the TGA analysis for kaolinite and pyrophyllite, respectively. Weight losses on the TGA results were only considered above 70 °C, as any loss mass below that temperature is considered to be inherent moisture. In all cases, the experiments performed with the polar oil mixture of dodecane and decanoic acid (with boiling points of 216 and269 °C respectively) showed a larger weight loss through the experiment, when compared to those samples aged in non-polar oil. This indicates a larger sorption of the polar oil mixture.

For kaolinite, the polar oil mixture experiment shows three distinct weight loss stages (Figure 7.6). The first stage, ranging from 70 to 150-170 °C (depending on the pre-treatment condition), encompasses the largest change of weight, exemplified by a rapid increase in slope in the graph (increased rate of mass loss) followed by an abrupt change to a low slope value (0.35% in 200 °C) around 150-170 °C. This weight loss is attributed to physically sorbed oil or inter-particle trapped oil (in addition to entrapped water, see Section 7.4.3). The second stage, from 150-170 to 450 °C shows a much more gradual (and almost constant) decline in sample weight loss as the temperature increases (low slope). Weight loss in this stage is regarded as arising due to release of strongly bonded or

chemically adsorbed molecules to the surface [24], in this case oil molecules. The last stage is considered the pyrolysis stage, where the sample suffers a very fast and large (>10%) weight loss in the temperature range between 450-550 °C. All samples (with all types of pre-treatment) showed this stage in the same way (similar decrease in weight at almost exactly the same temperature). Therefore, this stage is identified with the dehydroxylation of kaolinite, as has been reported in previous studies [40]. Alternatively, the samples aged in non-polar oil only show a very gentle weight loss (<2%) up to the start of the dehydroxylation stage (450 °C), replicating almost exactly the behaviour observed by the as-received kaolinite (Figure 7.6).

Pyrophyllite TGA results are shown in Figure 7.7. It can be seen that the behaviour of the samples aged with non-polar oil is almost equal to that shown by the untreated pyrophyllite samples. On the contrary, polar oil-aged samples show a more complex behaviour with three differentiated stages: the first stage extends from approximately 30 to 150 °C and shows a continuous increase in the weight loss as function of temperature (up to approximately 150 °C). This is followed by an abrupt change in slope (inflexion point) and much slower rate of weight loss (approximately 0.3% in 200 °C) until the temperature reaches approximately 480 °C. The final stage is composed of a step of rapid weight loss from 500-550 °C followed by a longer rapid decrease in weight between 550 to 800 °C. These two rapid weight loss steps have been linked to two dehydroxylation steps of pyrophyllite [41].

The preliminary TGA data clearly shows that polar-oil interacts much more strongly with both types of clay minerals than its non-polar (dodecane) counterpart. Moreover, differences in the dehydroxylation stage result from the differences in structure between kaolinite and pyrophyllite [42]. For pyrophyllite there is a double declining hydroxylation step whereas only one is observed for kaolinite. Both kaolinite and pyrophyllite dehydroxylation is the combination of processes of the removal of $2OH^-$ molecules from the octahedral face, the protonation of apical oxygen, and the formation of water [43]. For both structures this is accomplished through a series of sequential reactions and the formation of intermediates, but the fact that the octahedral face is “sandwiched” between two siloxane, tetrahedral layers, results in a more complex reaction sequence leading to the ultimate release of water [44].

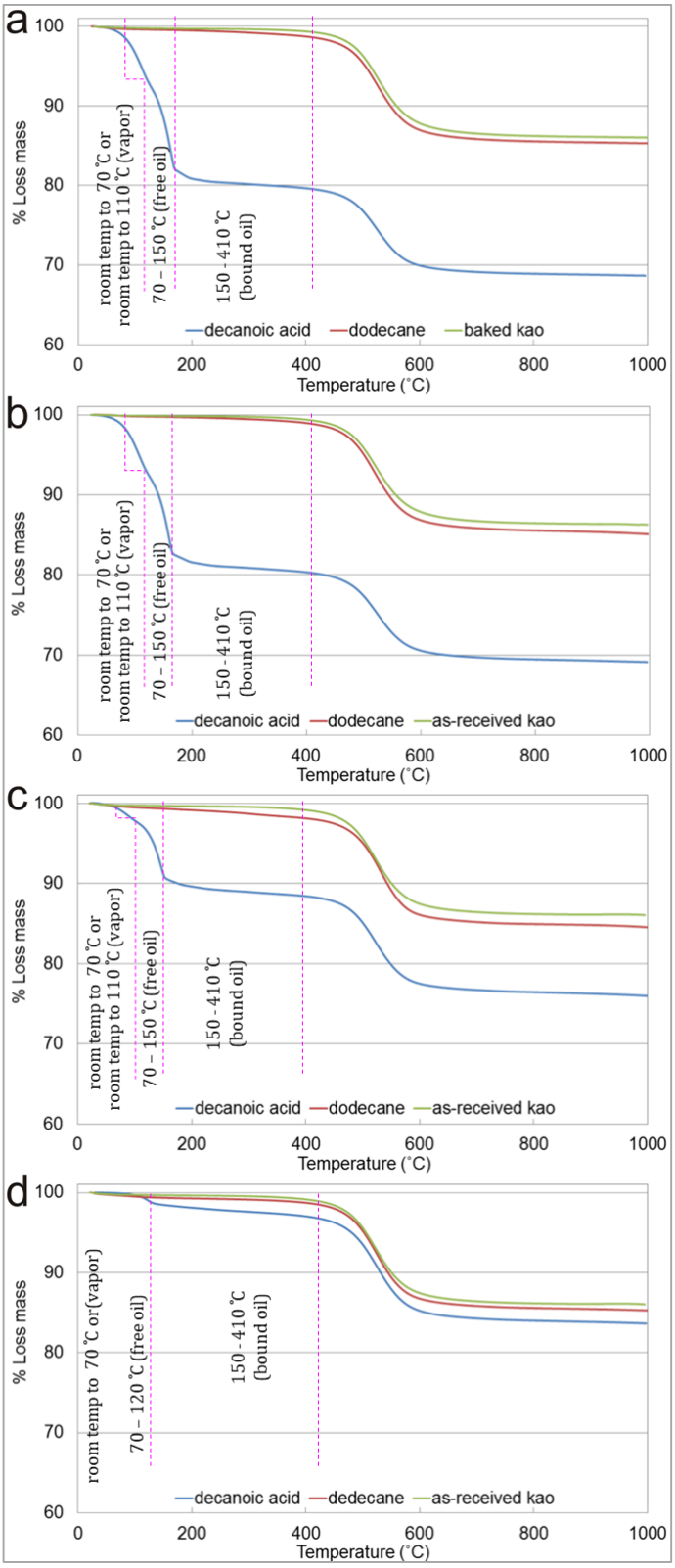

Figure 7.6 TGA comparison of polar and non-polar model oil on kaolinite a) baked kaolinite b) as-received kaolinite c) water-aged and dry d) water-aged and wet.

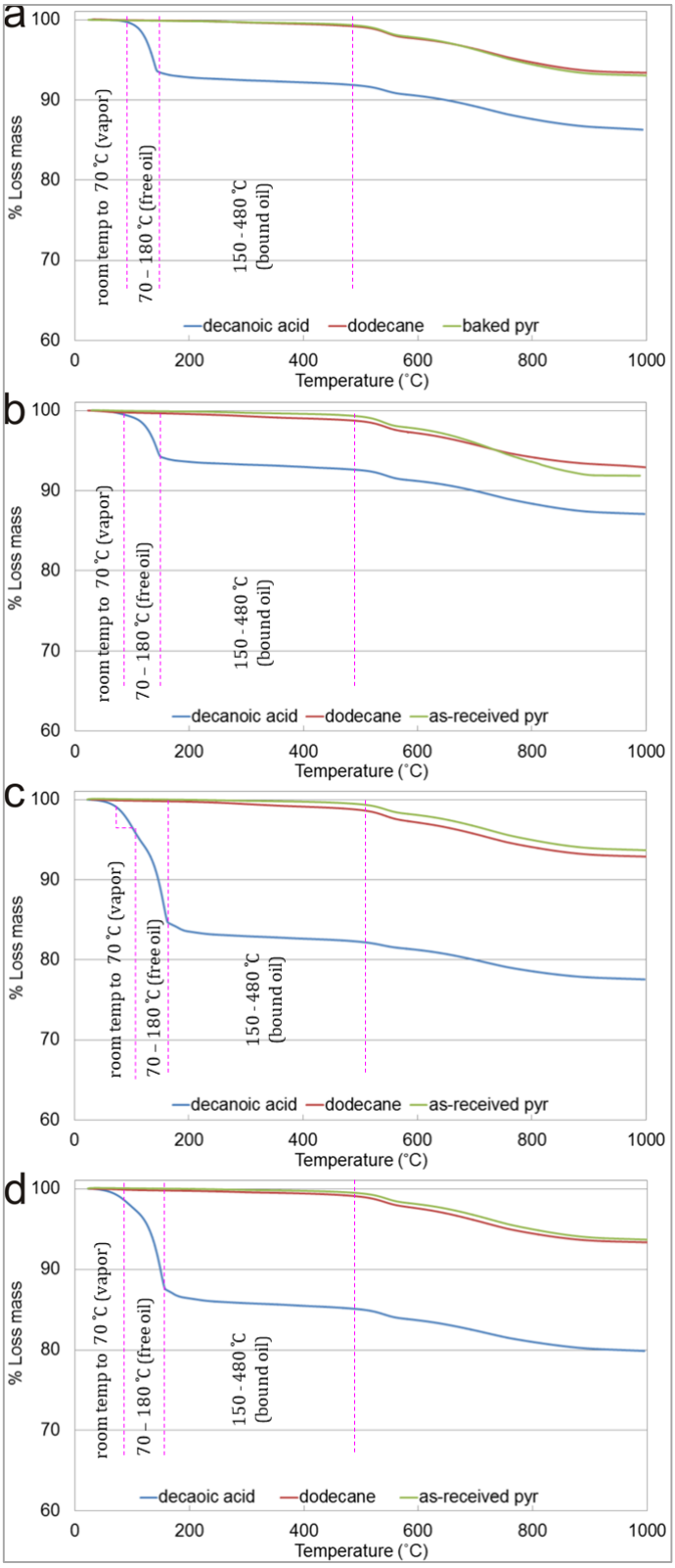

Figure 7.7 TGA comparison of polar and non-polar model oil on pyrophyllite a) baked pyrophyllite b) as-received pyrophyllite c) water-aged and dried d) water-aged and wet.

.

The estimation of oil sorption on kaolinite and pyrophyllite was calculated from the weight loss profiles (as described in Section 7.3.6) and shown in Figure 7.8 and Figure 7.9 respectively. In the case of kaolinite, all four types of sample pre-treatment polar oil sorption was significantly higher (up to a 100 times in some cases) than non-polar oil sorption (Figure 7.8). With regards to polar oil sorption, both, the baked and as received kaolinite samples showed almost the same oil sorption (≈20 mg/m^2), whereas the other two samples showed significantly less sorption, with ≈10 mg/m^2 for the water-aged and dry samples and ≈2 mg/m^2 for the water-aged and wet amount of polar oil adsorption between water-aged and non-water-aged are different.

With regards to pyrophyllite, polar oil sorption was also significantly higher (between 15 and 400 times) than that measured with non-polar oil, as can be seen in Figure 7.9. Therefore, for both kaolinite and pyrophyllite the data indicates that the thermal desorption of the polar fraction is significantly larger than that of the non-polar model oil. This observation is consistent with the investigations of Alvarado et al. [45] that found that both acidic and basic polar components are the most appropriate fraction to adsorb onto rock minerals. Tiab and Donaldson and RezaeiDoust et al. also showed that polar oil components attached to clay mineral surfaces act as anchoring molecules for crude oils in the sandstone rocks [46, 47].

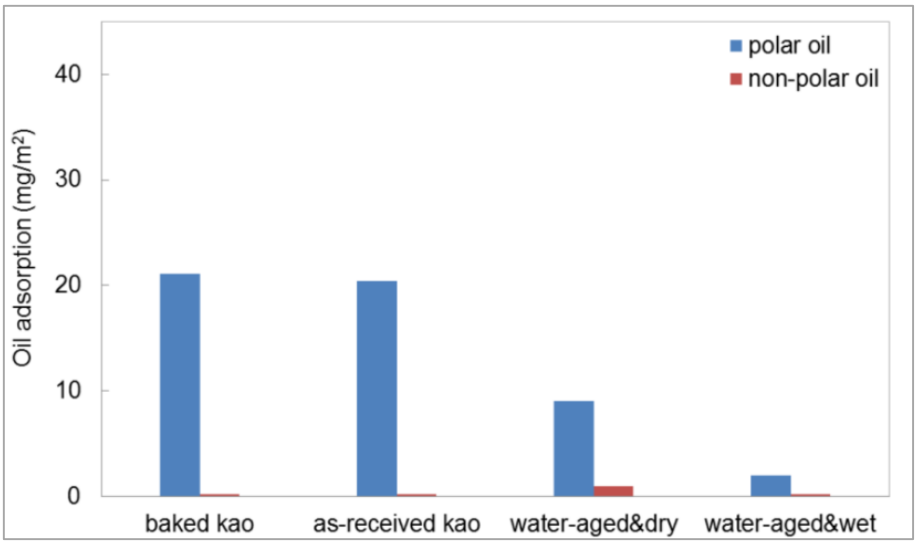

Figure 7.8 Graph comparison amount of polar and non-polar model oil on kaolinite.

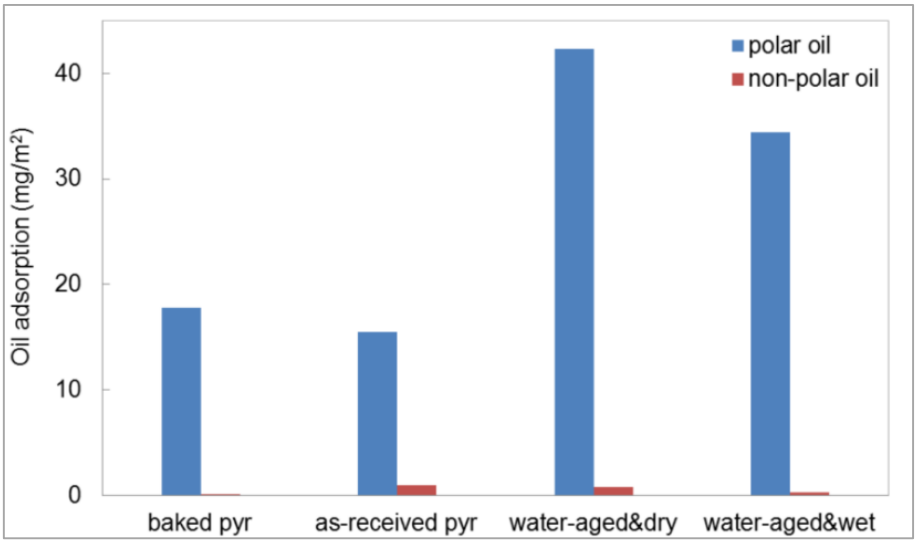

Figure 7.9 Graph comparison amount of polar and non-polar model oil on pyrophyllite.

Polar oil adsorption on the different pre-treated pyrophyllite samples showed a different behaviour than that measured for the kaolinite samples. As with kaolinite, oil sorption for the baked and as-received samples was similar in magnitude and achieved comparable values (to those measured in kaolinite) of approximately 18 and 15 mg/m^2, respectively. However, oil adsorption was measured to be much higher on the water-aged and dry samples (≈42 mg/m^2) and water-aged and wet (≈35 mg/m^2) samples. This in contrast with what was observed in kaolinite, where sorption was much lower (water aged and dry 9 mg/m^2 and water aged and wet 2 mg/m^2) than that observed for baked (≈21 mg/m^2) and as received samples (≈20 mg/m^2).

7.4.3 Influence of parameters: physical pre-treatment

Following the results from first set of experiments, a second set was performed using the same pre-treatment (Section 7.3.2), and the polar oil mixture only. For this batch, three-repeats of each experiment were done, and MS was performed along the TGA measurements.

Representative thermograms from the second set of experiments (one per experimental condition) are shown in Figure 7.10. Figures 7.11 and 7.12 show the corresponding mass spectrum (MS) measurement. Figures a, c, e, g, and i show data for water and Figures b, d, f, h, and j shows data for the possible decanoic acid. Thermograms illustrate the percentages of mass loss a function of temperature, whereas the mass spectrum presents mass loss (%) as a function of time (min). They are approximately comparable as each 10 min is equal to 10 °C in TGA.

The TGA for the untreated, as-received kaolinite (standard) shows almost no weight loss until reaching 400 °C. As a consequence, the corresponding mass spectrum (MS) shows no release of water or oil until that temperature (Figure 7.11a and Figure 7.11b), followed by release of water due to the de-hydroxylation stage. MS for all the pre-treatment conditions shows a more complex situation. In all cases, a peak on the water signal (release) was observed at the beginning of the experiment, this been higher on the water-aged and wet samples, as expected. In all cases, however the largest peak of water release coincides with the de-hydroxylation stage.

Oil release was observed, in most cases, to occur through the duration of the experiment, with increases close to the de-hydroxylation stage (around 450 °C). This confirms that both oil and water release can occur concurrently during the weight loss stages measured with the TGA. In addition, the fact that oil release is observed throughout the duration of the experiment indicates two different types of oil adsorption. The first type corresponds to physically sorbed or trapped oil between particles (inter-particle), which is released below the boiling point of dodecane and decanoic acid (216 and 269 °C, respectively) and is reflected, in part, by the sharp weight losses observed on the TGA between 70-150 °C, from hereafter this oil is also referred as "free" oil. Loss of oil at this temperature range has been reported before, for example, Zhu et al. and Chen et al. show TGA data on dodecane release from resin and silica materials at 50-140 °C and 60-160 °C [48, 49] and Konuklu et al. measured the release of decanoic acid from resin micro-capsules at slightly higher temperatures (100-180 °C). Release of oil above 150 °C is identified as chemically adsorbed (or intra-particle) and corresponds to the gentle loss weight (small slope) observed in the TGA data [50]. This oil is referred here after as "bound" oil [50].

TGA/MS experiments performed on pyrophyllite confirm that as-received pyrophyllite only releases water during the de-hydroxylation stage (Figure7.13), as expected from the near-absence of weight loss exhibited in the TGA (Figure 7.10). MS analysis of the experiments performed with pre-treated pyrophyllite show the release of water at the beginning of the experiment and during the de-hydroxylation stage. Oil release is also observed at the beginning of the experiment with an increase throughout the dehydroxylation stage. Therefore, as was the case for kaolinite, oil and water are released at the same time. In addition, it's also possible to differentiate between physically adsorbed and chemically adsorbed oil depending on the temperature of release. Finally, release of water during the de-hydroxylation stage shows a more complex behaviour than with kaolinite, indicative of the more complex process observed in this mineral [51].

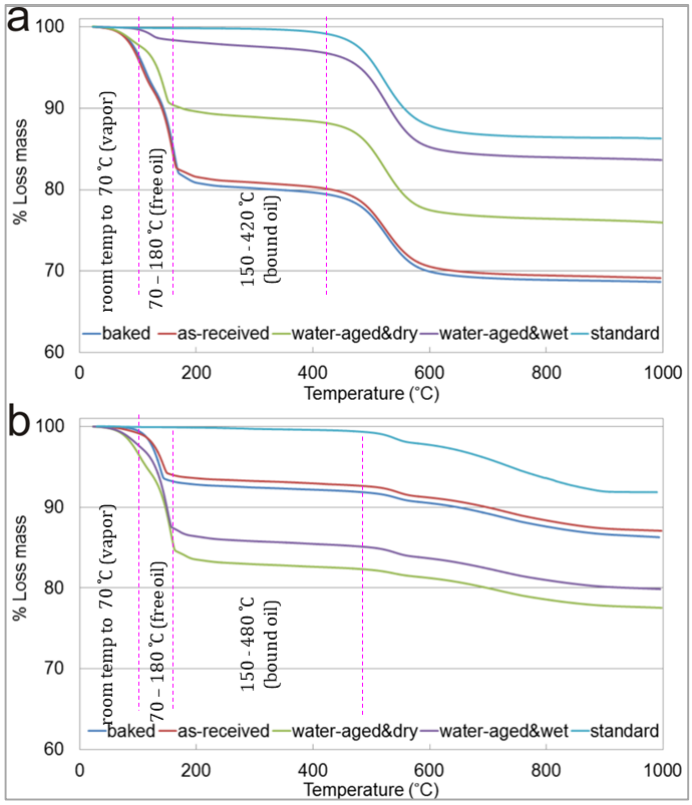

Figure 7.10 Comparison of TGA analysis for different sample pre-treatment and aged in 1 M decanoic acid on a) kaolinite and b) pyrophyllite.

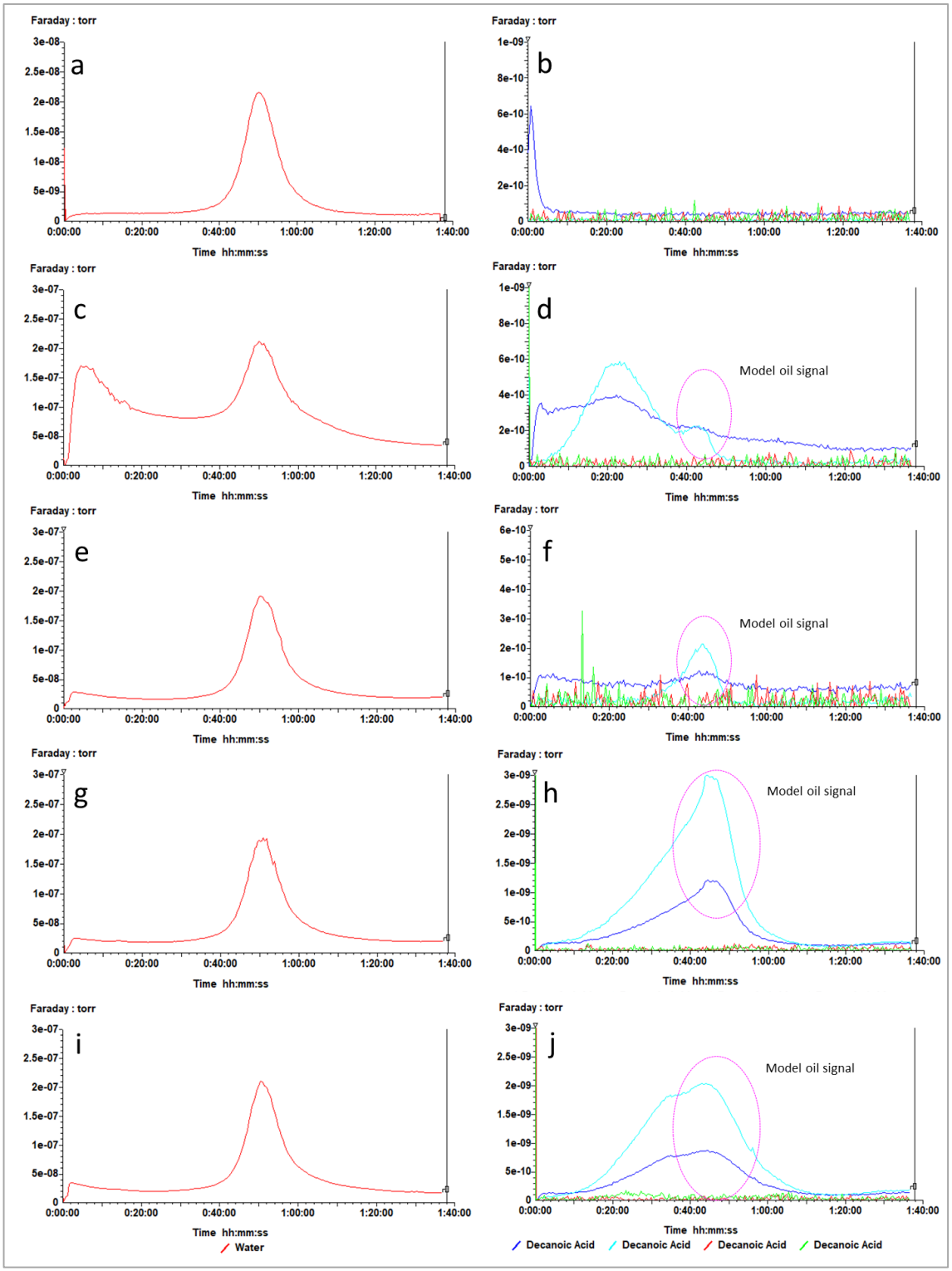

Figure 7.11 MS data of as-received kaolinite (a, b), and four different pre-treatment (plus aging in polar model oil): water-aged and dried (c, d), water-aged and wet (e, f), untreated (g, h), and baked (i, j).

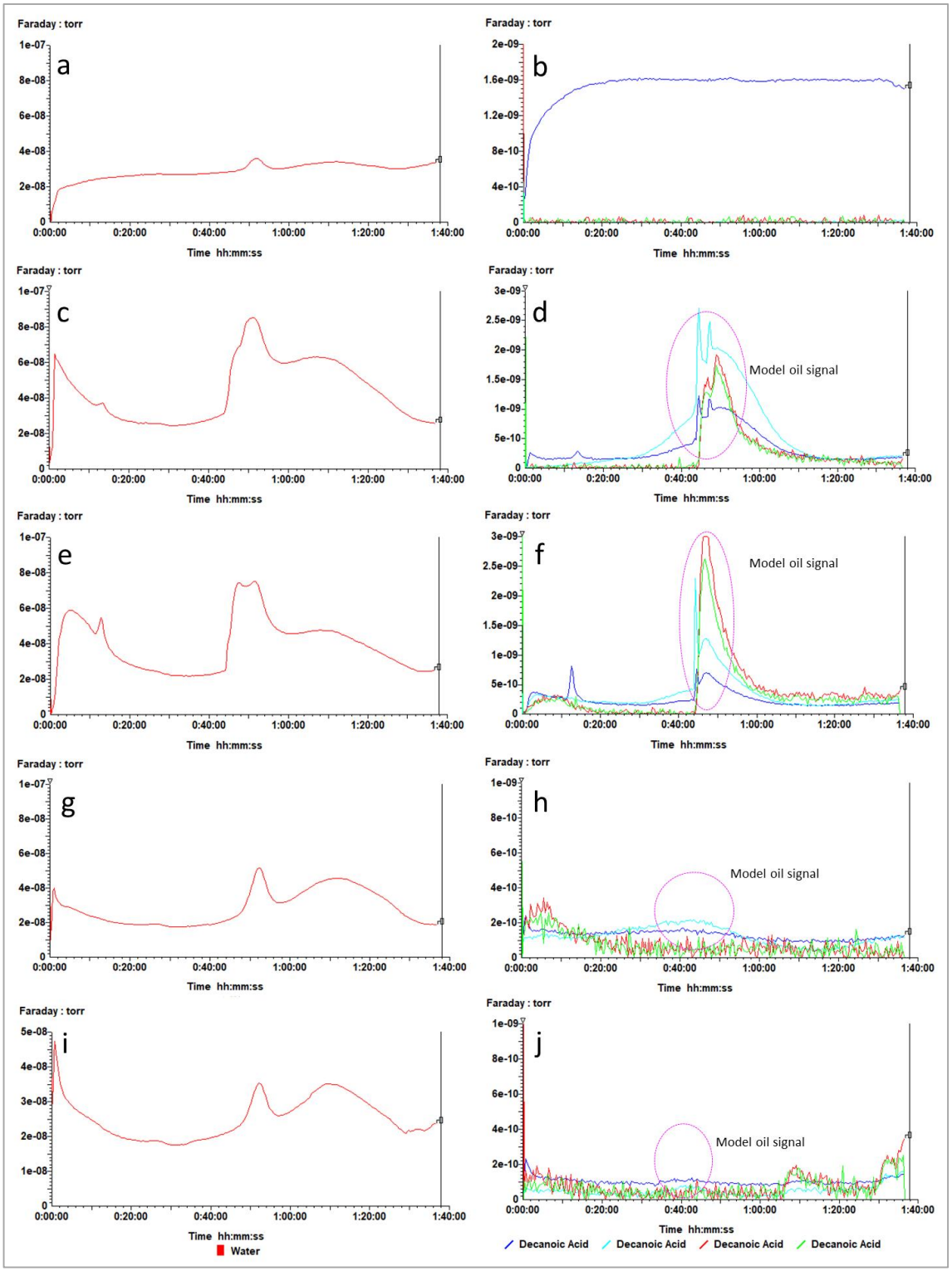

Figure 7.12 MS data of as-received pyrophyllite (a, b), and four different pre-treatment (plus aging in polar model oil): water-aged and dried(c, d), water-aged and wet (e, f), untreated (g, h), and baked (i, j).

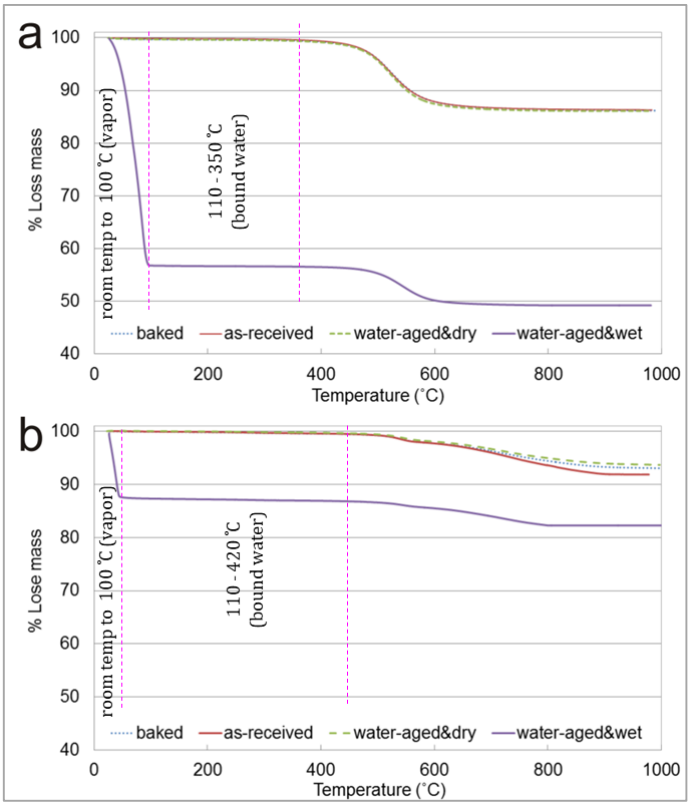

Figure 7.13 Comparison of TGA analysis of control experiment for different sample pre-treatment (water content) a) kaolinite and b) pyrophyllite.

Thermograms for kaolinite and pyrophyllite samples pre-treated only with water (control experiments) are shown in Figure 7.13. It can be seen that baked, as-received, and water-aged and dry do not show a change in weight up to 350 °C for kaolinite and 420 °C for pyrophyllite. In contrast, water-aged and wet samples show a very large drop in weight at very low temperatures (90 °C for kaolinite and 45 °C for pyrophyllite), as expected.

The average water adsorption (normalized to surface area) for the different pre-treatments of kaolinite and pyrophyllite samples, was calculated from the thermograph data and values are reported in Figure 7.14. It can be seen that three types of pre-treated samples (baked, as-received, and water-aged and dried) shows very low water content (in both inter-particle and intra-particle). The trends are the same for both kaolinite and pyrophyllite. As expected, the water-aged and wet samples show the largest amount of water content, especially inter-particle. When comparing water-aged and wet kaolinite to pyrophyllite, it can be seen that kaolinite has a higher content of both, inter-particle (twice) and intra-particle water (4 times).

After the analysis of water adsorption, the effect of the four pre-treatments on oil adsorption was calculated. Figure 7.15 shows that the amount of free and bound oil

adsorption (normalized to the surface area) for the different pre-treated kaolinite and pyrophyllite samples. For kaolinite, the amount of free oil sorbed fluctuated from ~6 to ~23 mg/m^2, whereas bound oil varied between 2 and 3 mg/m^2. The as-received kaolinite shows the highest amount of oil sorption of both inter-particle and intra-particle oil. For inter-particle oil, the baked kaolinite showed the second largest amount of sorption (12.28 mg/m^3), whereas the samples pre-treated with water showed a decrease of 72 % (water–aged and dried) and 65 % (water-aged and wet) with respect to the as received samples. For intra particle oil the difference was reduced, but it was still significant, with a decrease in oil sorption of 40 % for the water-aged and dried samples and 46 % for the water-aged and wet samples. For pyrophyllite, the amount of free oil varied between (30-38 mg/m^2) whereas that of bound oil varied between (4-6 mg/m^2). Given the variation in measurements between the three repeats (given by error bars), it can be concluded that the measured amount of oil sorbed did not statistically change for the four types of pre-treatment. In the case of bound oil, the samples pre-treated in water shows 10-20 % higher oil content than both dried and as-received sample. This is opposite to results observed in kaolinite.

Furthermore, the above observations demonstrate the different adsorption behaviour between the two types of clays, with pyrophyllite consistently showing a higher sorption capacity in term of both free and bound oil (Figure 7.15). In addition, as noticed above kaolinite shows a higher affinity for water than pyrophyllite. Therefore, both results indicate that kaolinite is more hydrophilic than pyrophyllite. This results correlated with the findings of Hu et al [52]. They found that the contact angle of water measured on pyrophyllite is ~ 40° at various pH, but the contact angle on kaolinite is less than 10°, indicating a higher affinity of water for kaolinite surfaces. This difference in behaviour can be explained by looking at the crystallographic structure of both minerals. Pyrophyllite is a 2:1 clay mineral type meaning, the only exposed basal surfaces are siloxane planes (composed of saturated Si-O-Si bonds) with low ionic substitution. These type of groups have been shown to be more hydrophobic due to low charge, low polarity, and the absence of Si-OH groups [53, 54]. In comparison, kaolinite exposes a siloxane face (almost identical to that of pyrophyilite) and an aluminol face (with exposed –OH groups). Both layers have small ionic substitutions (hence the low charge), however, the presence of -OH groups on kaolinite's basal planes causes stronger charge and polarity than pyrophyllite, resulting in a higher affinity for water (through hydrogen bonding) for the aluminol face. At the edges, pyrophyllite and kaolinite have similar terminal groups, defined through broken bonds. For kaolinite, the edges are composed of aluminol (Al-OH) and silanol (Si-OH) groups at similar ratios, whereas pyrophyllite's edges contain at least twice the number of silanol

groups than aluminol sites (due to the ratio of 2:1 of layer types). Both sites can be protonated and deprotonated, leading to pH-dependent interfacial properties [55] (more description in Chapter 3).

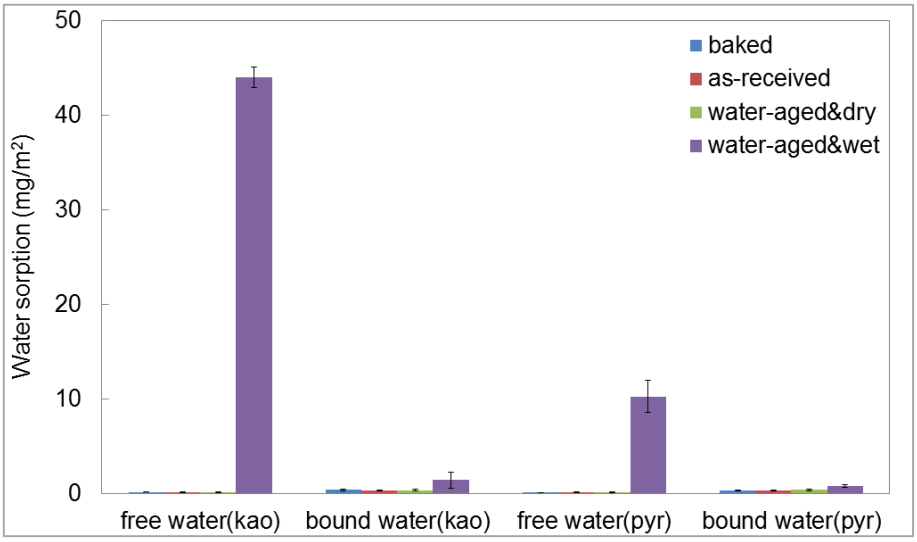

Figure 7.14 The amount water in four pre-treated kaolinite and pyrohyllite samples. Error bars calculated from the three experiments repeats.

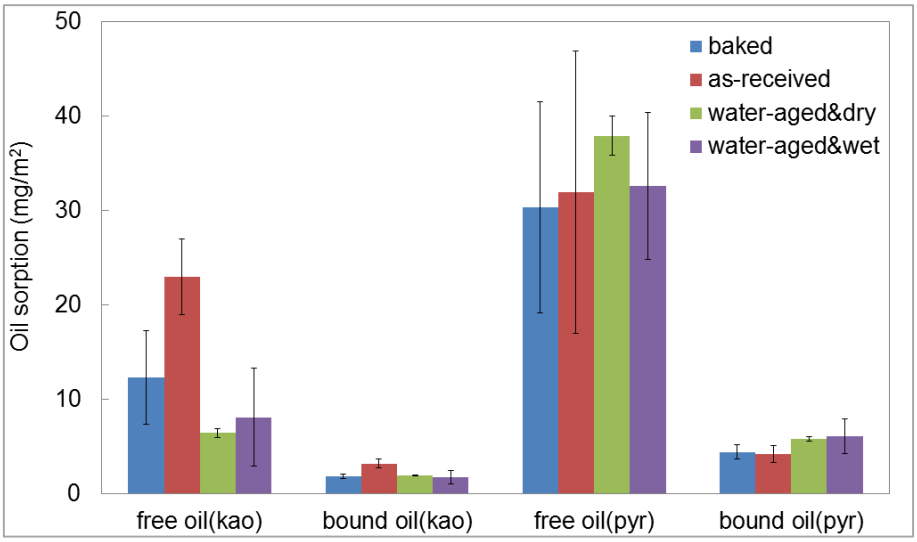

Figure 7.15 The amount oil sorption (inter and intra-particle) on four pre-treated kaolinite and pyrohyllite samples. Error bars were calculated from the three experiment repeats.

7.4.4 Influence of parameters: brine chemistry pre-treatment

A series of experiments were carried out to study the effect of brine concentration, composition and pH on the polar oil sorption of kaolinite and pyrophyllite. Kaolinite and pyrophyllite were aged in pre-treatment solutions with different cation identities, concentrations, and pH; and then they were exposed to the polar oil mixture (see Section 7.3.4). Figure 7.16 shows selected thermograms (one per brine type) for all experiments performed with kaolinite at the two initial pHs, 6.5 (Figure 7.16a) and 8 (Figure 7.16b). Figure 7.19 displays the same information but for the experiments performed with pyrophyllite. Most experiments on kaolinite and pyrophyllite show a similar trend to those presented in the previous section (no cations) i.e., they show three stages of mass loss. The first stage is a sharp weight loss seen between 70-170 °C, and accounts for inter-particle oil and water. The second stage shows a decline in mass between 150-450 °C, which corresponds mostly to the release of chemically bonded oil. The last stage corresponds to the pyrolysis of the clays, i.e. de-hydroxylation, at over 450 °C. The TGA data was linked with MS results to confirm the type of compound released, with results of these measurements shown in Figures 7.17 and 7.18 for kaolinite and Figures 7.20 and 7.21 for pyrophyllite. The only experiment that showed a behaviour different than the mentioned trend was the experiment performed with 1 M $CaCl_2$, which displays a different-looking first stage. For this experiment, weight loss started at a much lower temperature (around 30 °C) and proceeded relatively fast until 180 °C. After this temperature weight loss continued at a slower pace (low slope) until almost settling down at around 400 °C (this was considered the second stage). This was followed by a rapid weight loss interpreted as the de-hydroxylation stage. The difference in behaviour of this experiment could be explained by the variation in hydration number among cations which are 13 for Na^+, 29 for Ca^{2+}, and 5 for Cl^- [56]. This means that one molecule of NaCl can absorb 18 water molecules (after dissociation in Na^+ and Ca^{2+} ions), whereas $CaCl_2$ can adsorb over 39 molecules [56].Therefore, the experiment performed with over 1 M of $CaCl_2$ promotes the adsorption of water more than the others (i.e. those performed with NaCl or lower concentrations of $CaCl_2$). This water would be weakly bound and therefore is mostly released at the first stage (and starting at lower temperatures). The second stage proceeds in a similar way to the other experiments, albeit with a slightly steeper slope. MS data (Figures 7.17 and 7.18 for kaolinite and Figures 7.20 and 7.21 for pyrophyllite) identifies the different stages of water relesae. The figures confirm a fast release of water at the beginning of the experiment, related to the first stage on the TGA diagrams; followed by a stable signal during the second stage (10-40 min or temperature 100-400 °C), indicating a low release of water (except Figure 7.18c and Figure 7.20c, that show “peaks” at other temperatures, which could be

noise due to agglomeration of part of the sample. When this occurs, and the sample is heated up, it will show a very intense signal whenever the agglomerated sample abruptly releases its water [57]). Finally, the de-hydroxylation stage is clearly visible in the MS diagrams.

Calculations of free oil and water from the first stage of weight loss across all the experiments (including repeats) showed large uncertainties, and therefore, are not shown here. Bound oil loss mass was calculated from the second stage. Results are shown in Figure 7.22. For the case of kaolinite, it can be seen that the experiment performed with 1 M $CaCl_2$ solution show a much larger amount of bound oil compared to the low $CaCl_2$ (0.001 M) concentrations, and all concentration of NaCl, at both pH values studied (6.5 and 8). This shows that divalent cations play a crucial role in determining oil sorption behaviour of the kaolinite surface [8, 15].

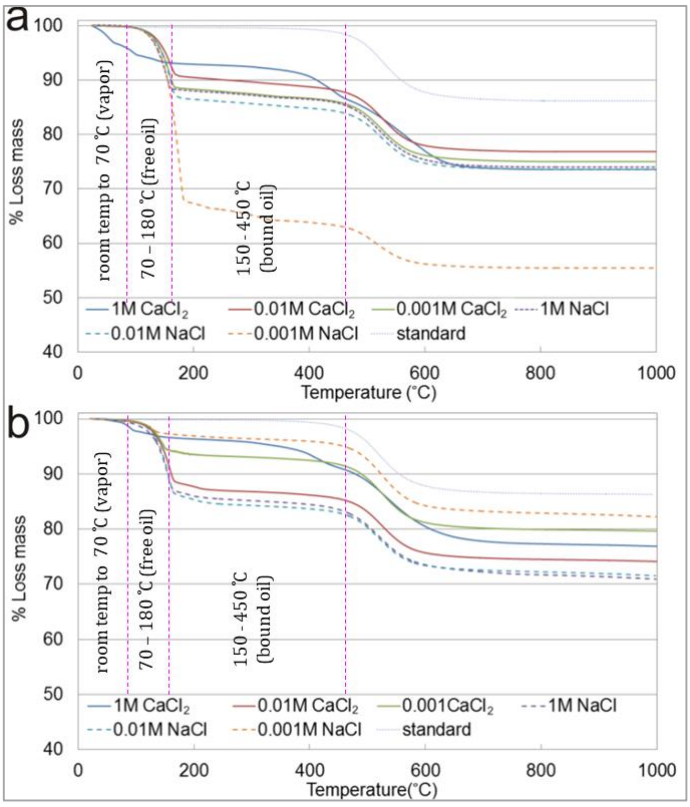

Figure 7.16 Thermograms of experiments performed on pre-treated kaolinite at pH 6.5 (a) pH 8 (b).

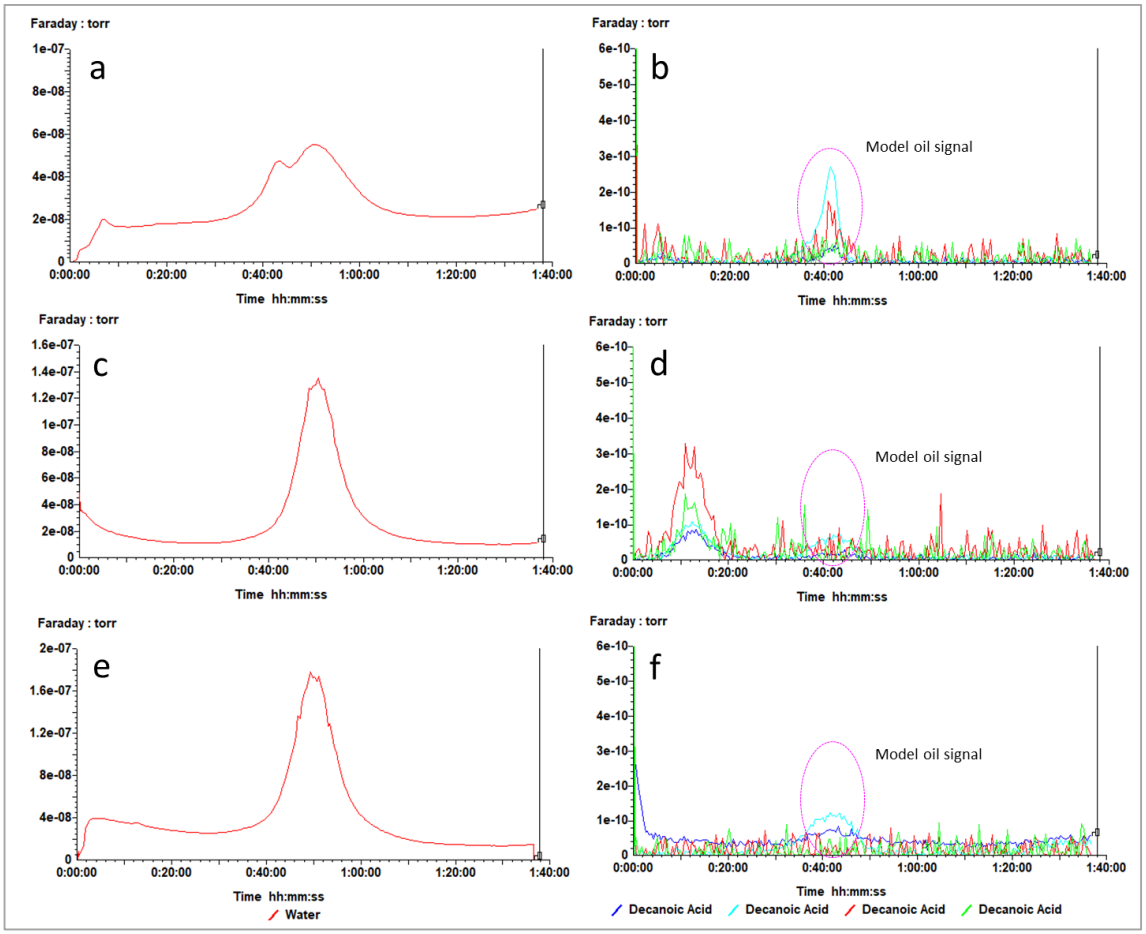

Figure 7.17 Selected MS data of experiments performed with pre-treated kaolinite; 1M of $CaCl_2$ (a, b), 0.01M of CaCl2 (c, d), 0.001M of CaCl2 (e, f).

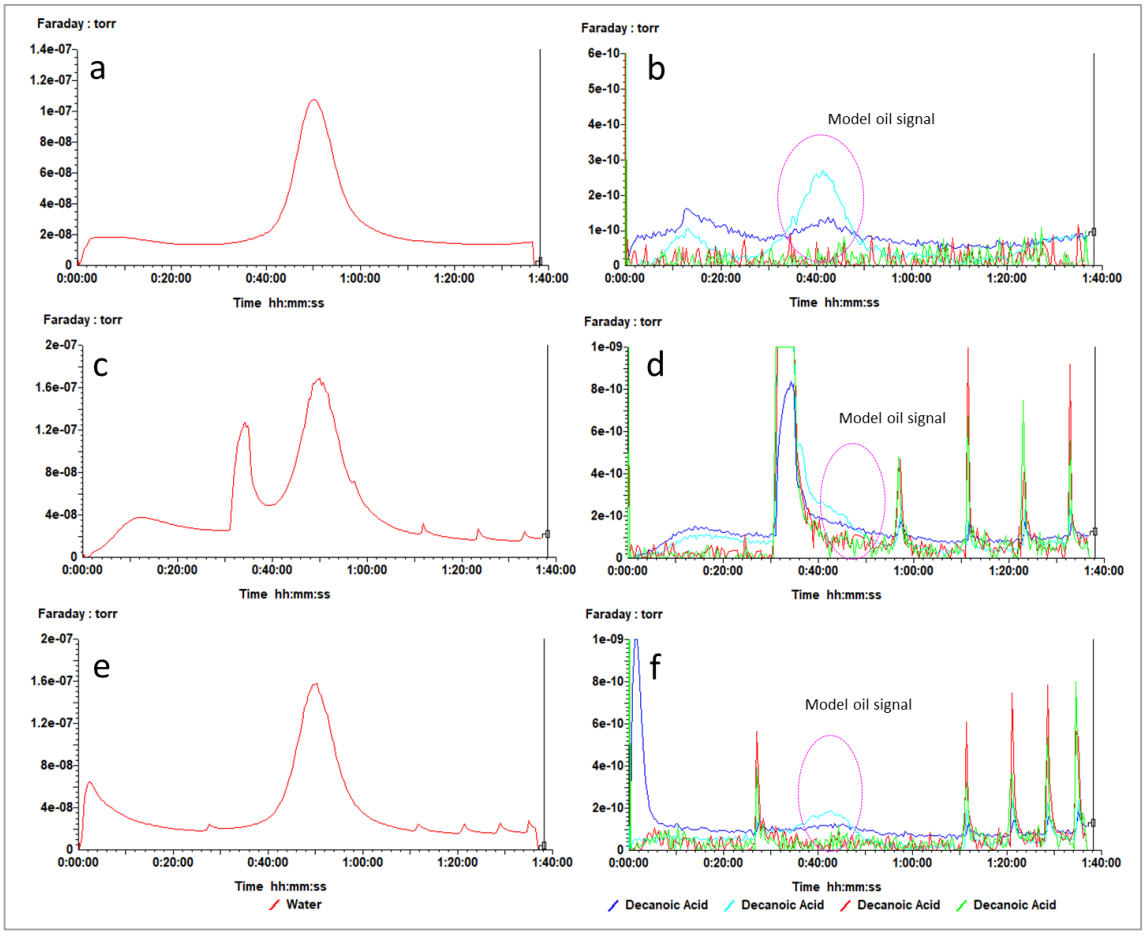

Figure 7.18 Selected MS data of experiments performed with pre-treated kaolinite; 1M of NaCl (a, b), 0.01M of NaCl (c, d), 0.001M of NaCl (e, f).

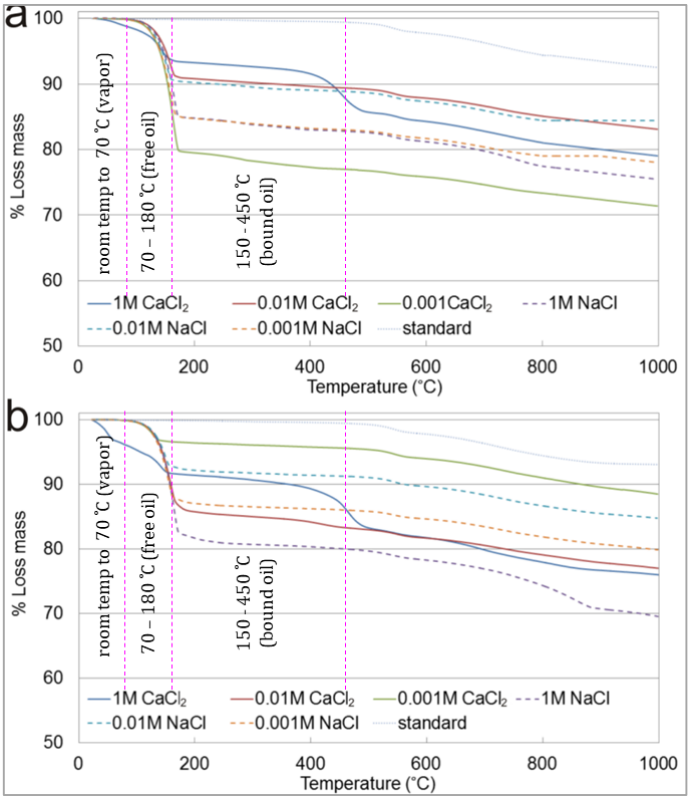

Figure7.19 Thermograms of experiments performed on pre-treated pyrophyllite at pH 6.5 (a) pH 8 (b).

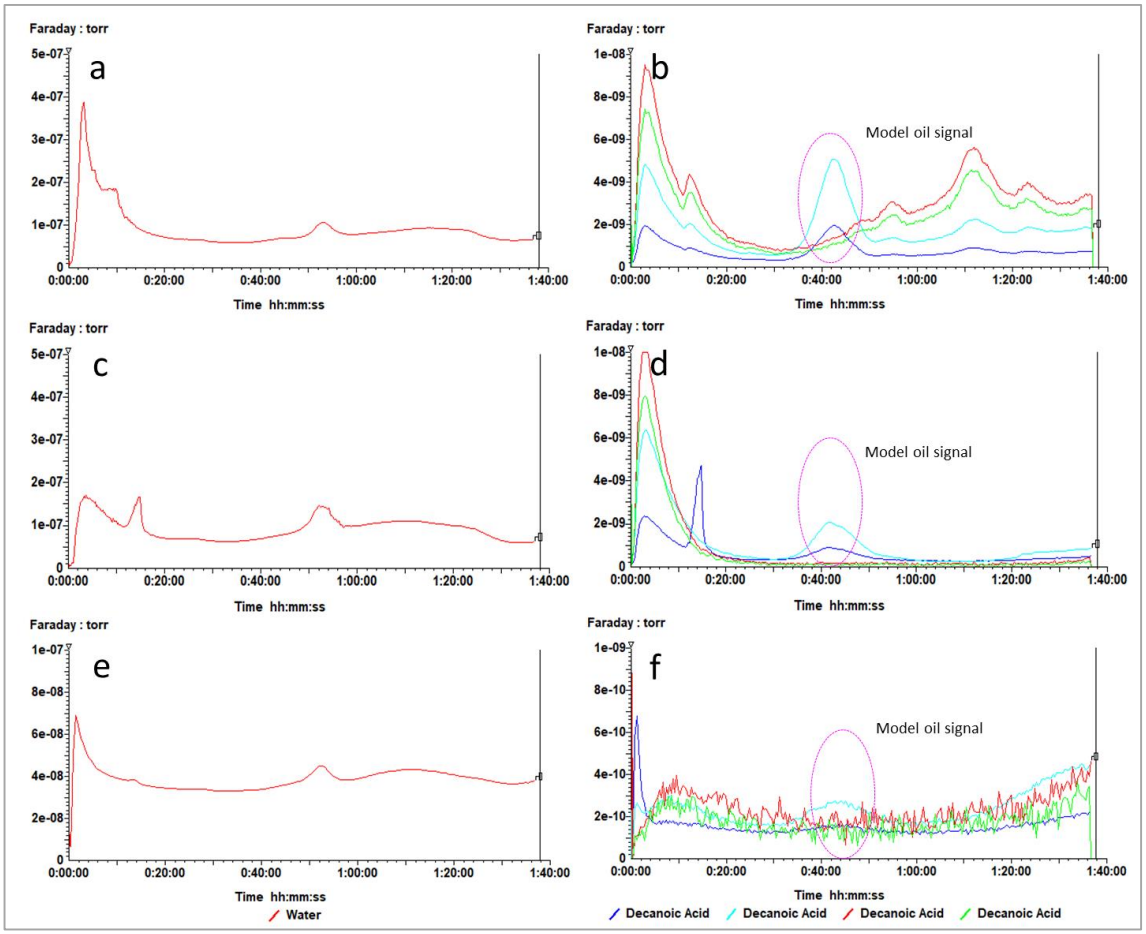

Figure 7.20 Selected MS data of experiments performed with pre-treated pyrophyllite; 1M of CaCl2 (a, b), 0.01M of CaCl2 (c, d), 0.001M of CaCl2 (e, f).

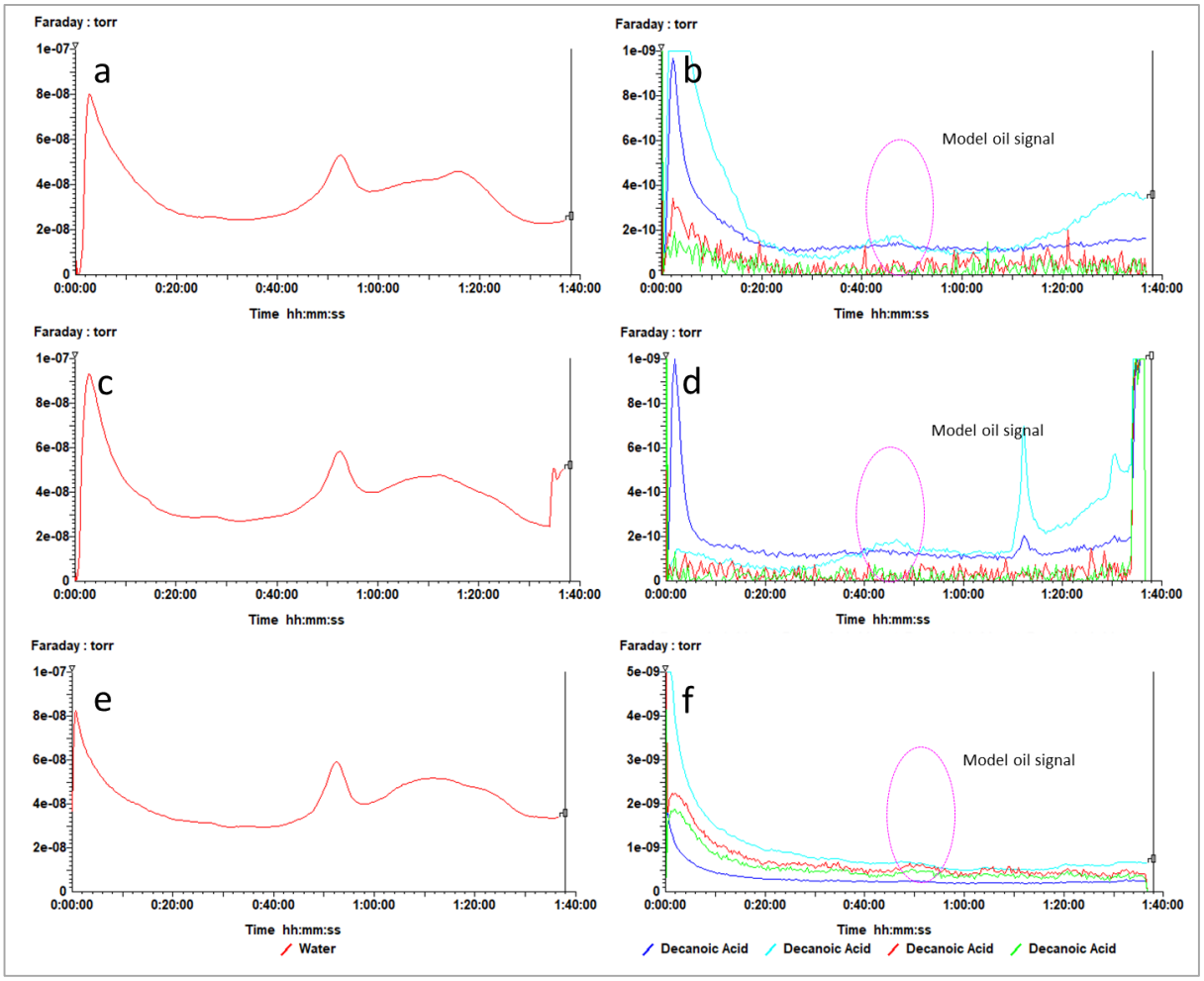

Figure 7.21 Selected MS data of experiments performed with pre-treated pyrophyllite; 1M of NaCl (a, b), 0.01M of NaCl (c, d), 0.001M of NaCl (e, f).

As can be seen in Figure 7.22a, for both pH values the amount of bound oil on kaolinite sharply decreased when the concentration decreased from 1 M to 0.001 M of $CaCl_2$. In contrast, the results from the experiments performed with NaCl do not show a clear trend in the measured oil sorption with varying concentration at either pH, and the measured relative variation (at constant pH) were much smaller than those measured for the experiments performed with $CaCl_2$. The effect of pH on the relative oil sorption was very small for the experiments performed with $CaCl_2$ (which, nevertheless, showed a small decrease in the amount of oil sorbed with increasing pH), but relatively large for those performed with NaCl. In all cases the amount of sorbed oil decreased with increasing pH, with value of 43, 13 and 53% for the experiments performed with 1, 0.01 and 0.001 M solutions, respectively. These results match the measurements performed by CFM (Chapter 5). For measured adhesion in the presence of Ca^{2+} (and using a -COOH probe) an increase in pH resulted in an increase in adhesion over the siloxane face (Figure 5.10), but a decrease

on the aluminol face (Figure 5.17), and although comparing absolute adhesion data on CFM was not possible, it would be expected that both effects would counteract each other to some extent, as seen in the data reported here (Figure 7.22) where pH change does not lead to a large variation in oil sorbed. In the case of the experiments performed on NaCl, however, CFM showed a decrease in the measured adhesion, as a function of increasing pH, for both the siloxane and aluminol face (Figures 5.11 and 5.17, respectively). When both faces are considered, that should lead to a relatively large decrease in oil sorption (specially one whose polar component is a –COOH containing acid), as observed in the TGA experiments shown in Figure 7.22. These results also imply that a decrease in both Ca and Na concentrations, coupled to an increase in pH may lead to a larger increase in oil recovery, if kaolinite is, indeed, the most crucial phase in determining the reservoir wettability state.

Figure 7.22b shows oil adsorption on pyrophyllite as a function of brine concentration at both pH 6.5 and pH 8. The observed behaviour is very similar to that displayed by kaolinite at both pH values, with the measured bound oil being significantly higher at 1 M $CaCl_2$ than at lower $CaCl_2$ concentrations or any NaCl concentration. The data from NaCl experiments showed a relatively small variation of oil sorption with concentration, and always smaller than that observed with $CaCl_2$. Significantly, the oil sorption behaviour showed no variation with respect to pH with either $CaCl_2$ or NaCl brines at all concentration.

Comparing kaolinite to pyrophyllite, they both show similar trends with varying concentration of $CaCl_2$ and NaCl. However, absolute values of oil sorption were consistently higher on pyrophyllite than kaolinite (2 or 3 times), across all brine compositions, highlighting the higher oil affinity for pyrophyllite surface. The hydrophobic character of pyrophyllity stems from its low charge and the fact that both exposed basal planes are siloxane in composition (REF to Yin 2012 paper). This hydrophobicity is partially counteracted by the fact that its edges are composed of hydrophilic silanol and aluminol groups, but not to the extent of reversing its affinity for oil molecules. On the contrary, it is known that the kaolinite silica phase is slightly hydrophobic, whereas the aluminol face is hydrophilic, due to the presence of OH groups (REF to Yin 2012). The net result being a smaller degree of hydrophobicity than the pyrophyllite crystals.). The observations identified that high concentration of Ca^{2+} supports increased oil sorption on the studied clay surfaces, but Na^{+} does not. This result confirms the divalent bridging theory and multi ion exchange mechanism for clay minerals [8], whereby divalent cations can form a bridge between the negatively charged clay surface and negatively charged of polar oil molecule, whereas in the case of monovalent cation such a Na^{+} this is not supported resulting in a small amount of oil sorption [8]. Results also support the observations performed with CFM

on siloxane face of kaolinite crystals, where a very different adhesion behaviour of -COOH molecules was observed between measurements taken in the presence of $CaCl_2$ solutions and those performed on NaCl brines, as described in Chapter 5.

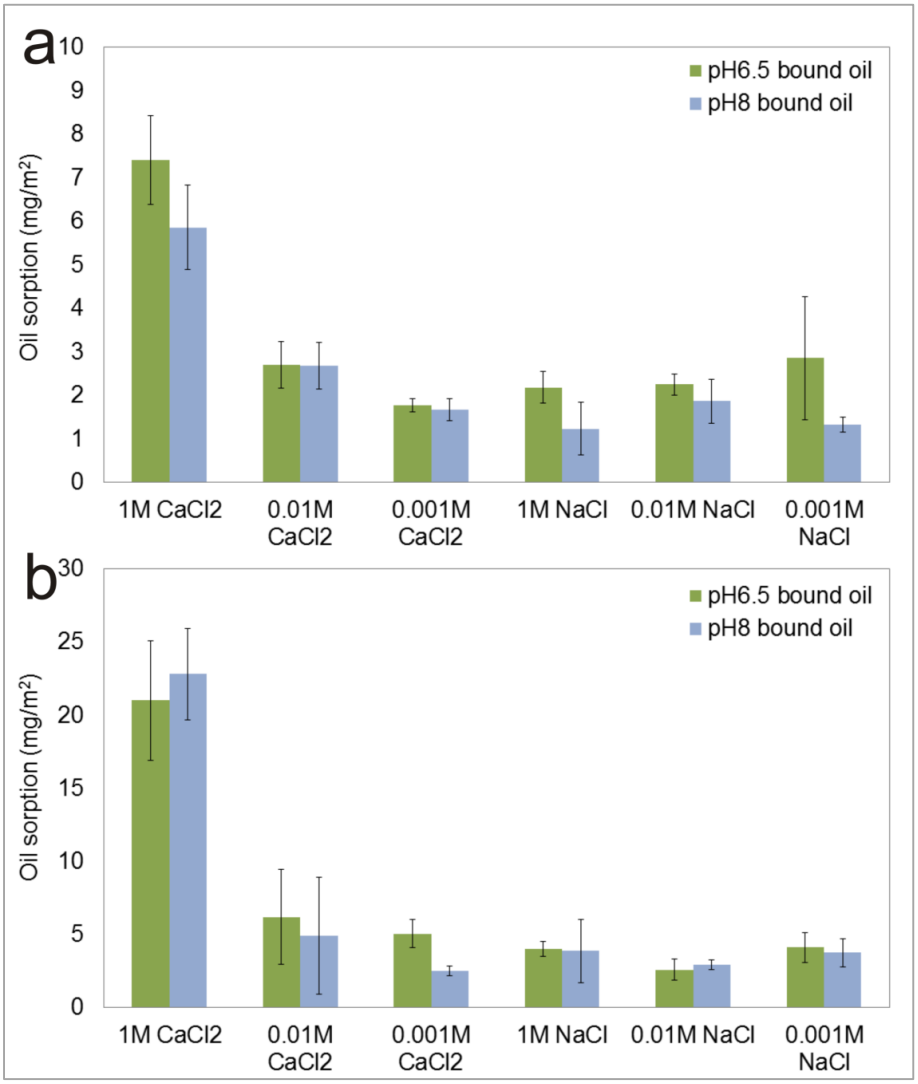

Figure 7.22 Diagram showing the amount of bound-oil adsorption in different pre-treatment solutions and pH on a) kaolinite and b) pyrophyllite.

7.4.5 Influence of parameters: ration of Na^+:Ca^{2+} and ionic strength of pre-treatment

In order to fully understand the effects of cation identity and ion-strength on oil sorption two series of experiments were performed: 1) constant ionic strength (1.5) and varying Na^+:Ca^{2+} ratios (from 20:1 to 1:1), and 2) constant Na^+:Ca^{2+} ratio (10:1, 5:1 and 1:1) at varying ionic strength (1.5, 1.0 and 0.1) (Table 7.5). Figure 7.23 shows the thermograms of all the experiments performed with kaolinite. Most of the thermograms show a three-stage mass loss, in a very similar way to previous experiments, with the exception of the

experiment performed with a 1:1 Na^+:Ca^{2+} ratio (ionic strength of 1.5), where the loss of mass, during the first stage,occurs at a lower temperature. This behaviour is similar to the one observed on the experiments performed with high (1 M) $CaCl_2$ and can be explained by the same process, i.e. a higher amount of loosely-bound water drawn into the sample due to the higher hydration numbers of Ca^{2+}, (Section 7.3.4). Overall, the initial stage shows the weight loss at 70-180 °C which is characterized by the release of a mixture of water and oil as can be seen in the MS data shown in Figure 7.24. On the second stage (180-450 °C) a few differences in behaviour across samples were observed, for the experimental series at constant ionic strength. The experiments performed with Na^+:Ca^{2+} ratios of 20:1 and 10:1 show a constant slope across the temperature range; in contrast the experiments performed with Na^+:Ca^{2+} ratios of 5:1 and 1:1 show a constant slope up to 350 °C followed by an increase in slope until 450 °C (the start of the de-hydroxylation stage). This behaviour is particularly evident on the experiment performed with a 5:1 ratio and results in the highest percentage of loss mass of all the experiments. For the experiments performed with variable ionic strength, no large differences in behaviour were observed across experiments. Lastly, as with all other experiments, the last stage corresponds to the dehydroxylation, as observed with the large release in water measured in the MS.

The thermograms of brine pre-treated pyrophyllite are shown in Figure 7.25, with associated MS spectra shown in Figure 7.26. It can be seen that those experiments performed at constant ionic strength (1.5) but different Na^+:Ca^{2+} ration follow a similar pattern as those performed with kaolinite, with three well defined stages of mass loss at similar temperature ranges. In this case, however, no early release of water at low temperature was observed for the experiment performed with Na^+:Ca^{2+} of 1:1. For stage 2 (180 to 450 °C), this experiment did show the same increase in the weight loss ratio (increase in slope in the thermogram) before 400 °C (i.e. well before the de-hydroxylation stage that starts around 450 °C). In addition, the experiment performed with Na^+:Ca^{2+} of 5:1 also showed a similar increase in mass loss ratio just before 400 °C. As was the case for kaolinite, the other two experiments showed a constant slope in the thermogram. With respect to the experiments performed with varying ionic strengths, they all showed the same behaviour, although the magnitude of total mass loss varied significantly across experiments, reflecting large differences in water adsorption at the first stage (also observed in control experiments).

Figure 7.27 shows the amount of bound oil sorption (as calculated from the TGA diagrams and control experiments (Section 7.3.6) as a function of the Na^+:Ca^{2+} ratio for the experiments performed at constant ionic strength (IS=1.5). The quantity of oil sorption on both kaolinite and pyrophyllite shows a similar trend. It can be seen that the amount of

bound oil rises linearly with increasing Na^+:Ca^{2+} ratio in the range 20:1 to 5:1. Bound oil then significantly increases when the solution contains 1:1 of Na^+:Ca^{2+}. Oil sorption on kaolinite increased from 1.4 mg/m^2 (20:1) to 5.2 mg/m^2 (1:1), whereas on pyrophyllite it started at 3.8 mg/m^2 and increased to 11.8 mg/m^2 at a 1:1 ratio. These observations confirm the dominant role of Ca^{2+} in increasing oil sorption, and reinforce the results from the single-ion experiments described before (Section 7.4.4), where the presence of Ca^{2+} lead to larger oil sorption (when compared to the Na^+ experiments).

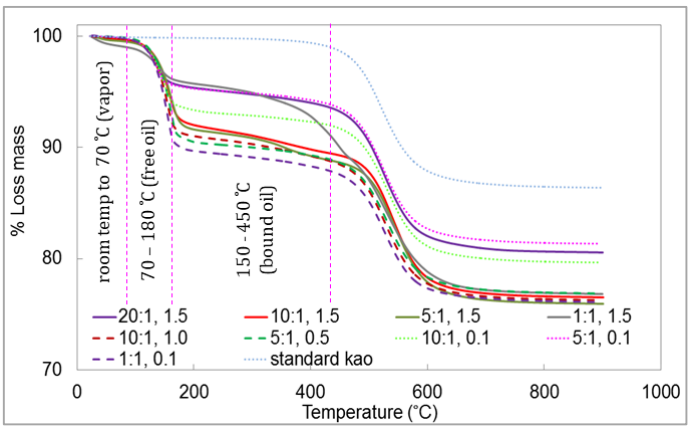

Figure 7.23 Thermograms of experiments performed with mixed-brine pre-treatment solutions (Na^+:Ca^{2+} ratio and ionic strength) on kaolinite.

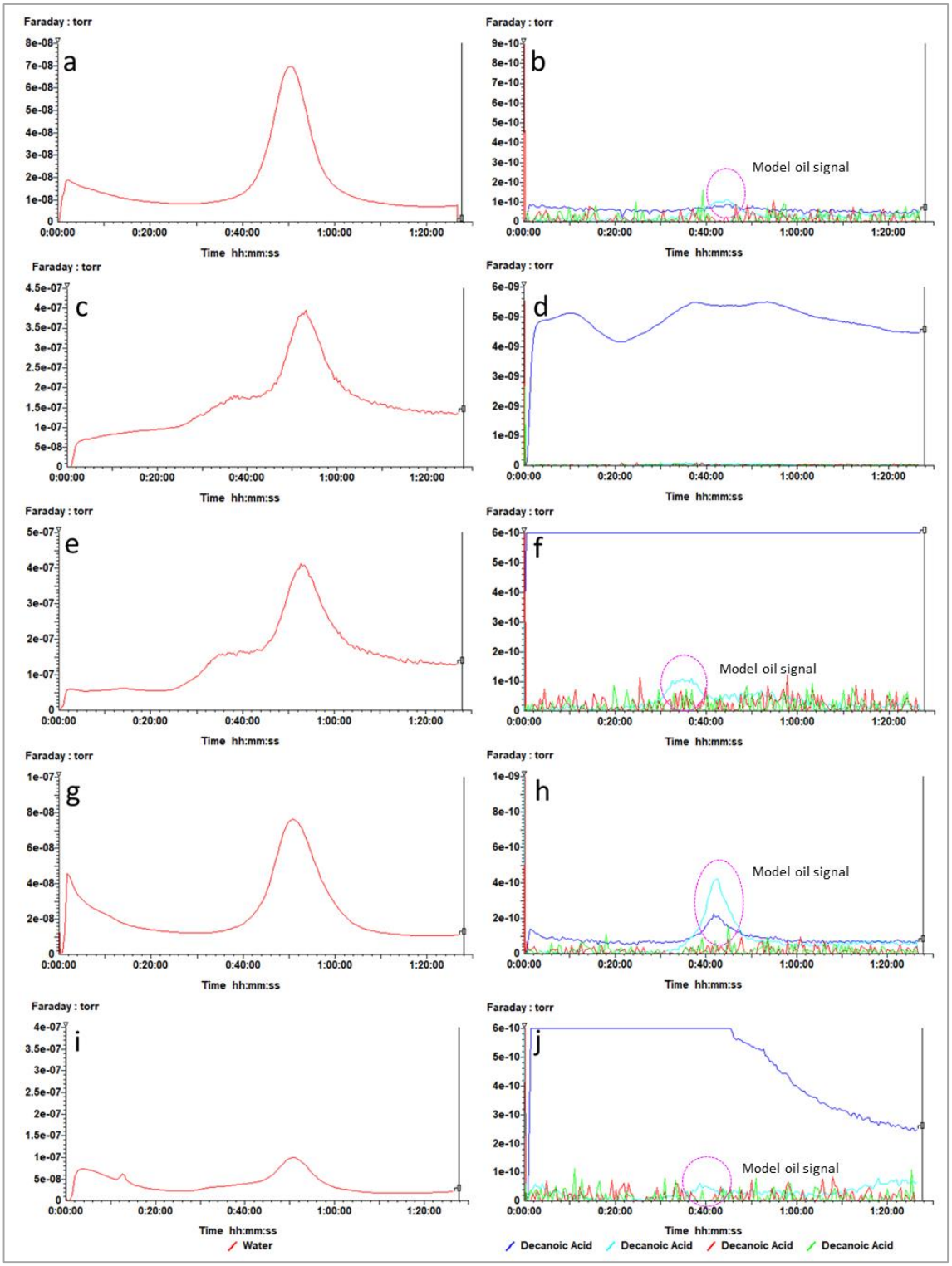
Faraday : torr
a
Time hh:mm:ss
Faraday : torr
b
Model oil signal
Time hh:mm:ss
Faraday : torr
c
Time hh:mm:ss
Faraday : torr
d
Time hh:mm:ss
Faraday : torr
e
Time hh:mm:ss
Faraday : torr
f
Model oil signal
Time hh:mm:ss
Faraday : torr
g
Time hh:mm:ss
Faraday : torr
h
Model oil signal
Time hh:mm:ss
Faraday : torr
i
Time hh:mm:ss
Water
Faraday : torr
j
Model oil signal
Time hh:mm:ss
Decanoic Acid
Decanoic Acid
Decanoic Acid
Decanoic Acid

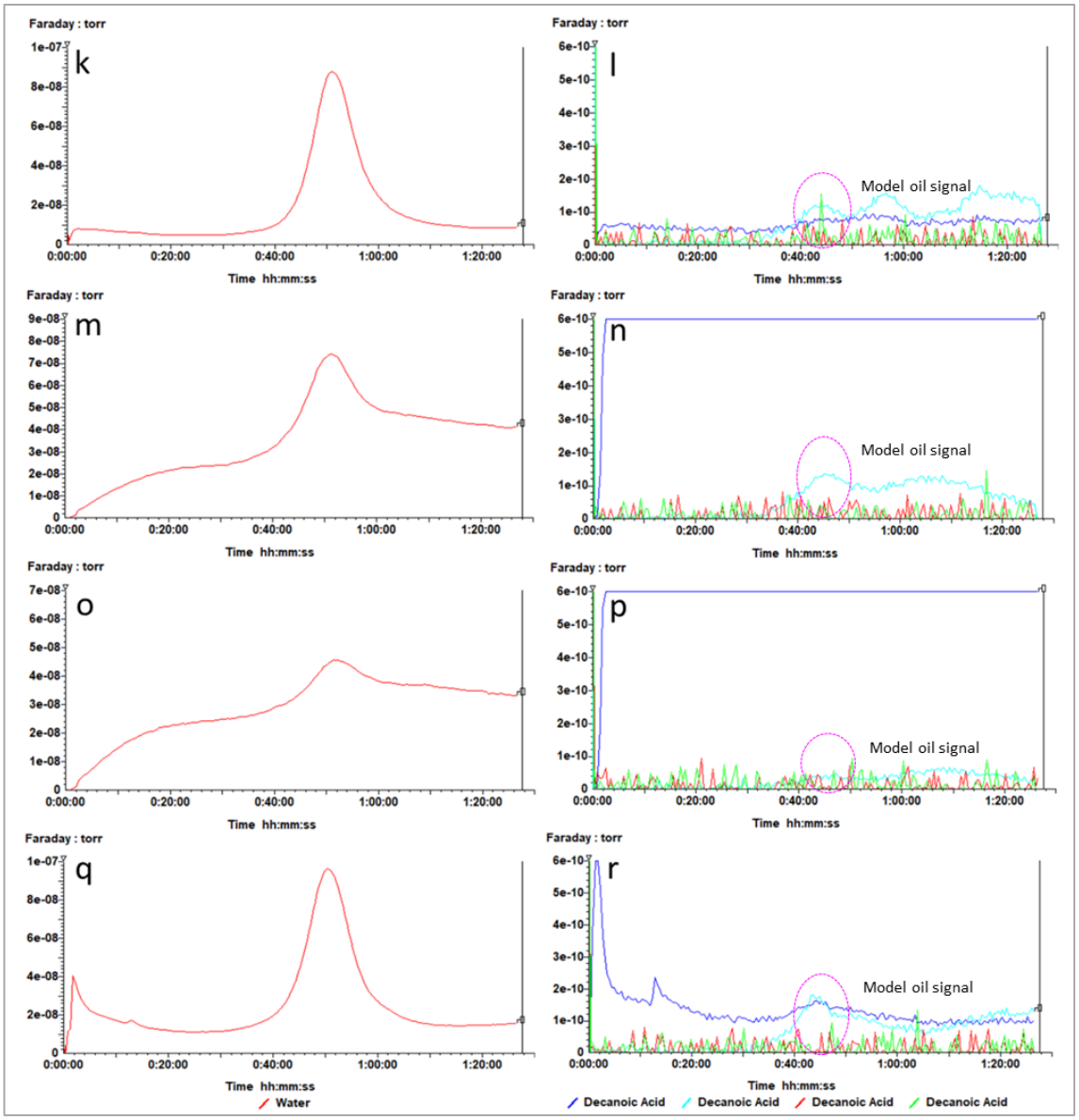

Figure 7.24 Selected MS data diagrams for experiments performed with mixed brines on kaolinite. Na^+:Ca^{2+} ratio of 20:1 and IS iof 1.5 (a, b); Na^+:Ca^{2+} ratio of 10:1 and IS of 1.5 (c, d); Na^+:Ca^{2+} ratio of 5:1 and IS of 1.5 (e, f); Na^+:Ca^{2+} ratio of 1:1 and IS 1.5 (g, h); Na^+:Ca^{2+} ratio of 10:1 and IS of 1.0 (i, j); Na^+:Ca^{2+} ratio of 5:1 and IS of 0.5 (k, l) ; Na^+:Ca^{2+} ratio of 10:1 and IS of 0.1 (m, n); Na^+:Ca^{2+} ratio of 5:1 and IS of 0.1 (o, p); Na^+:Ca^{2+} ratio of 1:1 and IS of 0.1 (q, r).

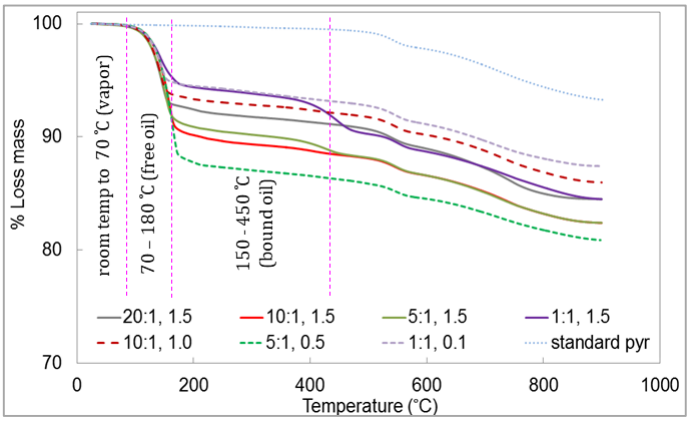

Figure 7.25 Thermograms of experiments performed with mixed-brine pre-treatment (Na^+:Ca^{2+} ratio and ionic strength) on pyrophyllite.

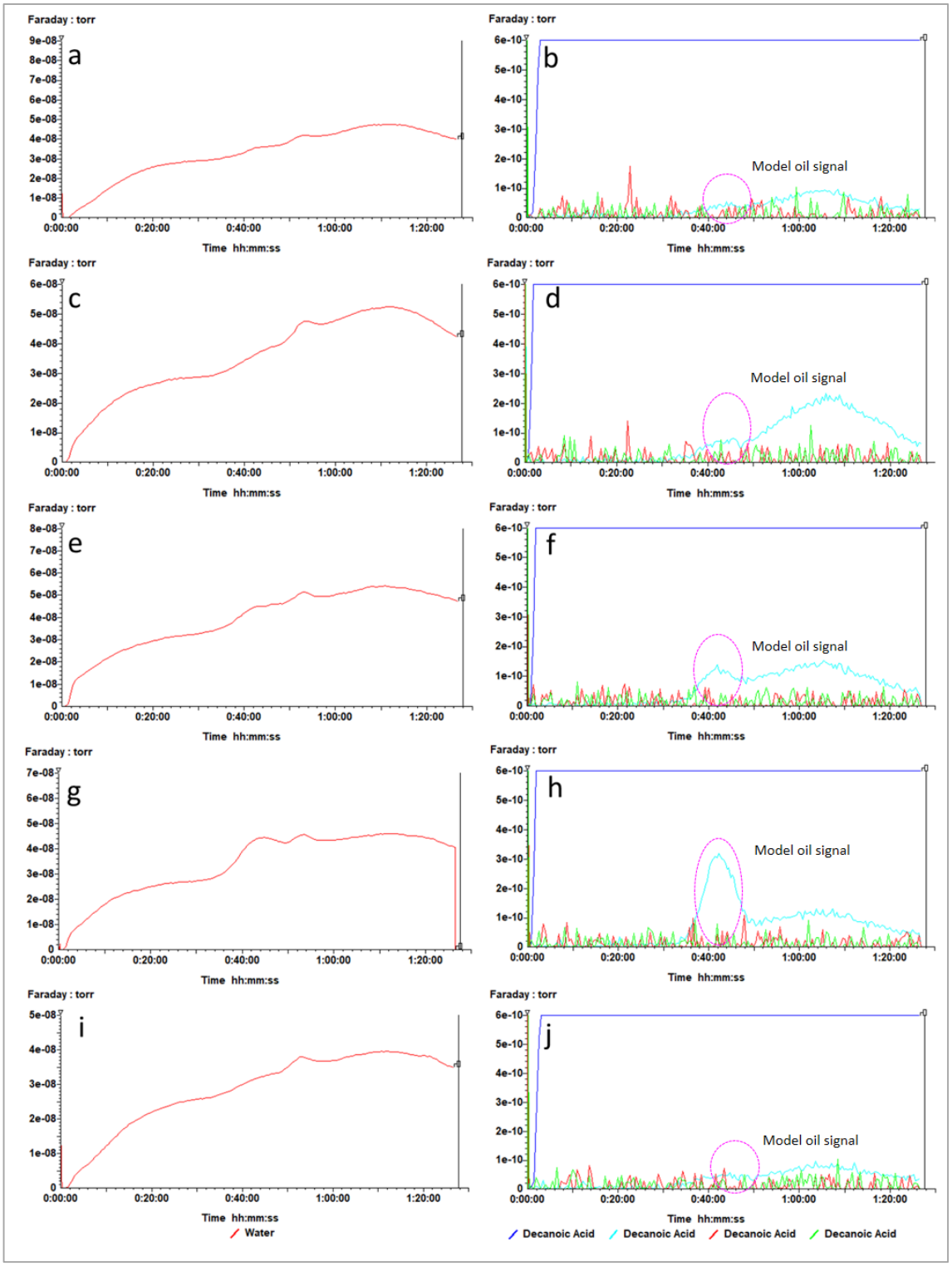
Faraday : torr
a
b
c
d
e
f
g
h
i
j
Model oil signal
Time hh:mm:ss
Water
Decanoic Acid
Decanoic Acid
Decanoic Acid
Decanoic Acid

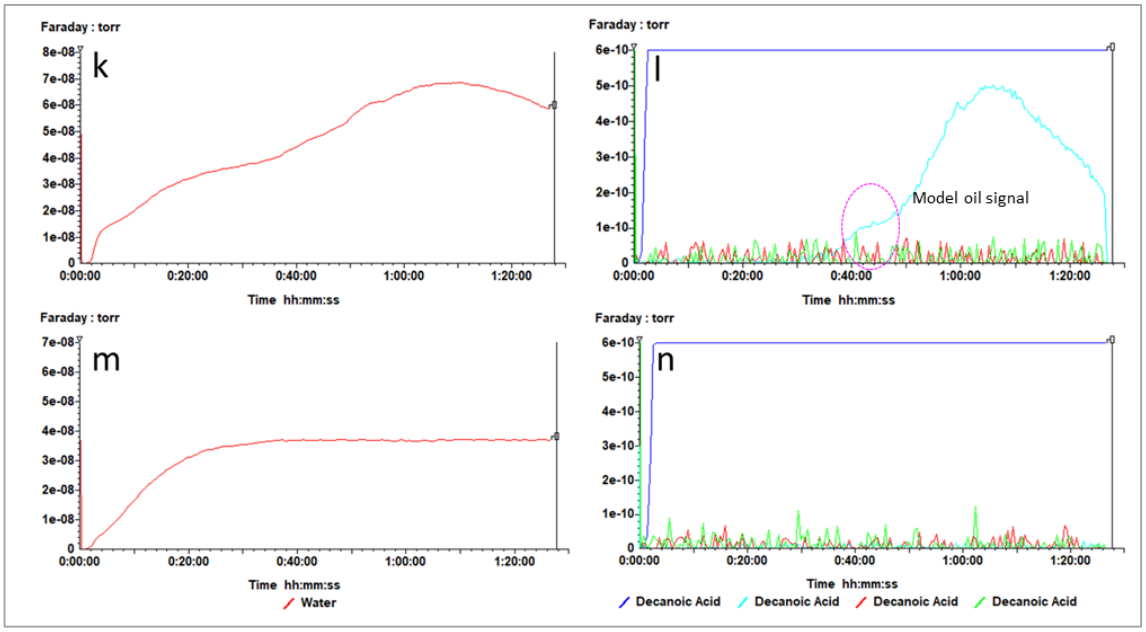

Figure 7.26 Selected MS data diagrams for experiments performed with mixed brines on pyrophyllite; Na^+:Ca^{2+} ratio of 20:1 and IS of 1.5, (a, b); Na^+:Ca^{2+} ratio of 10:1 and IS of 1.5 (c, d); Na^+:Ca^{2+} ratio of 5:1 and IS of 1.5 (e, f); Na^+:Ca^{2+} ratio of 1:1 and IS of 1.5 (g, h); Na^+:Ca^{2+} ratio of 10:1 and IS of 1.0 (i, j); Na^+:Ca^{2+} ratio of 5:1 and IS of 0.5 (k ,l) ; Na^+:Ca^{2+} ratio of 1:1 and IS of 0.1 (m, n).

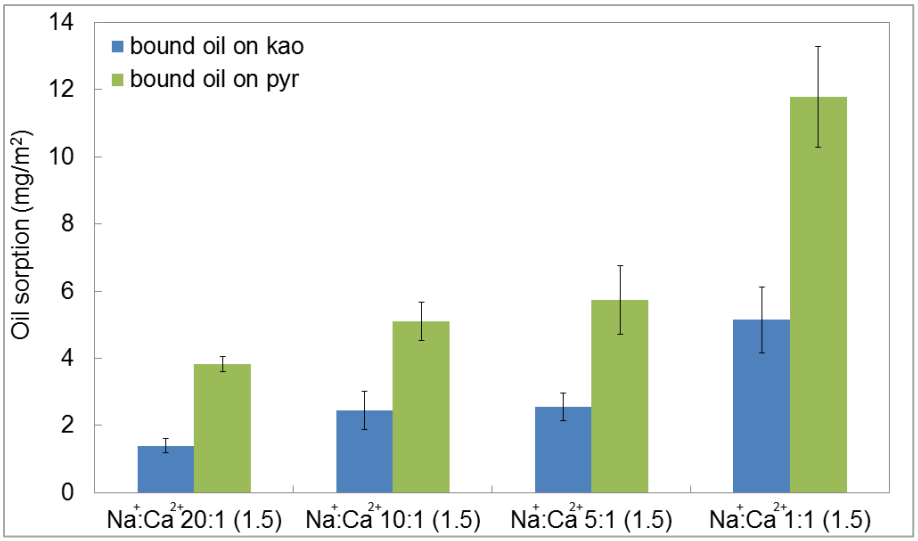

Figure 7.27 Bound oil absorbed on kaolinite and pyrophyllite with different pre-treated brines of Na^+:Ca^{2+} ratio and constant ionic strength (1.5).

The experiments performed with a constant Na^+:Ca^{2+} and varying ionic strength show an effect of this parameter (IS) on total oil sorption (Figure 7.28). It can also be seen that this

effect was more pronounced the smaller the Na^+:Ca^{2+} ratio was. For a Na^+:Ca^{2+} of 10:1, total oil sorption decreased by around 25% when the ionic strength IS decreased from 1.5 to 0.1. For a Na^+:Ca^{2+} of 5:1 the total decrease of oil sorption was approximately 45%. Finally, the experiments performed with a Na^+:Ca^{2+} of 1:1 showed the largest decrease in oil sorption (70%). In addition to this, the results indicate that at low ionic strength values (0.1) the ratio of Na^+:Ca^{2+} ions in solution does not lead to large variations in the amount of oil sorbed. These results indicate that an expansion in the electrical double layer (EDL) width (as controlled by a reduction in the ionic strength of the brines) leads to a decreasing affinity of the polar oil molecules to the kaolinite surfaces. Therefore, for this clay mineral type, both the cation identity and ionic strength play a role in determining its oil sorption behaviour.

Results from the experiments performed on pyrophyllite show a different behaviour. For the experiments performed with Na^+:Ca^{2+} ratios of 10:1 and 5:1 it can be seen that decreasing of the ionic strength resulted in an increase in oil sorbed at IS=1.0, which was then followed by a large decrease when the IS was reduced to 0.1. It is important to mention that a relatively high fluctuation in the measured values was observed on the experiments performed at ionic strength of 1, which led to the relatively large error bars, as can be seen in Figure 7.28. In fact a fourth repeat was added at these conditions, which fall close to the average value. For the 1:1 ratio only the experiments at low and high IS were carried out and they show a very large reduction in sorption with decreasing IS. Overall, it can be said that the effect of reducing the IS (from 1.5 to 0.1) on the oil sorption is higher on the pyrophyllite samples, when compared to kaolinite and again, that the presence of a larger amount of Ca^{2+} increases the IS effect.

The combination of the results from the experiments performed with a varying Na^+:Ca^{2+} ratio and ionic strength indicate a more complex picture regarding the main mechanism behind oil sorption into clay mineral surface. For kaolinite the results of the experiments performed with decreasing Na^+:Ca^{2+} ratio highlight the role of Ca^{2+} in increasing the oil sorption, which would be related to a cation bridging mechanism, however, the experiments with varying ionic strength show a clear influence of this parameter as well, but related to the Ca^{2+} content. This indicates that although Ca^{2+}, through its role as a bridge in "anchoring" polar organic molecules is crucial, at a certain point the reduction of the electrical double layer counter acts, to a great extent, that effect as can be seen when decreasing the IS from 1.5 to 0.1 on the experiments with the highest Ca^{2+} content (which shows both, the highest oil sorption and the lowest). For pyrophyllite the overall trends are the same, but the actual values of oil sorption are higher, due to the presence of two, hydrophobic, siloxane faces on this mineral (as opposed to just one for

kaolinite). This fact, seems to indicate that the aluminol face has a smaller role to play in determining the overall oil sorption mechanism, at least at the pH range studied here.

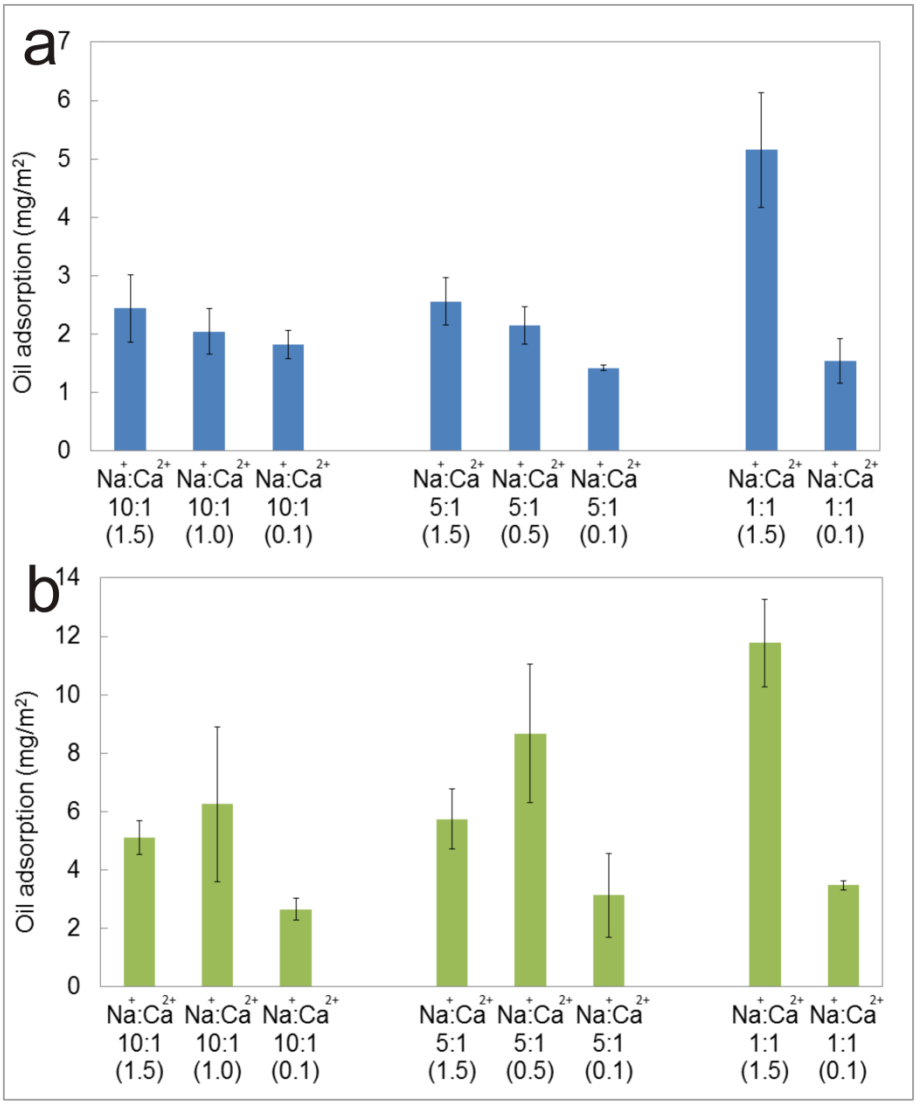

Figure7.28 Graphs showing the measured bound oil for the experiments performed with varying ionic strength and constant Na^{+}:Ca^{2+} ratios for both kaolinite (a) and pyrophyllite (b).

7.4.6 FTIR analysis

In this section, we report the results of the IR spectroscopy measurements used to probe the structure of clay-brine-oil in order to support the data from TGA-MS. As a starting point, the model oil (1 M decanoic acid dissolved in dodecane) was measured by IR spectrometry with results shown inFigure 7.29. In addition IR spectra of dodecane (non-polar model oil) and sodium decanoate (≥98% pure from Sigma Aldrich®) where taken. Spectrum of 1M of decanoic acid and sodium decanoate show the same peak at 1466, 1444, 1427, 1411 cm^{-1}

indicating symmetric C-H bending of alkane [58, 59].They also show a band at 1555 cm^{-1} which is characteristic of the asymmetric $–COO^-$ stretching [58, 60, 61]; while, dodecane only has the C-H bending bands of alkane at 1466, 1444, 1427, 1411 cm^{-1} [58, 59]. Therefore, the oil molecules can be divided between polar and non-polar oil by using the band at 1555 cm^{-1} (asymmetric $–COO^-$). This same band can be used to identify the complex between head group of model oil and salt [62].

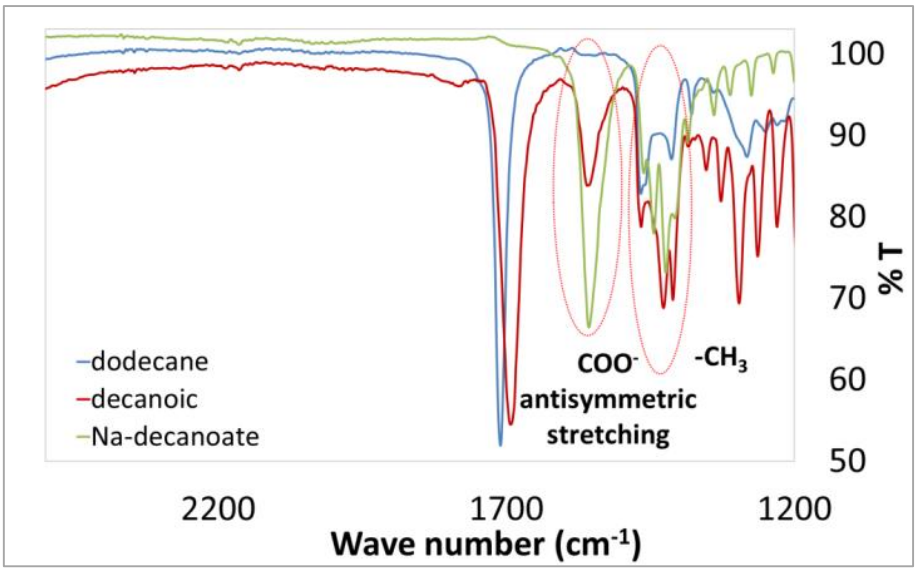

Figure 7.29 IR spectra of dodecane (non-polar model oil), decanoic acid (polar-model oil), and Na-decanoate (salt polar-model oil).

To elucidate the model oil adsorption on kaolinite and pyrophyllite, IR was performed on aged kaolinite and pyrophyllite by various brines (with different concentration, cation types, and pH). The samples were then aged in the polar model oil in the same way as the preparation for TGA-MS. IR results of as-received kaolinite and treated-kaolinite are shown in Figure 7.30. Spectrum of as-received kaolinite did not show any band at 1200-3600 cm^{-1}, but where shown on those kaolinite brines aged in 0.001M of $CaCl_2$, 1M of $CaCl_2$, 0.001 M of NaCl, and 1M of NaCl (both pH 5.6, 6.5, and 8) solutions, as can be seen in Figure 7.30a, b, c, and d respectively. IR spectra of all aged-kaolinite show a series of bands at 2985, 2923 and 2857 cm^{-1}, which were straightforwardly assigned to CH_3 asymmetric stretching C-H vibrations, CH_2 antisymmetric, and CH_2 symmetric respectively [63-65], and at 1467, 1410 cm^{-1} which identify to C-H bending [59].

Among the results of four different initial brines, the IR spectrum of the sample treated with 1M of $CaCl_2$ is different from the other three brines. Three distinct peaks can be only observed in the spectrum of 1 M of $CaCl_2$-aged kaolinite at 3495 and 3435 cm^{-1},

which were assigned to the water [60], and at 1539 cm^{-1}, which is the characteristic asymmetric $–COO^-$ and which may be identified as salt-oil adsorption on kaolinite [62].

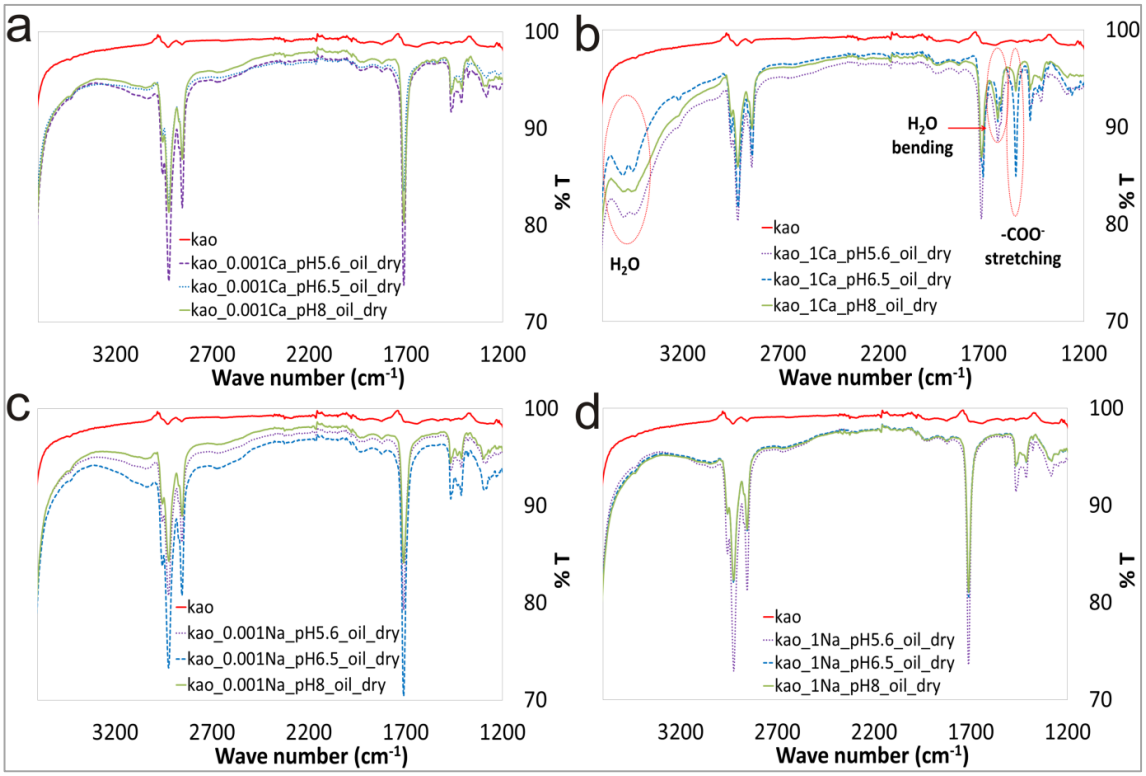

Figure 7.30 IR spectra of brine and oil aged kaolinite (at pHs of 5.6, 6.5 and 8) a) initial brine is 0.001M of $CaCl_2$; b) initial brine is 1M of $CaCl_2$; c) initial brine is 0.001M of NaCl; d) 1M of NaCl.

Similarly, pyrophyllite was aged in four solutions:0.001 M $CaCl_2$, 1 M $CaCl_2$, 0.001 M NaCl, 1 M NaCl. IR spectra from these samples are shown in Figure 7.31. All spectra from these experiments shows four peaks at 2850, 2872, 2922, and 2955 cm^{-1} which were assigned to the CH_2 symmetric, CH_3 symmetric, CH_2 antisymmetric and CH_3 asymmetric stretching C-H vibrations, respectively [1-3]. Peaks at 1629 and 1616 cm^{-1} reveals an increased amount of water [60]. Bands at 1468, 1429, 1406, and 1380 cm^{-1} were identified as symmetric bending of C-H groups of alkane. Exceptionally, for the pyrophyllite treated by 1M $CaCl_2$ (Figure 7.31b) additional peaks at 3472 and 3409 cm^{-1} were observed, which were assigned to water; and at 1539 cm^{-1} which was identified as the aysymetric stretching of $-COO^-$ which may indicate the interaction of calcium cations and polar oil molecules [62].

Therefore, these results confirm, to some extent, what was observed from TGA-MS. Only 1M of $CaCl_2$ aged clay showed water adsorption peak at 3495 and 3435 cm^{-1}. This indicates that 1M of $CaCl_2$ induced more water adsorption than other brines, which is

similar to what was observed on the TGA-MS measurements which showed a large mass loss in the first stage (0-70 °C). Also, the presences of the asymmetric stretching of $-COO^-$ identifyed the possible presence of protonated carboxylate groups of the polar model oil which may be participating incation bridging. The ion bridging would support oil adsorption on kaolinite, which was observed in its largest amount by TGA-MS analysis on those experiments performed with 1M $CaCl_2$. In the case of the experiments performed with the lower concentration of $CaCl_2$ and both concentrations of NaCl, only the $-CH_3$ and $-CH_2$ bands were found, indicating the absence of deprotonated carboxylate groups which could form cation bridging, which would translate in less amount of oil adsorption on kaolinite and pyrophyllite.

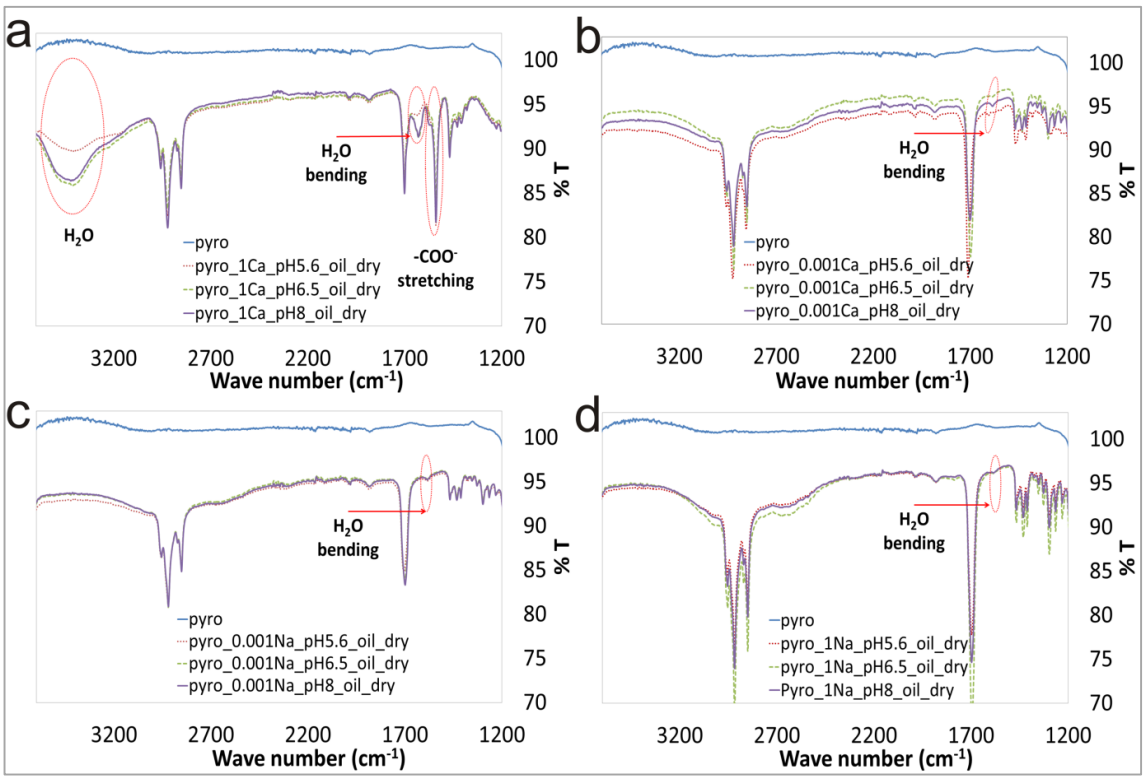

Figure7.31 IR spectra of initial water and oil aged pyrophyllite a) initial brine is 0.001M of CaCl2; b) initial brine is 1M of $CaCl_2$; c) initial brine is 0.001M of NaCl; d) 1M of NaCl.

7.5 Conclusions

Oil sorption analysis using TGA-MS was conducted to observe the influence of different parameters, including physical pre-treatment, water content, brine chemistry (cations identities, concentration, pH, Na^+:Ca^{2+} ratio, and ionic strength). On the basis of these analyses, the following conclusions can be drawn.

1) Only the polar fraction of model oil significantly adsorbs on kaolinite and pyrophyllite.
2) The presence of Ca^{2+} plays a crucial role in determining the extent of oil adhesion, with a clear correlation between cation concentration and the amount of oil sorbed. On the contrary, the presence of Na^+ does not leads to large oil sorption and changes in its concentration do not show a correlation with oil sorption either. Both effects were true for both kaolinite and pyrophyllite samples.
3) Pyrophyllite shows a consistent higher affinity for oil than kaolinite. This is because of the presence of two basal, hydrophobic, siloxane planes in pyrophyllite, as opposed to kaolinite which is bound by a hydrophobic siloxane face and a hydrophilic aluminol face.
4) The effect of Na^+: Ca^{2+}ratio shows that a clear increase in the amount of oil sorption, for both kaolinite and pyrophyllite, as it was decreased (from 20:1 to 1:1). This reinforces the role of Ca^{2+} ions in determining the overall oil sorption properties of both materials through the formation of cation bridges, highlighting the potential role of the MIE mechanism in LSEOR.
5) Results from the experiments performed with varying ionic strength show that EDL expansion may also play a role in determining oil sorption/desorption behaviour. For three different Na^+:Ca^{2+} ratios (10:1, 5:1 and 1:1), a decrease in IS from 1.5 to 0.1 lead to a decrease in oil sorption, but the effect was much more pronounced on the experiments performed with a 1:1 ratio (i.e. when the oil sorption should be the highest). This indicates that a reduction of the double layer width in the presence of large amounts of Ca^{2+} would still lead to a repulsion of most of oil molecules in the vicinity of the clay surfaces. The phenomenon of EDL expansion as a possible function of higher IS might also be explained by increasing Ca^{2+} concentration. This leads to a more complicated picture of the oil sorption mechanism where both EDL and MIE effects will play a competing role depending on the ion concentrations although cation bridging still showed the largest effect on the conditions studied here.

7.6 References

[1] S. KoKal, A. Al-Kaabi, Enhanced oil recovery: challenges & opportunities, Global Energy Solutions, World Petroleum Council: Official Publication 2010 (2010) 4.

[2] A. Muggeridge, A. Cockin, K. Webb, H. Frampton, I. Collins, T. Moulds, P. Salino, Recovery rates, enhanced oil recovery and technological limits, 2014.

[3] V. Alvarado, E. Manrique, Enhanced Oil Recovery: An Update Review, Energies 3(9) (2010) 1529-1575.

[4] M.D. Jackson, J. Vinogradov, G. Hamon, M. Chamerois, Evidence, mechanisms and improved understanding of controlled salinity waterflooding part 1: Sandstones, Fuel 185 (2016) 772-793.

[5] J.J. Sheng, Critical review of low-salinity waterflooding, Journal of Petroleum Science and Engineering 120(0) (2014) 216-224.

[6] T. Austad, A. Rezaeidoust, T. Puntervold, Chemical Mechanism of Low Salinity Water Flooding in Sandstone Reservoirs, Society of Petroleum Engineers, 2010.

[7] G.-Q. Tang, N.R. Morrow, Influence of brine composition and fines migration on crude oil/brine/rock interactions and oil recovery, Journal of Petroleum Science and Engineering 24(2â€“4) (1999) 99-111.

[8] A. Lager, K.J. Webb, I.R. Collins, D.M. Richmond, LoSal Enhanced Oil Recovery: Evidence of Enhanced Oil Recovery at the Reservoir Scale, Society of Petroleum Engineers, 2008.

[9] R.A. Nasralla, M.A. Bataweel, H.A. Nasr-El-Din, Investigation of Wettability Alteration and Oil-Recovery Improvement by Low-Salinity Water in Sandstone Rock, (2013).

[10] S. Strand, T. Puntervold, T. Austad, Water based EOR from clastic oil reservoirs by wettability alteration: A review of chemical aspects, Journal of Petroleum Science and Engineering 146 (2016) 1079-1091.

[11] T.J. Al-aulaqi, Q.J. Fisher, Crude Oil, Brine Salinity and Sandstone Interaction - Nanoscale Resolution, Society of Petroleum Engineers.

[12] A. Lager, K.J. Webb, C.J.J. Black, M. Singleton, K.S. Sorbie, Low Salinity Oil Recovery - An Experimental Investigation1, Petrophysics 49(01) (2008) 8.

[13] K.S. Sorbie, I. Collins, A proposed pore-scale mechanism for how low salinity waterflooding works, SPE improved oil recovery symposium, Society of Petroleum Engineers, 2010.

[14] J. Yang, Z. Dong, M. Dong, Z. Yang, M. Lin, J. Zhang, C. Chen, Wettability alteration during low-salinity waterflooding and the relevance of divalent ions in this process, Energy & Fuels 30(1) (2015) 72-79.

[15] N. Santha, P. Cubillas, A. Saw, H. Brooksbank, C.H. Greenwell, Chemical Force Microscopy Study on the Interactions of COOH Functional Groups with Kaolinite Surfaces: Implications for Enhanced Oil Recovery, Minerals 7(12) (2017).

[16] D.J. Ligthelm, J. Gronsveld, J. Hofman, N. Brussee, F. Marcelis, H. van der Linde, Novel Waterflooding Strategy By Manipulation Of Injection Brine Composition, EUROPEC/EAGE Conference and Exhibition, Society of Petroleum Engineers, Amsterdam, The Netherlands, 2009.

[17] E. Hilner, M.P. Andersson, T. Hassenkam, J. Matthiesen, P.A. Salino, S.L.S. Stipp, The effect of ionic strength on oil adhesion in sandstone – the search for the low salinity mechanism, Scientific Reports 5 (2015) 9933.

[18] R.A. Nasralla, H.A. Nasr-El-Din, Double-Layer Expansion: Is It a Primary Mechanism of Improved Oil Recovery by Low-Salinity Waterflooding?, (2014).

[19] S.Y. Lee, K.J. Webb, I. Collins, A. Lager, S. Clarke, M. O'Sullivan, A. Routh, X. Wang, Low salinity oil recovery: increasing understanding of the underlying mechanisms, SPE improved oil recovery symposium, Society of Petroleum Engineers, 2010.

[20] E.J.W. Verwey, J.T.G. Overbeek, J.T.G. Overbeek, Theory of the stability of lyophobic colloids, Courier Corporation1999.

[21] T.S. Arnarson, R.G. Keil, Mechanisms of pore water organic matter adsorption to montmorillonite, Marine Chemistry 71(3) (2000) 309-320.

[22] D.L. Geatches, A. Jacquet, S.J. Clark, H.C. Greenwell, Monomer Adsorption on Kaolinite: Modeling the Essential Ingredients, Journal of Physical Chemistry C 116(42) (2012) 22365-22374.

[23] T. Underwood, V. Erastova, P. Cubillas, H.C. Greenwell, Molecular Dynamic Simulations of Montmorillonite–Organic Interactions under Varying Salinity: An Insight into Enhanced Oil Recovery, The Journal of Physical Chemistry C 119(13) (2015) 7282-7294.

[24] K.A. Rezaei Gomari, R. Denoyel, A.A. Hamouda, Wettability of calcite and mica modified by different long-chain fatty acids (C18 acids), Journal of Colloid and Interface Science 297(2) (2006) 470-479.

[25] J.-L. Bantignies, C.C.D. Moulin, H. Dexpert, Wettability contrasts in kaolinite and illite clays: characterization by infrared and X-ray absorption spectroscopies, Le Journal de Physique IV 7(C2) (1997) C2-867-C2-869.

[26] V. Alipour Tabrizy, R. Denoyel, A.A. Hamouda, Characterization of wettability alteration of calcite, quartz and kaolinite: Surface energy analysis, Colloids and Surfaces A: Physicochemical and Engineering Aspects 384(1–3) (2011) 98-108.

[27] A.A. Hamouda, K.A. Rezaei Gomari, Influence of Temperature on Wettability Alteration of Carbonate Reservoirs, SPE/DOE Symposium on Improved Oil Recovery, Society of Petroleum Engineers, Tulsa, Oklahoma, USA, 2006, p. 12.

[28] O. Karoussi, A.A. Hamouda, Imbibition of Sulfate and Magnesium Ions into Carbonate Rocks at Elevated Temperatures and Their Influence on Wettability Alteration and Oil Recovery, Energy & Fuels 21(4) (2007) 2138-2146.

[29] G. Buckton, Contact angle, adsorption and wettability — a review with respect to powders, Powder Technology 61(3) (1990) 237-249.

[30] G. Hansen, A.A. Hamouda, R. Denoyel, The effect of pressure on contact angles and wettability in the mica/water/n-decane system and the calcite+stearic acid/water/n-decane system, Colloids and Surfaces A: Physicochemical and Engineering Aspects 172(1) (2000) 7-16.

[31] M.M. Thomas, J.A. Clouse, Thermal analysis of compounds adsorbed on low-surface-area solids. Part 1. measurement and characterization by TGA, Thermochimica Acta 140(C) (1989) 245-251.

[32] K. Jarrahian, O. Seiedi, M. Sheykhan, M.V. Sefti, S. Ayatollahi, Wettability alteration of carbonate rocks by surfactants: A mechanistic study, Colloids and Surfaces A: Physicochemical and Engineering Aspects 410 (2012) 1-10.

[33] V. Gupta, J.D. Miller, Surface force measurements at the basal planes of ordered kaolinite particles, Journal of Colloid and Interface Science 344(2) (2010) 362-371.

[34] S. Brunauer, P.H. Emmett, E. Teller, Adsorption of Gases in Multimolecular Layers, Journal of the American Chemical Society 60(2) (1938) 309-319.

[35] R.J. Pruett, H.L. Webb, Sampling and analysis of KGa-1B well-crystallized kaolin source clay, Clays Clay Miner. 41(4) (1993) 514-519.

[36] Y. Bereznitski, M. Jaroniec, P. Maurice, Adsorption characterization of two clay minerals society standard kaolinites, J. Colloid Interface Sci. 205(2) (1998) 528-530.

[37] R.L. Sanders, N.M. Washton, K.T. Mueller, Measurement of the Reactive Surface Area of Clay Minerals Using Solid-State NMR Studies of a Probe Molecule, The Journal of Physical Chemistry C 114(12) (2010) 5491-5498.

[38] B. Kitabi, Effects of Intensive Milling on the Structural Characteristics of Pyrophyllite Ore, IMMC 2016 (18th International Metallurgy & Materials Congress) (2016) 4.

[39] H. Desai, N.R. Biswal, S. Paria, Rheological Behavior of Pyrophyllite–Water Slurry in the Presence of Anionic, Cationic, and Nonionic Surfactants, Ind. Eng. Chem. Res. 49(11) (2010) 5400-5406.

[40] G.K. Dedzo, C. Detellier, Intercalation of two phenolic acids in an ionic liquid–kaolinite nanohybrid material and desorption studies, Applied Clay Science 97-98 (2014) 153-159.

[41] L. Wang, M. Zhang, S. Redfern, Z. Zhang, Dehydroxylation and transformations of the 2:1 phyllosilicate pyrophyllite at evaluated temperature: An infrared spectroscopic study Clays and Clay Minerals 50(2) (2002) 272-283.

[42] R.L. Frost, A.M. Vassallo, The dehydroxylation of the kaolinite clay minerals using infrared emission spectroscopy, Clays and Clay minerals 44(5) (1996) 635-651.

[43] D. YEsrrs, A.K. vAN Gnoos, S. GuccENHETM, The dehydroxylation of kaolinite.

[44] E. Molina-Montes, D. Donadio, A. Hernández-Laguna, C.I. Sainz-Díaz, M. Parrinello, DFT research on the dehydroxylation reaction of pyrophyllite 1. First-principle molecular dynamics simulations, The Journal of Physical Chemistry B 112(23) (2008) 7051-7060.

[45] V. Alvarado, G. Garcia-Olvera, P. Hoyer, T.E. Lehmann, Impact of Polar Components on Crude Oil-Water interfacial Film Formation: A Mechanisms for Low-Salinity Waterflooding, SPE Annual Technical Conference and Exhibition, Society of Petroleum Engineers, Amsterdam, The Netherlands, 2014, p. 15.

[46] D. Tiab, E.C. Donaldson, Petrophysics: theory and practice of measuring reservoir rock and fluid transport properties, Gulf professional publishing2015.

[47] A. RezaeiDoust, T. Puntervold, T. Austad, Chemical Verification of the EOR Mechanism by Using Low Saline/Smart Water in Sandstone, Energy & Fuels 25(5) (2011) 2151-2162.

[48] K.Y. Zhu, H.Z. Qi, S. Wang, J.W. Zhou, Y.H. Zhao, J.F. Su, X.Y. Yuan, Preparation and characterization of melamine-formaldehyde resin micro- and nano-capsules filled with n-dodecane, 2012.

[49] J. Chen, Z. Ling, X. Fang, Z. Zhang, Experimental and numerical investigation of form-stable dodecane/hydrophobic fumed silica composite phase change materials for cold energy storage, Energy Conversion and Management 105 (2015) 817-825.

[50] Y. Konuklu, H.O. Paksoy, M. Unal, S. Konuklu, Microencapsulation of a fatty acid with Poly(melamine–urea–formaldehyde), Energy Conversion and Management 80 (2014) 382-390.

[51] L. Wang, M. Zhang, S.A.T. Redfern, Z. Zhang, Dehydroxylation and transformations of the 2:1 phyllosilicate pyrophyllite at elevated temperatures: An infrared spectroscopic study, Clays Clay Miner. 50(2) (2002) 272-283.

[52] Y. Hu, X.-w. Liu, Z. Xu, Role of crystal structure in flotation separation of diaspore from kaolinite, pyrophyllite and illite, Minerals Engineering 16(3) (2003) 219-227.

[53] X. Yin, V. Gupta, H. Du, X. Wang, J.D. Miller, Surface charge and wetting characteristics of layered silicate minerals, Advances in Colloid and Interface Science 179-182(0) (2012) 43-50.

[54] X. Yin, J. Miller, Wettability of kaolinite basal planes based on surface force measurements using atomic force microscopy, Minerals and Metallurgical Processing 29(1) (2012) 13-19.

[55] G. Lagaly, M. Ogawa, I. Dékány, Chapter 7.3 Clay Mineral Organic Interactions, in: F. Bergaya, B.K.G. Theng, G. Lagaly (Eds.), Developments in Clay Science, Elsevier2006, pp. 309-377.

[56] A.J. Rutgers, Y. Hendrikx, Ionic hydration, Transactions of the Faraday Society 58(0) (1962) 2184-2191.

[57] P.D. Archer, D.W. Ming, B. Sutter, The effects of instrument parameters and sample properties on thermal decomposition: Interpreting thermal analysis data from Mars, Planetary Science 2(1) (2013) 2.

[58] J. Umemura, H.H. Mantsch, D.G. Cameron, Micelle formation in aqueous n-alkanoate solutions: A fourier transform infrared study, J. Colloid Interface Sci. 83(2) (1981) 558-568.

[59] S. Kang, B. Xing, Adsorption of Dicarboxylic Acids by Clay Minerals as Examined by in Situ ATR-FTIR and ex Situ DRIFT, Langmuir 23(13) (2007) 7024-7031.

[60] J.J. Max, C. Chapados, Infrared Spectroscopy of Aqueous Carboxylic Acids: Comparison between Different Acids and Their Salts, The Journal of Physical Chemistry A 108(16) (2004) 3324-3337.

[61] C. Nyambo, P. Songtipya, E. Manias, M.M. Jimenez-Gasco, C.A. Wilkie, Effect of MgAl-layered double hydroxide exchanged with linear alkyl carboxylates on fire-retardancy of PMMA and PS, J. Mater. Chem. 18(40) (2008) 4827-4838.

[62] T. Bala, B. Prasad, M. Sastry, M.U. Kahaly, U.V. Waghmare, Interaction of different metal ions with carboxylic acid group: a quantitative study, The Journal of Physical Chemistry A 111(28) (2007) 6183-6190.

[63] M.D. Porter, T.B. Bright, D.L. Allara, C.E.D. Chidsey, Spontaneously organized molecular assemblies. 4. Structural characterization of n-alkyl thiol monolayers on gold by optical ellipsometry, infrared spectroscopy, and electrochemistry, J. Am. Chem. Soc. 109(12) (1987) 3559-3568.

[64] D. Lin-Vien, N.B. Colthup, W.G. Fateley, J.G. Grasselli, The handbook of infrared and Raman characteristic frequencies of organic molecules, Elsevier1991.

[65] M.A. Osman, U.W. Suter, Surface Treatment of Calcite with Fatty Acids: Structure and Properties of the Organic Monolayer, Chem. Mater. 14(10) (2002) 4408-4415.

8
Conclusions and future work

8.1 Conclusions

This thesis has focussed on the study of the microscopic and nano-scale mechanisms of clay-oil-brine interactions that underpin the wettability alteration in low salinity enhanced oil recovery using three main experimental techniques: chemical force microscopy, contact angle measurements, and thermogravimetric analysis-mass spectrometry. The overall aims of the research were:

To study the adhesion of several functional groups present in crude oil (-COOH and $-NH_2$ to kaolinite crystals under different brine conditions (cation type, concentration and pH) at the atomic scale using chemical force microscopy (CFM).

To understand the role of the two types of kaolinite basal faces (silica tetrahedral *vs*. aluminol octahedral) in determining the adhesion of functional groups (-COOH and $-NH_2$) under different brine conditions (cation type, concentration and pH) at the atomic scale using chemical force microscopy.

To understand how the chemical properties of brine (salinity, cation type, pH, ionic strength and Na^+:Ca^{2+} ratio) determine the adhesion of model oil compounds (both polar and non-polar) to kaolinite basal surfaces at the microscopic scale, using contact angle measurements.

To determine how the chemical properties of brine (salinity, cations type, pH), as connate (formation) water, determine the sorption of model oil (both polar and non-polar) to kaolinite and pyrophyllite crystals, by means of thermal gravimetric analysis-mass spectrometry.

A wide number of experiments were carried out in order to answer these aims and the accomplishments and contributions are summarized as follows:

Aim 1: To study the adhesion of several functional groups present in crude oil (-COOH, and $-NH_2$) to kaolinite crystals under different brine conditions (cation type, concentration and pH) at the atomic scale using chemical force microscopy (CFM).

Results from the CFM experiment were discussed in detail in Chapter 5. These were focused on gaining an understanding of the atomic-level adhesion between acidic (-COOH) and basic ($-NH_2$) polar components. The results indicate that the presence of Ca^{2+} ions enhances the adhesion of acidic functional group (-COOH) to the siloxane face when its concentration is increased (low salinity effect) at pH 8. On the contrary, at pH 5.5, an increase in the concentration of Ca^{2+} leads to the reverse effect (a decrease in adhesion). Importantly, at both pHs no clear effect on the adhesion with concentration was observed when the cation in solution was the monovalent Na^+, which illustrates the critical role of divalent cations. In addition it was observed that an increase of pH (at constant Ca^{2+}) lead to a sharp increase in the recorded adhesion. In the case of the functional group $-NH_2$, an increase in pH (in the presence of Ca^{2+}) lead to a decrease in the measured adhesion. It was also observed that for the $-NH_2$ probes that the effect of varying $CaCl_2$ was pH dependent. Although at pH 6.5 a low salinity effect was observed, the situation was reversed when the measurements were performed at pH 8. Both groups of results (with –COOH and $-NH_2$ probes) highlight the crucial role that the presence of divalent cations have on adhesion, but also illustrate the role of surface complexation and protonation state (both determined by pH). In addition electric double layer effects certainly play also a role (albeit smaller) in determining the adhesion of functional groups at certain high pHs. Therefore, results from the CFM experiment paint a more complex picture on the interactions between organic molecules and the siloxane face of kaolinite than can be described by a single mechanism.

Aim 2: To understand the role of the two types of kaolinite basal surfaces (silica tetrahedral vs. aluminol octahedral) in determining the adhesion of functional groups (-COOH andNH_2) under different brine conditions (cation identity, concentration and pH) at the atomic scale using chemical force microscopy.

Results from the model oil adsorption TGA-MS experiments at pH 6.5 and pH 8 and on various brines (0.001, 0.01, 1 M of either $CaCl_2$ or NaCl) reported in Chapter 6 also bring additional insight to the role of the two distinct faces in the kaolinite structure. Under the same conditions, the siloxane surface (pyrophyllite) prefer polar oil rather than water, while siloxane and aluminol face (1:1) in kaolinite showed less adsorption of the polar model oil. This indicated that siloxane face is more oil wetting than the aluminol face.

Aim 3: To understand how the chemical properties of brine (salinity, cation type, pH, ionic strength and Na^+:Ca^{2+} ratio) determine the adhesion of model oil compounds (both polar and non-polar) to kaolinite surfaces at the microscopic scale, using contact angle measurements.

In Chapter 6, contact angle measurements were taken over oriented kaolinite films (siloxane face). The results indicate that pH is a far more important parameter in determining the initial oil adhesion (as formation water) than cation identity with only increases in pH showing a clear effect of increasing oil adsorption over the surface, and with changes in cation type and concentrations showing almost no effect in changing the resulting wettability state. Moreover, the results of brine treatment after oil-aging suggest that low concentration of $CaCl_2$ and NaCl induced the surface to be more water, whereas 1M concentration of $CaCl_2$ is less effective for changing the surface from oil-wetting to water-wetting.

Aim 4: To determine how the chemical properties of brine (salinity, cations types, pH), as connate water, determine the sorption of model oil (both polar and non-polar) to kaolinite and pyrophyllite crystals, by means of thermal gravimetric analysis.

In Chapter 7 (TGA-MS), the quantity of oil adsorption upon clay mineral films was examined comparing the effect of two sets of brines. The first set of experiments studied the influence of brine concentration (0.001, 0.01, 1 M of $CaCl_2$ and NaCl) and pH (pH 6.5 and 8). It was observed that cation type played a major role in determining the adhesion of polar oil to both kaolinite and pyrophyllite, in particular the amount of oil adsorption is positively related with higher concentration of divalent cations, but no trends were observed with monovalent cations (which also showed a smaller overall oil sorption). pH did not have an effect on oil sorption on the presence of Ca^{2+}, probably because of competing effects between the siloxane and aluminol faces. However pH increase did result in important relative changes in oil sorption on the presence of Na^+, with a decrease recorded with increasing pH. The second set of experiment was extended to study the influence of ionic strength and Na^+: Ca^{2+} ratio. Both kaolinite and pyrophyllite adsorbed polar model oil when the relative concentration of Ca^{2+} was increased. This confirmed that divalent cations play a critical role in controlling oil adsorption. However, experiments were the IS was decreased at constant Na^+:Ca^{2+} showed a notable effect on reducing oil sorption, especially at high Ca^{2+} indicating, once again, that even though the presence of divalent cations is an important control on sorption, under certain conditions the double layer effect can also play a major role.

8.2 Future work

Based on conclusions drawn throughout the period of supervised study, several techniques were examined and shown to yield important qualitative and quantitative data of the oil-clay-brine interaction in both microscopic and nano-scales, in order to gain insight into low-salinity EOR. We have evidenced that surface complexation and divalent cation bridging are key features of the clay-oil-brine interfaces, but also that the electric double layer effect can play at role at specific salinity and pH conditions. To gain a better understanding of the clay-oil-brine interfaces, it would be noteworthy to extend this work and we can propose a number of research questions that arise from this study.

8.2.1 Wettability on aluminol octahedral in contact angle measurement

The experiments performed in Chapter 5 (CFM) showed marked differences in behaviour between the siloxane and aluminol surfaces, in part driven by changes in protonation state as a function of pH but also to the inherent differences in surface complexation due to the crystallographic particularities of each face. However, the study in Chapter 6 (contact angle measurement) was performed only on the silica tetrahedral surface of kaolinite films. According to the study of Miller group research, the authors state that the siloxane face of kaolinite also has isomorphous substitution of Al^{3+} for Si^{4+}, while the alumina octahedral layer has substitution of Mg^{2+} for Al^{3+}. This causes a slightly different charge between the silica face and alumina face of kaolinite. Eventually, the authors distinguished the two surfaces of kaolinite by using a microscopic glass slide and a fused alumina-substrate, because the negatively charged glass-substrate attached preferentially to the aluminol surface of kaolinite and glass slide would expose the silica face, while the positively charged fused alumina-substrate would expose the alumina face by allowing the silica face to attach. Hence, a possible direction of investigation is to produce the kaolinite film which exposed only aluminol octahedral surface. This proposed investigation could be carried out using a fused alumina-substrate (sapphire) instead of a microscopic glass slide as the substrate to deposit the clay film. Moreover, a possible extension of the experiments described in Chapter 6 in both siloxane surface of kaolinite film and aluminol tetrahedral of kaolinite film could be to further undertake a secondary and a tertiary brine treatment in order to mimic the secondary and tertiary water flooding during LSEOR.

8.2.2 Wettability at wider range of pH

The investigation in Chapter 7 (TGA-MS) and Chapter 6 (contact angle measurement) used brine in a narrow pH window (only pH 6.5 and pH 8). However, the demonstration of such an effect based on the results of Chapter 5 (CFM) which suggested that aluminol tetrahedral surface of kaolinite changes the surface charge at pH 5.5 to pH 8. Thus, for a further contact

angle and TGA-MS study, the aging brine could be prepared at a wider pH range from 4-10 before the aging in the model oil; while, additionally, for contact angle measurements it should be possible to extend the pH range in the measured brine in the captive bubble technique. Additionally, the contact angle measurements could be performed on a temperature controlled bath to study these effects at more relevant temperature conditions.

8.2.3 Spectroscopic methods

Although this thesis presented here describes the role of a range of key parameters can affect or determine the nanogeochemical mechanisms behind wettability alteration of clay minerals, there would be merit in using direct techniques to identify the chemical bonding between clay-oil-brine. On the basis of the work in this thesis, it mainly determines the wettability in microscopic scale using captive bubble technique, and examines proxy of wettability, including adhesion and amount of oil adsorption by CFM and TGA-MS respectively. Therefore, it is highly recommended to attempt to directly identify the chemical bonding between clay-oil-brine using FTIR, for which some initial trials were run during the final stages of this study.

Finally, the work presented in this thesis has made good progress in advancing our knowledge on the fundamental reactions driving the interactions of oil molecules with kaolinite. Although during the time it has taken to perform the study many other papers have been published in the literature concerning LSEOR and in particular the role of clay minerals. This study has made some important breakthroughs, including the publication of the first CFM study on kaolinite (studying both faces) and the use of a surface complexation model, along with DLVO theory, to discuss our results, bringing together different approaches used in past investigations separately. In addition, bringing together two additional techniques two additional techniques to study the role of “formation water” in determining the oil adhesion, and therefore the wettability state had not been reported together before. This thesis has also helped to bridge the gap between very detailed studies in model materials (mica, fused silica, sapphire) and those performed with crude oil and reservoir rocks, by employing natural, but well characterised kaolinite crystals and a realistic mixture of model oil. In that regard, is has been our intention to be able to reach to audiences from both the petroleum engineering and fundamental chemistry/physics fields, which sometimes do not collaborate as close as they should to bring about a better understanding of these complex and wide-reaching phenomena.